Novel Planar Interdigital Sensors for the Detection of Bacterial Endotoxins

A thesis presented in partial fulfilment of the requirements for the degree of
Doctor of Philosophy in Electronics Engineering
at Massey University, Palmerston North, New Zealand

MOHD SYAIFUDIN BIN ABDUL RAHMAN

2012

To my parents

Abdul Rahman Daud

Mariah Bt Deraman

To my wife

Nurhanina Mohamad Akib

And to my children

Nurafifah Afrina

Muhammad Afiq

Muhammad Ammar

Muhammad Asyraf

Muhammad Aiman

Abstract

Food poisoning caused by endotoxins or Lipopolysaccharide (LPS) are associated with Gram-negative bacteria. Foodborne pathogens, *Escherichia coli* (*E. coli*) and *Salmonella* are examples of Gram-negative bacteria which could cause large food poisoning outbreaks. New types of planar interdigital sensors have been fabricated with different coating materials to assess their response to endotoxins. A carboxyl-funtional polymer, APTES (3-Aminopropyltriethoxysilane) and Thionine were chosen for coating the novel interdigital sensors. All coated sensors were immobilized with PmB (Polymyxin B) which has specific binding properties to LPS. The sensors were tested with different concentrations of LPS O111:B4, ranging from 0.1 μg/ml to 1000 μg/ml. Analyses of sensors' performance were based on the Impedance Spectroscopy method. The impedance spectra were modelled using a Constant Phase-Element (CPE) equivalent circuit, and a Principal Component Analysis (PCA) was used for data classification. Sensors coated with APTES have shown better selectivity towards LPS detection. The experiments were repeated by coating APTES and immobilizing PmB to a newly improved design of silicon based interdigital sensor. Scanning electron microscope (SEM) and atomic force microscope (AFM) images were taken to analyse the APTES coating surface and PmB immobilization. The images of non-coated sensors and coated silicon sensors were studied and the thickness of a single layer coating was estimated (≈268 nm). Analyses of results with LPS O111:B4 showed that these silicon sensors have higher sensitivity and selectivity to the target biomolecule LPS. The complex non-linear least squares (CNLS) fitting method was used to fit the measured impedance spectra based on chosen equivalent circuit model. PCA results were clustered, showing the parameters were related and have identified process which related to the diffusion, charge transfer and adsorption of molecules on sensors' surface. It was also found that these sensors can detect the standard endotoxin as low as 0.01 EU/ml which is equivalent to 1 pg/ml. Selectivity, stability and sensitivity of different thickness of coated sensors were analysed. It was observed that the optimum thickness layer is 3-layers of coating which is equivalent to 800 nm. Analyses of results with food samples have shown the developed novel interdigital sensors can detect the presence of endotoxin in contaminated food samples.

Research Outputs

The research outputs which have been published are listed below. The research outputs are in conjunction with the author's Ph.D candidacy:

Book Chapters

1. Mohd Syaifudin Bin Abdul Rahman, Subhas C. Mukhopadhyay, Pak-Lam Yu, Michael J. Haji-Sheikh and Cheng-Hsin Chuang. *"Sensors for Food Inspections"*. Chapter 4 in Modern Sensors, Transducers and Sensor Networks (Book Series: *Advances in Sensors: Reviews, Vol. 1*). International Frequency Sensor Association (IFSA) Publishing. 15 May 2012. ISBN: 978-84-615-9012-4.

2. A. R. Mohd Syaifudin, Subhas Chandra Mukhopadhyay, Pak-Lam Yu, Michael J. Haji-Sheikh, and Cheng-Hsin Chuang. *"Impedance Spectroscopy of Novel Interdigital Sensors for Endotoxin Detection"*. Taylor and Francis Group- CRC Press: Lecture Notes on Impedance Spectroscopy - Measurement, Modelling and Applications - Kanoun (ed). Volume 2. Copyright 2012, CRC Press, Taylor & Francis Group, London. Pp. 103- 112. ISBN 978-0-415-69838-2.

Journals

1. Mohd Syaifudin Abdul Rahman, Subhas Chandra Mukhopadhyay, Pak-Lam Yu, Javier Goicoechea, Ignacio R. Matias, Chinthaka P. Gooneratne, and Jűrgen Kosel. *"Bacterial Endotoxin in Food: New Planar Interdigital Sensors based Approach". Elsevier:* Journal of Food Engineering 114 (2013). Pp. 346–360, DOI: 10.1016/j.jfoodeng.2012.08.026. 14th September 2012.

2. A. R. Mohd Syaifudin, Subhas Chandra Mukhopadhyay, Pak-Lam Yu, Michael J. Haji-Sheikh, Cheng-Hsin Chuang, John D. Vanderford, and Yao-Wei Huang. *"Measurements and Performance Evaluation of Novel Interdigital Sensors for Different Chemicals Related to Food Poisoning"*. IEEE Sensors Journal, Vol. 11, No. 11, Pp. 2957-2965. DOI: 10.1109/JSEN.2011.2154327. November 2011.

3. A. R. Mohd Syaifudin, S. C. Mukhopadhyay and P. L. Yu. *"Modelling and Fabrication of Optimum Structure of Novel Interdigital Sensors for Food Inspection"* Wiley: International Journal of Numerical Modelling: Electronic Networks, Devices and Fields. Vol. 24, Issue 6. Pp. 1-18. DOI: 10.1002/jnm.813. ISSN: 1099-1204. 1st February 2011.

4. Mohd. Syaifudin Abdul Rahman, Subhas C. Mukhopadhyay and Pak-Lam Yu. *"Novel Sensors for Food Inspections"*, Sensors & Transducers Journal**.** Vol. 114, Issue 3, March 2010, Pp. 1- 40. ISSN: 1726- 5479.

Proceedings and Conference Papers

1. A.R. Mohd Syaifudin, Asif I. Zia, S. C. Mukhopadhyay, P.L. Yu, Chinthaka P. Gooneratne and Jűrgen Kosel.*"Improved Detection Limits of Bacterial Endotoxins Using New Type of Planar Interdigital Sensors"*. Proceeding of IEEE Sensors 2012 Conference, Taipei, Taiwan. Pp. 2034-2037. 28th–31st October, 2012. IEEE Catalog Number: CFP12SEN-USB. ISBN: 978-1-4577-1765-9.

2. A.R. Mohd Syaifudin, S. C. Mukhopadhyay, P.L. Yu, Cheng-Hsin Chuang, Hsun-Pei Wu, Jürgen Kosel, and Chinthaka P. Gooneratne. *"Characterizations and Performance Evaluations of Thin Film Interdigital Sensors for Gram-Negative Bacteria Detection"*. Proceeding of 5th International Conference on Sensing Technology (ICST 2011), Palmerston North, New Zealand. Pp. 186 – 191. 28th Nov – 1st Dec 2011. IEEE Catalog Number: CFP1118E-CDR. ISBN: 978-1-4577-0167-2.

3. Asif. I. Zia, A.R. Mohd Syaifudin, S.C. Mukhopdhyay, I. H. Al-Bahadly and P.L. Yu, C.P. Gooneratne and Jürgen Kosel. *"Development of Electrochemical Impedance Spectroscopy Based Sensing System for DEHP Detection"*. Proceeding of 5th International Conference on Sensing Technology (ICST 2011), Palmerston North, New Zealand. Pp. 703 – 711. 28th Nov – 1st Dec 2011. IEEE Catalog Number: CFP1118E-CDR. ISBN: 978-1-4577-0167-2.

4. A.R. Mohd Syaifudin, S. C. Mukhopadhyay, P.L. Yu, Ignacio R. Matias, J. Goicoechea, Jürgen Kosel, and Chinthaka P. Gooneratne**.** *"Analyses of Performance of Novel Sensors with Different Coatings for Detection of Lipopolysaccharide"*. Proceeding of IEEE Sensors 2011 Conference, Limerick, Ireland. Pp. 588 – 591. October 28-31, 2011. IEEE Catalog Number: CFP11SEN-CDR. ISBN: 978-1-4244-9288-6. DOI: 10.1109/ICSENS.2011.6127023.

5. A.R. Mohd Syaifudin, S. C. Mukhopadhyay, P.L. Yu, Michael J. Haji-Sheikh, Cheng-Hsin Chuang and Hsun-Pei Wu*. "Detection of Natural Bio-Toxins Using an Improved Design Interdigital Sensors"*. Proceeding of IEEE Sensors 2011 Conference, Limerick, Ireland. Pp. 1028 - 1031. October 28-31, 2011. IEEE Catalog Number: CFP11SEN-CDR. ISBN: 978-1-4244-9288-6. DOI: 10.1109/ICSENS.2011.6127038.

6. A.R. Mohd Syaifudin, S. C. Mukhopadhyay, P.L. Yu, Michael J. Haji-Sheikh and Cheng-Hsin Chuang*. "Novel Interdigital Sensors: Analysis, Measurement and Evaluations"*. Proceeding of the IEEE: International Instrumentation and Measurement Technology Conference, (I^2MTC). Binjiang, Hangzhou, China. Pp 358-362. May 10-12, 2011. ISBN: 978-1-4244-7934-4.

7. A.R. Mohd Syaifudin, P.L. Yu, S. C. Mukhopadhyay, Michael J. Haji-Sheikh and J. Vanderford. *"A performance evaluation of new developed novel planar interdigital sensors"*. Proceeding of the International Instrumentation and Measurement Technology Conference, (I^2MTC). Hilton. Austin, Texas. United States. Pp 731-736 May 3-6, 2010. DOI: 10.1109/IMTC.2010.5488245.

8. A.R. Mohd Syaifudin, C.P. Gooneratne, S. C. Mukhopadhyay, P.L. Yu, C-H. Chuang, Y-W. Huang, Michael J. Haji-Sheikh and J. Vanderford. "*A comparative study of three different designs of novel planar interdigital sensors for food inspections.*" Proceeding of the 4th International Conference on Sensing Technology (ICST 2010). *Lecce, Italy.* Pp 560-564. June 3-5, 2010.

9. A.R. Mohd Syaifudin, M. A. Yunus, K. P. Jayasundera and S. C. Mukhopadhyay. *"A Novel Planar Interdigital Sensor for Environmental Monitoring"*. Proceeding of the IEEE SENSORS 2009 Conference. Christchurch Convention Centre, Christchurch, New Zealand. Pp 105-110, 25-28 October 2009. DOI: 10.1109/ICSENS.2009.5398227.

10. A.R. Mohd Syaifudin, K. P. Jayasundera , and S. C. Mukhopadhyay. *"A novel planar interdigital sensor based sensing and instrumentation for detection of dangerous contaminated chemical in seafood"*. Proceeding of the IEEE: International Instrumentation and Measurement Technology Conference (I²MTC), Singapore. Pp 701-706, 5-7 May 2009. DOI: 10.1109/IMTC.2009.5168540.

11. A. R. Mohd Syaifudin, S. C. Mukhopadhyay and P. L. Yu. *"Electromagnetic Field Computation using COMSOL Multiphysics to Evaluate the Performance of Novel Interdigital Sensors"*. Proceeding of the IEEE Applied Electromagnetic Conference. Hyatt Regency Kolkata, India. 4 pages. 14-16 Dec 2009. DOI: 10.1109/AEMC.2009.5430661.

Seminars

1. A.R. Mohd Syaifudin, S. C. Mukhopadhyay and P. L. Yu. *"Bacterial Endotoxin: Analyses using New Type of Planar Interdigital Sensors"*. Electronics, Information and Communication System (EICS) Seminar, 2nd August 2012. Massey University, New Zealand.

2. A.R. Mohd Syaifudin, S. C. Mukhopadhyay and P. L. Yu. *"Characterization and Measurement of Novel Interdigital Sensors using Impedance Spectroscopy"*. 2011 IEEE (NZ) Sensors, Measurement and Instrumentation Workshop. AUT, Auckland. 10th – 11th March 2011.

3. A. R. Mohd Syaifudin, S. C. Mukhopadhyay, and P.L. Yu. *"Novel Planar Interdigital Sensors for Detection of Dangerous Toxins*". IEEE Instrumentations

and Measurement Society New Zealand Chapter Workshop, 1st – 2nd September 2010. Victoria University, Wellington. New Zealand.

4. A. R. Mohd Syaifudin, S. C. Mukhopadhyay and P.L. Yu. *"Novel Interdigital Sensors Analysis, Measurement and Performance Evaluations*". IEEE Postgraduates Seminar, IEEE New Zealand Central. 31st August 2010. Massey University, Palmerston North. New Zealand.

5. A. R. Mohd Syaifudin. *"Novel Sensors for Endotoxins Detection"*. Electronics, Information and Communication System (EICS) Seminar, 31st May 2010. Massey University, New Zealand.

6. A. R. Mohd Syaifudin. *"Novel Sensors for Food Inspections"*. PhD confirmation seminar. 17th February 2010. Massey University, Palmerston North. New Zealand.

7. A. R. Mohd Syaifudin. *"A Smart Sensor System for Raw Seafood Inspection"*. IEEE Post Graduate Presentations. 4th September 2009. Victoria University. Wellington. New Zealand.

Awards

1. Listed in 10 best articles award in 2010 from International Frequency Sensor Association (IFSA) and Sensor & Transducers Journal's Editorial Board for the article titled: *"Novel Sensors for Food Inspections"*, Sensors & Transducers Journal**.** Vol. 114, Issue 3, March 2010, Pp. 1- 40. ISSN: 1726- 5479.

Acknowledgements

All praise due to Allah the Al-Mighty for His blessing and benevolence.

I wish to acknowledge the people who have helped and supported me throughout the Ph.D program and also their contributions towards the completion of the thesis.

I would like to express my deepest gratitude to Professor Dr. Subhas Chandra Mukhopadhyay and Associate Professor Dr. Pak-Lam Yu for their support and supervisions. Thank you for the invaluable guidance, constructive criticisms and opinions and constant encouragement throughout this study.

I would like to express my sincere thanks to Dr. Chinthaka Gooneratne, Dr. Javier Goicoechea, and Associate Professor Dr. Michael J. Haji-Sheikh, Associate Professor Dr. Cheng-Hsin Chuang for their active collaborations in the research. Also to Mrs. Ann Mary, Mrs. Judy, Miss Julia, Mr. Ken Mercer, Mr. Collin Plaw, Mr. Bruce Collins, Mr. Doug, Mr. Nagender Suryadevaraj, Mr. Haidar Khan, Mr. Nathan Eichler, Mr. Brendon, Mr. Asif Zia, Mr. Mohd Salihin and Dr. Amri Mohd Yunus for your assistance and support during my research were most appreciated.

Special thanks to my beloved parents, family and friends for their unconditional love and support for my success. Also I would like to thank Massey University and Malaysian Agricultural Research and Development Institute (MARDI) for the financial support and assistance.

Last but not least, I am indebted to my wife Nina, who has sacrificed her time accompanying me in New Zealand. Thank you for your love, support, patience throughout my study. To my lovely and beautiful children, Afrina, Afiq, Ammar, Asyraf and Aiman, thank you for your patience and being such wonderful companies through my years of study in New Zealand.

Table of Contents

List of Figures

List of Tables

Abbreviations

SEAT	School of Engineering and Advanced Technology
LPS	Lipopolysaccharide
PmB	Polymyxin B
E. coli	*Escherichia coli*
VTEC	Verotoxin-producing *Escherichia coli*
STEC	Shiga Toxin-producing *Escherichia coli*
DNA	Deoxyribonucleic Acid
PCR	Polymerase Chain Reaction
ELISA	Enzyme Linked Immunosorbent Assays
LAL	Limulus Amoebocyte Lysate
FDA	United States Food and Drug Administration
EU	Endotoxin Unit
LOD	Limit of Detection
AMP	Antimicrobial Peptides
SPR	Surface Plasmon Resonance
FTIR	Fourier Transform Infrared Spectroscopy
ISE	Ion-Selective Electrodes
ISFET	Ion-Sensitive Field Effect Transistors
EIS	Electrochemical Impedance Spectroscopy
IS	Impedance Spectroscopy
AC	Alternating Current
QCM	Quartz Crystal Microbalance
SAW	Surface Acoustic Wave
NMR	Nuclear Magnetic Resonance
SNR	Signal to Noise Ratio
IDTs	Interdigital Transducers
IDAM	Interdigitated Array Microelectrode
IDES	Interdigitated Electrode Structures
EC	Electrolyte Conductivity
MUT	Material Under Test
DUT	Device Under Test

dH_2O	Distilled water
APTES	3-aminopropyltrietoxysilane
NaCl	Sodium Chloride
LPS O111:B4	Lipopolysaccharides from *Escherichia coli* O111:B4
CNLS	Complex Non-linear Least Square
PCA	Principal Component Analysis
PC	Principal Component
SAS	Statistical Analysis Software
SEM	Scanning Electron Microscope
AFM	Atomic Force Microscope
Sensor 1_11	Sensor with eleven negative electrodes in between two positive electrodes. The configuration is 1_11_1
Sensor 1_5	Sensor with five negative electrodes in between positive electrodes. The configuration is 1_5_1_5_1
Sensor 1_3	Sensor with three negative electrodes in between positive electrodes. The configuration is 1_3_1_3_1_3_1
Din_10mil	Conventional interdigital sensor design of pitch length 10 mil
Din_20mil	Conventional interdigital sensor design of pitch length 20 mil
Din_40mil	Conventional interdigital sensor design of pitch length 40 mil
FR4	Fiberglass reinforced epoxy laminates for PCB fabrication
Alumina-Al_2O_3	Aluminium Oxide
PCB	Printed Circuit Board
PR	Photo Resist
MEMS	Micro-electromechanical Systems
Si	Silicon
SiO_2	Silicon Dioxide
TMAH	Tetra-Methyl Ammonium Hydroxide
Cr	Chromium
Au	Gold
Si_3N_4	Silicon Nitride
PECVD	Plasma enhanced chemical vapour deposition
RIE	Reactive ion etching
LCR 821	Measuring instrument for impedance (inductance, capacitance and

	resistance)
RS232	Serial communication port
HFORCE	Carries the signal current source. Connected to the +ve side of the DUT
LFORCE	Accepts the signal current return. Connected to the –ve side of the DUT.
HSENSE	Together with Lsense, monitors the Potential,V. Connected to the +ve side of the DUT.
LSENSE	Together with Hsense, monitors the Potensial, V. Connected to the –ve side of the DUT
GND	Electrical ground
CPE	Constant Phase-Element
PDEs	Partial differential equations
R	Resistance
C	Capacitance
Q	Charge
V	Voltage
I	Current
f	Frequency
Z	Impedance
θ	Phase Angle, theta
W_e	The electrostatic energy density
D	The electric displacement
E	The electric field intensity
ε_0	The permittivity of vacuum which sets to be 8.854×10^{-2} F/m
ε_r	The relative permittivity
ε	The permittivity
ω	The angular frequency
UV	Ultra-violet
Nyquist	Data presentation in complex impedance plot
Bode	Data presentation as a function of frequency
MilliQ	Ultra-pure water which undergo the proses filtration and deionisation that has been characterised in terms of resistivity (typically 18.2 MΩ·cm)
pH	Potential of hydrogen
H^+	Hydrogen ions

OH^-	Hydroxide ions
Coating A	Electrospun membrane of Carboxylic functional polymer
Coating B	Spin coated Carboxylic functional polymer
Coating C	Dip-Coated silica coating funcitonalized with APTES
Coating D	Dip coated silica with Thionine
$Na_2B_40_7*10H_20$	Sodium Tetraborate
H_3BO_3	Boric Acid
$Na_2HPO_4.2\ H_2O$	Disodium Hydrogen Phosphate
KH_2PO_4	Potassium Dihydrogen Phosphate
TEOS	Tetraethylorthosilicate
EtOH	Ehanol
HCl	Hydrochloric Acid
C_{dl}	Double-layer capacitance
R_s	Solution resistance
R_{ct}	Charge/electron transfer resistance
Z_W	Warburg impedance
σ_w	Warburg coefficient
C_{ad}	Adsoption capacitance

CHAPTER 1

Introduction

1.1 Food Poisoning

Food poisoning is a general term used to describe illness caused by food-borne microorganisms. Foodborne diseases have occurred worldwide because of the contaminated food with these microorganisms. Figure 1.1 shows the number of cases of foodborne illness worldwide which has been compiled by GRAIN (A research group that supports community-controlled and biodiversity-based food systems) [1]. According to the report, study has been conducted by Singaporean authorities, which indicates that about 1.5 billion of people worldwide are affected by foodborne outbreak each year, resulting in 3 million deaths. Typical symptoms of food poisoning include nausea, vomiting, diarrhea, and abdominal cramping. These symptoms may occur suddenly or within 48 hours after consuming a contaminated food or drink. Fever and chills, bloody stools, dehydration, and nervous system damage may follow after these symptoms depending on how serious the contamination is. These symptoms may affect one person or a group of people who has consumed the same food or drink which is called an outbreak.

Ingesting contaminated food by bacteria, viruses and parasites can cause food poisoning or foodborne diseases outbreak. Table 1.1 [2] shows the estimates of foodborne illness due to microbial hazards in USA [3], Australia [4], England and Wales [5] and Netherlands [6] which has been caused by bacteria, virus and parasites. Table 1.2 shows the potentially foodborne conditions which has been reported in the New Zealand Foodborne Disease Annual Report 2010 [2]. It was observed that most of the foodborne diseases in New Zealand for 2010 were caused by bacteria or bacterium. The study of economic cost caused by foodborne disease in New Zealand has been conducted and it was estimated the economic cost of these foodborne diseases in 2009 was $161.9 million. This includes government outlays of $16.4 million, industry cost of $12.3 million and $133.2 million for incident case cost of disease associated with treatment, loss of output and residual lifestyle loss [7]. Details of the economic cost are shown in Table 1.3. It was calculated the total cost to New Zealand society from foodborne illness mainly caused by *Campylobacter, Salmonella, Listeria, E. coli,*

Yersinia and *norovirus*. The study has indicated that the economic cost from these foodborne diseases mainly caused by contaminated food with bacteria.

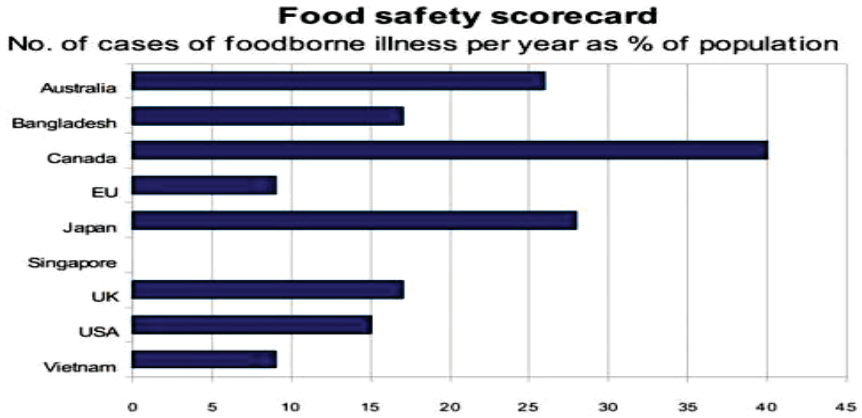

Figure 1.1: Number of cases of foodborne illness worldwide (Source: Data compiled by GRAIN from government and UN sources, 2008-2010, except Australia in 2005) [1]

Table 1.1: The estimates of foodborne illness due to microbial hazards from four countries; USA, Australia, England and Wales and Netherlands [2].

Hazard	% Foodborne			
	USA (2011)	Australia (2005)	England and Wales (2002)	Netherlands (2008)
Bacteria				
Bacillus cereus	100	100	100	90
Campylobacter spp.	80	75	80	42
Clostridium perfringens	100	100	94	91
Shiga toxin-producing *Escherichia coli*(STEC) O157:H7	68	65	63	40
STEC non-O157	82	NE	63	42
Listeria monocytogenes	99	98	99	69
Salmonella non-typhoidal	94	87	92	55
Shigella spp.	31	10	8	NE
Staphylococcus aureus	100	100	96	87
Yersinia enterocolitica	90	75	90	NE
Parasitic				
Cryptosporidium parvum	8	10	6	12
Giardia lamblia	7	5	10	13
Viral				
Hepatitis A virus	7	10	11	11
Norovirus	26	25	NE	17

NE = not estimated

Table 1.2: The potentially foodborne conditions in the New Zealand Foodborne Disease Annual Report 2010 [2].

Disease	Type	Source(s)	ICD*-10 code
Bacillus cereus intoxication	Bacterium	N, O, H	A05.4 Foodborne *Bacillus cereus* Intoxication
Campylobacteriosis	Bacterium	N, O, H	A04.5 *Campylobacter* enteritis
Ciguatera poisoning	Toxin	N, O, H	T61.0 Toxic effect: Ciguatera fish poisoning
Clostridium perfringens intoxication	Bacterium	N, O, H	A05.2 Foodborne *Clostridium perfringens* [*Clostridium welchii*] intoxication
Cryptosporidiosis	Protozoan	N, O, H	A07.2 Cryptosporidiosis
Giardiasis	Protozoan	N, O, H	A07.1 Giardiasis [lambliasis]
Hepatitis A	Virus	N, O, H	B15 Acute hepatitis A
Listeriosis (total and perinatal)	Bacterium	N, O, H	A32 Listeriosis
Norovirus infection	Virus	O, H	A08.1 Acute gastroenteropathy due to Norwalk agent
Salmonellosis	Bacterium	N, O, H, L	A02.0 *Salmonella* enteritis
Scombrotoxicosis	Toxin	N, O	T61.1 Toxic effect: Scombroid fish Poisoning
Shigellosis	Bacterium	N, O, H, L	A03 Shigellosis
Staphylococcus aureus intoxication	Bacterium	N, O	A05.0 Foodborne staphylococcal Intoxication
Toxic shellfish poisoning	Toxin	N, O	T61.2 Other fish and shellfish poisoning
VTEC/STEC infection	Bacterium	N, O, L	A04.3 Enterohaemorrhagic *Escherichia coli* infection
Yersiniosis	Bacterium	N, O, H	A04.6 Enteritis due to *Yersinia enterocolitica*

Data Sources: *EpiSurv notifications (N), EpiSurv outbreaks (O), MOH hospitalisations (H), ESR laboratory data (L)
VTEC = Verotoxin-producing *Escherichia coli* STEC = Shiga Toxin-producing *Escherichia coli*
* International Classification of Diseases
* EpiSurv – Notifiable disease surveillance database

Table 1.3: The economic cost caused by foodborne diseases in New Zealand, 2009 ($ million)[7]

Cost	Campylo-bacteriosis	Salmonellosis	Norovirus	Yersiniosis	STEC	Listeriosis	Total
Government outlays	§	§	§	§	§	§	16.40
Industry costs[1]	§	§	§	§	§	§	12.30
Treatment costs	2.17	0.20	1.45	0.12	1.51	0.74	6.19
Output loss	17.82	0.36	7.66	1.06	0.35	0.06	27.32
Residual private costs	16.00	14.85	40.96	0.73	12.76	14.38	99.67
Total, excl govt. & ind.[2]	*36.00*	*15.41*	*50.07*	*1.90*	*14.63*	*15.18*	*133.19*
Grand total	**-**	**-**	**-**	**-**	**-**	**-**	***161.90***

[§] Totals not apportioned to individual diseases
[1] Excludes undocumented business compliance costs covering Food Safety Programmes and their implementation
[2] Total cost excluding government and industries

1.2 Gram-Negative Bacteria and Endotoxins

Foodborne illness caused by bacteria is the major challenge to the food sectors [8]. Figure 1.2 shows the research interest on pathogen detection in food industry is the highest compared to other sectors. Within the pathogens, the bacteria are clustered into Gram-positive and Gram-negative type according to their cell wall staining, which have different cell wall structure. Almost 90 % - 95 % of Gram-negative bacteria are pathogens [9]. Endotoxins or Lipopolysaccharide (LPS) are part of the outer membrane of the Gram-negative bacteria cell wall which comprises of O antigen, Core and Lipid A [10] as shown in Figure 1.3. Lipid A is where the endotoxin is being produced. Endotoxins are dangerous toxins which are released when the Gram-negative bacteria died [11].

The detection of endotoxins which are caused by the pathogens is the main concerns to the food industries [12]. *Escherichia coli* (*E. coli*) and *Salmonella* are examples of Gram-negative bacteria which have been identified as two major foodborne pathogens. The chart in Figure 1.4 has shown most of the research conducted to study and detect these two bacteria. The latest *E. coli* outbreak happened in Europe in 2011 where more than 50 people died and thousands more have been hospitalized as shown in Figure 1.5.

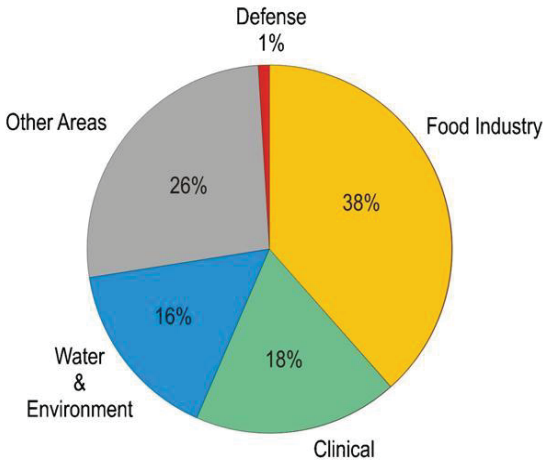

Figure 1.2: Areas of research interest for pathogen detection (Source: ISI Web of Science.ca. which indicates about 2500 research articles found on pathogen detection over last 20 years) [12]

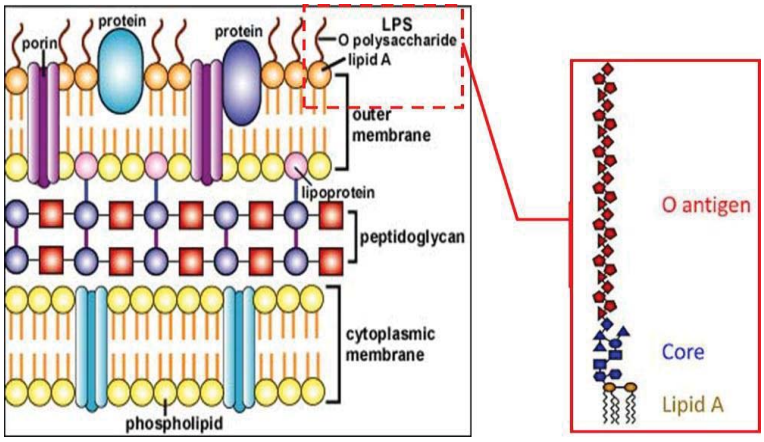

Figure 1.3: Cell wall of Gram-Negative bacteria and LPS structure.

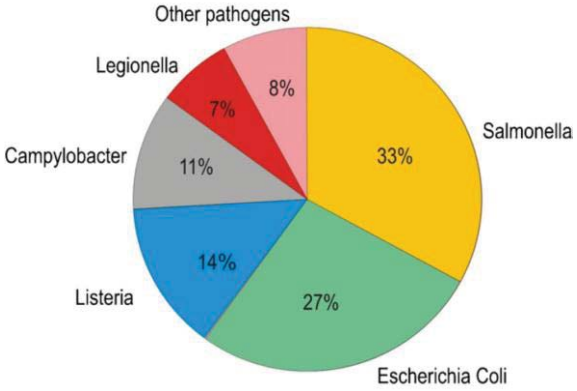

Figure 1.4: The relative number of research conducted for different bacteria. (Source: ISI Web of Science.ca. which indicates about 2500 research articles found on pathogen detection over last 20 years) [12].

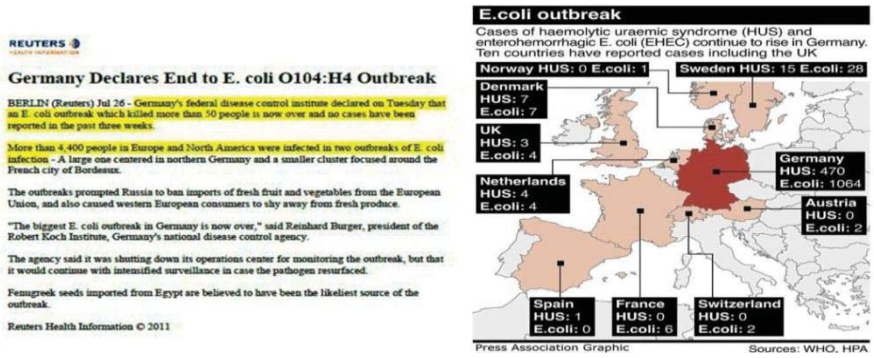

Figure 1.5: *E. coli* outbreak in Europe 2011 (Source: Reuters, WHO and HPA)

These two gram-negative bacteria also have caused significant high number of incident cases including death of foodborne diseases in New Zealand which has been reported in 2009 [7] and shown in Table 1.4. The incident case of foodborne disease caused by Salmonellosis is higher than STEC (*E. coli*). Figure 1.6 shows the geographic

distribution of salmonellosis notification in New Zealand in 2007–2010. Figure 1.7 (a) and (b) shows the foodborne of *Salmonella* spp. and VTEC/STEC and their associated cases reported by year 2001 – 2010 [2]. These bacteria are commonly found on many raw foods. High risk foods which are commonly affected by these bacteria are meat, poultry, seafood, dairy products, and eggs. Food may be contaminated because of poor food processing, handling and storage, poor hygiene, food poisoning bacteria in the soil, water, on animals and people [13]. A large amount of endotoxin is released when the mass of gram-negative bacteria died and if these amount of toxins exceed the human body ability to fight or to get rid of them then the significant symptoms (septicemia) occurs which includes fever, chill, muscle pain, headaches and skin lesions [9]. Without proper treatment it may causes death in the form of septic shock.

Table 1.4: Foodborne diseases in New Zealand (2009): Based on notified and estimated incident cases [7].

Enumeration of cases	Disease					
	Campylo-bacteriosis	***Salmon-ellosis***	***Noro-virus***	***Yersin-iosis***	****STEC***	***List-eriosis***
Notified incident cases	7,176	1,129	349	431	143	28
Notified incident cases estimated as foodborne	4,126	685	138	242	57	23
Reported deaths	0	1	0	0	1	4
Multiplier	10	4	1000	19.4	3.7	1
Estimated actual food-related cases	41,262	2,741	138,204	4,699	210	23
Estimated actual deaths	0	4	0	0	4	4

*STEC – Shiga toxin-producing *E. coli*

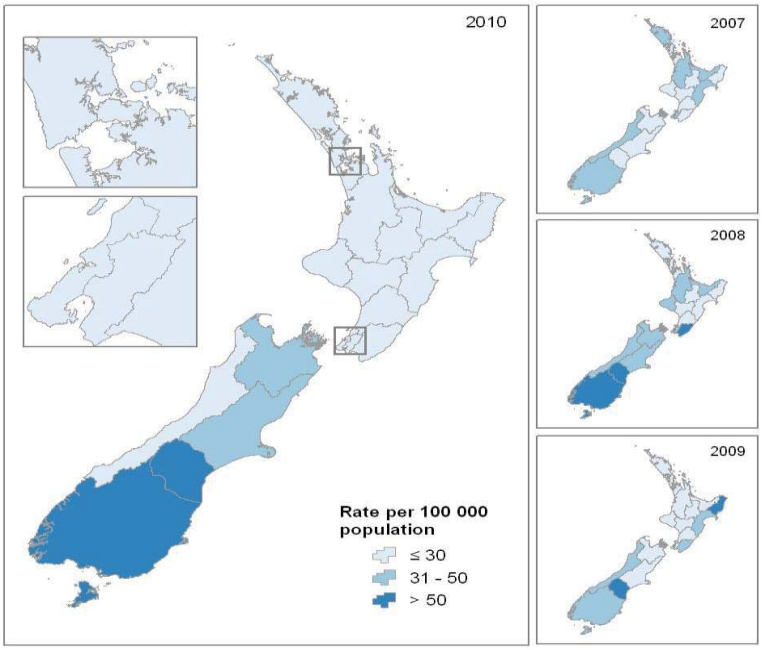

Figure 1.6: Geographic distribution of *Salmonellosis* cases reported in 2007 – 2010 [2]

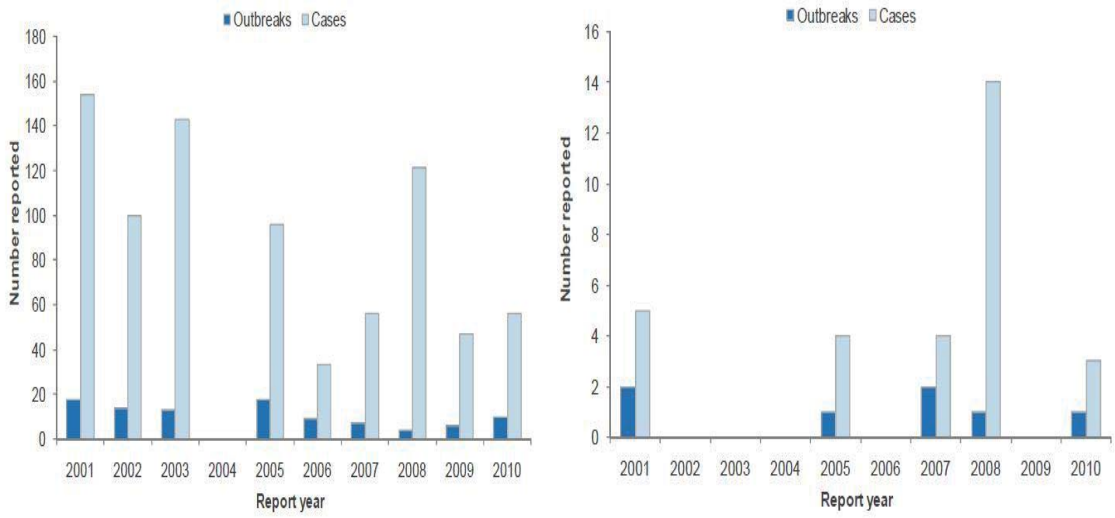

Figure 1.7: Number of reported outbreaks and associated cases for; (a) Foodborne *Salmonella* spp. and (b) Foodborne VTEC/STEC [2]

1.3 Conventional Method of Pathogens Detection and Endotoxins Detection

Several detection methods have been used to detect the pathogenic Gram-negative bacteria or the endotoxins. Pathogen detection will specifically detect the Gram-negative bacteria whereas the endotoxin detection method specifically detects the LPS structure on the outer membrane of Gram-negative bacteria.

1.3.1 Pathogen Detection

Conventional methods of pathogen detection and identification are based on specific microbiological and biochemical identification [14]. Three types of conventional methods that have been used are culturing and colony count method, immunology based method and polymerase chain reaction method (PCR) [12, 14, 15]. The culturing technique is a conventional method of pathogen detection which is capable of giving accurate results because of high selectivity and sensitivity [16, 17]. This technique is conducted by enriching the food sample and performing various media-based metabolic tests on (liquid and agar cultures). The technique depends on the growth of the microorganisms on selected culture media (pre-enrichment, selective enrichment,

selective plating, identifications), which required several days to produce the results. This method of detection is tedious, and also time-consuming.

Immunological detection with antibodies has been successfully employed for the detection of bacterial cells, spores, viruses and toxins alike [18, 19]. The methods utilised the antigen-antibody bindings have been widely used for pathogen detection especially for Gram-negative bacteria. This immunology-based method has successfully detected *Salmonella* and *E. coli* [20, 21]. Examples of the immunological methods include in the enzyme immunoassay (EIA) [22, 23], enzyme linked immunosorbent assays (ELISA)[24-26], enzyme linked fluorescent assay (ELFA) [27, 28], flow injection immunoassay [29], and others immunological methods [30, 31]. Schematic diagram of Immunology-based technique using indirect ELISA and sandwich ELISA is shown in Figure 1.8. Immunological methods provide less time of assay preparation compared to culture technique but still lacking the ability to detect the pathogens in real time [32].

One of the most popular molecular biology methods of pathogen detection uses Polymerase Chain Reaction (PCR) [33], which is based on the isolation, amplification and quantification of a short DNA sequence. PCR has been used to target specific nucleic acid sequence of bacteria [34-36], viruses [37, 38], and protozoa [39, 40]. Different PCR methods have been used for pathogen detection which includes; real time PCR [41], multiplex PCR [42], reverse transcript PCR (RT-PCR) [43, 44]. Figure 1.9 (a) shows the schematic diagram of PCR cycle and Figure 1.9 (b) shows one of PCR method using multiplex PCR to extract DNA from bacteria for pathogen detection [45]. However, PCR methods are expensive (PCR equipment) and need trained personnel to operate.

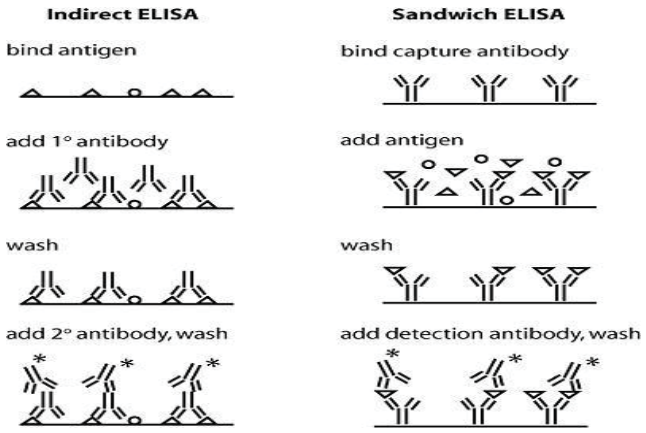

Figure 1.8: Schematic diagram of immunology-based technique using indirect ELISA and Sandwich ELISA [46]

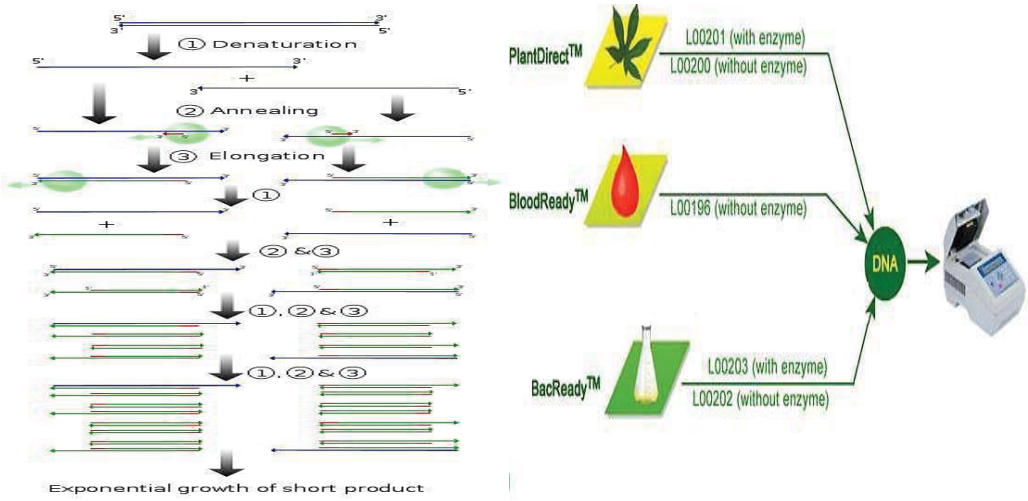

Figure 1.9: Diagram showing (a) Schematic representation of PCR cycle and (b) DNA extraction and PCR system for molecular biology research (source: GenScript - Direct PCR system)

1.3.2 Endotoxin Detection

The conventional method of endotoxin detection is based on rabbit pyrogen test [47, 48] and Limulus Amoebocyte Lysate (LAL) assay [49, 50]. These methods have been approved by FDA (United States Food and Drug Administration). The rabbit pyrogen test has been developed in 1920 which injecting rabbits with a test solution and then observing the response in their body temperature. However this method is expensive, time consuming and prompted protest from animal rights group. Therefore it has been diminished and now only LAL test has been used for the routine check of Lipopolysacharide (LPS) in biological solution. LAL was discovered 60 years ago by Dr. Frederik Bang in 1950 [51] from the observation that horseshoe crab blood forms clots when exposed to endotoxins.

Amoebocyte extract derived from horseshoe crab blood is mixed with a contaminated sample with endotoxin, and a reaction is observed if endotoxins are present. Four test methods have been approved by FDA which include; gel-clot, turbidimetric (spectrophotometric), colorimetric (lowry protein), and chromogenic assay [52]. The differences in these methods are based on characteristics of the amoebocyte/endotoxin reaction. Gel clot technique is based on gel formation, the turbidimetric is based on the development of turbidity after cleavage of an endogenous

substrate and the chromogenic technique is based on the development of color after cleavage of a synthetic peptide-chromogen complex [53].

The LPS concentration is indicated in EU/ml or EU/mg. The unit EU stands for endotoxin unit which describes the biological activity of LPS. A Gram-negative bacteria contains approximately 10^{-15} g of LPS, 1 EU therefore can be generated by only 10^5 bacteria. The LAL assay test is fast (approx. 30 minutes) and highly sensitive which the lowest concentration detected is 0.005 EU/ml. The LAL test need trained personnel as it requires several steps which need carefully conducted to avoid contamination on sample test. The price of the LAL assay kit is quite expensive for a bulk of sample testing. Some of the documented in-vitro effect of endotoxin contamination has been reported by J. Ryan et.al. in [54] and their lowest limit concentration of endotoxin that show effects is shown in Table 1.5.

Table 1.5: Some of the documented In-Vitro effects of endotoxin

Cell Type	Concentration (ng/ml)*	Endotoxin Effects	Reference
Equine macrophages	0.5	Induced production of IL-6[a]	[55]
Human IVF embryos	1	Reduced pregnancy success rates in in-vitro fertilization programs 3-4 fold	[56, 57]
Aortic rings	1	Reduced contractility and induced of IL-1[a] and TNF[b]	[58]
Aortic endothelium	10	Dose dependent alterations in heparin sulfate proteoglycan production	[59]
Murine B lymphomas	10	Increased production of immunoglobulin light chain 30-40 fold	[60]
Recombinant CHO[c]	10	Altered protein production	[61]
Cardiac myocytes	10	Induced contractile dysfunction	[62]
Human T Cells	100	Induced proliferation and lymphokine production in precense of monocytes	[63]
Uretal epithelium	5000	Altered clonal efficiency	[64]

[a] IL - Interleukin
[b]TNF – Tumor necrosis factor
[c]CHO – Chinese hamster ovary
* Lowest concentration of endotoxin that showed the effect

1.4 Biosensors and Chemical Sensors for Pathogen and Endotoxin Detection

Sensor is a device that measures a physical stimulus (physical or chemical quantity) and converts it into an electrical signal which can be read by an observer or by an instrument [65]. Sensors are a type of transducers, which means that they change one form of energy into another. Sensors that provide physical quantity include temperature, stress and strain, proximity, acceleration, distance, time radiation, acoustic and sensor array (video and image) whereas sensors which provide chemical quantity can be categorized in chemical sensors, biosensors, physical sensors for chemical analysis, sensor array (e-nose and e-tongue) [66, 67]. Definition of chemical sensors and biosensors are dependent on the viewpoint but they can be used for the same purpose. Hulanicki has stated that some biosensors are subgroup of the chemical sensors [67].

Biosensors have been widely used for pathogens detection in food [8, 12, 14, 68]. Figure 1.10 shows that the numbers of research works in biosensors applications are growing and this has been compiled and reported by Lazcka et.al. in 2007 [12]. There are different transductions methods used in biosensors which can be classified as optical, electrochemical, and massed based transducers. Bioreceptor or bio-probe surface is biological recognition elements for specificity in biosensor applications [14]. It is a molecular species which make recognition possible by binding the analyte of interest to the sensor for measurement. Different bioreceptor has been introduced in biosensors application which include; antibody/antigen [69, 70], enzymes [71, 72], nuclei acids/DNA [73, 74], cellular cells [75], biomimetic [76] and bacteriophage [77]. Figure 1.11 shows the schematic diagram to represent biosensors applications and their transduction methods. It can be said that the biosensor applications based on various kind of transduction methods. Some of these methods are very expensive (i.e. optical) but give accurate measurements and some can be considered as low cost system (i.e. electrochemical) which is less accurate but can be coupled with other biosensing techniques to enhance their performances. Figure 1.12 shows the schematic diagram of pathogen captured on biosensors surface with different bioreceptors or bio-probe surface. Knowledge and selection of these bioreceptors or bio-probes are important to determine the success of the developed biosensors.

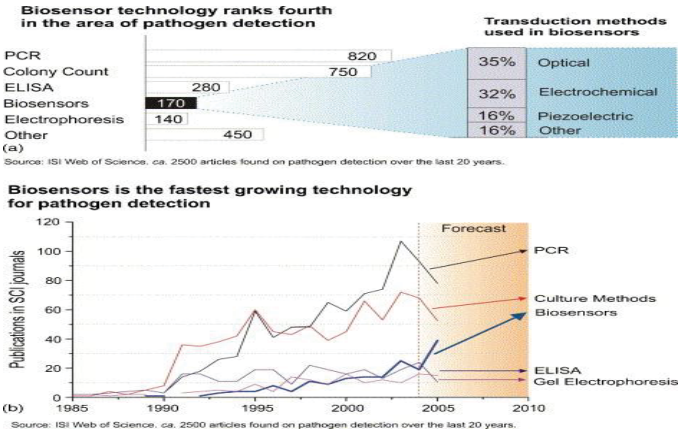

Figure 1.10: Diagram shows numbers of research works in biosensor application is growing (source: ISI Web of Science compiled and reported by Lazcka et.al.)[12]

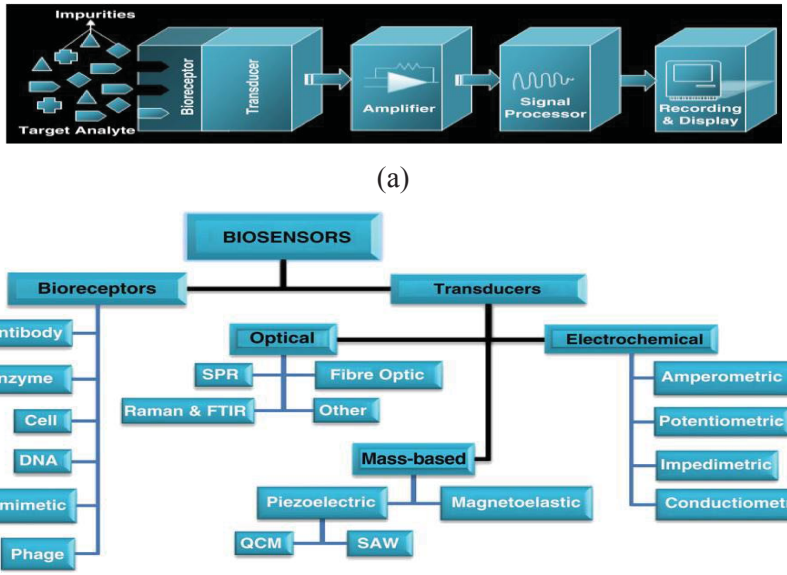

Figure 1.11: Diagram showing (a) Schematic representation of biosensor application (b) Classifications of biosensor showing bioreceptors and transducers [14]

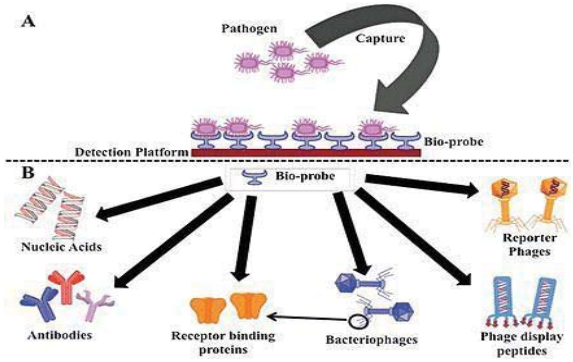

Figure 1.12: Schematic diagram (A) Illustration how the pathogen can be captured onto the sensor platform (B) Different bioreceptor or bio-probe surface in biosensor applications [77]

1.4.1 Optical based Biosensors

One of the most popular pathogen and endotoxin detection is based on optical biosensors [78]. The detection method of optical biosensors are based on absorption, reflection, refraction, dispersion, infrared, Raman and fluorescence. The transduction method used in optical biosensors mainly based on optical fibre, surface plasmon resonance, Raman spectroscopy and infrared spectroscopy [79].

The optical fibre biosensors are based on tapered fibre to send excitation laser light to the detection surface and then received emitted light. The light propagates through the fibre or waveguide sensitive to the surroundings, which works as excellent detector for identification and detection of foodborne pathogens and endotoxin. Optical fibre biosensors have been widely used for detection of pathogen such as *E. coli* [80, 81], *Salmonella* [82, 83], *Listeria* [84, 85] and others [86, 87]. The optical biosensors are also popular for endotoxin detection which has been reported by Su et.al.[88] and Marazuela et.al.[89].

Surface plasmon resonance (SPR) uses reflectance spectroscopy for pathogen and endotoxin detection. SPR is able to detect minor changes in refractive index. It measures the changes in angle of the reflected light when cells bind to the receptor which has been immobilized on the transducer surface [90]. A lot of research works in pathogen detection and endotoxin detection have been reported using SPR based biosensors in [91-94].

Others optical biosensors applications for pathogen and endotoxin detection are fluorescence detection [95], Raman and FTIR spectroscopy [96, 97] and optical micro-ring resonators [98].

1.4.2 Electrochemical Biosensors

Electrochemical biosensors mainly based on the observation of current or potential changes due to interaction between electrodes/sensors with sample interface. It can be classified according to observed parameter such as current (amperometric), potential (potentiometric), impedance (impedimetric) and conductance (conductometric) [99]. The electrochemical based biosensors is low cost, has ability to work with turbid samples and easy to miniaturise. The sensitivity and selectivity are slightly limited if

compared to optical biosensors but their applications can be coupled with other biosensing technique to enhance the detection [14].

The most common electrochemical biosensors application for pathogen detection is amperometric transduction. It is basically based on the relationship between analyte concentrations with current measurement. Amperometric transduction method works as the sensor potential is set at a certain value where the analyte produces current at the electrode [100]. The excitation potential drives the electron transfer function, thus the current produced is a direct measure of the rate of electron transfer. It has better sensitivity compared to potentiometric method [101]. Amperometric biosensors have been used for detection of *E. coli* [102, 103] and *Salmonella* [104] and others [105].

Potentiometric biosensors methods make use of bio-recognition process which is converted into a potential signal. They are based on ion-selective electrodes (ISE) and ion-sensitive field effect transistors (ISFET). The primary output signal is due to the accumulated ions at the ion-selective membrane interface. Current flowing through the electrode is equal to or near zero. The electrodes response to the presence of the ions resulting from the enzyme reaction as reported in [106]. Some of the research works using the potentiometric biosensors for pathogen detection has been reported in [107-109].

The impedimetric biosensors are based on measurement of impedance as a result of biological reaction. The development of this method widely spread in the recent years as reported by Yang et.al.[110]. Electrochemical impedance spectroscopy (EIS) plays important role in the development of impedimetric biosensors. EIS is a powerful method to study the electrical properties of materials and their interfaces with surface-modified electrodes [111]. A small AC signal is applied as excitation voltage at certain frequency range to the electrode terminal which will produce current to flow through the biosensors. The change of impedance due to bioaffinity interaction on the surface was measured and analyzed using EIS techniques. This technique has been used widely in pathogen detection [112-115]. New trend of the impedimetric biosensors for pathogen detection has been reported by Wang et.al. [68]. The endotoxin detection has been reported by Su e.t al in [88] by using aptamer-based impedance biosensor.

Conductometric biosensors are based on conductance changes due to the bioaffinity events. A change in ionic species concentration resulting a change in electrical conductivity or current flow. The conductometric biosensor has been reported

for foodborne pathogen detection by Muhammad-Tahir and Alocilja [116] and Pal et.al [117].

1.4.3 Mass Sensitive Biosensors

Mass sensitive biosensors includes; Quartz Crystal Microbalance (QCM) which is a piezoelectric mass-sensing device and Surface Acoustic Wave (SAW). A QCM device works by sending an electrical signal through a gold-plated quartz crystal which produces vibration at specific resonant frequency [118]. The QCM then measures the frequency of oscillation in the crystal. The QCM has been utilised as a biosensor applications where it can detect the changes in frequency of the crystal due to the changes in mass on the surface of the QCM transducer [119]. The QCM has been used for pathogen detection [120] and endotoxin detection [121].

SAW devices generate and detect acoustic waves on the surface of the piezoelectric substrate by means of Interdigital Transducers (IDTs) [122]. SAW method has been used for various applications including for detection of pathogen and endotoxin. The pathogen detections have been reported by Rocha-Gaso et.al. [123] and Large et.al. [124] and endotoxin detection has been reported by Hammer et.al.[125].

Table 1.6 and 1.7 shows the summary of pathogen detection using conventional method and biosensors method. The summaries only focus on pathogens from Gram-negative bacteria; *E. coli* and *Salmonella*. Both tables have shown biosensors method can provide reliable information of the contaminated samples and give fast detection for real time in-situ monitoring.

Table 1.6: Summary of existing methods on *E. coli* detection

Detection Method	**Detection time (approx.)**	**Detection Limit (CFU mL^{-1})**	**Reference**
Plate/culturing	1 day to 1 week	Low CFUs	[126]
Biochemical test	1 day to several days	Low CFUs	[127]
Fluorescent bacteriophage assay	10 h	10-100	[128]
Capillary immunoassay	7h	0.5 – 1	[129]

Time-resolved fluorescence immunoassay	6h	10-100	[130]
ELISA	Next day	1.2×10^3	[131]
PCR ELISA	5 h	100	[132]
Real Time PCR	5 h 20 min	5 cell	[133]
Fiber Optic Immunosensor	10 h	2.9×10^3	[134]
SPR Biosensor	60 min	10^2	[135]
QCM Immunosensor	170 min	10^3	[136]
Amperometric biosensor	30 min	100–600	[137]
Conductimetric biosensor	10 min	79	[116]
Impedimetric biosensor	10 min	10^4 in culture and 10^7 in water	[138]

Table 1.7: Summary of existing methods on *Salmonella* detection

Detection Method	**Detection Time (approx.)**	**Detection Limit (CFU mL^{-1})**	**Reference**
IMS-Plating	Next day	1-10	[139]
Electrochemical sandwich ELISA	Same day	1-10 cells/25g	[140]
PCR-ELISA	Next day	10^3	[141]
QCM	60 min	10^4	[142]
Amperometric biosensor	1-2 h	5×10^4	[143]

1.4.4 Chemical Sensors

"A chemical sensor is a device that transforms chemical information, ranging from the concentration of a specific sample component to total composition analysis, into an analytically useful signal. The chemical information, mentioned above, may originate from a chemical reaction of the analyte or from a physical property of the system investigated" – definition given by Hulanicki et.al. [67]. Chemical sensors have two important parts; a receptor and a transducer. In some cases, a membrane is introduced as a separator between those parts. The receptor part includes; physical response (no chemical reaction), chemical response (chemical reaction from analyte) and biomedical response (biomedical process or biosensors). The transduction method of chemical sensors includes; optical devices, electrochemical devices, electrical devices, mass

sensitive devices, magnetic devices and thermometric devices. Details of the classification scheme of these chemical sensors have been reported by Richard et.al [66].

Most of the transductions methods/techniques of the chemical sensors are the same with what have been discussed in biosensors sections. Figure 1.13 illustrates several method of chemical sensing approach. The applications of fibre-optics chemical sensors and biosensors for various applications including pathogen detections have been reported by Wolfbeis et.al [144]. A photonic badgap (PBG) structures have been developed by Ouyang et.al that can be used for biosensing applications [145]. The fabricated porous silicon PBGs are sensitive to small changes of refractive index, which is capable to detect the binding of target molecules to the bioreceptors. The sensors are able to detect biological matters of small molecules to large proteins. Ultrasensitive detection for pathogen using surface-engineered impedimetric immunosensor has been reported by Joung et.al [146].

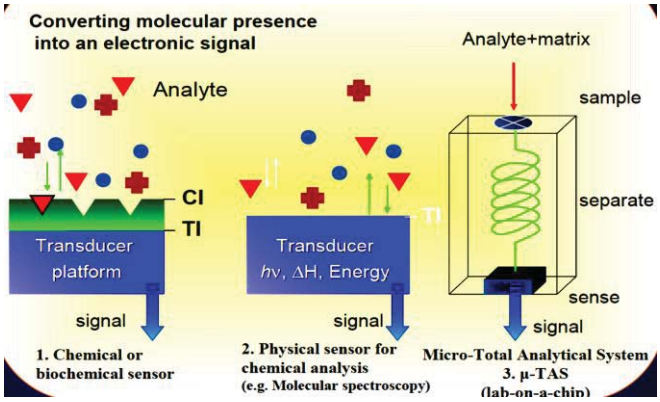

CI – Chemical interface; TI – Transducer interface

Figure 1.13: Common methods of chemical sensing approaches [147]

Different methods of endotoxin detections have been established. Ding et.al. has successfully using electrochemical impedance spectroscopy (EIS) to detect interaction of endotoxin with polymyxin B (PmB) immobilized on 4,4-dithiodibutyric acid coated gold electrodes [148]. The technique can detect the endotoxin contamination between 0.2 – 0.8 ng/mL concentrations. New electrochemical endotoxin sensors based on TLR4/MD-2 complexes immobilized on gold electrodes was developed by Yeo et.al [149]. This endotoxin sensor was based on human recombinant toll-like receptor 4 (rhTLR4) and myeloid differentiation-2 (MD-2) complex. The estimated limit of detection (LOD) was fairly low, 0.0002 EU/mL. Another rapid high-sensitive endotoxin

detection system is using stress-responsive magnetoelastic sensors, which has been reported by Ong et.al.[150]. It was reported that the magnetoelastic sensor based technology can detect the presence of endotoxin at 0.0105 EU/ml in approximately 20 min. Capacitive sensors/biosensors for detection of endotoxin has been developed by Limbut et.al.[151]. A self-assembled thiol layer on Au biosensor transducer was obtained by immobilized with endotoxin-neutralizing protein derived from American horseshoe crab. Decrease in the capacitive signal was observed after injection of a sample containing endotoxin to the sensor layer. It was reported that the endotoxin could be determined under optimum conditions with a detection limit of 1.0×10^{-13} M and linearity ranging from 1.0×10^{-13} M to 1.0×10^{-10} M.

It can be said from the literature that the recent trend of chemical sensors and biosensors applications was based on the planar interdigital sensors or interdigitated electrodes type as a sensing platform especially in impedimectic biosensors, SAW, microfluidic chips and MEMs based sensors. The development of these sensors is low cost, easy to manufacture and miniaturize, robust, better signal to noise ratio (SNR) and can be coupled with other biosensing techniques to enhance the sensitivity, selectivity and specificity.

1.5 Description of the Planar Interdigital Sensors

The planar interdigital sensing approaches have long been employed. There are different terms for interdigital sensors which include interdigitated electrodes, microelectrodes, interdigital transducers (IDTs), interdigitated array microelectrode (IDAM), interdigitated electrode structures (IDES) and others. Planar interdigital sensor is based on the interdigital electrode structures which have been widely used in photosensitive detectors [152-155], surface acoustic wave (SAW) [156-160], humidity sensors [161-164], sensors for chemicals and gasses [165-170], measurement of electrolyte conductivity (EC) [171], determination of components contained in aqueous solutions [172], determination of moisture, fiber and titanium dioxide in paper pulp [173, 174], measurement of complex permittivity and characterization of materials [175, 176], measuring tablet hardness and coating thickness (pharmaceutical products) [177], and the detection of small amount of magnetic beads over the surface of micro sensors

[178]. Design and applications of interdigital capacitive sensors were discussed by Mamishev et.al. [179].

Currently, the numbers of research works in developing planar interdigital sensors are increasing. Planar interdigital sensors have been used for estimation of properties of dielectric material such as milk, saxophone reeds, meat and leather [180-187] . Evaluation of diffusion-driven material property profiles using three-wavelength interdigital sensor has been reported by Mamishev et. al. [188]. The dielectric behaviour of nematic liquid crystals was studied with interdigital capacitors [189]. New development of interdigital sensors have been reported for corrosion monitoring [190, 191], structural health monitoring [192, 193] and environmental monitoring [194, 195].

Planar interdigital sensors have been utilized as sensing platforms for chemical sensors and biosensors applications for pathogen and endotoxin detections. Most of the impedimetric biosensors and chemical sensors are based on the design of planar interdigital sensors as their platform. Latest development of impedimetric chemical sensors and biosensors and their applications have been discussed in [68, 196-198]. Interdigital type of micro-impedance biosensor has been developed for bacterial detection [112-114]. Suehiro et.al. [199] has developed impedance detection of bacterial cell using interdigitated microelectrode as shown in Figure 1.14. The study was based on the difference of conductance or admittance measurement of the bacterial cells interactions. AMP (antimicrobial peptides) based electrical detection for *E. coli* has been developed by Mannoor et.al [115]. The work has been conducted to monitor water-quality from bacterial contamination for pharmaceutical products. The interdigital electrode structure has been used as the study conducted on selective and sensitive detection of infectious agents based on antimicrobial peptide-fictionalized micro-capacitive electrode arrays. Figure 1.15 shows the schematic diagram of the AMP-based sensing approach.

Surface Acoustic Wave (SAW) is based on the Interdigital Transducers or IDTs. Figure 1.16 shows the schematic diagram of SAW chemical sensors sensing mechanism. The piezoelectric substrate was coated with cross-linker and binding molecules were immobilized. SAW biosensors and chemical sensors have been used to detect pathogen and endotoxins as being discussed previously.

Interdigital electrode design has been used in developing microfluidic biochip for pathogen detection. Varshney et.al. [202] has developed an IDAM chip with

microelectrodes using conventional interdigital design in order to assemble the microfluidic flow cell as shown in Figure 1.17. It was developed to detect bacteria E. coli. Another microfluidic biochip which was designed using interdigitated microelectrodes was reported by Ertl et.al. [200].

Rana et.al [201] has successfully developed interdigitated electrodes for electrochemical sensors. The work has been done to characterize the sensors based on impedance spectra analysis. Figure 1.18 shows the electrochemical sensors based on interdigitated electrodes that have been developed by Rana et.al.

Planar inetrdigitated sensors are commercially available in the market which can be used for various applications. Figure 1.19 shows some of the commercially available planar interdigitated electrodes.

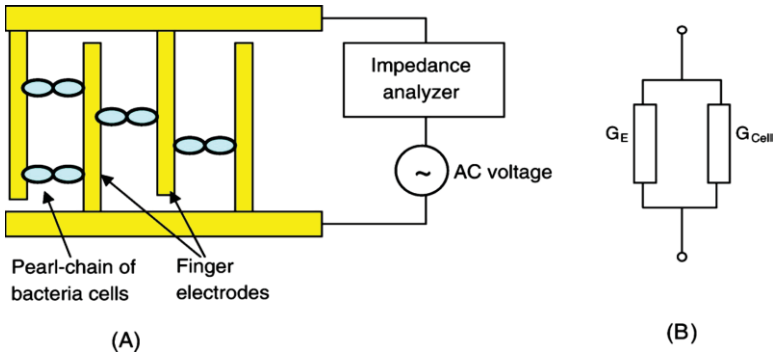

Figure 1.14: A schematic diagram of; (A) An interdigitated microelectrode based sensing system for bacterial cells detection and (B) The equivalent circuit based on conductance measurement [199]

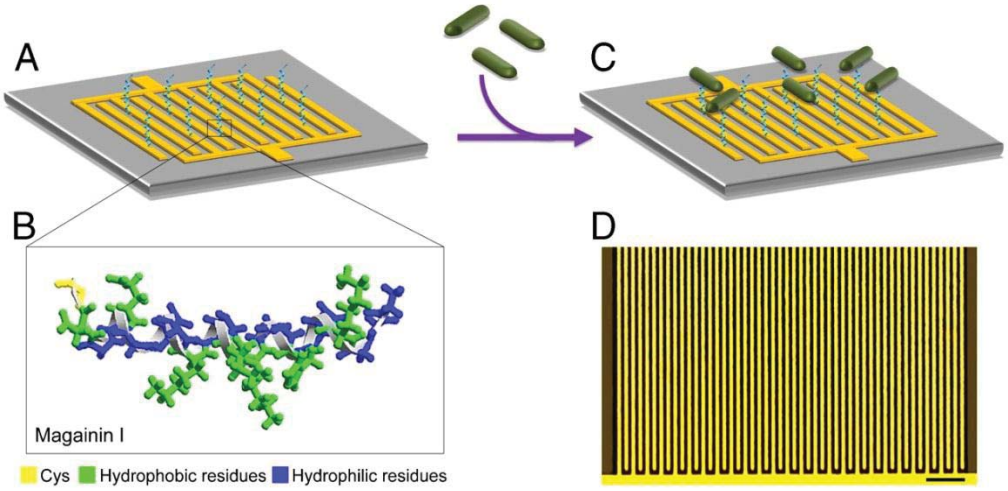

Figure 1.15: Schematic diagrams of AMP-based electrical detection showing; (A) Immobilization of AMPs on the interdigitated microelectrode array. (B) Images of AMP magainin I chemical structures (C) The binding of target cells to the immobilized AMPs for bacteria detection (D) Image of developed interdigitated microelectrode array [115]

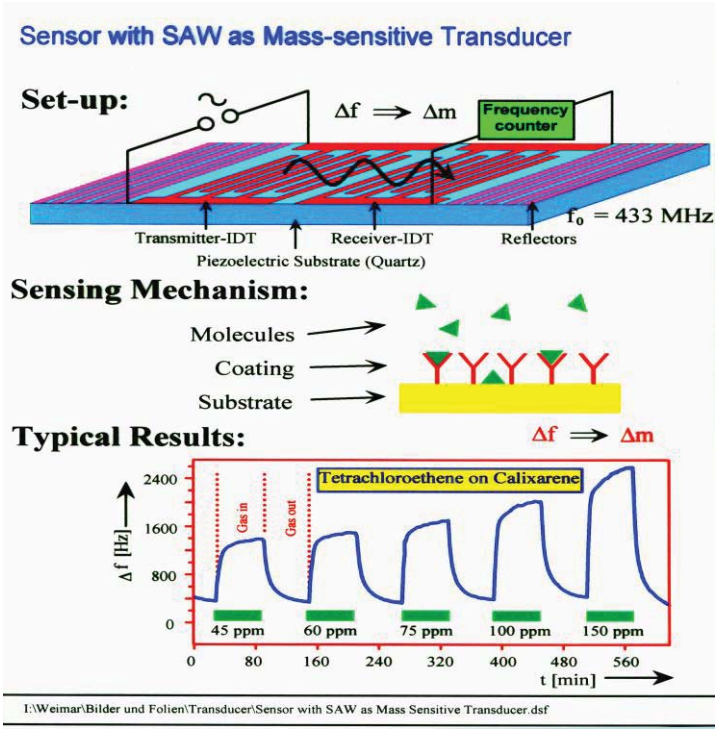

Figure 1.16: The schematic diagram of surface acoustic wave (SAW) sensing approach [147]

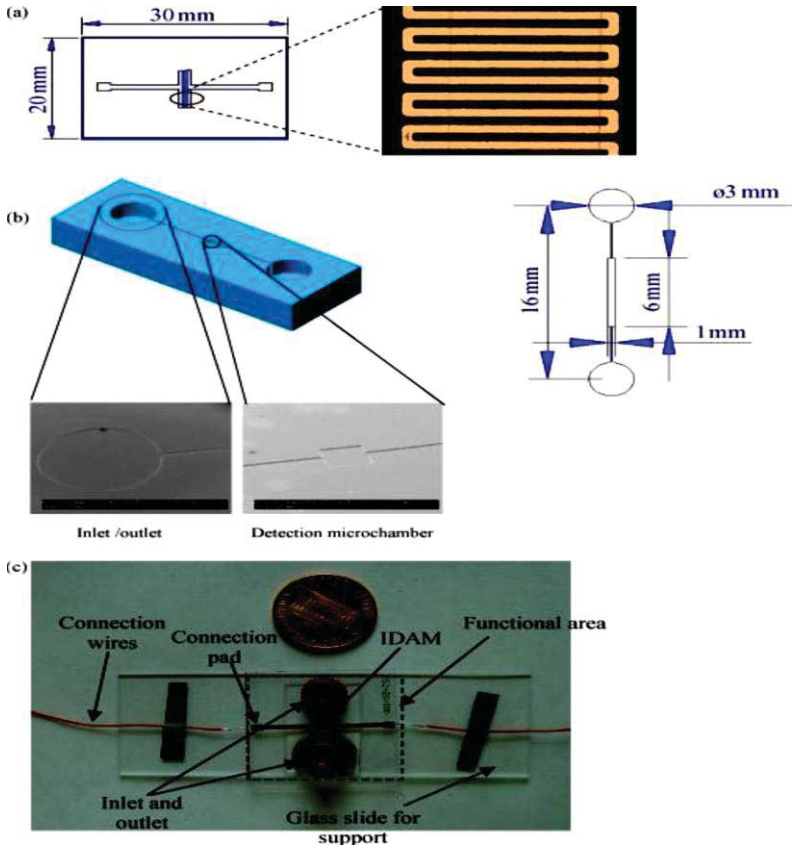

Figure 1.17: Schematic diagrams of; (a) IDAM chip with gold microelectrodes on a glass wafer, (**b**) A micro-channel showing micro-chamber, inlet and outlet channels, and (**c**) Microfluidic flow cell with embedded IDAM and their connection wires [202]

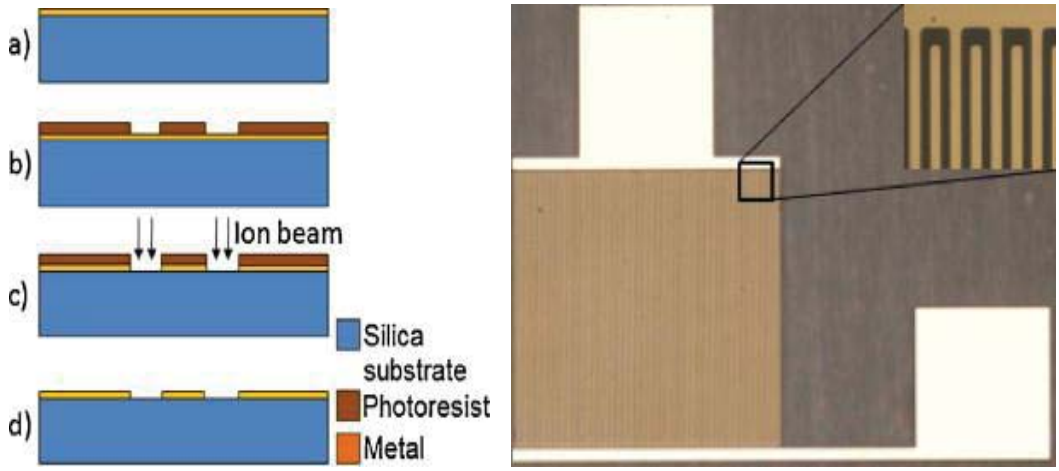

Figure 1.18: Schematic diagram of the electrode fabrication process and (b) Image of a set of interdigitated electrodes [201]

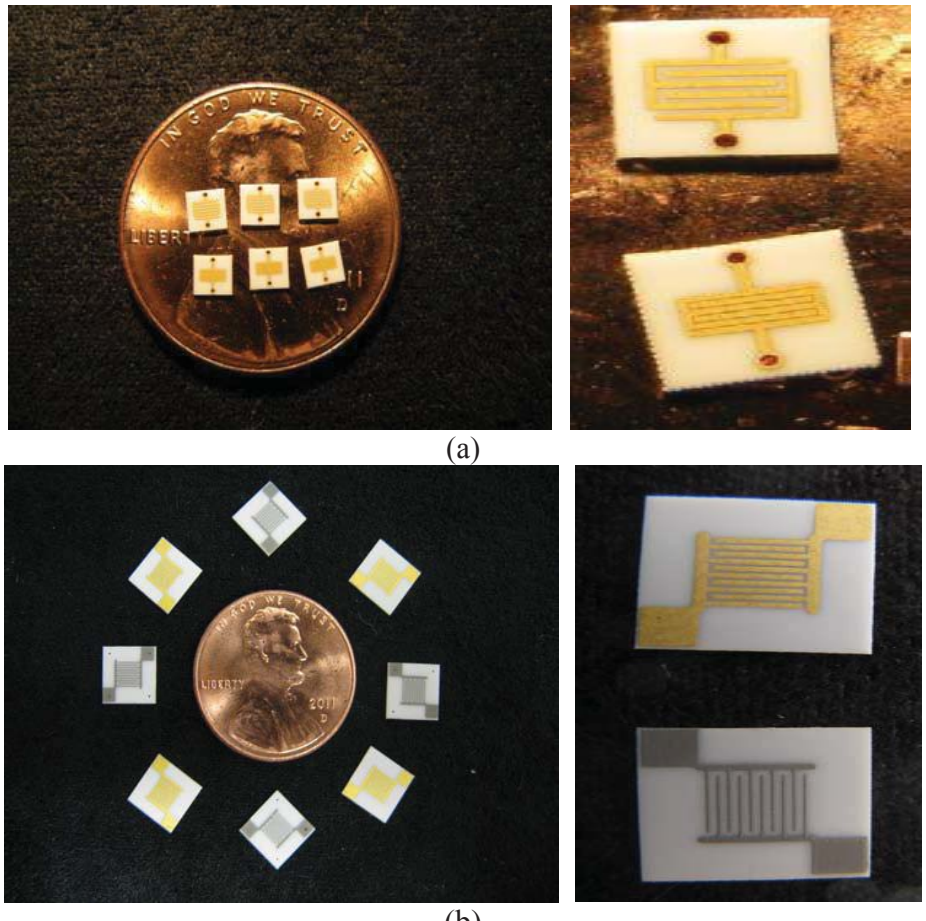

(a)

(b)

Figure 1.19: (a) Interdigitated electrodes on 0.10" x 0.10" substrates. Top sensor:4 mil spacing. Bottom sensor: 1 mil spacing. Contact pads on reverse side. (b) Gold and platinum interdigitated electrodes on 0.25" x 0.25" substrates (source: SYNKERA Technology Inc.)

1.5.1 Research Works at Massey University on Planar Interdigital Sensors

The research works were conducted under the School of Engineering and Advanced Technology (SEAT). All developed interdigital sensors were planar type and were designed in a simple structure. These sensors have been used in various applications. The related research works have been conducted by undergraduate students and post-graduate students at Massey University.

1.5.1.1 Quality of Materials

1.5.1.1.1 Inspection of Quality of Saxophone Reeds

Two types of planar electromagnetic sensors have been used to evaluate the quality of saxophone reeds [185]. The mesh type sensor and network analyser has been used in the experiment as shown in Figure 1.20. Results of mesh-type sensors were found to be very effective at high operating frequency of 500 MHz. The experimental setup was very expensive as it required the use of high-end equipment (network analyser). Therefore, a low-cost solution has been employed using planar interdigital sensors sensing approach as shown in Figure 1.21. The results were very promising as the sensors can differentiate between “good” and “bad” saxophone reeds.

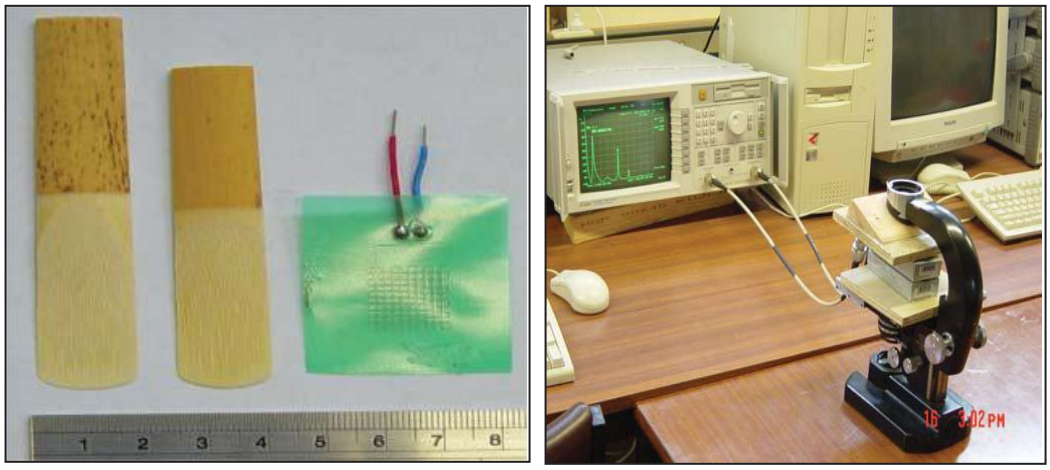

(a) (b)

Figure 1.20: (a) Mesh type sensor and different sections of a tenor and alto saxophone reed and (b) Experimental setup used to test the reeds.

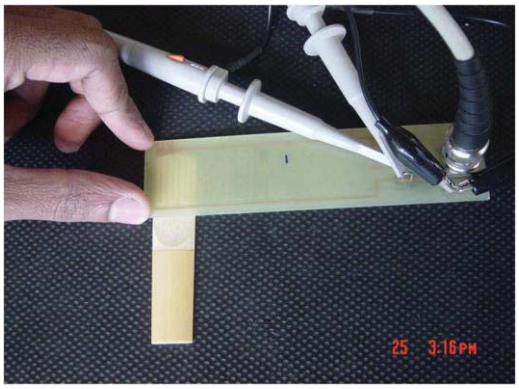

Figure 1.21: Testing saxophone reed using planar interdigital sensor.

1.5.1.1.2 Quality Improvement of Leather Tanning Process

Novel interdigital based sensing system has been developed to evaluate the quality of leather during tanning process [180, 203]. The developed sensing system has been used to measure looseness in the sheepskin. The interdigital sensors were developed to have different configurations compared to conventional interdigital structures. The measured reactance depended on the dielectric properties of the materials, configuration of electrodes structures and also on the material geometry. The effective permittivity of material can be estimated to evaluate the leather quality. The developed system is able to provide useful information of skin quality during various stages of tanning process. The experimental setup to access the quality of leather is shown in Figure 1.22.

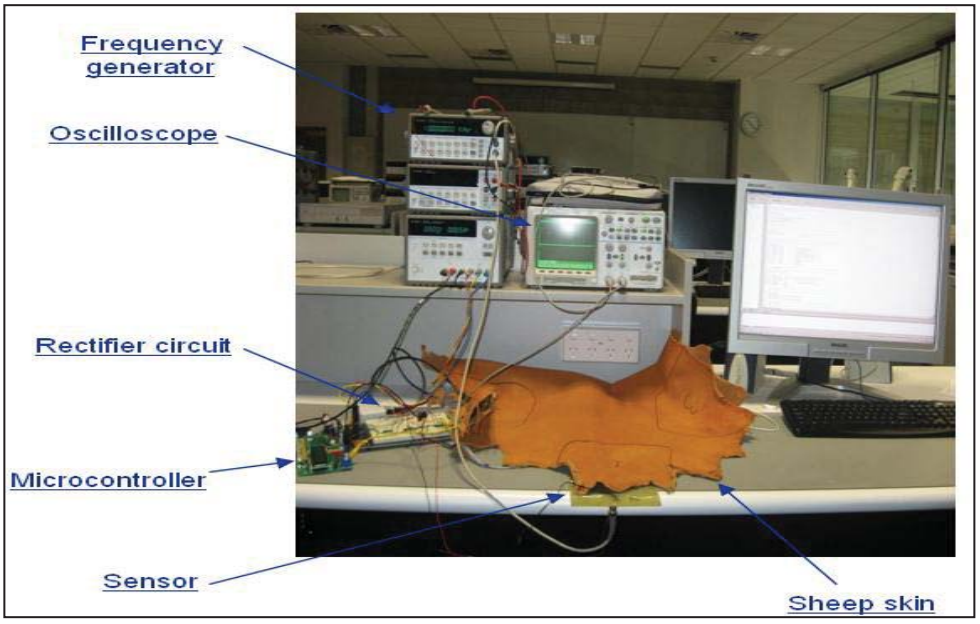

Figure 1.22: Experimental setup to access the quality of leather

1.5.1.2 Food Quality and Environmental Monitoring

1.5.1.2.1 Estimation of Fat Content in Pork Meat

The impedance characteristics of interdigital sensors with pork belly cuts has been investigated [187]. Three different interdigital sensors have been tested with pork belly pieces. The electric field lines pass through the material under test (MUT), and the measured capacitance between the two electrodes will depend on dielectric properties of the materials and also the material geometry. The interdigital sensors were driven by AC voltage of 10 V peak to peak. The measurements were made at frequencies in the range from 5 kHz to 1 MHz.

The pork pieces were placed on the sensing area according to four different orientations**.** Each of the six pieces was tested for four different orientations at the same frequency range. The AC signal is provided by the Agilent 33120A waveform generator and the Agilent 54622D oscilloscope, measured the input voltage, output current and the phase angles. The experimental setup is shown in Figure 1.23. The results were analyzed to determine the relationship between the reactance with the fat content of the pork belly. The mathematical analysis was used to estimate the fat content and was compared to the results obtained by the chemical analysis. Results from the experiments have shown that planar interdigital sensors can be used to determine the fat content of pork meat in a non-destructive way.

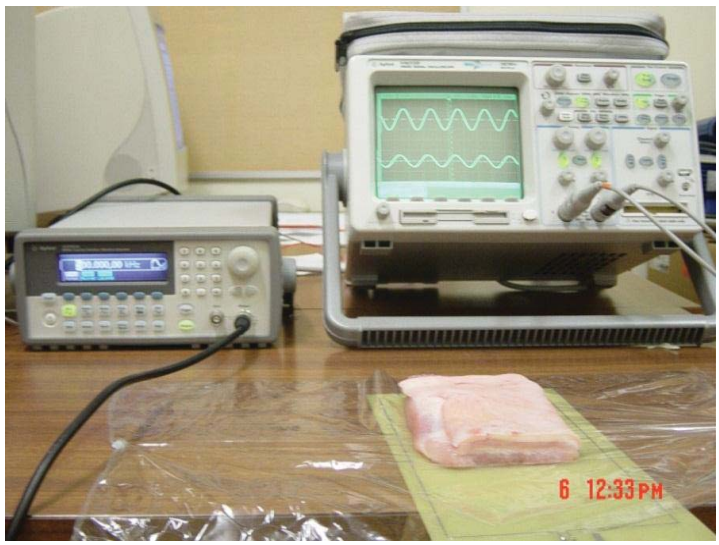

Figure 1.23: Experimental setup to determine fat content in pork meat.

1.5.1.2.2 Quality Monitoring of Dairy Products

The planar type electromagnetic sensors (mesh, meander and interdigital) for estimation dielectric properties of materials of dairy products such as milk, butter, cheese, and yogurt have been investigated [186]. The results have shown variations of impedance characteristics with frequency for different type of dairy products. The relationships between dielectric materials of the dairy products with the transfer impedance of planar electromagnetic sensors have been studied. The results have shown that the planar electromagnetic sensors have the potential to be used to determine composition of dairy products.

1.5.1.2.3 Novel Interdigital Sensors for Seafood Inspection

A novel planar interdigital sensor based sensing system has been developed for detection of dangerous marine biotoxins in seafood [204]. The main objective is to sense the presence of dangerous contaminated acid in mussels and other seafood by observing the change of reactance of the planar interdigital sensors. Initial studies were conducted with three peptide derivatives namely sarcosine, proline and hydroxylproline [205]. These three chemicals are structurally closely related to our target molecule. The proline molecule is arguably the most important amino acid in peptide conformation, contains the basic structural similarity to the domoic acid.

Three novel interdigital sensors have been designed and fabricated. All sensors have the same effective area but having different sensor configurations. The initial results show that sensors respond very well to the chemicals and it is possible to discriminate the different chemicals from the output of the sensor. The sensor with the best sensitivity was chosen for experiment using proline and mussels. The changes in sensor sensitivity were analysed with mussels before and after adding the proline. The presence of proline on the mussel surface and also injected proline to the mussels was clearly detected by the sensor. Further experiment was conducted with small amount of domoic acid (0.5 mg–5.0 mg) injected to mussels and it was found that the chosen sensor was able to detect small amount of domoic acid (1.0 mg) injected into the mussel samples. The result shows that the sensor was able to detect approximately 12.6 mg/g of domoic acid in mussel meat. Figure 1.24 shows the prototype of seafood inspection

tools. The outcomes from the experiments provide chances of opportunity for further research in developing a low cost miniature type of sensors for reliable sensing system for commercial use.

Figure 1.24: 1st Prototype of seafood inspection tools

1.5.1.2.4 Planar Electromagnetic Sensors for Environmental Monitoring

Planar electromagnetic sensors have been developed to monitor the water contamination from nitrates [195]. The developed sensors are the combination of planar interdigital and meander type. Two different forms of nitrates were used for the experiment; sodium nitrates and ammonium nitrates. They were dissolved in 1 L of distilled water (dH_2O) at different concentrations. The output from the developed sensors were observed and analysed. Results have shown that the sensors response very well to the presence of nitrate in dH_2O. Further experiments were carried out on studying the contamination level of water samples which were taken from various sources and locations in New Zealand. Measurement results from the sensors were compared with measurement taken from nuclear magnetic resonance (NMR) technique. There is good correlation between both results which indicates that the planar electromagnetic sensing system can be one option to access the water quality for environmental monitoring [206]. Figure 1.25 shows the experimental setup conducted in the laboratory.

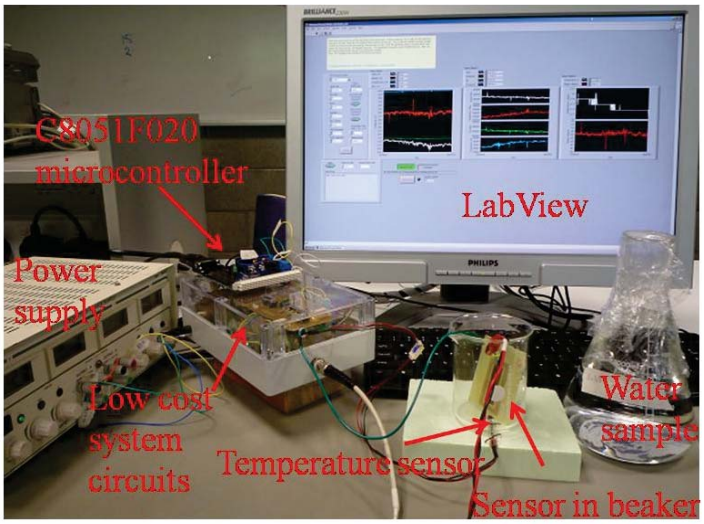

Figure 1.25: Experimental setup to measure nitrate contamination in water

1.6 Contributions of This Thesis

The primary contribution of the research work is on the development of novel sensors for detection of bacterial endotoxin. This is based on the current trend of endotoxin detection looking at the needs for a low cost sensing system which is easy to manufacture and miniaturization, easy to be coupled with different biosensing or chemical sensing techniques, able to provide fast information and can be used in-situ for real time monitoring or pre-screening process. The contribution of the thesis can be summarized as follows;

1. To design novel sensors which are different from conventional interdigital sensors with different electrode structure and the analysis of the concept design of the sensors using circuit analysis and finite element analysis.

2. To fabricate novel planar interdigital sensors of new configurations with better substrate and different fabrication methods.

3. To analyse the characteristic impedance of the fabricated sensors with different chemicals and finalize the best configuration.

4. To established a good coating procedures using a cross-linker and then immobilized the coated electrodes with binding molecules of capable to selectively target the endotoxin or Lipopolysaccharides (LPS).

5. To establish good experimental setup with reliable measuring instruments with auto measurement capability (LabVIEW).

6. To conduct proper experiments with commercially available of pure LPS 0111:B4 and standard endotoxin and to conduct analysis based on impedance characteristic and Impedance Spectroscopy Method.

7. To conduct further analysis using equivalent circuit model with complex non-linear least square method to estimate the related parameters. And to use the statistical analysis technique based on principal component analysis.

8. To verify the sensing measurements with standard endotoxin test kit of Limulus Amebocyte Lysate test assay (LAL) that has been approved by FDA for standard endotoxin detection method.

9. To study the effect of different coating thicknesses on sensing performance and to find the optimum thickness layer. To evaluate the stability and reproducibility of the coated sensors for continuous measurements.

10. Finally to test the developed novel sensors with several food samples in which the sensors able to differentiate the non-contaminated food samples from the contaminated food samples with a very small amount of endotoxin of concentration 0.05 EU/ml.

1.7 Organization of The Thesis

The thesis is organized into eight chapters. Chapter 1 highlight the problem statement which is the bacterial food poisoning caused by Gram-negative bacteria. The literature review covers; the foodborne diseases worldwide and in New Zealand, the economic cost caused by foodborne diseases and the number of incidence; the conventional methods of detection of pathogens and endotoxin; the sensing methods based on biosensors and chemical sensors applications and their different transduction techniques; general description of planar interdigital sensors, design and methodology and lastly the related research works at Massey University were covered in Chapter 1. In Chapter 2, the operating principle of interdigital sensors has been discussed, analysis of concept design based on circuit analysis and finite element analysis (COMSOL modelling). The sensors design of conventional electrode structures and novel design of interdigital sensors with new electrode structures of different configurations have been described in details. Explanation on different fabrication process with different sensors substrates (platform), the experimental setup, measurement method and procedures and basic theory of impedance spectroscopy (IS) method were discussed in Chapter 3 of the thesis. In Chapter 4, experimental investigations have been conducted for impedance characterizations of the fabricated sensors of different configurations. The experiments includes; characterization in air, characterization with sodium chloride (NaCl) and different pH buffers, characterization with different peptides (sarcosine and proline) and characterization with LPS O111:B4 purchased from Sigma. Chapter 5 explain the coating and immobilization procedures to achieve selectivity. Different coating materials or cross linkers (carboxyl-functional polymer, APTES (3-aminopropyltrietoxysilane), and Thionine) have been introduced with different coating techniques to study which cross linker can effectively bind to the Polymyxin B (PmB) molecules and improve the selectivity and sensors performance. In this chapter, the details on immobilization steps and procedures are described. Chapter 6 describes the experimental investigations with endotoxin from LPS O111:B4 and standard endotoxin from LAL test assay. Detail analysis according to IS method, introduced an appropriate equivalent circuit model to estimate impedance parameter and do curve fitting using complex non-linear least square method (CNLS). Statistical analysis using principal component analysis (PCA) has been carried out. In this chapter, the images of non-

coating, coating electrodes and immobilized PmB have been taken using Scanning Electron Microscope (SEM) and Atomic Force Microscope (AFM). Also being described in the chapter is the experiments of different coating thickness and their response to standard endotoxins. The validation of sensors measurement as compared to standard endotoxin test with chromogenic LAL endotoxin assay kit. Finally, the stability, selectivity and reproducibly of coating sensors has also been explained in Chapter 6. Food sample test and analysis are described in Chapter 7 of the thesis. Analyses have been conducted to observe whether sensors can discriminate between non-contaminated food samples with contaminated food samples with very minimum endotoxin concentration. Analyses were also conducted for contaminated food samples at different temperature conditions. Lastly in Chapter 8, the current research works have been concluded and the future works have been proposed.

CHAPTER 2

Development of Novel Planar Interdigital Sensor

2.1 Planar Interdigital Sensors

The operating principle of planar interdigital sensor basically follows the rule of two parallel plate capacitors, where electrodes open up to provide a one sided access to the material under test (MUT) [179]. The electric field lines of parallel plate capacitor and an interdigital sensor are shown in Figure 2.1. The electric field lines generated by the sensor penetrate into the MUT and will change the impedance of the sensor. The sensor behaves as a capacitor in which the capacitive reactance becomes a function of system properties. Therefore by measuring the capacitive reactance of the sensor the system properties can be evaluated.

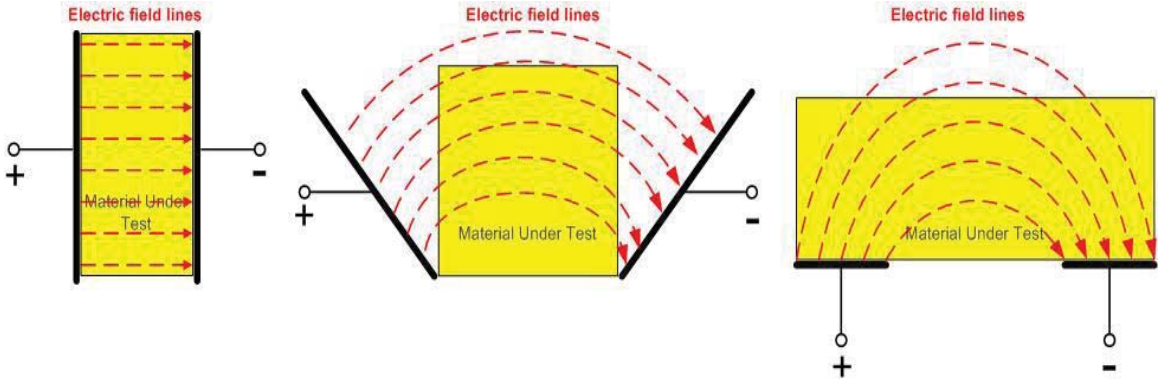

Figure 2.1: Electric field lines of parallel plate capacitors and on coplanar interdigital sensors

Since the electrodes of an interdigital sensor are coplanar, therefore the measured capacitance will give a high signal-to-noise ratio. In order to get a strong signal, the electrode pattern of the interdigital sensor can be repeated many times. The term "interdigital" refer to a digit-like or finger-like periodic pattern of parallel in-plane electrodes, used to build up the capacitance associated with the electric fields that penetrate into a material sample [179]. The conventional interdigital sensor is shown in Figure 2.2. AC voltage source will be applied as an excitation voltage between the positive terminal and the negative terminal. An electric field is formed from positive terminal to negative terminal. Mamishev, also stated that for a semi-infinite homogeneous medium placed on the surface of the sensor, the periodic variation of the

electric potential along the X-axis creates an exponentially decaying electric field along the Z-axis, which penetrates the medium. Figure 2.3 illustrates Mamishev statement.

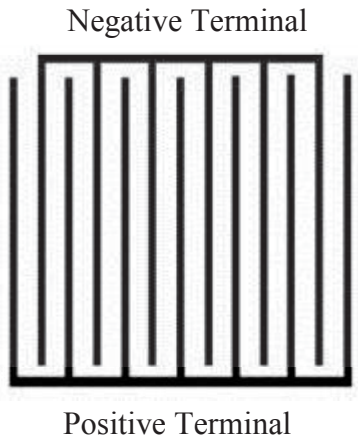

Figure 2.2: Configuration of conventional planar interdigital sensor

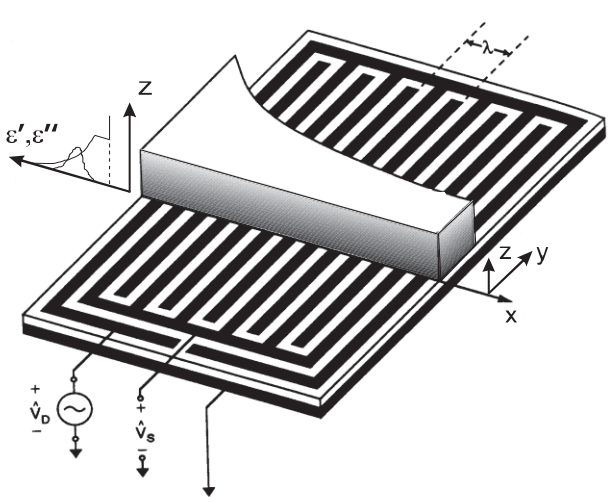

Figure 2.3: Fringing electric field of interdigital sensor [179]

Figure 2.4 shows the side view of the interdigital sensor showing how electric field was formed between positive and negative electrodes. It is seen clearly in Figure 2.4 that the penetration depths of the electric field lines is different for different pitch length. The pitch length of the conventional interdigital sensors is the distance between two consecutive electrodes of the same polarity. Also in Figure 2.4, there are three pitch length (l_1, l_2 *and* l_3) showing the different penetration depths with respect to the pitch length of the sensor. The penetration depth can be increased by increasing the pitch length, but the electric field strength generated at the neighbouring electrodes will be weak. Planar interdigital sensors can be used for different sensing application. Figure 2.5 illustrates on the sensing possibilities of planar interdigital sensors. These sensing

possibilities for various characteristic of samples have given us the opportunity to design and fabricate new type of planar interdigital sensors.

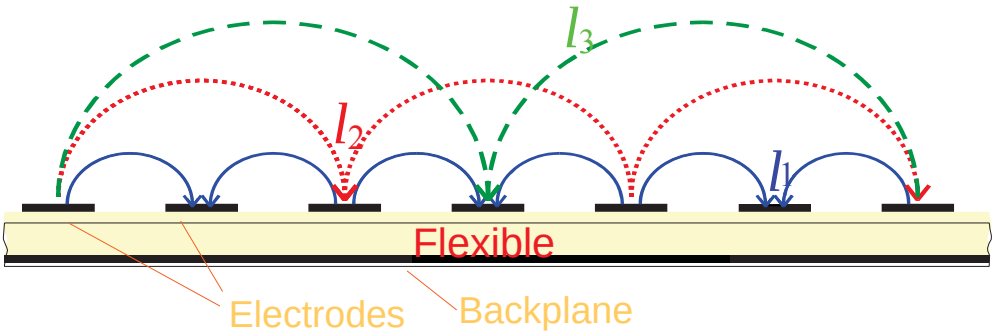

Figure 2.4: Electric field formed between positive and negative electrodes for different pitch lengths, (l_1, l_2 *and* l_3) [179]

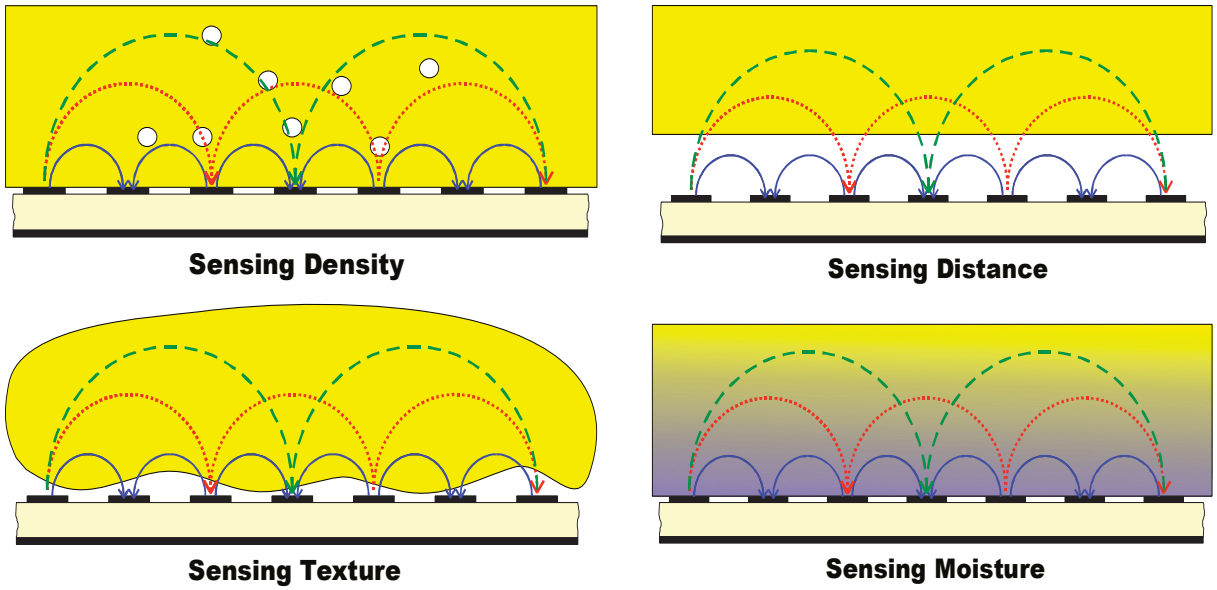

Figure 2.5: Sensing possibilities to detect various characteristic of samples [179]

2.2 Analytical Model and Analysis

New configuration of electrode structure will be discussed in this section. The new structure was designed to have more negative electrodes in between positive electrodes. The optimum numbers of negative electrodes is an important factor to design a better performance of interdigital sensors as reported by the author in [204, 205]. More negative electrodes will result of more uniform electric filed generated within the

sensors geometry. The uniformity of electric field distribution as well as higher capacitance values is two important factors in designing novel intergital sensors.

New types of planar interdigital sensors have been designed to have better sensitivity. Three different configurations of electrode structure have been designed. The configurations of electrode structure were based on the arrangement of different numbers of positive and negative electrodes within the sensing area. These were based on the theory discussed that the numbers of negative electrodes have strong influence on distribution of electric field, penetration depth and sensing signal to create sensors with uniform electric field distribution, higher penetration depth, measureable output signal and give high sensitivity. The three configurations are 1_11, 1_5 and 1_3 which indicate that one corresponds to positive electrode and eleven, five and three are referred to negative electrodes. All designs have same electrode width, pitch length, sensing area and total numbers of electrodes (positive and negative). The combination of electrodes were designed as follows; 1-11-1, 1-5-1-5-1 and 1-3-1-3-1-3-1.The analysis of capacitance of different configurations has been conducted to study how the distribution of capacitance towards each sensor geometry.

2.2.1 Calculation of Capacitance using Circuit Analysis

The equivalent capacitance for each sensor's geometry has been calculated in analytical way. The equivalent capacitive circuit for each sensor's geometry is shown in Figure 2.6. All the sensors have the same area and electrodes spacing between two consecutive electrodes. The capacitors are formed between the positive and negative electrodes.

$$C = \frac{\varepsilon_0 \varepsilon_r A}{d} \qquad \textbf{2.1}$$

where

C = capacitance in farads, F

ε_0 = the permittivity of free space (ε_0 = 8.854x10^{-12} F/m)

ε_r = the relative static permittivity or dielectric constant (vacuum = 1)

A = effective area, square meters

d = effective spacing between positive and negative electrode, meters

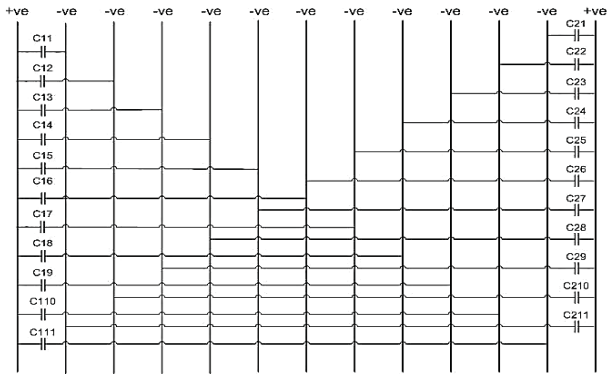

(a)

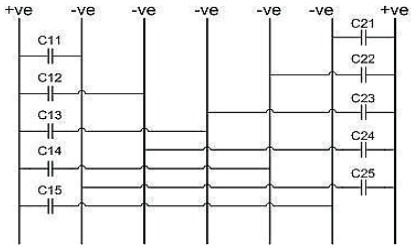

(b)

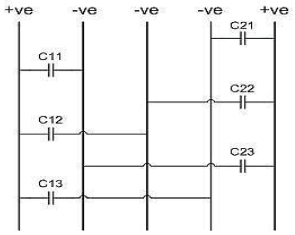

(c)

Figure 2.6: The capacitive circuit of three different sensors; (a) 1_11 electrodes configuration (1-11-1) (b) 1-5 electrodes configuration (1-5-1-5-1) and (c) 1_3 electrodes configuration (1-3-1-3-1-3-1)

All capacitors are effectively connected in parallel. The capacitance is a function of distance between two positive and negative electrodes, d and is given by (with referenced to Figure 2.6);

$$C_{12} = \frac{1}{2}\, C_{11}; \ldots C_{1n} = \frac{1}{n}\, C_{11} \qquad \textbf{2.2}$$

and

$$C_{22} = \frac{1}{2}\, C_{21}; \ldots C_{2n} = \frac{1}{n}\, C_{21} \qquad \textbf{2.3}$$

where $C_{11} = C_{21}$; C_{11} is the capacitance between the positive electrode and closest negative electrode.

Therefore the total equivalent capacitance (C_{eq}) for each sensor's geometry is given by;

$$C_{eq(1)} = C_{11} + C_{12} + \ldots . C_{1n} \quad \textbf{2.4}$$

$$C_{eq(2)} = C_{21} + C_{22} + \ldots . C_{2n} \quad \textbf{2.5}$$

where $C_{eq(1)}$ is for equivalent capacitance in the first geometry of each sensor while $C_{eq(2)}$ is the equivalent capacitance in the second geometry of each sensor.
Therefore total capacitance within sensor geometry is given by;

$$C_{Total} = C_{eq(1)} + C_{eq(2)} + \cdots . + C_{eq(n)} \quad \textbf{2.6}$$

The estimated capacitance within each sensor's geometry is shown in Figure 2.7. It is shown that Sensor 1_11 has better uniformity in terms of distribution of effective capacitance throughout the sensors geometry compared to Sensor 1_5 and Sensor 1_3, but has lower total capacitance value. The result from analytical analysis is in line with the result shown in the simulation using COMSOL. It is important to achieve better sensitivity in terms of uniform distribution of total capacitance value and the uniformity of electric field distributions throughout the sensor geometry. The performance of the sensors depends on the characteristic of the sensor and also the characteristic of the material under test (MUT). Therefore the experiments of sensors with MUT will determine the best sensing performance of different sensor configurations.

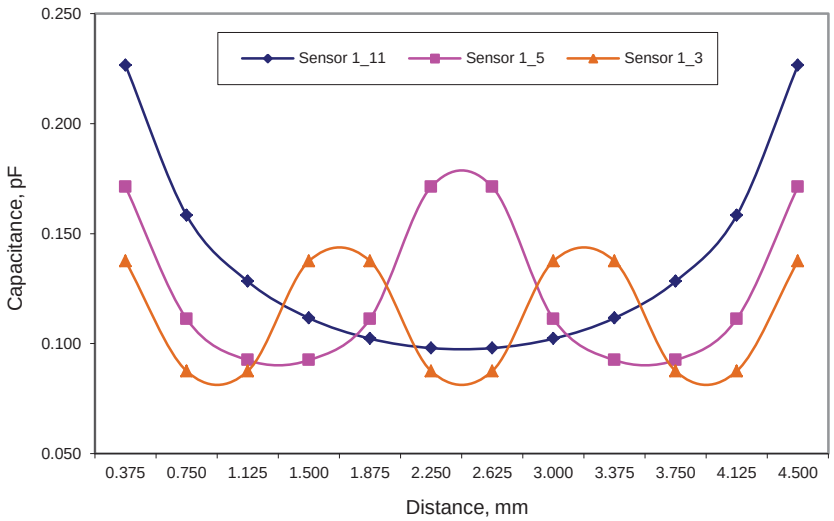

Figure 2.7: Equivalent capacitance within each sensor geometry

2.3 Modelling using Finite Element Analysis: COMSOL Multiphysics

2.3.1 Introduction

Finite element analysis is a computational program used to study and analyse model of material or design. Finite element analysis has been used widely for modelling of planar interdigital sensors for various applications [207-210]. The COMSOL Multiphysics® (formerly FEMLAB) is a finite element analysis and solver software package for various physics and engineering applications, especially coupled phenomena, or multiphysics. The software applications are based on partial differential equations (PDEs) [211]. The sensors were modelled to derive the optimum structure of sensor for better performance. The Electromagnetic module of COMSOL was used for analysis of novel interdigital sensors. The application was in 3D and AC/DC module for electrostatics mode for dielectric material was selected. Figure 2.8 shows the arrangement of positive electrodes and negatives electrodes of the sensor design in 3D view. The sensors were modelled using the actual size of the fabricated sensors. COMSOL Multiphysics has been used to characterize the planar meander sensor and interdigital sensor as discussed in [212] and [213]. This following section will discuss in detail the capability of the COMSOL Multiphysics to simulate and analyse the novel planar interdigital sensors.

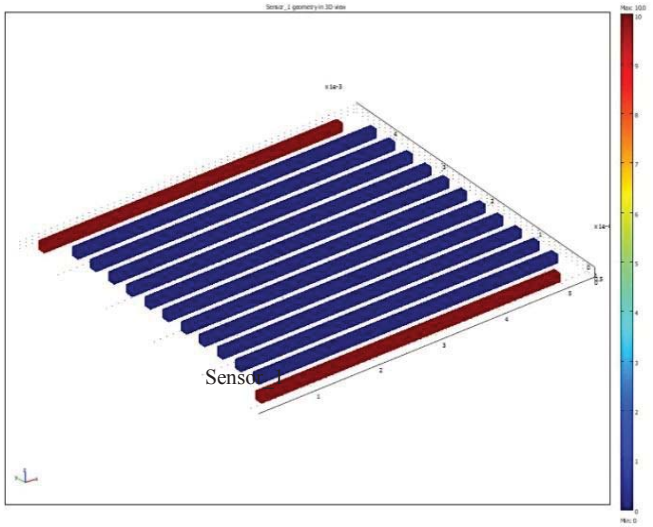

Figure 2.8: The geometry of interdigital sensor in 3D view

2.3.2 Model Definition - COMSOL Implementation

The analysis using COMSOL was carried out to observe how optimum number of negative electrodes between two positive electrodes of interdigitated configuration contributes to highest sensitivity measurement. Analysis was conducted for different number of negative electrodes between two positive electrodes. All electrodes were modeled to have the same pitch (250 μm), same electrode length (4750 μm), electrode width (125 μm) and same sensing area configurations.

The capacitance value of each sensor design can be calculated from COMSOL applications. The value for electrostatic energy density, W_e can be obtained from the simulation. The energy required to charge a capacitor should equal that of the electrostatic field, which is given by;

$$W_e = \frac{Q^2}{2C} \tag{2.7}$$

W_e is available in the Electrostatics application mode; the software calculates it by integrating across the domain

$$W_e = \int_{\Omega} (D.E) d\Omega \tag{2.8}$$

where, D is the electric displacement, E is the electric field intensity and dΩ is the domain boundary. The capacitance, C, is related to the charge on the two conductive plates, Q, and the voltage difference across those plates, ΔV, by;

$$C = \frac{Q}{\Delta V} \tag{2.9}$$

The calculation of C is carried out from the stored electric energy, W_e, and the voltage across the two plates, ΔV, and is given by;

$$C = \frac{Q^2}{2W_e} = \frac{C^2 \Delta V^2}{2W_e} \Rightarrow C = \frac{2W_e}{\Delta V^2} \tag{2.10}$$

$$Therefore, \quad C = \frac{2W_e}{\Delta V_0^2} \tag{2.11}$$

where; W_e is the stored electrostatic energy density and V_0 is the applied voltage to the positive electrode. The negative electrode is kept at 0 V.

The calculated capacitance and reactance as a function of number of negative electrodes between two positive electrodes obtained from simulation are shown in Figure 2.9 and Figure 2.10 respectively. It was observed that the number of negative electrodes between five to thirteen has the highest capacitance and consequently the lowest reactance value. This is true since from equation (2.1) the capacitance only depends on effective area (A) as other parameters remain constant (ε_0, ε_r and d). Therefore, as the number of negative electrodes increase the effective area (A) also increase and consequently the capacitance increases. This is only true for certain number of negative electrodes as with the increase number of negative electrodes, the electric field strength becomes weak and the capacitance is reduced.

Further analysis was conducted to evaluate the distribution of electric field and to measure the electric field intensity for all three sensors. Figure 2.11 shows the simulation results of electric field distribution of each sensor. As for Sensor 1_11, the magnitude of electric field strength is stronger at neighbouring electrodes but as it goes to the middle it becomes weak. It is also shown in Figure 2.11 that the electric field strength becomes weak as it goes up. The same results were observed from the simulation results of Sensor 1_5 and Sensor 1_3 having different configuration. It is shown that optimum numbers of negative electrodes between positive electrodes will give better distribution of electric field but comparatively weak in field strength. The electric field strength needs to be sufficient to interact with material under test.

The variation of electric field intensity was then analysed for each sensor designed. Electric field intensity is a measurement of electric field (V/m) along the z-axis. The cross-section line data were set starting from coordinates X_0=2.75 mm, Y_0= 0 mm, Z_0= 0.125 mm and X_1=2.75 mm, Y_1=4.75 mm, Z_1=0.125 mm. The coordinate of Z_0 and Z_1 were replaced from 0.125 mm to 3.50 mm and electric field intensity data were recorded. The average of electric field intensity is shown in Figure 2.12. Sensor 1_11 has been chosen for analysis. Table 2.1 shows the calculated capacitance value of each sensor measured from the simulation.

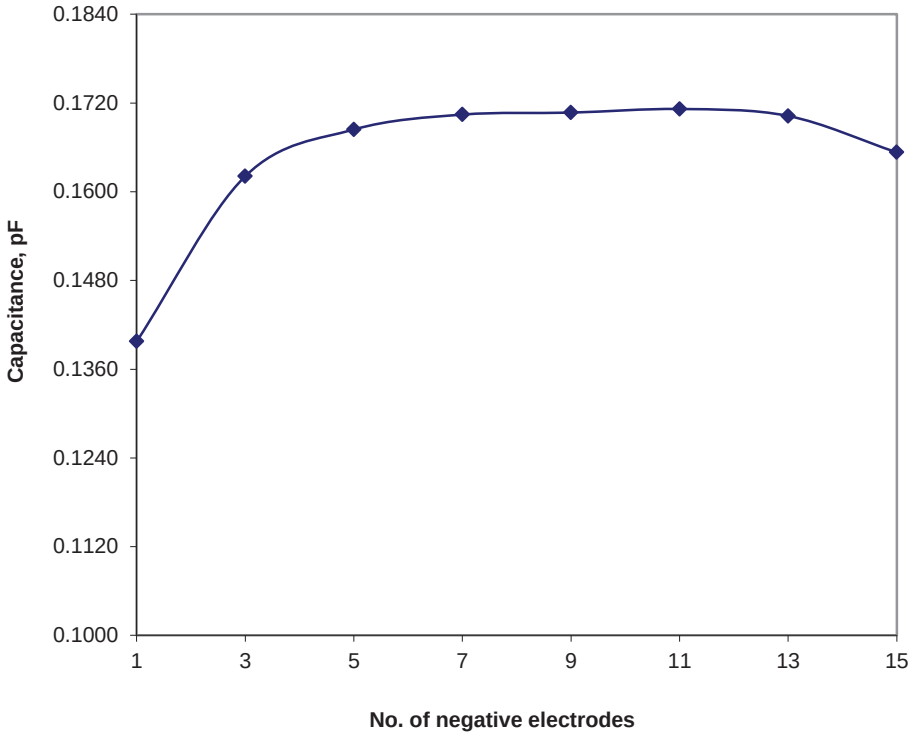

Figure 2.9: The relationship between Capacitance and no. of negative electrodes

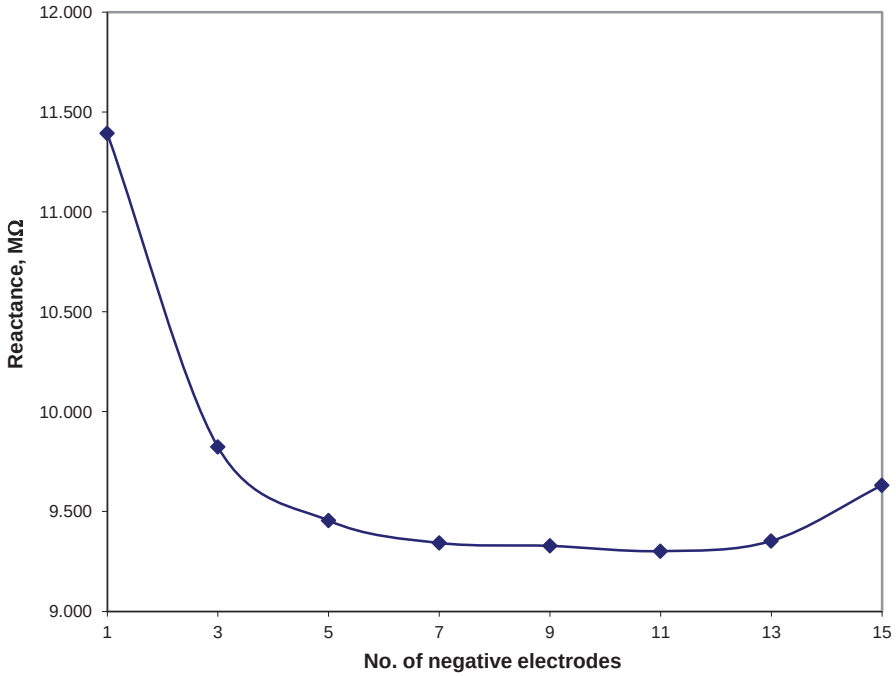

Figure 2.10: The relationship between Reactance and no. of negative electrodes

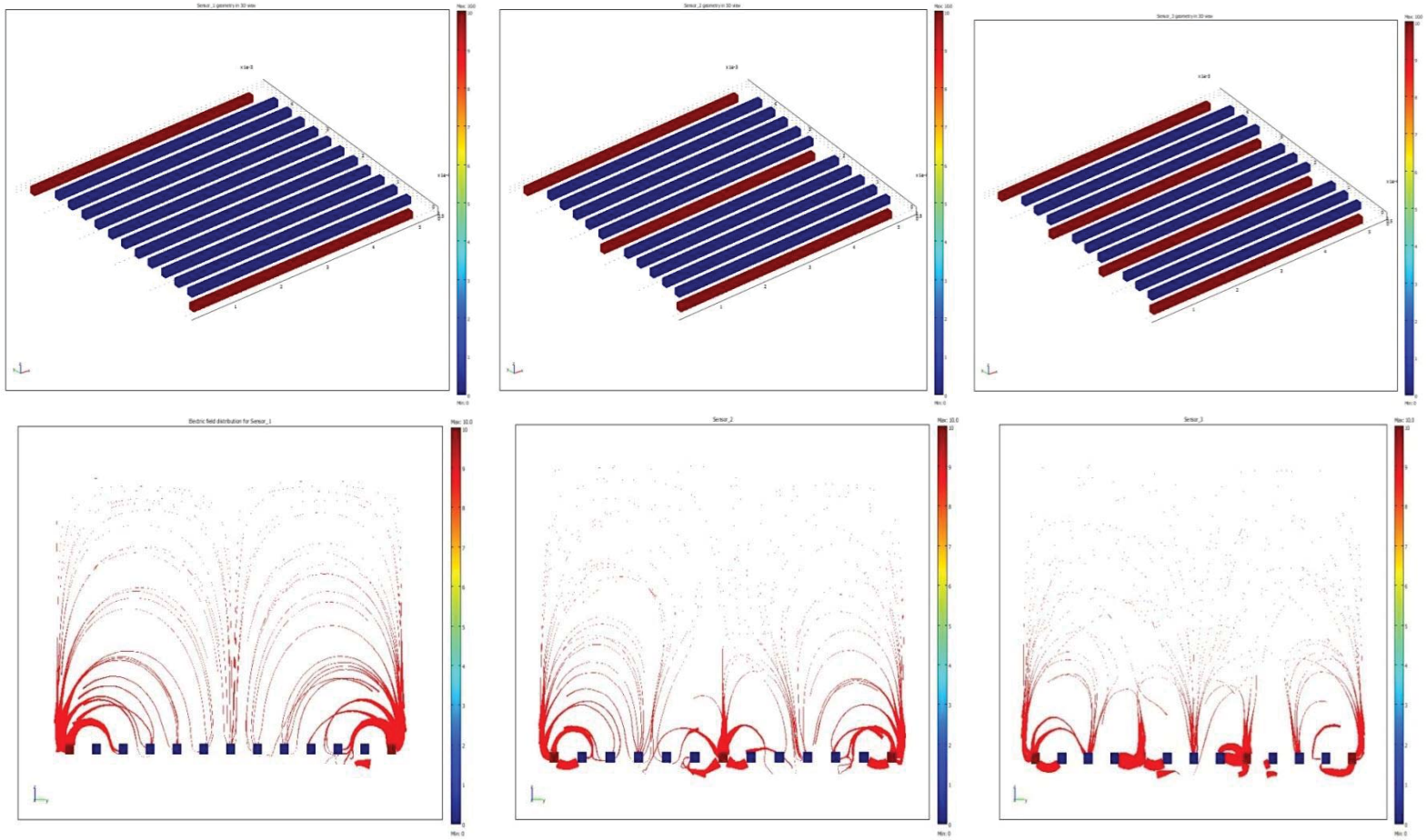

(a) (b) (c)

Figure 2.11: Electric field distribution of each sensors; (a) Sensor 1_11, (b) Sensor 1_5 and (c) Sensor 1_3.

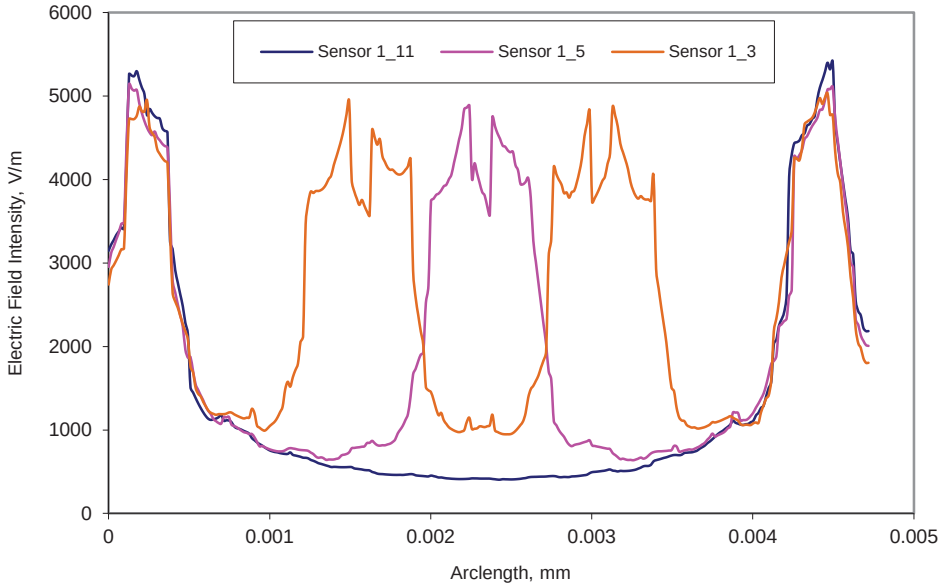

Figure 2.12: Electric field intensity of each sensor

Table 2.1: Calculated capacitance from the modelling using COMSOL multiphysics for interdigital sensors

Sensor Type	Simulation Parameters			Calculated Parameters
	V_e (V)	Frequency (kHz)	Electrostatic energy density (J)	Capacitance (pF)
Sensor 1_11	10.0	10.0	8.5421×10^{-11}	1.709
Sensor 1_5	10.0	10.0	1.3823×10^{-11}	2.765
Sensor 1_3	10.0	10.0	1.7091×10^{-10}	3.418

Sensor 1_11 was chosen for further analysis using COMSOL. The analysis was conducted by placing sample into the model. Two analyses have been conducted. The first analysis was to observe the relationship of capacitance for different values of effective permittivity (ε_r) of sample while maintaining the same thickness (1 mm). The second analysis was to evaluate the capacitance produced by the sensor with different sample thickness while keeping the permittivity value constant (air gap, ε_r =1 and sample, ε_r =3.6). The 3D model for the analysis is shown in Figure 2.13. The model consists of Sensor 1_11, a sample and a box with constant height of 3 mm (enclosed system). The electric field passing through the sample and the effect of permittivity of sample and air is shown in Figure 2.14. From Figure 2.15, it is seen that the capacitance has increased with the increase in permittivity of the sample. The increase of

capacitance is not proportional to sample permittivity due to significant influence of air. Result in Figure 2.16 shows that the capacitance value decrease as the sample thickness increases.

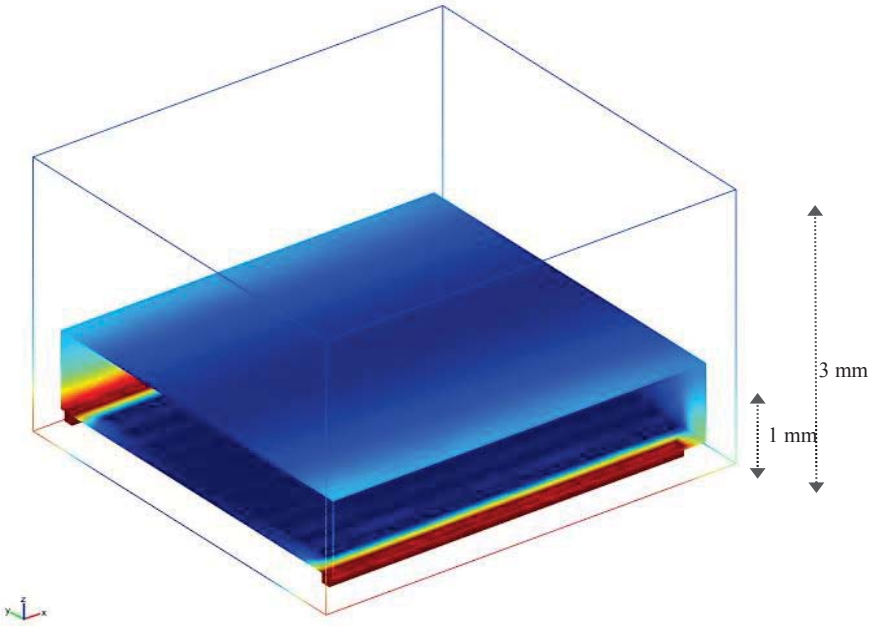

Figure 2.13: 3D view of Sensor 1_11 with a known sample

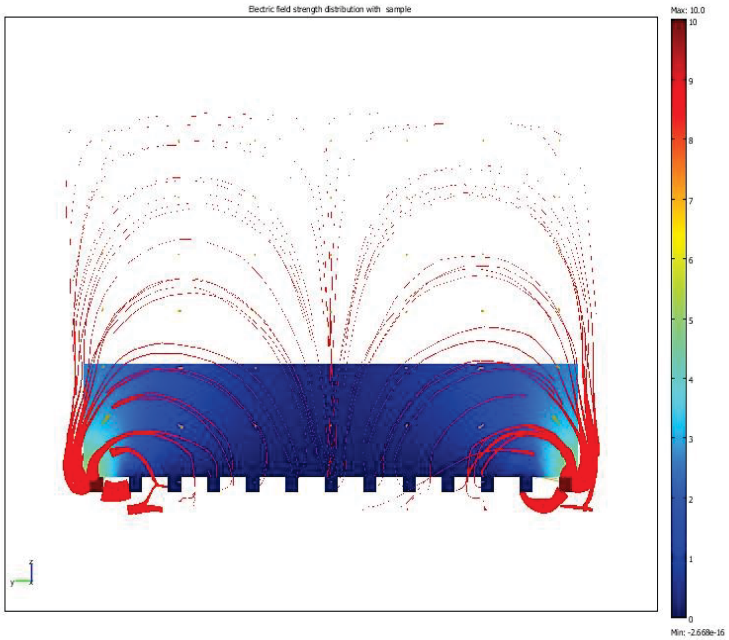

Figure 2.14: Electric field distribution of Sensor 1_11 for a known sample

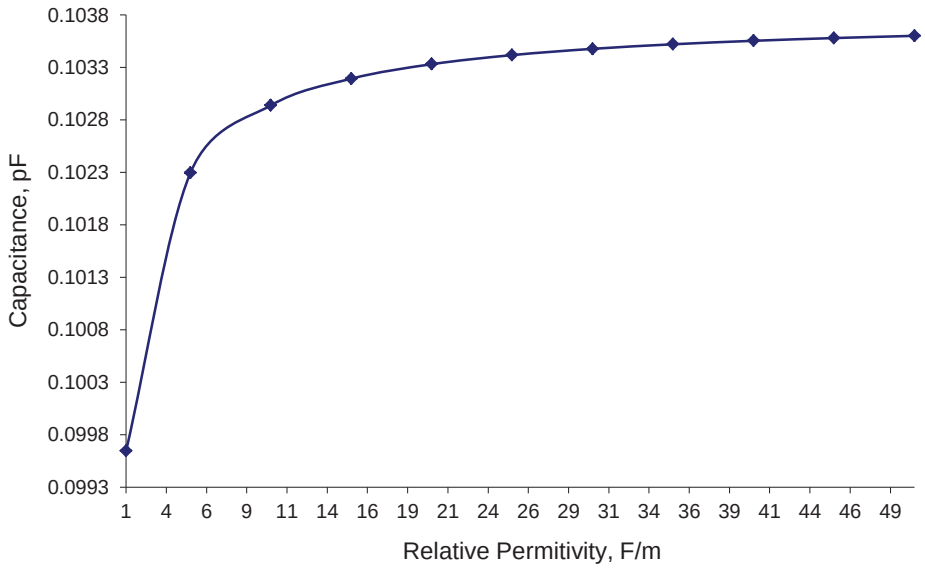

Figure 2.15: Calculated capacitance for different values of sample permittivity

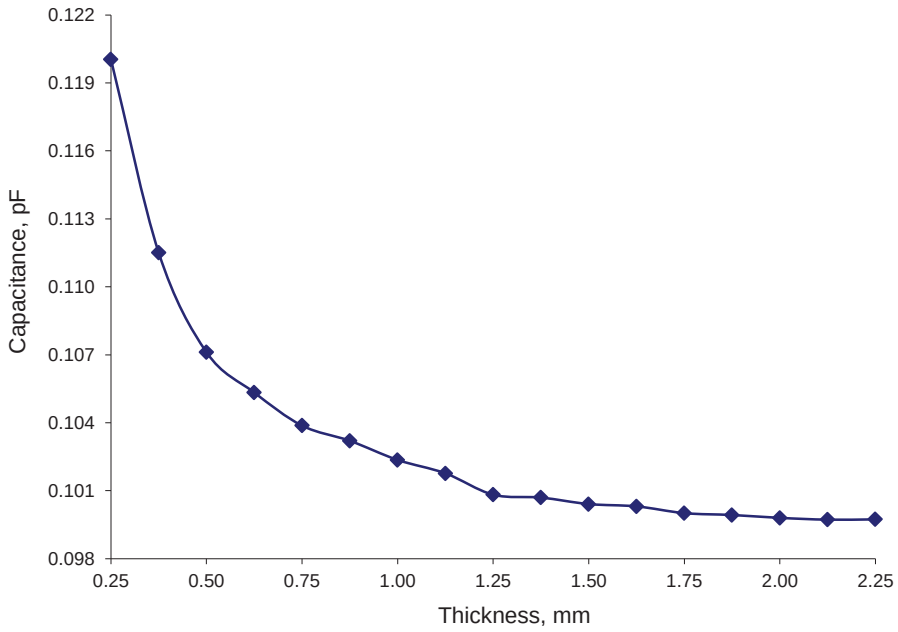

Figure 2.16: Calculated capacitance for different values of sample thickness

2.4 Sensor Design and Fabrication

2.4.1 Design and Fabrication Process

Initial design on the sensors was done using Altium Designer 6 software. The fabrication process of the sensors was done in Massey Electronics Laboratory. The final design of each sensor from the Altium Designer was printed in negative and then was

transferred into a film. The conducting layers of the board are typically made of thin copper foil. The insulating layers (dielectric) are typically laminated together with epoxy resin pre-impregnated. The film together with the board was exposed to the UV light. This process will impress and burn the desired sensor design onto the board. The printed circuit was developed. The printed circuit board was immersed into a chemical for etching process to remove the unwanted copper, leaving only the desired copper trace. The sensor was cut to a desired design to make it suitable for testing.

2.4.2 Conventional Interdigital Sensors

Initial part of the research works were involved design and fabrication of three conventional planar interdigital sensors. The initial goal is to understand how conventional interdigital sensor works and respond to materials. All three sensors were designed with different configurations, so that the difference of their response can be evaluated. Each sensor was designed to have same effective area of 5000 μm by 5000 μm but with different pitch lengths of 250 μm, 510 μm and 1020 μm. The negative and positive electrodes have the same length of 4750 μm and width of 250 μm. Table 2.2 shows the parameters for conventional interdigital sensors. Figure 2.17 shows the representation of conventional interdigital sensor with configuration #1 (Din_10mil) and Figure 2.18 shows the representation of conventional interdigital sensor with configuration #2 (Din_20mil) and configuration #3 (Din_40mil). Figure 2.19 shows the fabricated conventional interdigital sensors.

Table 2.2: Conventional interdigital sensor parameters

Sensor	Sensing area, (mm^2)	Pitch length, (mm)	Number of electrodes	
			Positive	Negative
Din_10mil	25	0.25	5	6
Din_20mil	25	0.51	4	4
Din_40mil	25	1.02	2	3

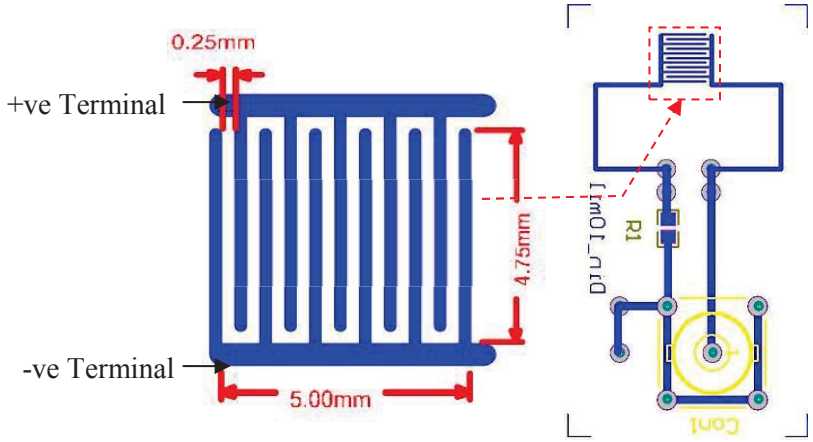

Figure 2.17: Representation of conventional interdigital sensor with configuration #1

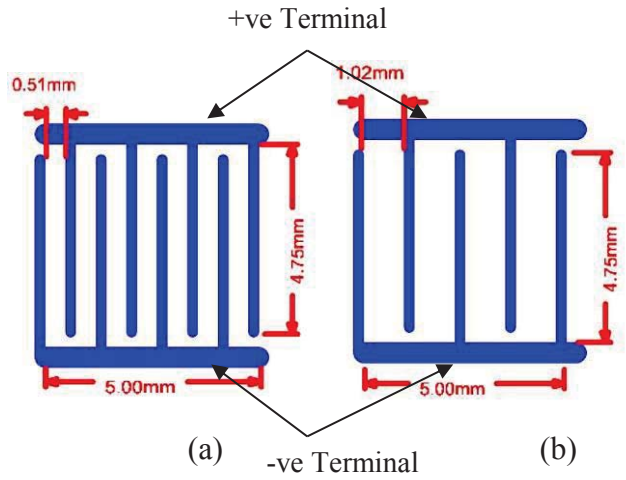

Figure 2.18: Conventional sensor with (a) Configuration #2 and (b) Configuration #3

Figure 2.19: The fabricated conventional interdigital sensors compared to 20¢ New Zealand coin

2.4.3 Novel Planar Interdigital Sensors

Novel planar interdigital sensors were developed to have better sensitivity measurement with better response to material under test. The design of novel planar interdigital sensors is unique because they are different compared to conventional interdigital sensors. The uniqueness of the novel sensors because they were designed to have more negative electrodes in between positive electrodes with different configurations of electrode structure. All sensors were designed to have same effective area of 4750 μm by 5000 μm and having pitches of 250 μm. The positive and negative electrodes have the same length and width of 4750 μm and 125 μm respectively. The sensors were fabricated on three different materials with different fabrication process.

2.4.3.1 FR-4 Sensors

The initial sensors were fabricated on FR4 at Massey University using the normal printed circuit board technology. All sensors have equal numbers of electrodes (thirteen). The only parameter changing in the sensor design is the *d*, spacing between two adjacent positive and negative electrodes between which the electric field-lines exist. Sensor 1_11 was designed to have two positive electrodes at each end separated by eleven negative electrodes. Sensor 1_5 and Sensor 1_3 were designed with the same dimensions but with different configurations. Sensor 1_5 has five negative electrodes between two positive electrodes and has the same pitch like Sensor 1_11. Sensor 1_3 has three negative electrodes between two positive electrodes. Table 2.3 shows the parameters for novel interdigital sensors. Figure 2.20 shows the representation of sensor configuration #1 (Sensor 1_11). Figure 2.21 shows sensor configuration #2 (Sensor 1_5) and sensor configuration #3 (Sensor 1_3). The fabricated novel interdigital sensors are shown in Figure 2.22.

Table 2.3: Novel interdigital sensor parameters

Sensor	Sensing area, (mm^2)	Pitch length, (mm)	Number of electrodes	
			Positive	Negative
Sensor 1_11	23.75	0.125	2	11
Sensor 1_5	23.75	0.125	3	10
Sensor 1_3	23.75	0.125	4	9

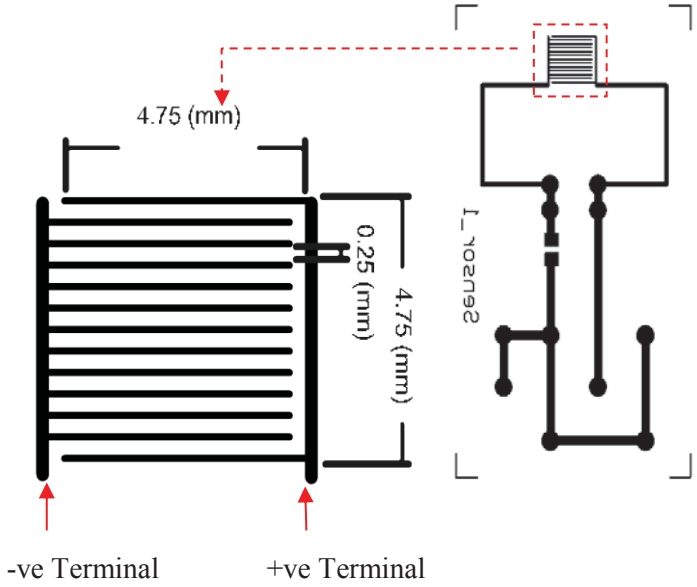

Figure 2.20: Representation of Sensor 1_11 configuration

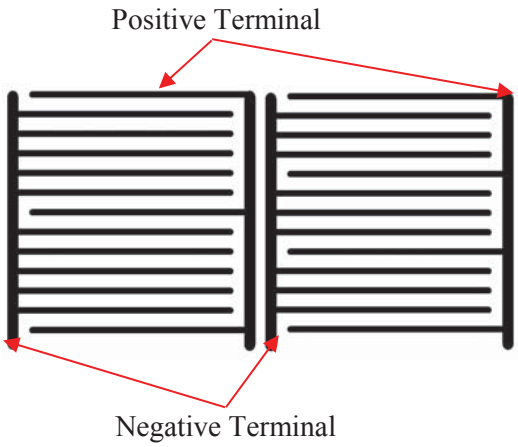

Figure 2.21: Sensor 1_5 and Sensor 1_3 with different configurations

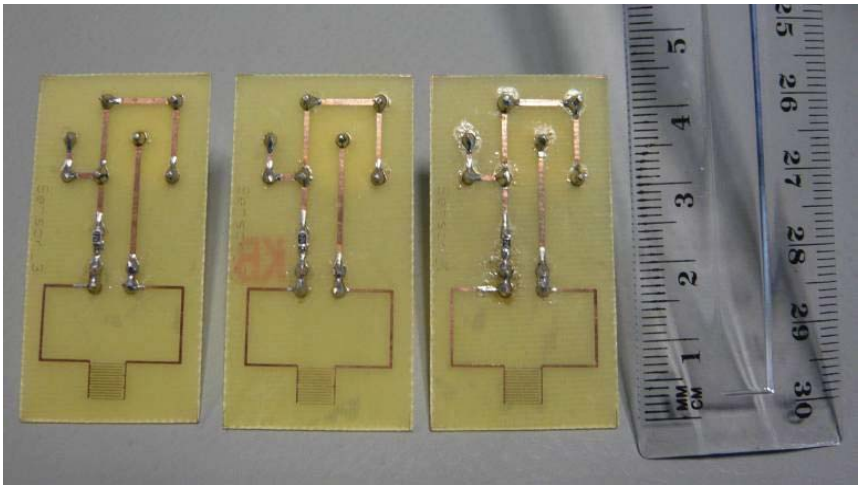

Figure 2.22: The fabricated novel interdigital sensors (FR4)

2.4.3.2 Alumina Sensors

The second sensors were fabricated at Northern Illinois University, United States using alumina as its platform. The sensors were constructed using standard thick film printing methodologies. The pattern was drawn in AutoCad and then printed on a Fire 9500 photoplotter. The patterns were then transferred to three 325 mesh screens. The printer used in the fabrication was a Presco 435, which is capable of printing up to a 100 mm x 100 mm substrate. The top trace layer was printed using a PdAg 850°C firing alloy while the ground plane was made using a 850°C silver material. The solder dam was made using a 600°C of low k dielectric to prevent solder bridging. The wet paste was dried and fired after each individual layer was printed. The paste was dried at 150°C then was inspected consistently. The dried substrate was then placed on the belt of a BTU firing furnace profiled to deliver 850°C +/- 5°C for 10 minutes. The duration of the entire firing cycle is approximately 30 s. The substrates were then patterned for the next layer and the cycle was repeated. The final layer is a low k dielectric to limit the solder flow during the mounting of a chip resistor. Figure 2.23 shows the design of fabricated sensors which were fabricated at Northern Illinois University, United States. Figure 2.24 shows the fabricated sensors.

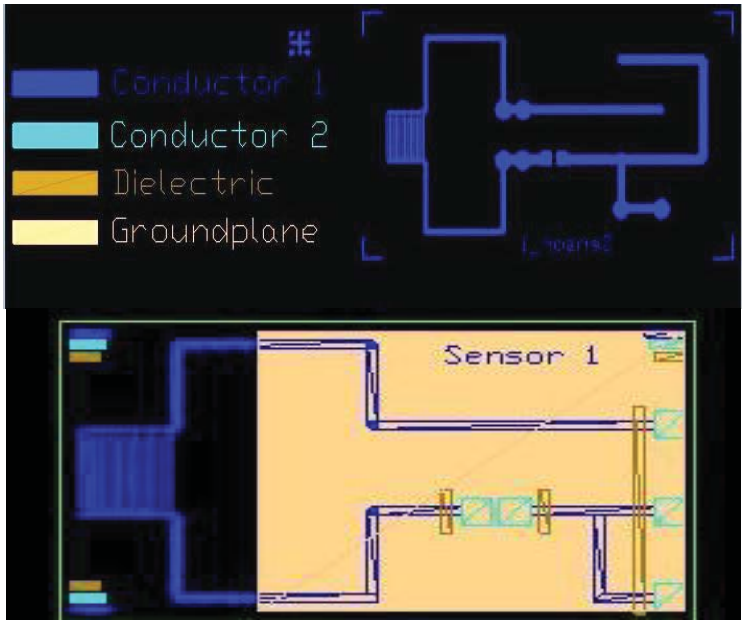

Figure 2.23: The representation of interdigital sensor (Sensor 1_11)

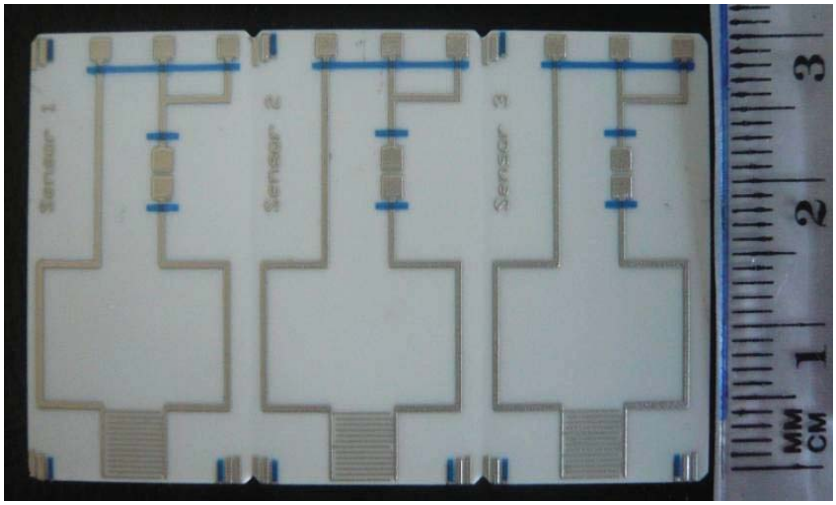

Figure 2.24: The fabricated interdigital sensors (Alumina)

2.4.3.3 Glass Sensors

The third sensors were fabricated on glass using MEMS technology and were fabricated in Taiwan at Southern Taiwan University. The plastic photo mask design was used because of low cost and easy to prepare. The glass slip (sensor platform) was first cleaned with acetone. Then, an ultrasonic cleaning machine was used to clean the glass in methanol solution. N_2 gun was used to dry the glass slide. The IDT electrode fabrication process starts by depositing the Cr or Au on the glass slide using E-beam evaporated machine. Then, the positive photo-resist (PR) was coated on the metal layer by using spin coater. The coated metal layer was exposed to the UV light. The Developer machine was used to remove the unexposed PR.

The etching process was done to remove the surplus metal and also to remove the remaining PR leaving only the patterned electrode. Figure 2.25 shows the IDT electrode fabrication process. Figure 2.26 shows the representation of interdigital sensor which were using MEMS and have been fabricated at Southern Taiwan University, Taiwan. Figure 2.27 shows the fabricated interdigital sensors using MEMS technology. Figure 2.28 shows the three different designs of fabricated novel interdigital sensors.

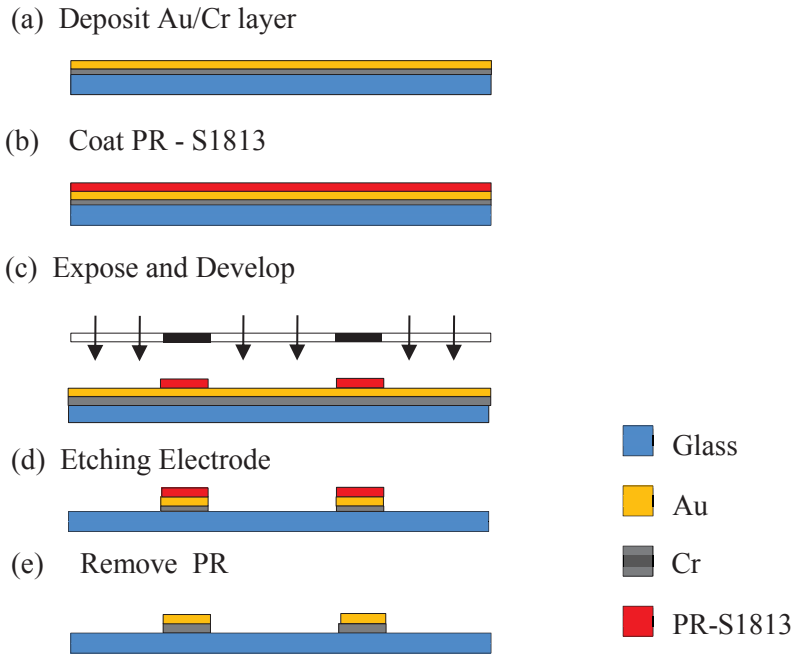

Figure 2.25: The IDT electrode fabrication process

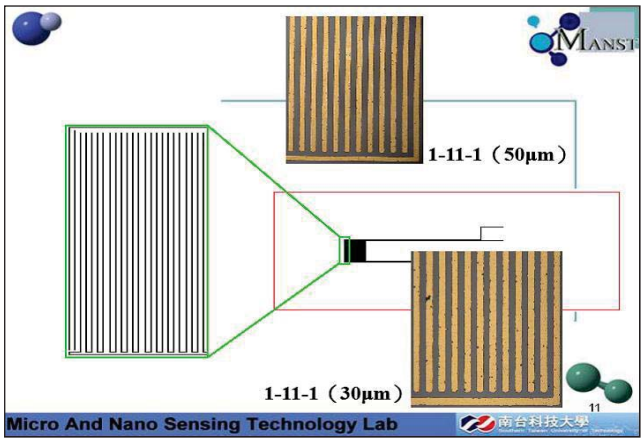

Figure 2.26: The representation of interdigital sensor (Glass)

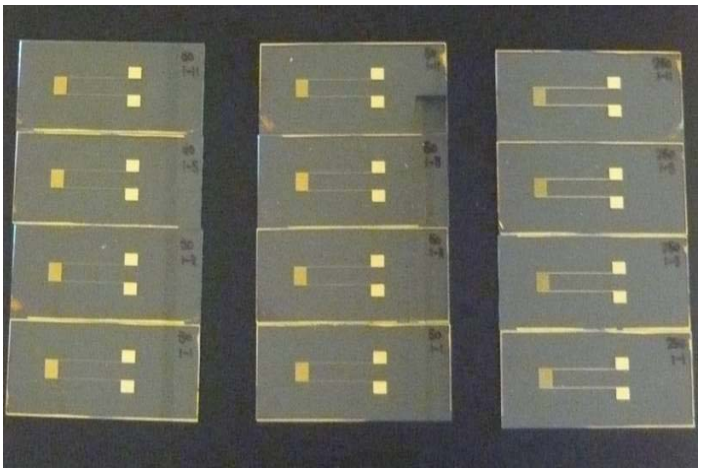

Figure 2.27: The fabricated interdigital sensors using MEMS technology

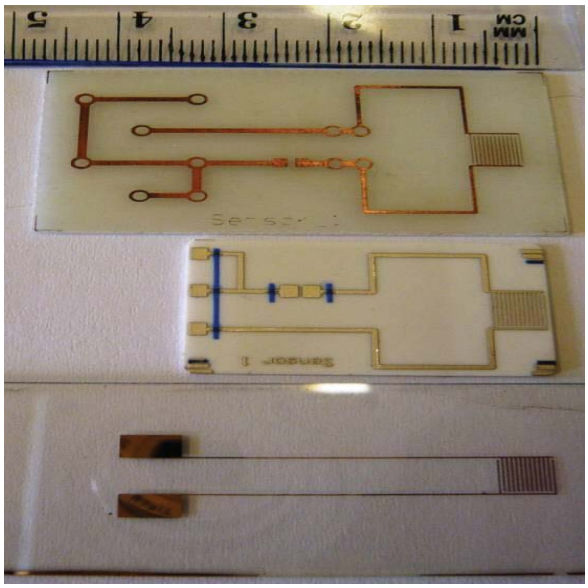

Figure 2.28: The representation of three different designs of novel interdigital sensors

2.4.3.4 Silicon Sensors

The latest design of the thin film planar interdigital structure was fabricated by photolithography and etching techniques on a Silicon/Silicon Dioxide (Si/SiO_2) wafer (single side polished). The schematic diagram of electrode configurations is shown in Figure 2.29. Figure 2.30 shows the fabrication process of the new silicon sensors. The sensor was fabricated to have multiple configurations of 1_11, 1_5 and 1_3. The sensors are designed to have better output signal, low impedance and improved sensitivity. The fabricated dies have a rigid substrate which is advantageous in noncontact measurements. In order to implement model-based parameter estimation algorithms effectively it is important to maintain a well-defined geometry of the electrode structure. CoventorWare was used to design the patterns of the ID structures. The patterns varied according to the spatial wavelength of the periodic interdigital strucuture while the width of electrodes and the sensing area was set to constant values of 25 μm and 2.5 mm × 2.5 mm respectively.

All patterns were printed on a 5 inch soda lime transparent mask using a mask laser writer. Pre-baking was performed at 150 ºC on the wafer substrate so that the photoresist attached better to the surface. A spin coater was used to coat 4 μm of positive photoresist (EC13027) on a 4 inch wafer. An oven was used to post bake the wafer at 100 ºC for 1 minute. A UV light exposure tool was used to transfer the ID

patterns to photoresist of the wafer. A constant dose of 200 mJ/cm^3 was used at a separation of 30 μm between the wafer and the mask. The wafer was then developed for 1 minute under a solution Tetra-Methyl Ammonium Hydroxide (TMAH) based solution (AZ 726). Plasma ashing at 70 ºC was used to perform a "Descum" process to remove residual photoresist in trenches. Following this, 20 nm of Chromium (Cr) and 500 nm of Gold (Au) in which the latter acts as a barrier layer for good adhesion, were sputtered on to the wafer substrate by DC magnetron sputtering. Gold electrodes have the advantage of being inert and flexible. Argon gas was used at a pressure of 30 mTorr and the DC power was set to 800 W. Lift-off was then performed under a solution of acetone. After lift-off, the unpolished side of the wafer was also sputtered with 20 nm of Chromium (Cr) and 500 nm of Gold (Au). This will act as the guard plane. A follower op-amp can drive the guard plane to be equal to the sensing voltage hence eliminating any current between the sensing and guard electrodes through the substrate. Thus, the conductance and capacitance between the sensing and guard plane are eliminated, leading to simplified response analysis and improved device sensitivity. The fabricated silicon based interdigital sensor is shown in Figure 2.31.

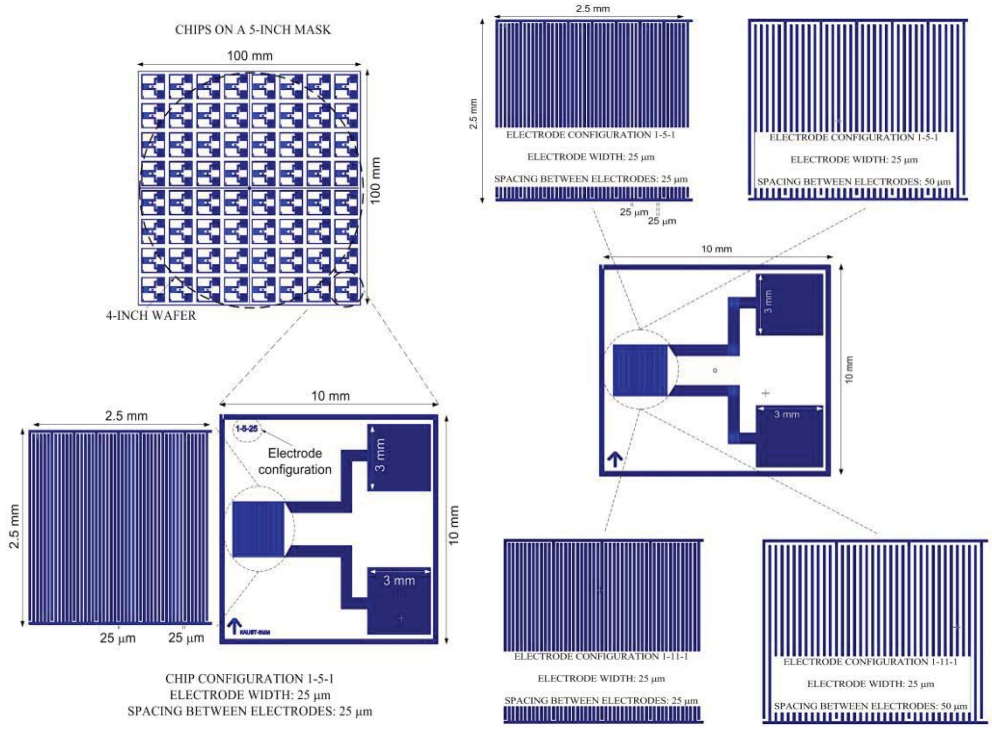

Figure 2.29: Interdigital electrode configurations.

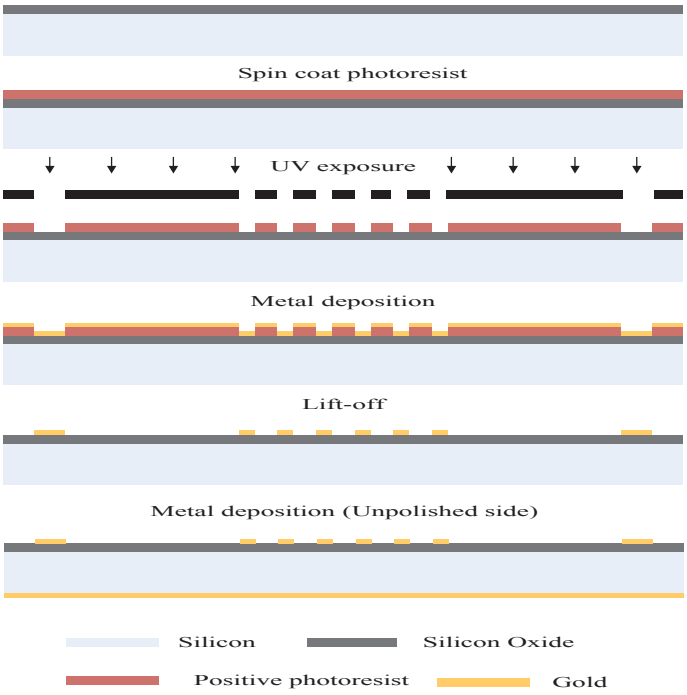

Figure 2.30: The fabrication process on silicon wafer (Mask 1)

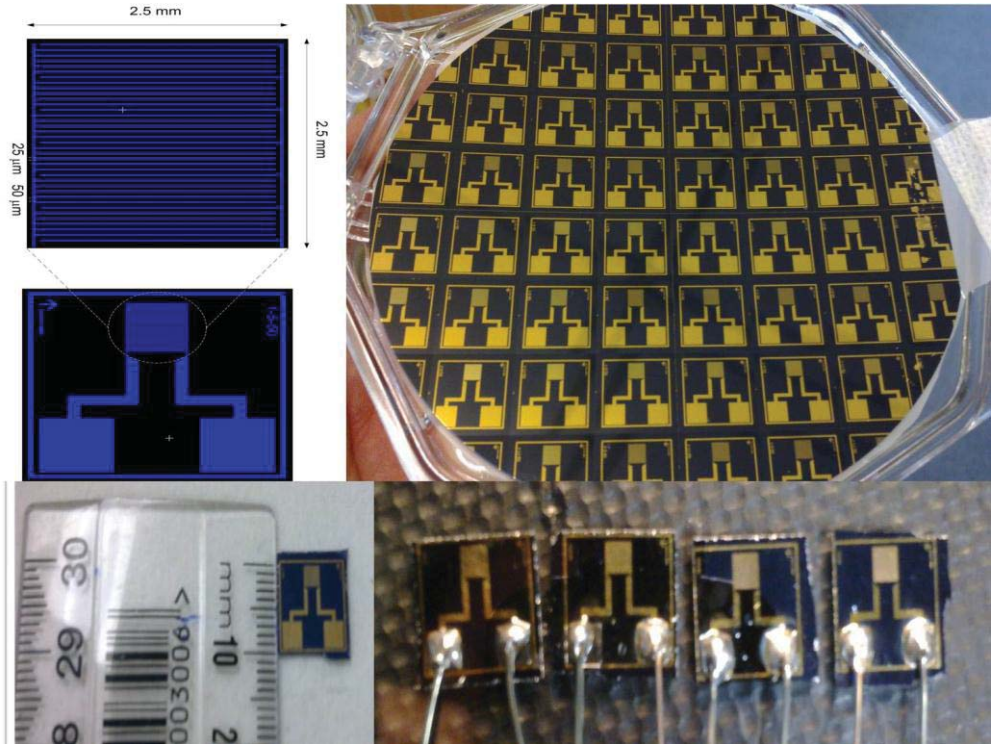

Figure 2.31: Miniature type of thin film silicon based interdigital sensor.

An improved design of the silicon sensors has been fabricated. The initial fabrication process is the same for Mask 1 as in Figure 2.30. The improved part was in fabrication of Mask 2 as shown in Figure 2.32. After lift-off, the wafer was coated with a 200 nm layer of Silicon Nitride (Si_3N_4) by plasma enhanced chemical vapor

deposition (PECVD). Si_3N_4 has been used in many microdevices as a passivation layer since its film properties can be easily controlled and modified by varying its deposition methods and conditions. Moreover, Si_3N_4 can withstand continuous exposure to air at high temperatures for long periods of time. The deposition of Si_3N_4 using the PECVD technique results in films that have good adhesion, low pinhole density, good step coverage and uniformity. All areas except the electrodes and bonding pads were covered with Si_3N_4. Since the electrodes are open complementary biomolecules can be coated directly on top of the electrodes. This way target biomolecules will be attached as close as possible to the electrodes leading to high detection signals. After Si_3N_4 coating 4 μm of positive photoresist (EC13027) was coated on the wafer. A UV light exposure tool was used to soften the resist over the electrodes and bonding pad windows. After development reactive ion etching (RIE) was used to open the area with electrodes and the bonding pads. RIE is one method of dry etching and it prevents the undercutting cause by wet etching. In dry etching an anisotropic etches is created. An anisotropic etch is critical for high-fidelity pattern transfer. The latest silicon sensors is shown in Figure 2.33.

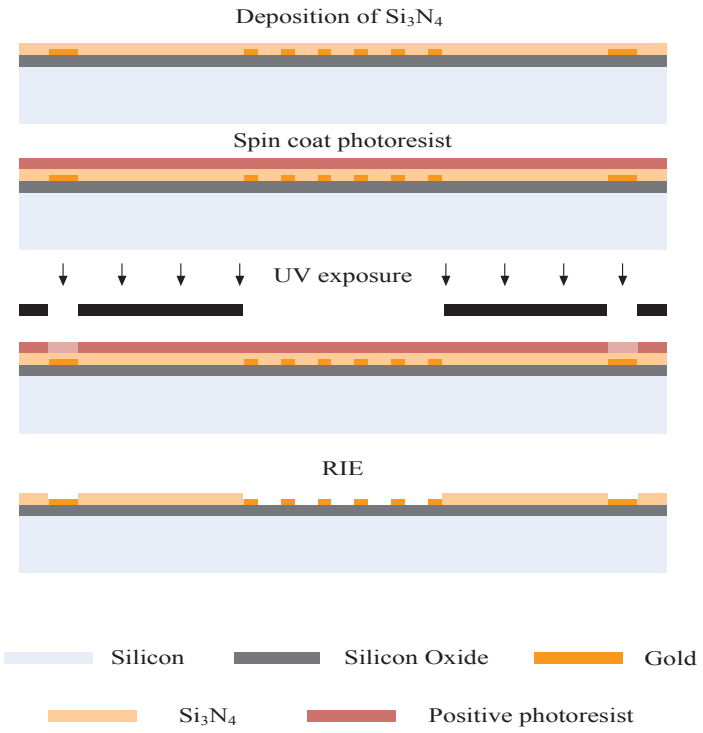

Figure 2.32: Fabrication process (Mask 2 – Deposition of Si_3N_4 by PECVD and etching by RIE)

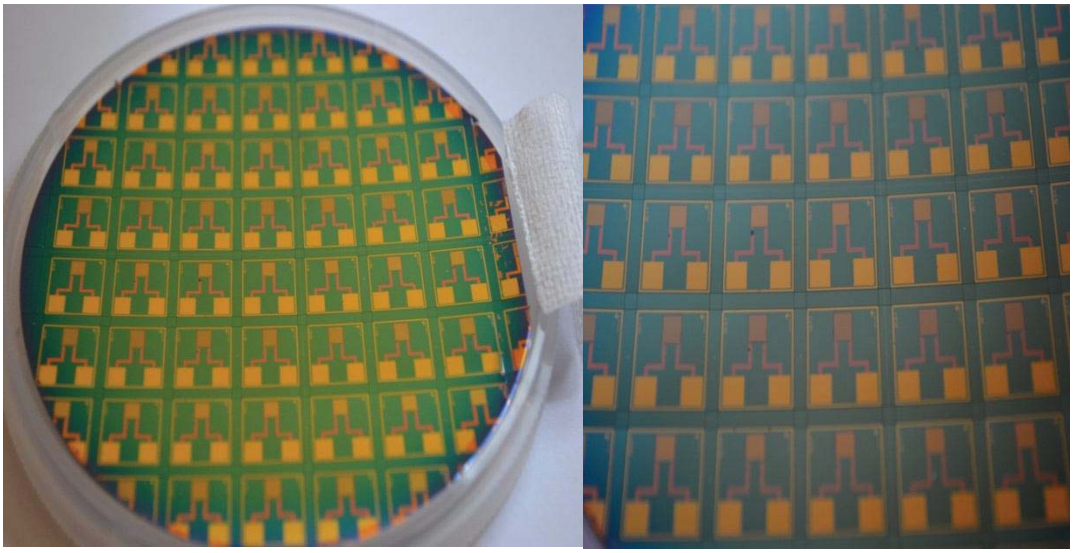

Figure 2.33: Newly improved silicon based interdigital sensor.

2.5 Conclusion

Four novel interdigital sensors have been analysed and fabricated. All sensors have different configurations of electrode structures compared to the conventional interdigital sensors. Three different configurations have been designed which are 1_11, 1_5 and 1_3. The optimum number of negative electrodes is important in the design consideration of novel interdigital sensors. Uniformity of electric field distribution with highest capacitance value within the sensor's geometry contributes to the highest sensitivity. Modelling using COMSOL Multiphysics and analytical methods have been used to evaluate the sensors characteristic and their performance. The sensors have been fabricated using different methods of manufacturing. Each manufacturing technique has used different substrates. Due to different values of permittivity of different substrate, the capacitance values and corresponding impedance values are influenced by these substrates. A new silicon based interdigital sensors were fabricated for better sensitivity. The sensors were developed in miniature size for low cost fabrication process where more sensors can be fabricated from a single silicon wafer. These sensors will have better sensing performance, which provide high sensitivity, low impedance and better sensing signal with low noise.

CHAPTER 3

Experimental Setup, Measurement and Impedance Spectroscopy

3.1 Introduction

This chapter will highlight the measuring instruments and software program used for the experimental setup, how measurement data were collected, basic of impedance spectroscopy (IS) and data representation. The measuring instruments have been interfaced with LabVIEW program for auto measurement method. The connection of wires between measuring instruments to device under test (DUT) has been discussed. Basic applications of impedance spectroscopy method for characterization of sensors and material under test (MUT) have also been discussed in this chapter. The objectives are to measure and characterize the developed sensors according to IS method. There are three important measurement parameters involved. The parameters which have been taken from measuring instruments are frequency, f, impedance, Z and phase angle, θ. These parameters were converted into real part and imaginary part for analysis of impedance characteristics.

3.2 Experimental Setup

The experiment setup consist of high precision LCR meter (Instek LCR-821), Kelvin 4 wire (Instek LCR-06A), interfaced through RS232 to a LabVIEW program along with, thermometer and humidity meter, The sensors and material under test (MUT) are placed in the desiccator where temperature and humidity are monitored. The whole experiment is conducted under control laboratory conditions in MicroSuite Lab, Massey University, Palmerston North. Figure 3.1 shows the block diagram and the experimental setup conducted in the laboratory.

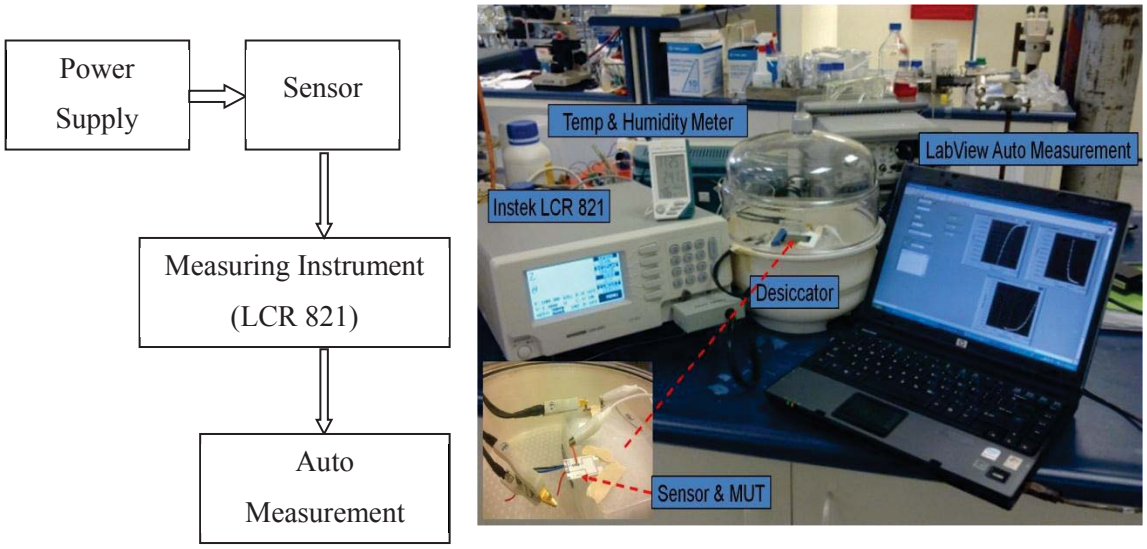

Figure 3.1: The block diagram and the experimental setup

3.2.1 Equipment and Instrumentations

The high precision LCR meter Instek 821 has been used for data measurements. Figure 3.2 shows the front panel of Instek high precision LCR 821. The specifications of the equipment are given in Table 3.1.

Figure 3.2: Instek LCR 821

Table 3.1: Specifications LCR 821

Specifications			
Test Frequency			12Hz ~ 200kHz (504 steps)
Basic Accuracy			0.1%
Test Signal Levels			5mV ~ 1.275V (5mV/step)
DC BIAS	**External:**		2V
	Internal:		0 to 35V
Display Range	**Impedance/Resistance**	**R**	0.00001Ω ~ 99999kΩ
	Capacitance	**C**	0.00001pF ~ 99999μF
	Inductance	**L**	0.00001mH ~ 99999H
	Quality Factor	**Q**	0.0001 ~ 9999
	Dissipation Factor	**D**	0.0001 ~ 9999
	Impedance	**|Z|**	0.00001Ω ~ 99999kΩ
	Phase Angle (Degree)	**Θ**	-180.00° ~ 180.00°
Test Mode	R/Q, C/D, C/R, L/Q, Z/Θ, L/R		
Equivalent Circuit	Parallel or serial selectable		
Memory	100 memory blocks totally		
Average	1 to 255 times		
Test Speed	SLOW, MEDIUM and FAST		
Display Mode	Value, Δ, Δ%		
Display	240 x 128 dot matrix C.C.F.L back light LCD		
Interface	RS-232C		
Power Source	100V ~ 240V, 50/60Hz		
Dimensions & Weight	330(W) x 149(H) x 437(D)mm, Approx. 5.5kg		

3.2.2 Fixture Connection

The standard fixture is a four-wire type or known as Kelvin 4 wire (LCR-06A 4 Wire Leads Kelvin). Figure 3.3 shows the test lead LCR-06A. There are two terminals. The outer terminal (HFORCE and LFORCE) provide the current and the inner terminals (HSENSE and LSENSE) measures the potential. Figure 3.4 shows the diagram of the Kelvin 4 wire fixture. Detail description is shown in Table 3.2 Figure 3.5 shows the details of fixture connection with shielding to device under test (DUT).

Figure 3.3: Instek LCR-06A 4 Wire Leads Kelvin

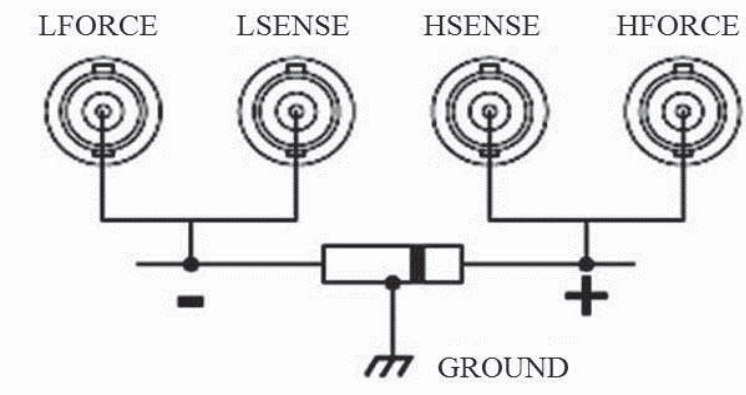

Figure 3.4: Standard fixture of Kelvin 4 wire

Table 3.2: Detail description of fixture connection of LCR-06A 4 wire leads kelvin

	Description
HFORCE	Carries the signal current source. Connected to the +ve side of the DUT.
HSENSE	Together with Lsense, monitors the Potential, V. Connected to the +ve side of the DUT.
LSENSE	Together with Hsense, monitors the Potential, V. Connected to the –ve side of the DUT
LFORCE	Accepts the signal current return. Connected to the –ve side of the DUT.
GND	If the test component has a larger metal area NOT connected to either of the terminals, connected to the GND input to minimize noise level

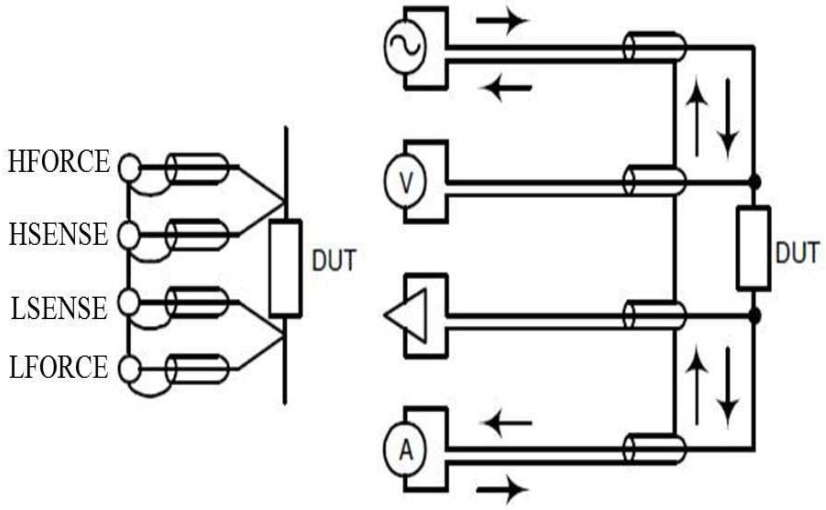

Figure 3.5: Terminal connection of test lead to DUT

3.2.3 LabVIEW Program

The LabVIEW program has been developed to interface with the LCR 821 for auto measurement. The command overview lists for LCR 821 is referred to the user manual in [214] to construct the LabVIEW program. There are different instrument commands and queries. A command sends instructions or data to the LCR meter and a query receives data or status information from the LCR meter. Measurements are automatically sent when a measurement is made in manual mode. The auto measurement program was developed to automatically measure and save the impedance data in *.csv format. These data were analysed to study the impedance characteristics of the developed sensors and material under test. The program consists of eight parts (*.vi): (a) the Main panel (Main.vi), (b) the Open panel (Open.vi), (c) the Close panel (Close.vi), (d) the Set Speed panel (Set speed.vi). (e) the Set Frequency panel (Set frequency.vi) (f) the Set Mode panel (Set mode.vi) (g) the Start measurement panel (Start Measurement.vi), and (h) the Execute Command panel (Execute command.vi). Details of the LabVIEW program constructions can be referred in the appendices as shown in Table 3.3.

Table 3.3: LabVIEW program constructions for auto-measurement and the appendices

Panels	SubVis	Appendices
Main	Main.vi	Appendix 1
Open	Open.vi	Appendix 2
Close	Close.vi	Appendix 3
Set Speed	Set Speed.vi	Appendix 4
Set Frequency	Set Frequency.vi	Appendix 5
Set Mode	Set Mode.vi	Appendix 6
Set Measurement	Set Mesurement.vi	Appendix 7
Set Execute	Set Execute.vi	Appendix 8

3.3 Impedance Spectroscopy Method

The impedance spectroscopy (IS) is a powerful technique used to evaluate electrical properties of materials and their interfaces with surface-modified electrodes [215]. This method have been widely used to study of electrochemistry [216, 217], biomedical applications [218, 219], material science [220, 221] and others. There are two main categories of IS as mentioned by J. Ross Mcdonald in [222], the Electrochemical Impedance Spectroscopy (EIS) and others which are not involving electrochemical reaction.

EIS involves measurements and analysis of materials which involves ionic conduction which includes solid and liquid electrolytes, ionically conducting glasses and polymers, fused salts, and nonstoichiometric ionically bonded single crystals, where conduction can involve motion of ion vacancies and interstitials. EIS is also conducted to study of fuel cells, rechargeable batteries, and corrosion. Other category of IS applies to dielectric materials: solid or liquid non-conductors whose electrical characteristics involve dipolar rotation, and to materials with predominantly electronic conduction [111]. This section presents the basic fundamentals and theory to Impedance Spectroscopy method.

3.3.1 Fundamental Theory of IS Method

Impedance is a measure of the ability of a circuit to resist the flow of electrical current. In an AC circuit the impedance is a representation of complex values where it involves real and imaginary components. The basic Ohm's law in equation (3.1) defines the resistance in term potential, V, and current, I;

$$R = \frac{V}{I} \qquad \textbf{3.1}$$

Electrochemical impedance can be measured by applying an AC potential to an electrochemical cell and then measuring the current through the cell. The response of the sinusoidal potential excitation is an AC current signal which can be analysed as a sum of sinusoidal functions. Electrochemical impedance is measured using a small excitation signal so that the cell's response is pseudo-linear. In a linear system, this current response to a sinusoidal excitation potential will result a sinusoidal current at the same frequency but shifted in phase as shown in Figure 3.6.

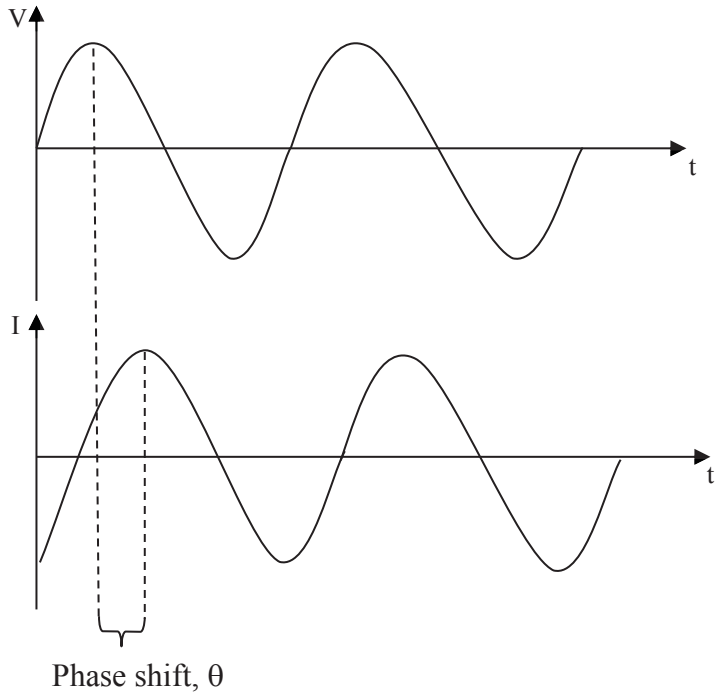

Figure 3.6: Sinusoidal current, I, response from the excitation potential, V, in a linear system

The excitation signal can be expressed as a function of time;

$$V_t = V_0 \sin \omega t \quad \textbf{3.2}$$

where V_t is the potential at time t, V_0 is the amplitude of the signal, and ω is the angular frequency given by ($\omega = 2\pi f$) expressed in radians/second and frequency, *f,* in hertz.

For a linear system, the response signal, I_t, has a phase shift, θ, with amplitude of I_0 which can be expressed by

$$I_t = I_0 \sin(\omega t - \theta) \quad \textbf{3.3}$$

An expression in equation 3.1 for Ohm's Law can be used to calculate the impedance of the system given by;

$$Z = \frac{V_t}{I_t} = \frac{V_0 \sin \omega t}{I_0 \sin(\omega t - \theta)}$$

$$= Z_0 \frac{\sin(\omega t)}{\sin(\omega t - \theta)} \quad \textbf{3.4}$$

The impedance, Z, now can be expressed in term of a magnitude of Z_0 and a phase shift, θ. Equation 3.4 can also be expressed in term of Euler's relationship given by;

$$e^{j\theta} = \cos \theta + \mathrm{j}\sin \theta \quad \textbf{3.5}$$

The impedance, Z, can be expressed in term of potential, V, and current response, I, given by;

$$V_t = V_0 e^{j\omega t} \quad \textbf{3.6}$$

$$I_t = I_0 e^{j(\omega t - \theta)} \quad \textbf{3.7}$$

Therefore the impedance, Z;

$$Z(\omega) = \frac{V_t}{I_t} = \frac{V_0 e^{j\omega t}}{I_0 e^{j(\omega t - \theta)}} = Z_0 e^{j\theta} \quad \textbf{3.8}$$

$$= Z_0(\cos \theta + j \sin \theta) \quad \textbf{3.9}$$

The impedance now is in the form of real part ($Z_0 \cos\theta$) and imaginary part ($Z_0 \sin\theta$). The data presentations of impedance characteristics can be analysed using Nyquist plot and Bode plot.

3.3.2 Nyqusit plot and Bode plot Data Presentations

Nyquist plot and Bode plot are very important data presentations to perform analyses of impedance characteristic in Impedance Spectroscopy method [223]. Nyquist plot is representing Z(ω) in complex plane while the Bode plot is representing Z (ω) and phase angle θ(ω) in frequency domain. The Nyqusit plot is data presentation in complex impedance plane consist of real part on the X-axis and the imaginary part on the Y-axis. Since the impedance, Z consist of these two parts, real and imaginary, the Nyqusit plot make it easy to understand the characteristic impedance of material under test (MUT) or device under test (DUT). While Bode plot make an easy interpretation in the scale view. There are two important RC circuits which are related to both plots of the sensors and MUT. To express the total impedance of the circuit, RC circuits can be separated to equivalent parallel RC circuit and series RC circuit. The total impedance which is related to equivalent RC circuits depends on the characteristic of the sensors and also the characteristic of MUT.

3.3.2.1 Parallel RC Circuit

The equivalent parallel RC circuit is illustrated in Figure 3.7 and the Nyquist plot in Figure 3.8 shows a semicircle with a single time constant of a RC circuit [224]. As for parallel RC circuit, the impedance (Z), and phase angle (θ) can be expressed as follows;

$$Z = \frac{R}{1 + j\omega RC} \tag{3.10}$$

$$\theta = -\arg(Z) = -\tan^{-1}(\omega RC) \tag{3.11}$$

The Nyquist plot shown the impedance is represented by vector of |Z|, and phase angle, θ, with angular frequency, ω, where if ω→0 impedance is pure resistive and if ω→∞ (at very high frequency), impedance approaches zero.

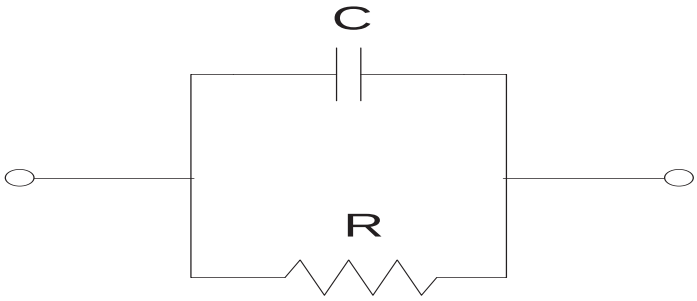

Figure 3.7: A simple parallel RC equivalent circuit

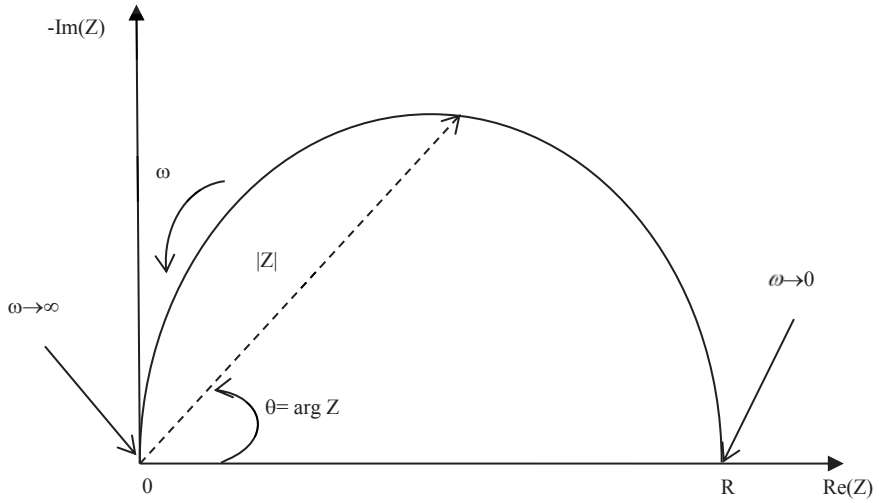

Figure 3.8: Nyquist plot to represent the complex impedance plane of the circuit shown in Figure 3.7

Figure 3.9 shows the Bode plot for impedance, Z, and phase angle, θ, against angular frequency, ω (=2π*f*). The impedance, Z, at Y-axis is plotted against the angular frequency, ω, on the X-axis. Both absolute values of impedance, |Z|, and phase angle, θ, can be plotted at certain frequency range.

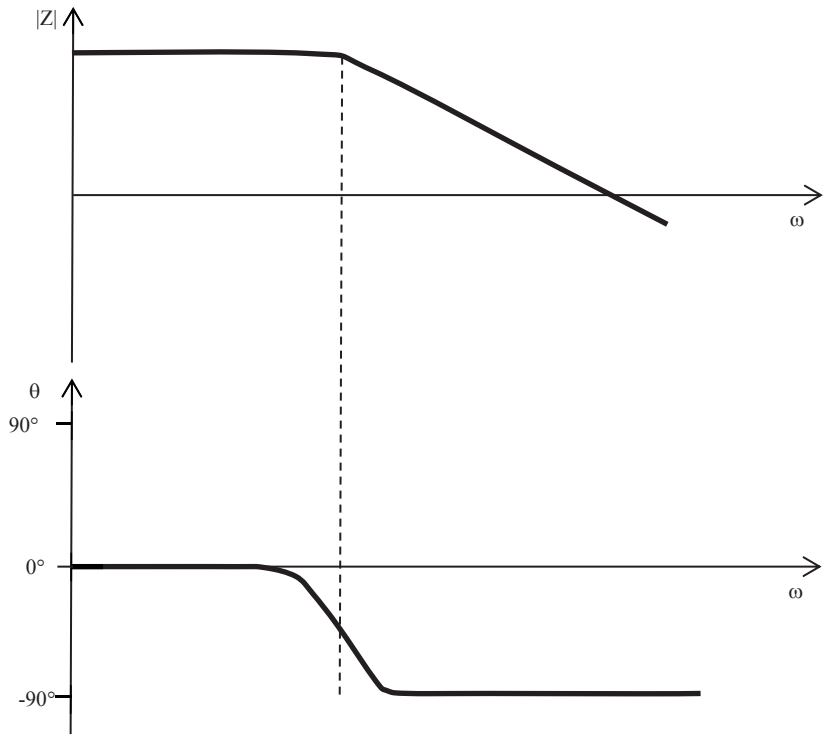

Figure 3.9: Bode plot showing impedance and phase angle behaviour with frequency

3.3.2.2 Series RC Circuit

The Nyquist plot is shown in Figure 3.22 and the equivalent series RC circuit is shown in Figure 3.23. Figure 3.24 shows the Bode plot for impedance, Z, and phase angle, θ, against angular frequency, ω(=2π*f*). As for series RC circuit, the impedance (Z), and phase angle (θ) can be expressed as follows;

$$Z = R + \frac{1}{j\omega C} \quad \textbf{3.12}$$

$$\theta = -arg(Z) = \tan^{-1}(\frac{1}{\omega RC}) \quad \textbf{3.13}$$

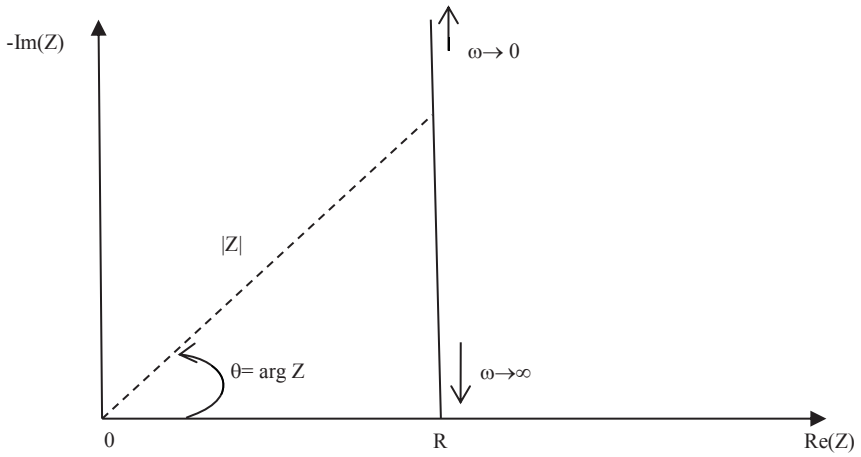

Figure 3.10: Nyquist plot to represent the complex impedance plane

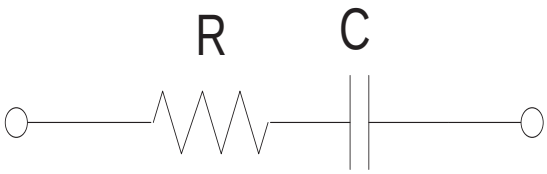

Figure 3.11: A simple series RC equivalent circuit

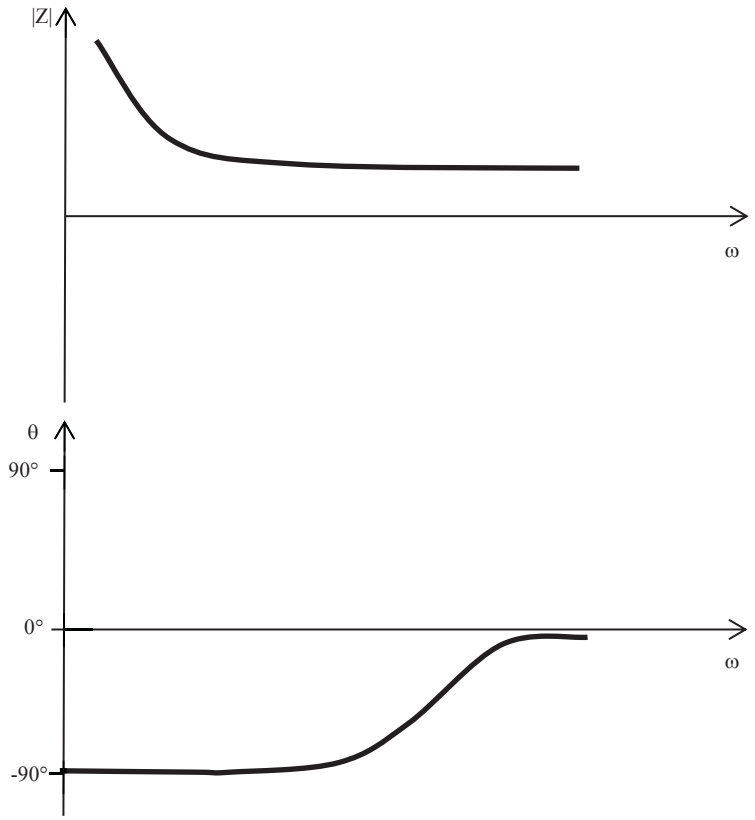

Figure 3.12: Bode plot showing impedance and phase angle behaviour with frequency

Most of the analysis and data presentations of the research work using impedance spectroscopy method which has been mentioned above. Experimental results and discussion on the characteristic of impedance of developed sensors and material under test will be discussed in Chapter 5. Further information on this subject will be discussed in Chapter 6 in details which involve the analysis of electrode-solution interface, analysis on mixed kinetic and diffusion process, "constant phase element (CPE)", modelling using equivalent electrical circuit model and statistical and mathematical analysis.

3.4 Conclusion

The experimental setup, instrumentation, program and measurement method has been discussed in this chapter. High precision LCR meter interfaced with the LABVIEW program has been established. Details of the experimental setup, connection cables, instruments settings, program syntax and program interface were explained in the chapter. Basic theory of measurement method using Impedance Spectroscopy (IS) has also been discussed.

CHAPTER 4

Experimental Investigation: Impedance Characterization

4.1 Introduction

The fabricated sensors have been tested and analysed to study their impedance characteristics. A good capacitive sensor has bigger change of the imaginary part (reactance) compared to the real part (resistive) with respect to frequencies. The developed sensors must show capacitive behaviour with very low value of resistive part as well as very small change of resistive value. It is also important to study whether different configurations of electrode structure give better sensitivity measurements. All fabricated sensors were tested to observe their characteristic impedance. There are several different experiments to characterize the sensors as described in this chapter. The first experiment conducted was to characterize the sensor with air (no material under test). Then the sensors were coated with very thin incralac (< 5 μm) to study how coated-sensors respond to different chemicals. The initial experiments were conducted to test the coated-sensors with ionic solutions (NaCl) of different concentrations and buffer solutions of different pH values. Then the experiments were conducted to test the selected sensors with different toxins. The LCR-821 interfaced with LabVIEW program was used as the experimental setup. The measurement was set to slow for 0.05% accuracy with input voltage of 1 V_{rms}. The frequency range is set to 12 Hz – 100 kHz. All different fabricated sensors were characterized based on Impedance Spectroscopy Method.

4.2 Characterization of Sensors in air

4.2.1 Characterization of FR4 Sensors

The characterizations of sensors are very important to investigate the behaviour of each developed sensors. Since the developed sensors were fabricated using different substrates using different fabrication process therefore the characteristic impedance of the sensors are different. The characteristic impedance of sensors with air at room

temperature (20°C - 28°C) with humidity level between 40% - 45% was measured. The experiments setup has been discussed in Chapter 3. The characteristic impedance of FR4 sensors with three different configurations are shown in Figure 4.1. Figure 4.1 shows the Nyqusit plot of the complex impedance plane. Figure 4.2 (a) shows the Bode plot of impedance (Z) and phase angle as a function of frequency. The impedance spectra of real and imaginary part are shown in Figure 4.2 (b). The impedance characteristic with respect to air was observed to have higher change of imaginary part compared to real part. This indicates that the capacitive reactance has higher role to play compare to resistive part. The phase angles measured were closed to 90 degree which indicates that the sensor behave as capacitive sensors. The Nyquist plots show change of the real part is significant smaller compared to the imaginary part for certain frequency range. The sensor configuration 1_11 has higher impedance compared to sensor 1_5 and 1_3 for frequency less than 10 kHz.

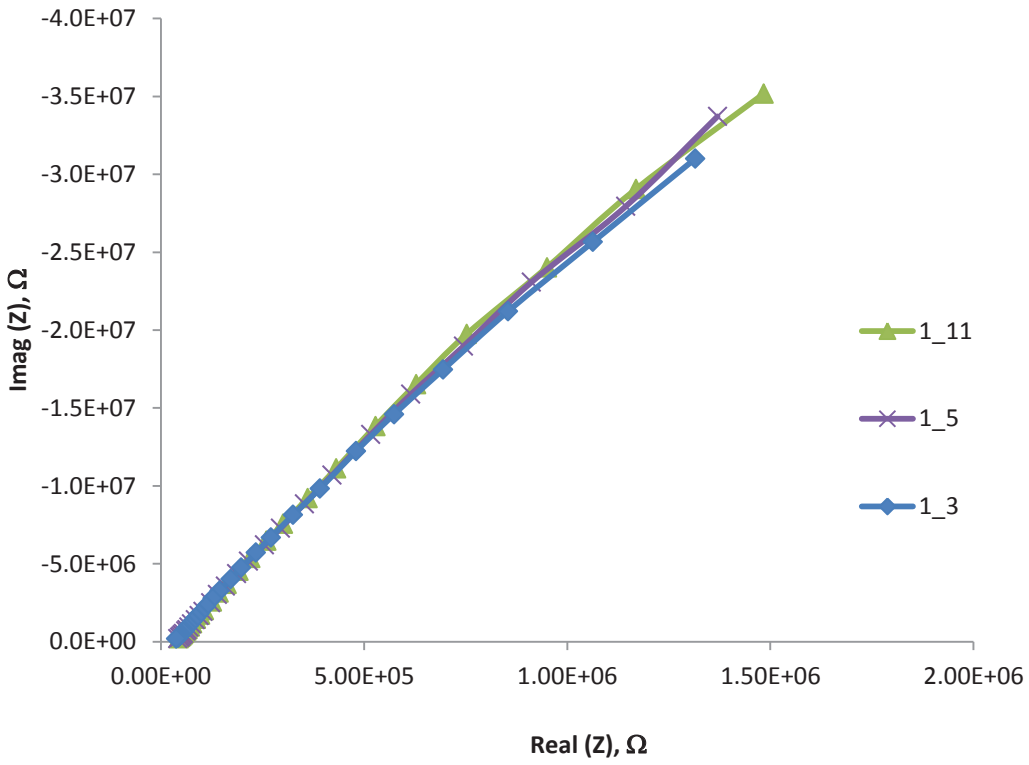

Figure 4.1: Nyquist plot showing impedance characteristics of FR4 sensors

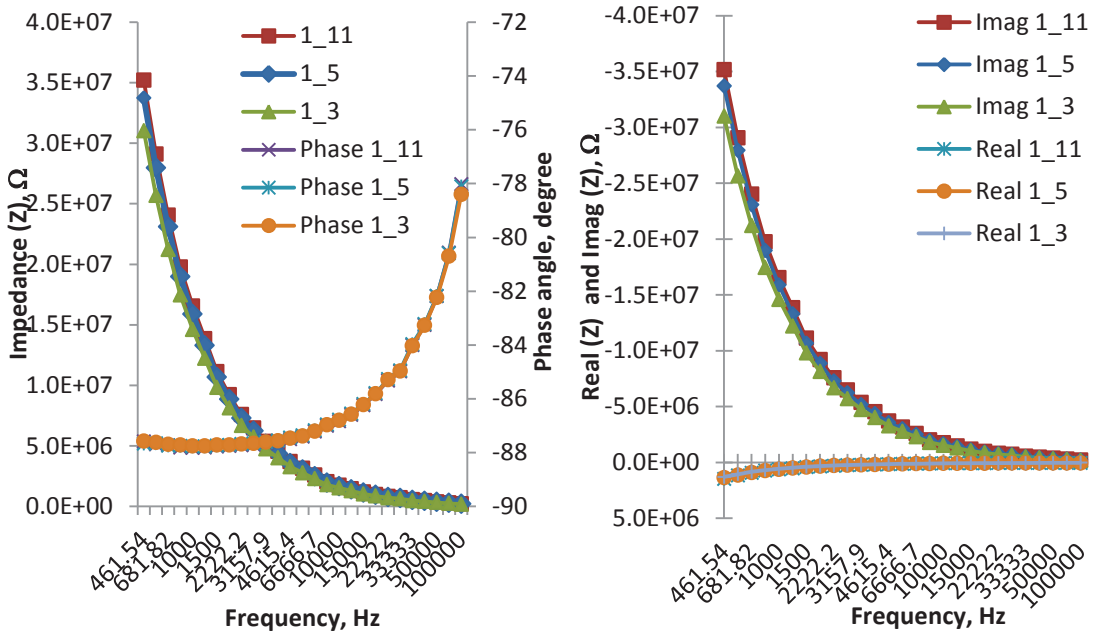

(a) (b)

Figure 4.2: Impedance characteristics of FR4 sensors showing Bode plots of; (a) Impedance and Phase angle (b) Real and Imaginary part

4.2.2 Characterization of Alumina Sensors

The impedance characteristics of alumina sensors are shown in in Figure 4.3 and Figure 4.4. Figure 4.3 shows the Nyqusit plot of the complex impedance plane. Figure 4.4 (a) shows the Bode plot of impedance (Z) and phase angle and Figure 4.4 (b) shows the impedance spectra of real and imaginary part. The Alumina sensors have also shown that the changed of imaginary part is much higher compared to its real part. The phase angles measured were close to 90 degree which indicates that the sensor behaves as capacitive sensors. The Nyquist plots show that the change of real part is significantly smaller compared to the imaginary part for certain frequency range. The sensor configuration 1_11 has higher impedance compared to sensor 1_5 and 1_3 for frequency less than 10 kHz. The Nyquist plot of Alumina sensors show better response compared to FR4 sensors for different configurations. The impedance for all configurations is lower compared to FR4 sensors which indicated that the different substrates have significant effect on the sensing performance.

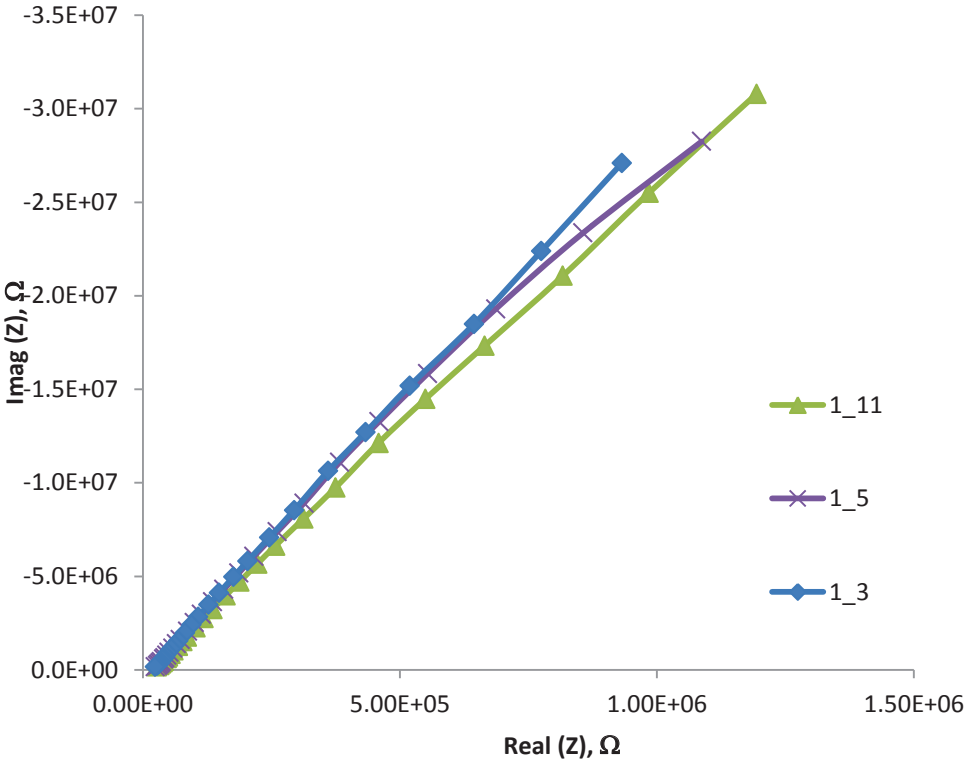

Figure 4.3: Nyquist plot showing impedance characteristics of Alumina sensors

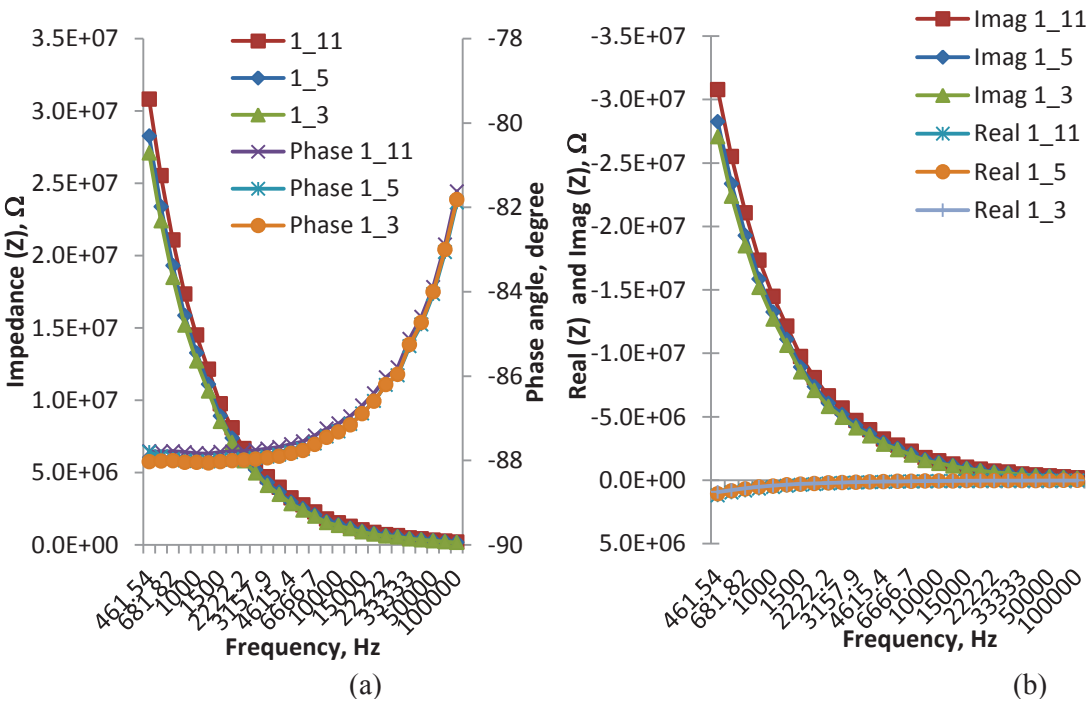

(a) (b)

Figure 4.4: Impedance characteristics of Alumina sensors showing Bode plots of; (a) Impedance and Phase angle (b) Real and Imaginary part

4.2.3 Characterization of Glass Sensors

The impedance characteristics of Glass sensors with three different configurations are shown in Figure 4.5 and Figure 4.6. Figure 4.5 shows the Nyqusit plot of the complex impedance plane. Figures 4.6 (a) and (b) show Bode plot and impedance spectra of Glass sensors. The same characteristic were observed for Glass sensors for different configurations. The results for Glass sensors were observed to have less discrimination between configurations for imaginary part compared to results shown for Alumina and FR4 sensors but has lower impedance compared to FR4 sensors.

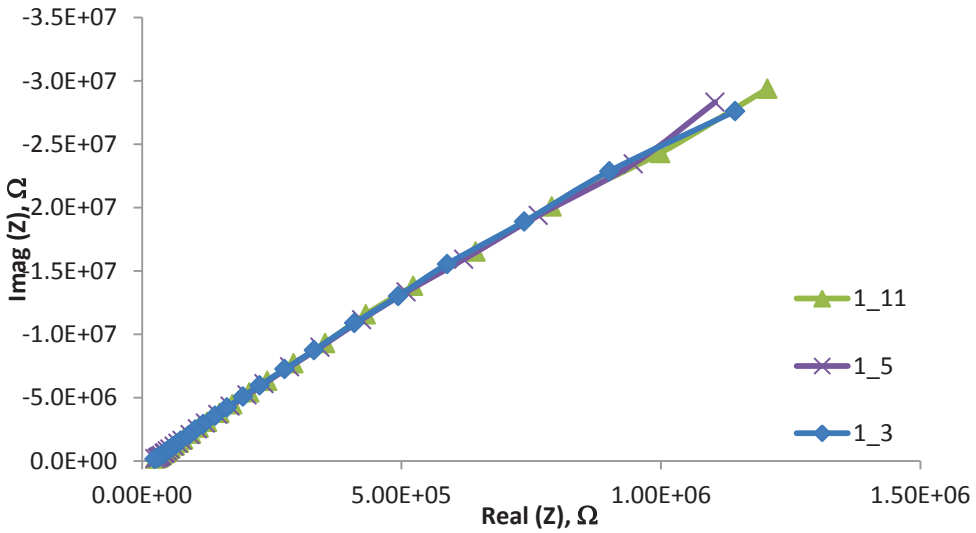

Figure 4.5: Nyquist plot showing impedance characteristics of Glass sensors

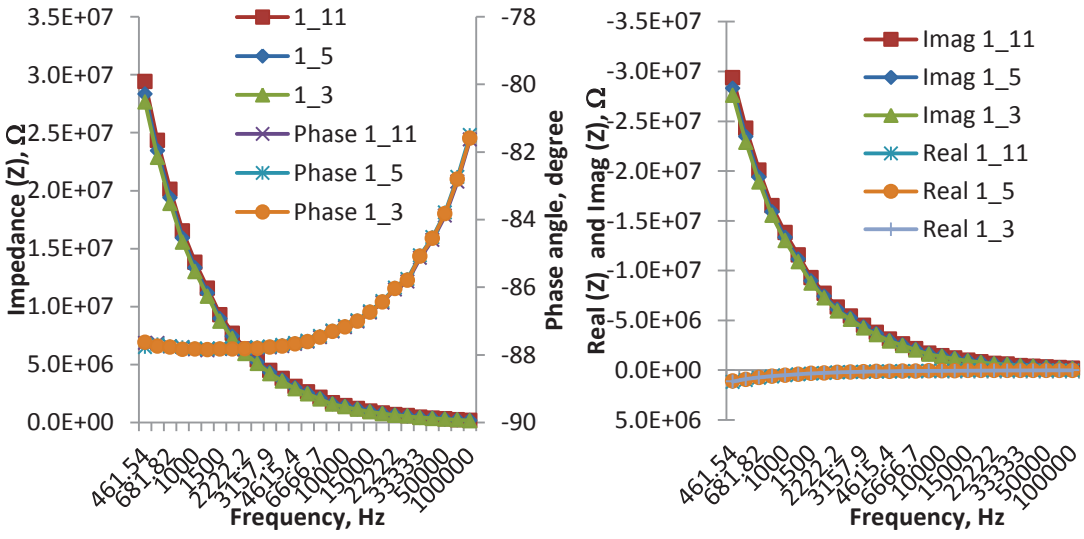

(a) (b)

Figure 4.6: Impedance characteristics of Glass sensors showing Bode plots of; (a) Impedance and Phase angle (b) Real and Imaginary part

Based on the results observed from impedance characteristics the fabricated sensors with air, all sensors show the behaviour of capacitive sensors where the change of the imaginary parts (reactance) is much higher than the change of real part (resistive) as a function of frequency. The Alumina sensors have lower impedance value (higher capacitance) and better phase angle measurement compared to sensors fabricated on Glass and on FR4. Alumina sensors also show better discrimination between different configurations. Therefore for characteristic impedance with air shows Alumina sensors have shown better performance.

4.2.4 Characterization of Silicon Sensors

The characterization of sensors was further investigated with new silicon based interdigital sensors. These new sensors are based on thin film fabrication process and were fabricated on Silicon/Silicon Dioxide (Si/SiO2) wafer as discussed in Chapter 2. Three different configurations of electrode structure has been tested. The results are shown in Figure 4.7 and Figure 4.8. Figure 4.7 shows the Nyquist plot on the complex impedance plane of different configurations. Figure 4.8(a) showing the Bode plot of impedance (Z) and phase angle. Figure 4.4 (c) shows the impedance spectra of real and imaginary part. It was observed that the silicon sensors show the characteristics of capacitive sensors with lower impedance value (higher capacitance). The change of the imaginary part (reactance) is higher compared to the change in real part (resistive). The imaginary part shows clearly different configurations have different characteristic impedance. It is also noticed that at lower frequency, the real part seemed to have different values for different configurations. But the change of its value is very small compared to change of the imaginary part. The total impedance and phase angles change significantly showing different configurations have different effects on impedance characteristics.

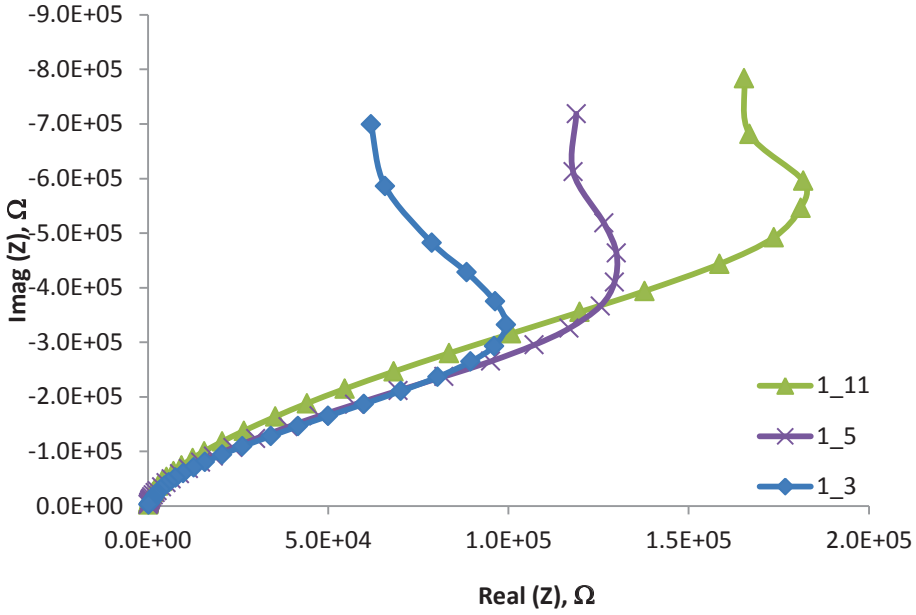

Figure 4.7: Nyquist plot of Silicon sensors

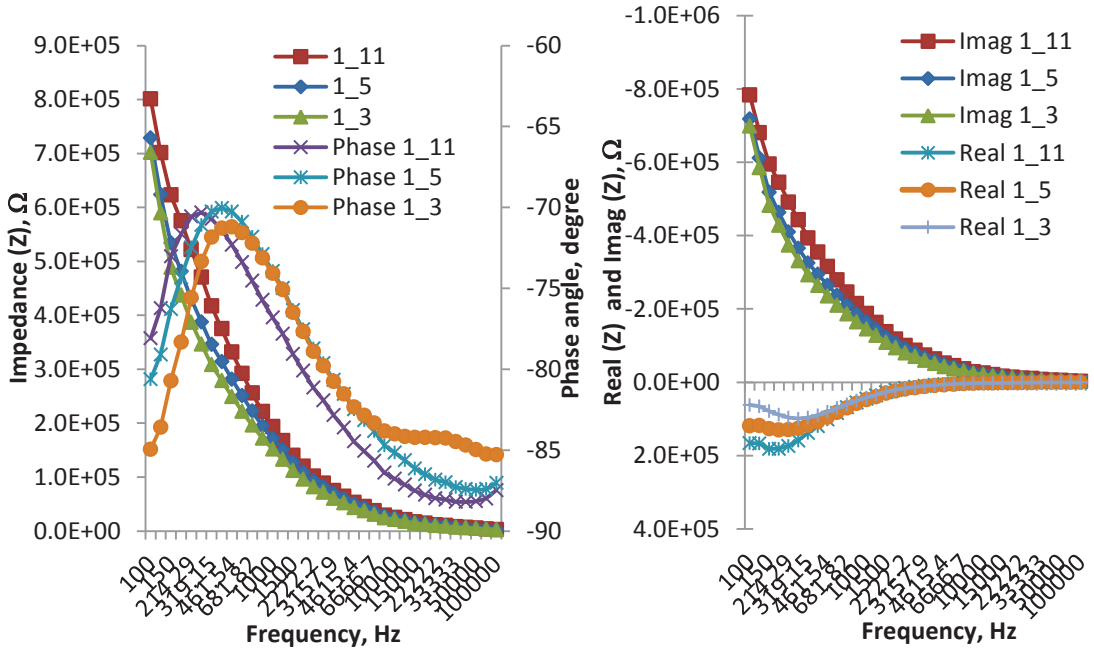

(a) (b)

Figure 4.8: Impedance characteristics of Silicon sensors showing Bode plots of; (a) Impedance and Phase angle (b) Real and Imaginary part

The experiments were then conducted on the improved silicon sensors. The structure of the sensors has been modified by providing a layer of silicon nitride (Si_3N_4) at the top layer. This layer of Si_3N_4 is expected to provide better impedance characteristics in term of low impedance, high capacitance and high output signal. The

detail descriptions of these sensors have been discussed in Chapter 2. Figure 4.9 shows the Nyquist plot of complex impedance plane of different configurations. The Nyquist plot shows these sensors behave as capacitive sensors with better output signals (low impedance value). Figure 4.10 (a) shows the Bode plot of impedance (Z) and phase angle of different configurations. Both plots have shown that there are significant impedance and phase angles change from low frequency to high frequency range. The phase angles plots have shown better discrimination between different configurations as the frequency increases from 1 kHz to 100 kHz. The impedance shows at higher frequency (above 1 kHz) the values almost the same and saturated. Figure 4.10 (b) shows the impedance spectra of real part and imaginary part. It was observed the improved silicon sensors have reduced the change of the real part at low frequency compared to the previous silicon sensors. The change of the imaginary part is much higher compared to the real part which has shown good capacitive sensor behaviour. The experimental results have shown that the improved silicon based interdigital sensors have improved sensing performance compare to initial silicon sensors. It can be said that the silicon sensors have significantly improved the impedance characteristics of the planar interdigital sensors where results have shown the silicon sensors have low impedance, high capacitance value with high output signal compared to FR4, Alumina and Glass sensors.

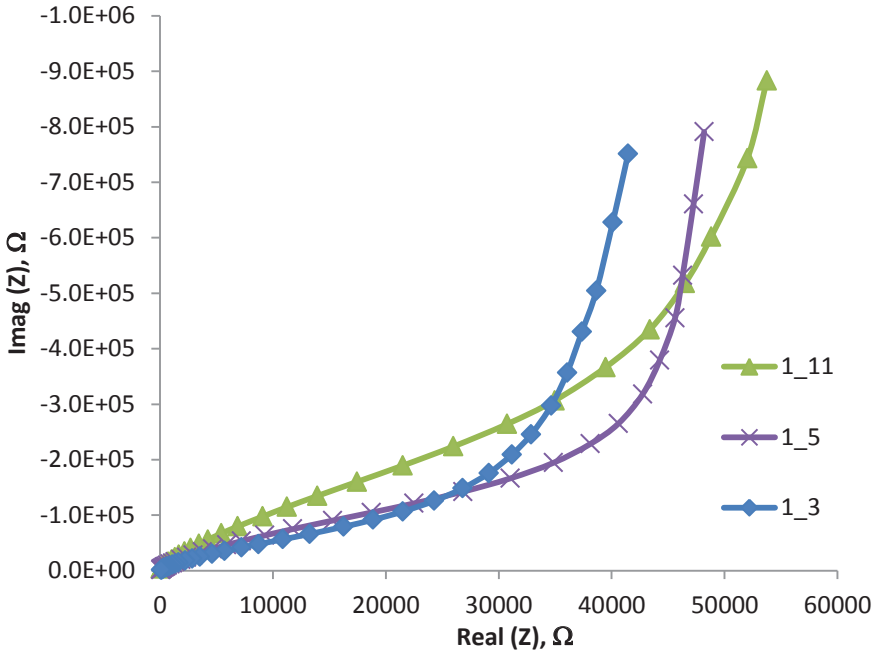

Figure 4.9: Nyquist plot of improved Silicon sensors (Si_3N_4)

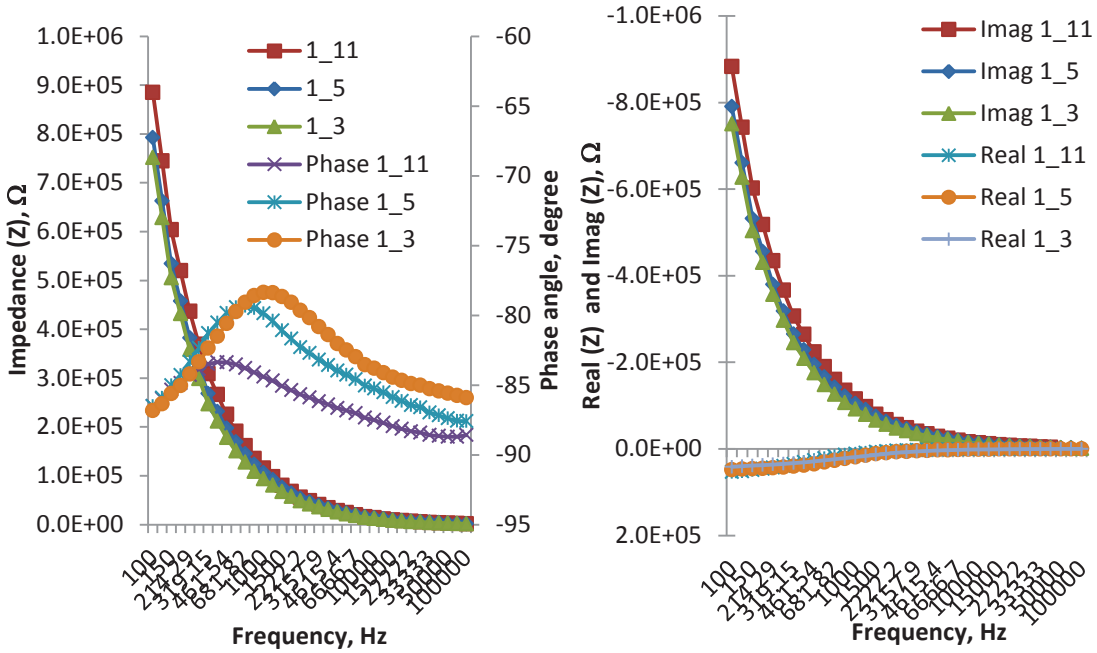

(a) (b)

Figure 4.10: Impedance characteristics of improved Silicon sensors (Si_3N_4) showing Bode plots of; (a) Impedance and Phase angle and (b) Real and Imaginary part

4.3 Characterization of sensors with ionic solution, Sodium Chloride (NaCl)

Experiments with sodium chloride (NaCl) have been conducted. The exposure time of the ionic solution to sensor electrodes was set to 12 minutes. The experiments were replicated three times and mean values of three runs were taken. The experiments were conducted to study the behaviour of different configuration of all sensors response to the different molar of ionic solutions. Sodium chloride (NaCl) of different molar has been used. Sodium chloride is a salt, it is a chemical compound that consists of a positively charged cation, the sodium ion (Na^+), and a negatively charged anion, the chloride ion (Cl^-). Dissolve the sodium chloride in MilliQ water for required molarity. Bring the volume to 1 litre with MilliQ water using volumetric plus. Finally, sterilize by autoclaved the solutions. The stock solution preparation as follows;

Sodium Chloride solution

Sodium chloride (NaCl) MW = 58.44 g/mol (pH 9.28)

1M NaCl = Dissolve 58.44 g of NaCl (1 mol*58.44 g/mol) in one litre of MilliQ water.

1 M NaCl is 5.844% (w/v).

The prepared NaCl solutions have different molarity between 0.01 M and 0.1 M. All sensors were coated with thin Incralac (< 5 μm) and cured overnight at room temperature. Incralac has been widely used as a coating material to protect metallic substrates and studies have been conducted using EIS (electrochemical impedance spectroscopy) to analyse its performance [225]. The coating was introduced to slow the electron flow from ionic solution to the sensor electrodes so that the analysis can be conducted. Without coating the output will be meaningless due to the fast electron transfer from solution to electrode. This experiment was also conducted to study how coatings electrode can improve the sensitivity and most importantly the selectivity of different molecules on sensing electrodes. Details on the coating materials and process shall be discussed in Chapter 5. Forty microliter of control solution (MilliQ) and NaCl of different molarity were applied to the sensors. The data of each sensor configurations were then taken and analysed.

4.3.1 NaCl on FR4 Sensors

Results of FR4 sensor of 1_11 configuration are shown in Figure 4.11, where Nyquist plot and Bode plot of impedance behaviour were analysed. It was observed for 1_11 configuration, the response of the sensor is very poor for different molarity of NaCl. The 1_5 and 1_3 configurations of the FR4 sensor show better response to different molarity of NaCl. These are shown in Figure 4.12 and Figure 4.13 respectively. The Nyquist plots have shown a semi-circle plot with single time constant. The results show the coating delay the electron transfer from solution to sensor electrodes. Both of the Nyqusit plots have shown a significant difference of the NaCl molarity. It was also observed that the total impedance decreases as the molarity increases which indicates the presence of more ions that increase the current flow to the system. As for 1_5 configuration, at low frequency (< 1 kHz), both real part and imaginary part changes but the change is much higher for the imaginary part compared to the real part. As for 1_3 configuration the imaginary part changes at frequency between 100 Hz – 10 kHz but the

real part changes only at frequency lower that 1 kHz. 1_5 configuration has better response to NaCl.

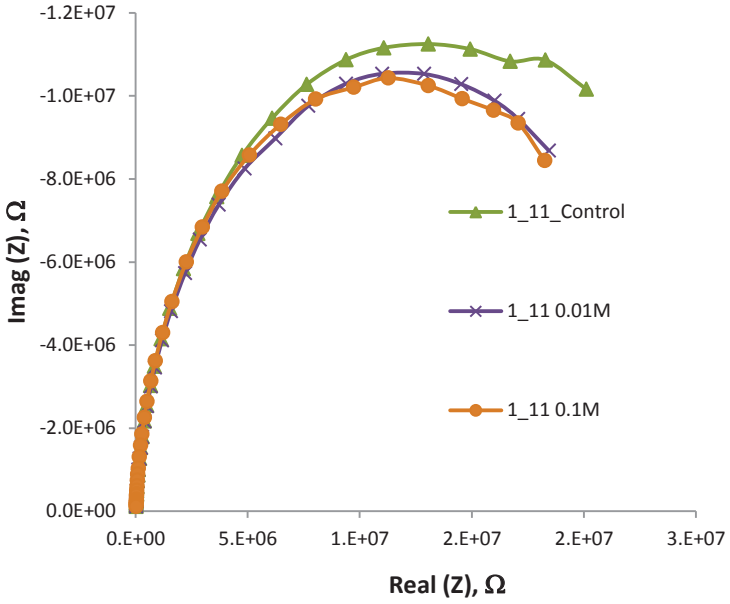

(a)

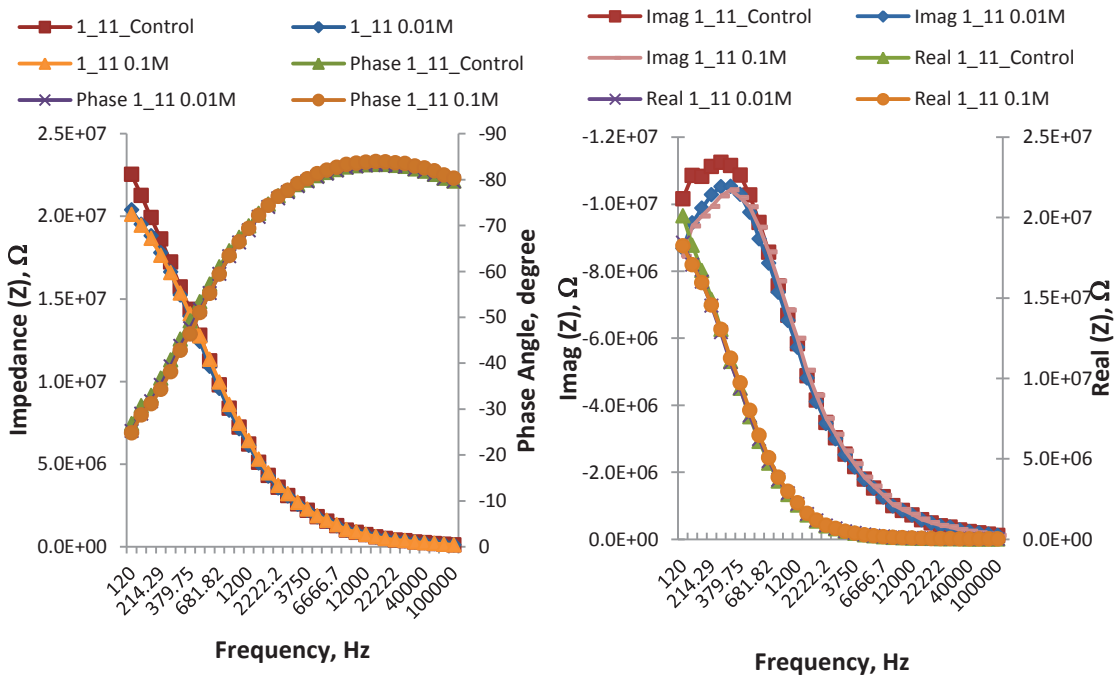

(b) (c)

Figure 4.11: NaCl characterization of FR4 1_11 sensor; (a) Nyqusit plot showing complex impedance plane (b) Impedance and phase measurement plot (c) Impedance behaviour in showing the Real, Z and the Imaginary, Z

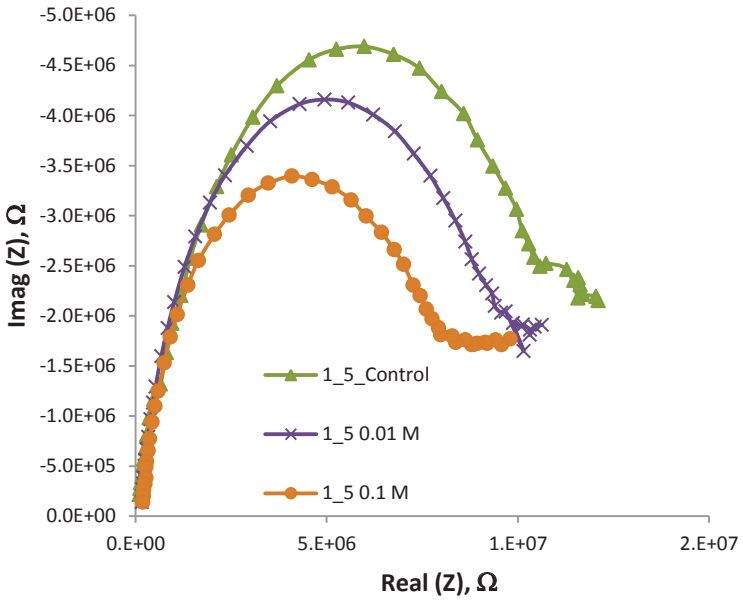

(a)

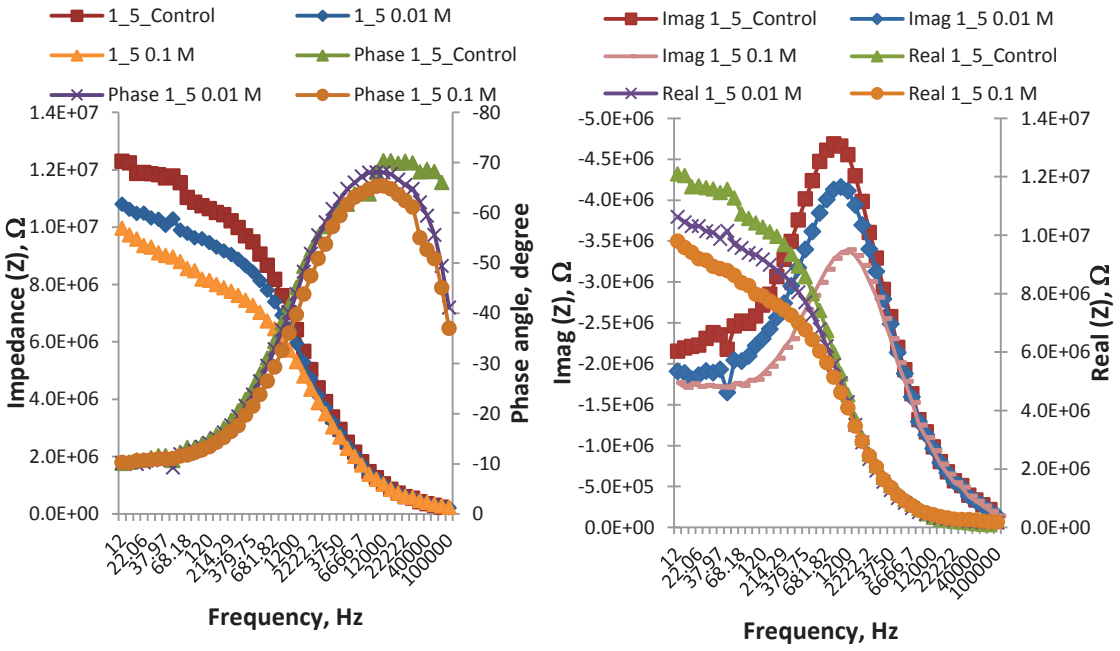

(b) (c)

Figure 4.12: NaCl characterization of FR4 1_5 sensor; (a) Nyqusit plot showing complex impedance plane (b) Impedance and phase measurement plot (c) Impedance behaviour in showing the Real, Z and the Imaginary, Z

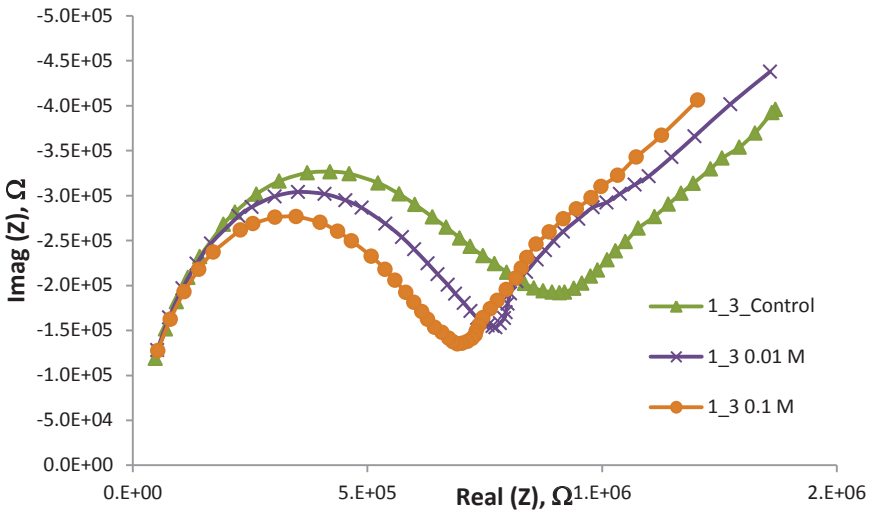

(a)

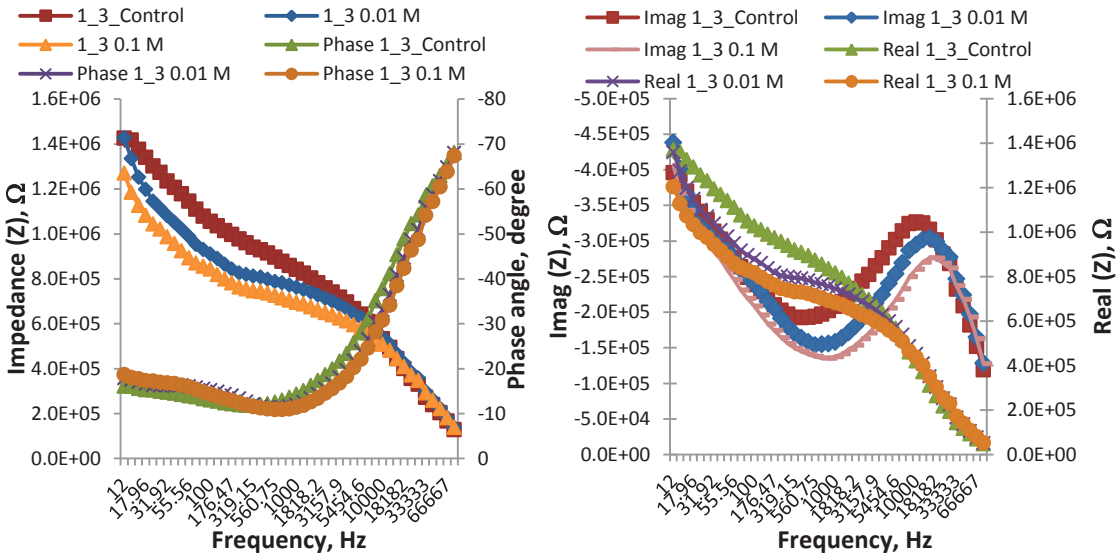

(b) (c)

Figure 4.13: NaCl characterization of FR4 1_3 sensor; (a) Nyqusit plot showing complex impedance plane (b) Impedance and phase measurement plot (c) Impedance behaviour in showing the Real, Z and the Imaginary, Z

4.3.2 NaCl on Alumina Sensors

Figures 4.14, 4.15 and 4.16 show the results of Alumina sensors of configuration 1_11, 1_5 and 1_3 with different molarity of NaCl. It can be said that Alumina sensors response better compared to FR4 sensors. Results have shown that all configurations can clearly discriminate NaCl of different molarity. The Nyquist plots have shown all configurations show a semi-circle with a single time constant in the frequency of 12 Hz – 100 kHz.

The coatings successfully retard the electron transfer to the electrodes and this is shown by a large semi-circle for different molarity of NaCl. Alumina with configuration 1_5 has better performance compared 1_11 and 1_3. As shown in Figure 4.15 (a) the Nyquist plot shows 1_5 configuration has highest sensitivity measurement based on it responses to NaCl solution. The 1_11 configuration has higher impedance value and 1_3 configuration show almost the same response as FR4 1_3 configuration where the imaginary part only changes between frequency 1 kHz – 10 kHz. As for 1_5 configuration the result of impedance behaviour in Figure 4.15 (c) shows the imaginary and the real part change significantly for frequency less than 10 kHz.

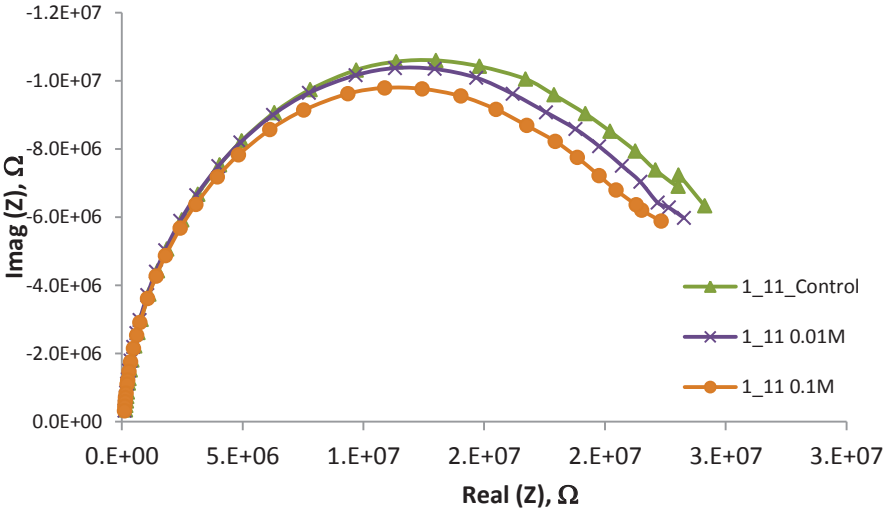

(a)

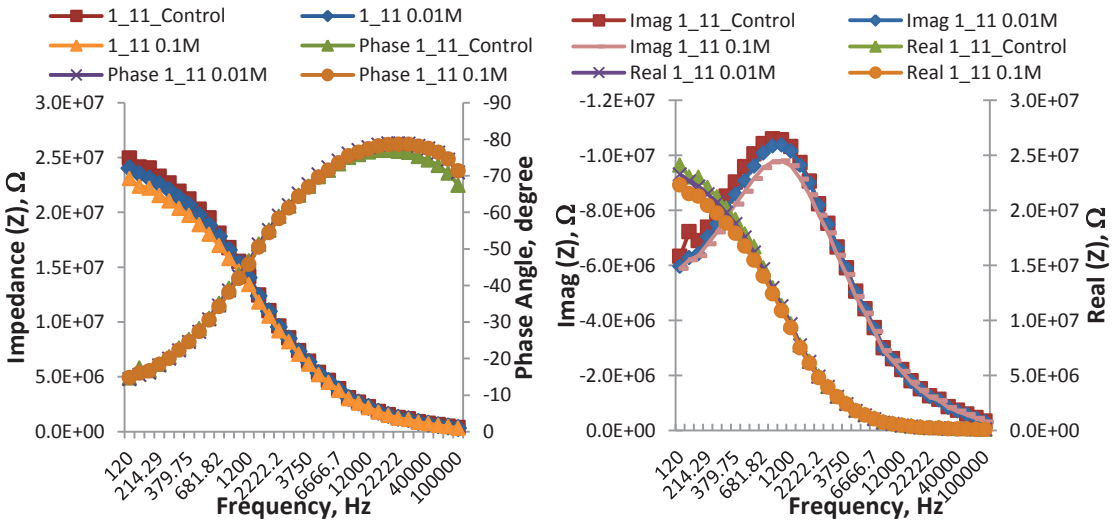

(b) (c)

Figure 4.14: NaCl characterization of Alumina1_11 sensor; (a) Nyqusit plot showing complex impedance plane (b) Impedance and phase measurement plot (c) Impedance behaviour in showing the Real, Z and the Imaginary, Z

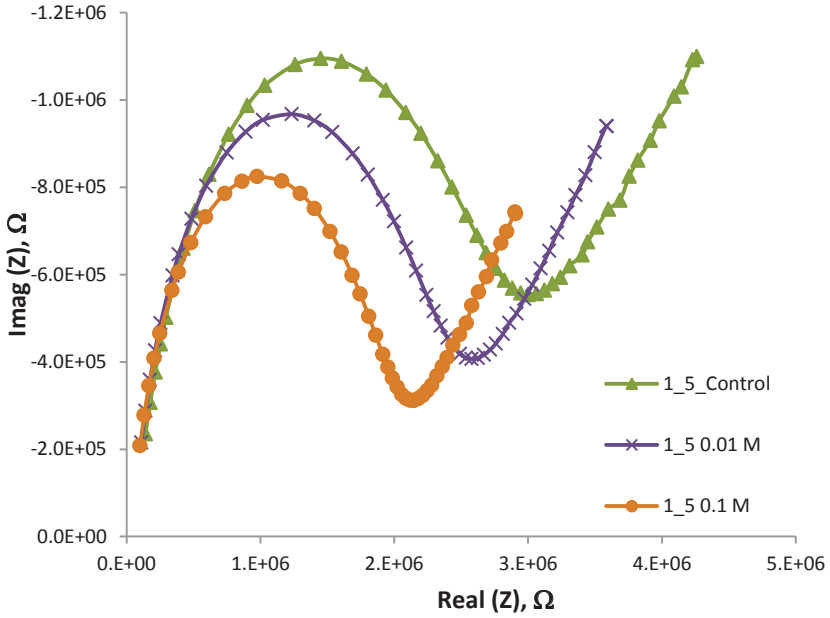

(a)

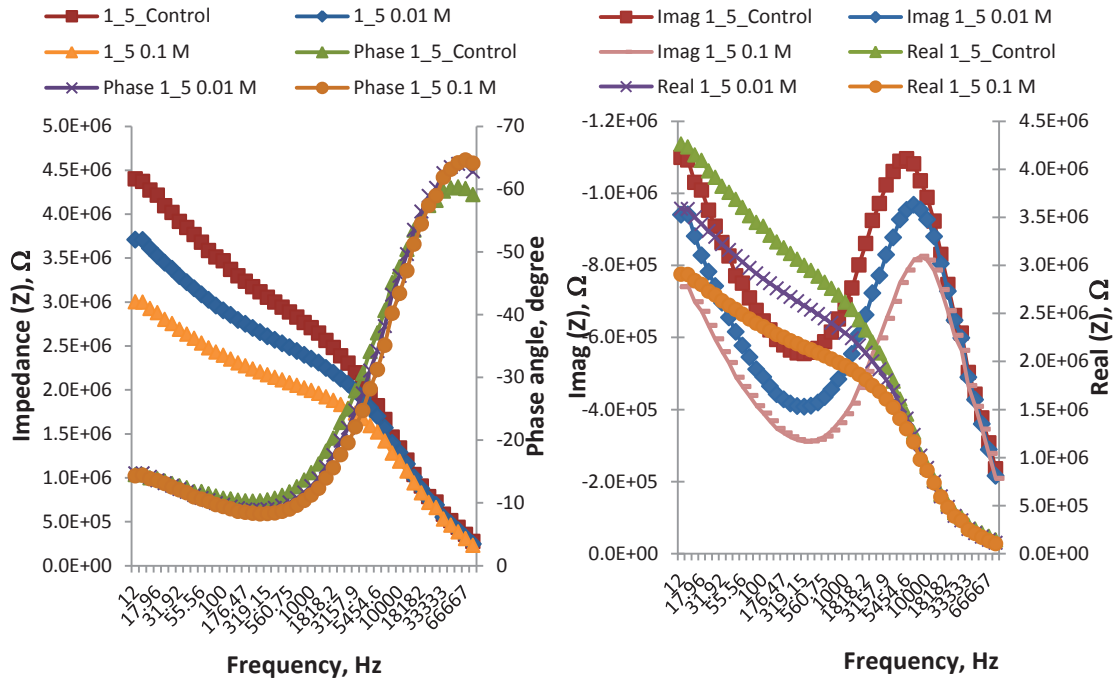

(b) (c)

Figure 4.15: NaCl characterization of Alumina1_5 sensor; (a) Nyqusit plot showing complex impedance plane (b) Impedance and phase measurement plot (c) Impedance behaviour in showing the Real, Z and the Imaginary, Z

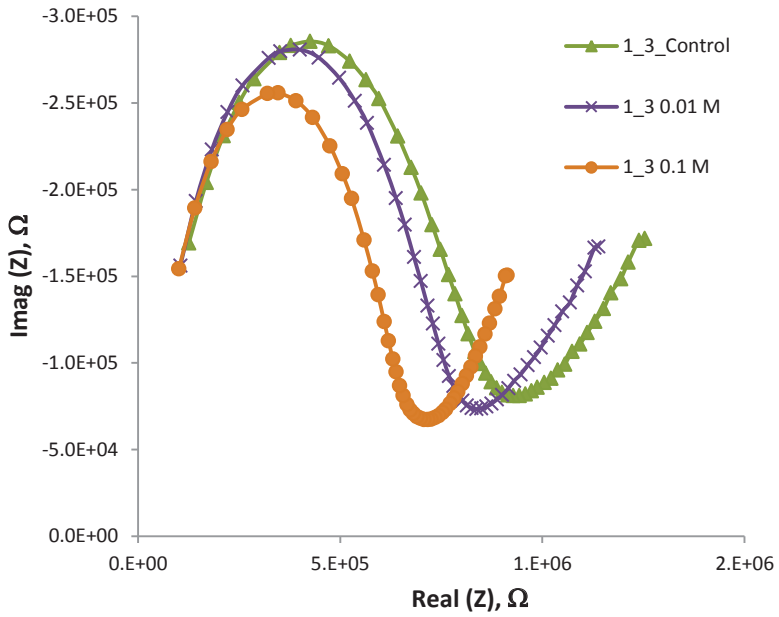

(a)

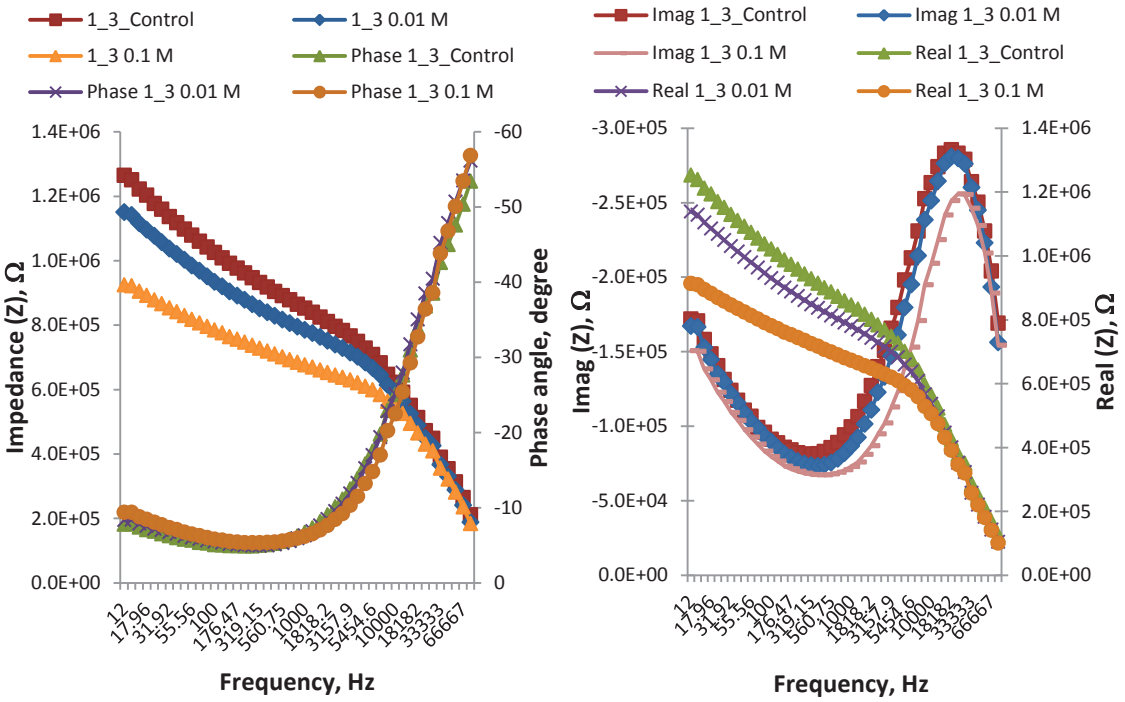

(b) (c)

Figure 4.16: NaCl characterization of Alumina1_3 sensor; (a) Nyqusit plot showing complex impedance plane (b) Impedance and phase measurement plot (c) Impedance behaviour in showing the Real, Z and the Imaginary, Z

4.3.3 NaCl on Glass Sensors

Figure 4.17 shows the results for 1_11 configuration, Figures 4.18 shows results of 1_5 configuration and results of 1_3 configuration is shown in Figure 4.19. Similar results were shown by Glass sensors where 1_11 configuration has higher impedance compared to 1_5 and 1_3 configurations. The Nyqusit plots of 1_5 and 1_3 shows semi-circle with a single time constant for frequency 12 Hz- 100 kHz. 1_5 configuration has better responses compared other configurations of Glass sensors.

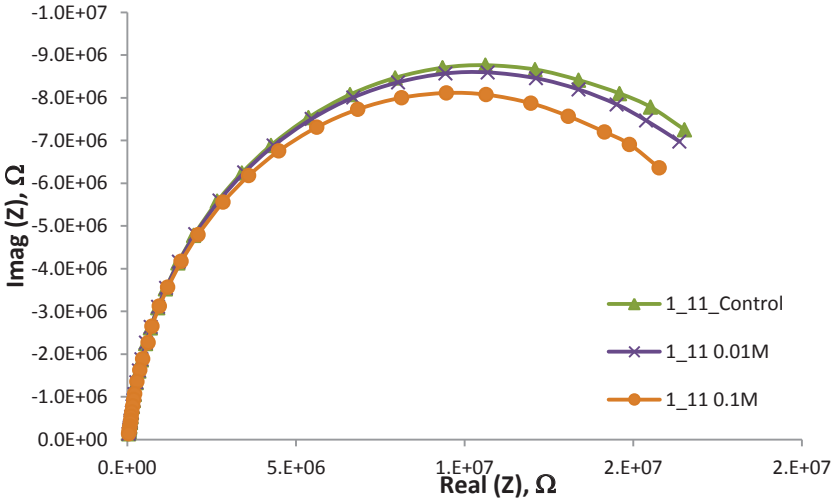

(a)

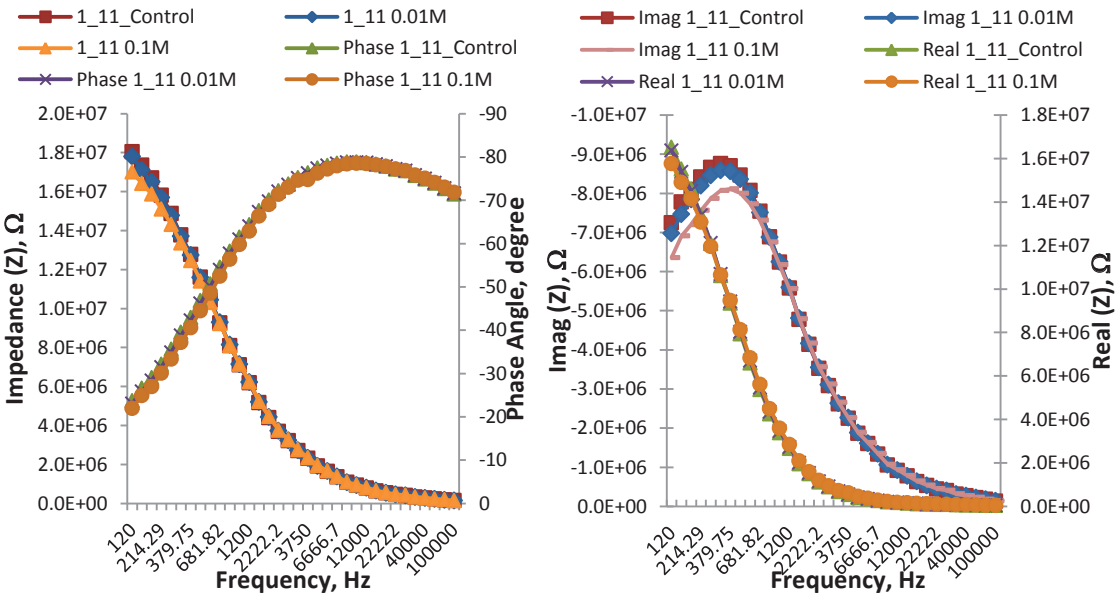

(b) (c)

Figure 4.17: NaCl characterization of Glass 1_11 sensor; (a) Nyqusit plot showing complex impedance plane (b) Impedance and phase measurement plot (c) Impedance behaviour in showing the Real, Z and the Imaginary, Z

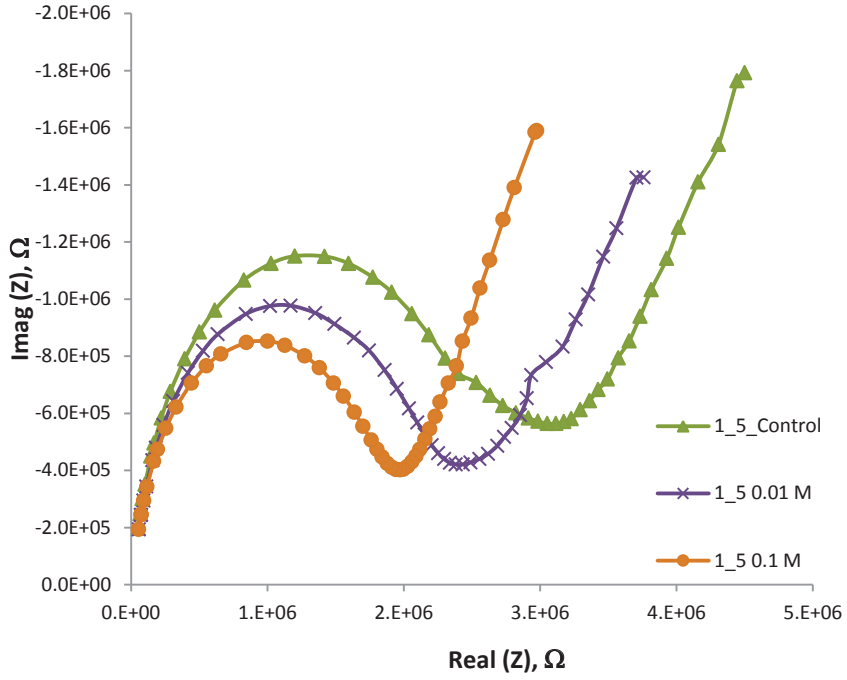

(a)

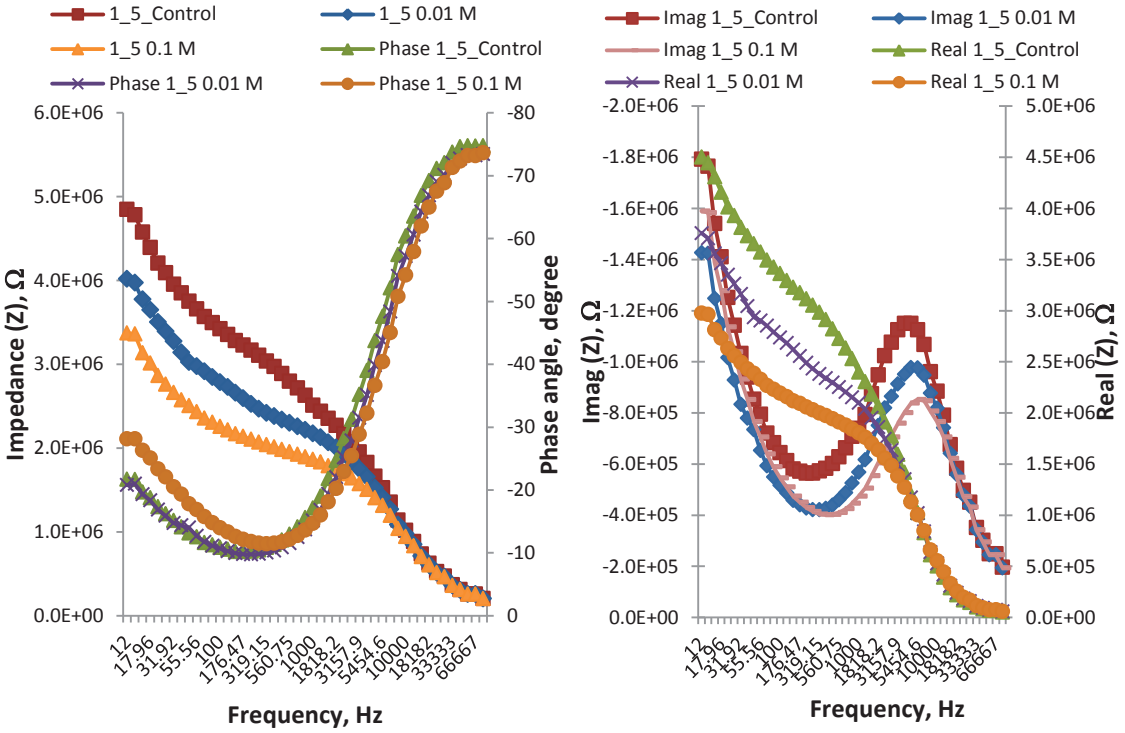

(b) (c)

Figure 4.18: NaCl characterization of Glass 1_5 sensor; (a) Nyqusit plot showing complex impedance plane (b) Impedance and phase measurement plot (c) Impedance behaviour in showing the Real, Z and the Imaginary, Z

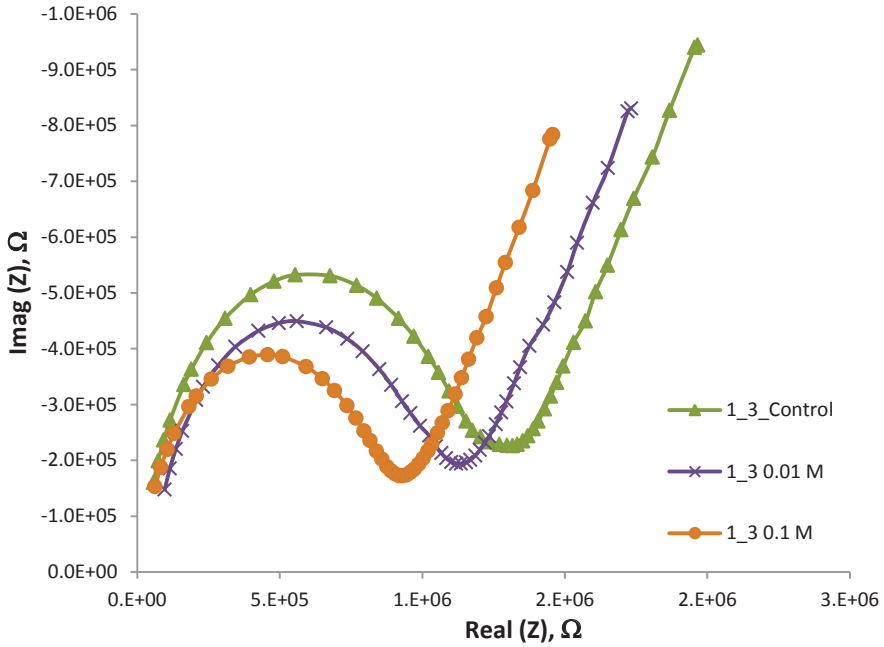

(a)

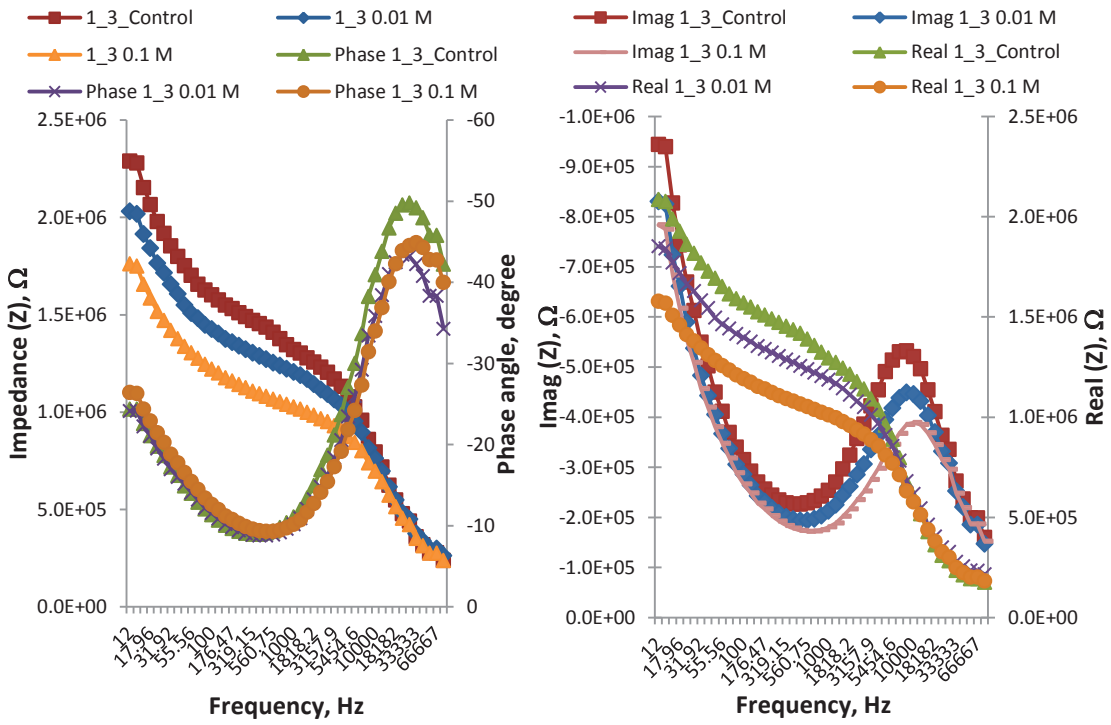

(b) (c)

Figure 4.19: NaCl characterization of Glass 1_3 sensor; (a) Nyqusit plot showing complex impedance plane (b) Impedance and phase measurement plot (c) Impedance behaviour in showing the Real, Z and the Imaginary,Z

Results have shown that all sensors behave differently with NaCl solution of different molarity. The real part of the impedance spectra shows the ionic conductivity while the imaginary part shows the dielectric capacitance of the NaCl solution. The ionic conductivity and the dielectric capacitance of the NaCl solution change as the molarity increase which indicates that the increase of the ions in the solution. More ions in the solution will reduce the impedance as shown in the plots. The Nyqusit plots show the diffusion and the charge transfer process as the frequency increases from 12 Hz to 100 kHz. These are shown from figures showing diagonal line at low frequency and as frequency increases showing a semi-circle curve with a single time constant. Results of the impedance characteristics of the sensors with NaCl have shown that sensors with 1_5 configuration show better sensing performance. Percentage of current sensitivity measurement for 1_5 configurations of all sensors at 100 Hz and 1 kHz have been calculated based on Equation 4.1. Results of sensitivity measurement in Figure 4.20 have shown Alumina sensor has better performance compared to FR4 and Glass sensors. Clearly this sensors can discriminate the NaCl of different molarity hence produced a better sensitivity to investigate the response of positively charged cation, the sodium ion (Na^+), and a negatively charged anion, the chloride ion (Cl^-) on the sensors.

$$\% \text{ Sensitivity} = \frac{I_{Target} - I_{Control}}{I_{Control}} * 100\% \qquad \textbf{4.1}$$

where I_{Target} is the sensing current in solution and $I_{Control}$ is the resulting current of control solution (MilliQ water) on the sensor.

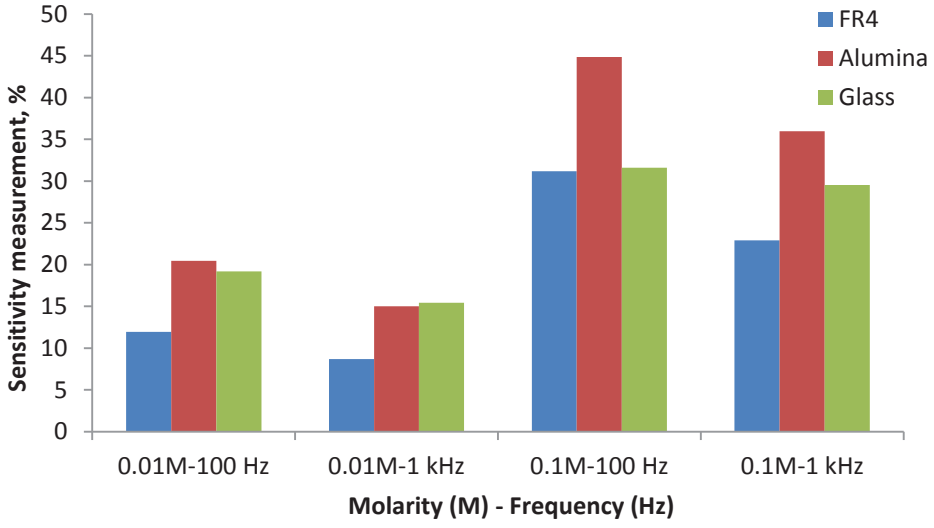

Figure 4.20: Sensitivity measurement for different sensors of 1_5 configuration at 100 Hz and 1 kHz (NaCl)

4.4 Characterization of sensors with different pH

Alumina and Glass sensors with 1_5 configuration was further investigate with standard pH buffer of pH 7, pH10 and pH 4 to study the impedance characteristic of the sensor with pH (potential of Hydrogen). pH is used to indicate the activity of hydrogen ion which measures the hydrogen ion concentration in a solution. Any solution with pH 7 is neutral where the molecules exist in equilibrium of hydrogen ions (H^+) and hydroxide ions (OH^-), for example pure water given by;

$$H_2O <-> H^+ + OH^- \quad \textbf{4.2}$$

Therefore if the solution has pH less than 7 showing acidity this indicates that ion H^+ increases and OH^- ion concentration decreases. If the solution is alkaline where the pH is greater than 7 therefore the ion concentration of OH^- increases and H^+ ion concentration decreases. The response of different pH will be analysed for Alumina and Glass sensors of 1_5 configuration. The same experimental setup was used with applying constant excitation voltage of 1 V_{rms}, slow measurement with frequency setting between 12 Hz – 100 kHz. All measurements were replicated three times and average values of three runs were taken.

4.4.1 pH on 1_5 Alumina Sensor

Results of pH characterization for Alumina sensor are shown in Figure 4.21. The Nyqusit plot shows the diffusion process occurs at low frequency and semi-circle curve indicating the charge transfer at higher frequency. The sensor is able to discriminate well each buffer of different pH value. The Bode plot in Figure 4.21 (b) shows that the impedance changes at frequency lower than 10 kHz but the phase angles not changing much. The impedance behaviour in Figure 4.21 (c) showing the real part changes from 12 Hz – 10 kHz but the imaginary part only have significant changes between frequency 200 Hz – 20 kHz. It can be said the sensor able to sense the difference of ion concentrations of hydrogen ions (H^+) and hydroxide ions (OH^-) in different buffers.

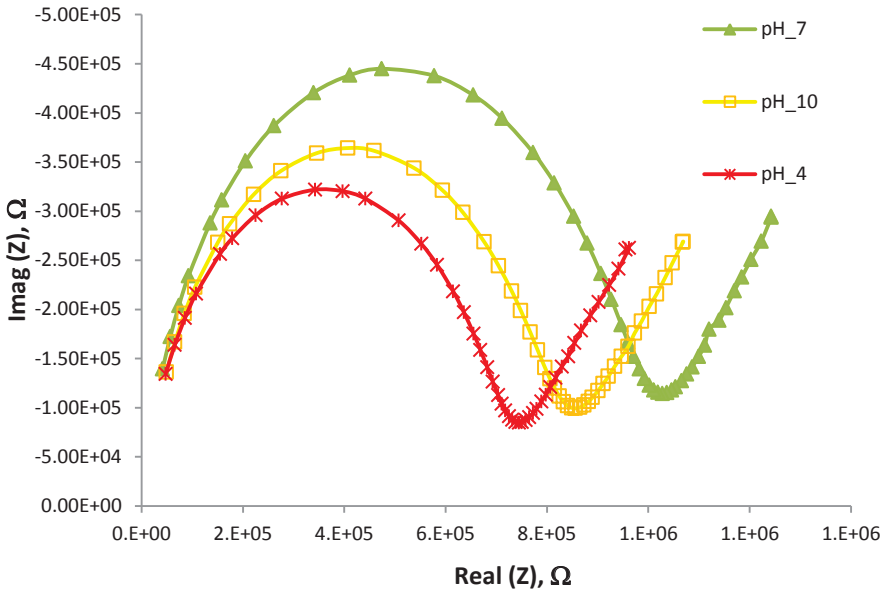

(a)

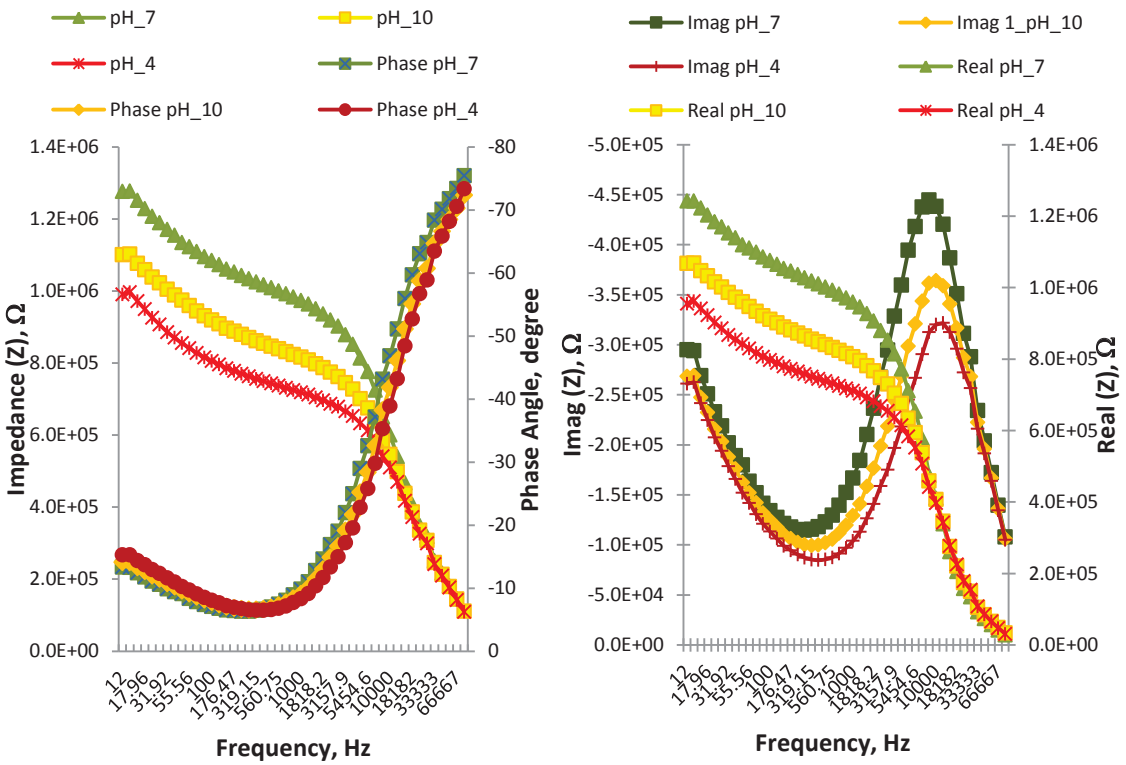

(b) (c)

Figure 4.21: pH characterization of Alumina 1_5 sensor; (a) Nyqusit plot showing complex impedance plane (b) Impedance and phase measurement plot (c) Impedance behaviour in showing the Real, Z and the Imaginary, Z

4.4.2 pH on 1_5 Glass Sensor

Figure 4.22 (a) – (c) shows the Nyquist plot, Bode plot and impedance behaviour of the buffers with Glass sensor of 1_5 configuration. The results show the sensor able to distinguish buffers of different pH values. The results also show similar analysis which have been discussed earlier for Alumina sensor but with lower sensitivity measurement.

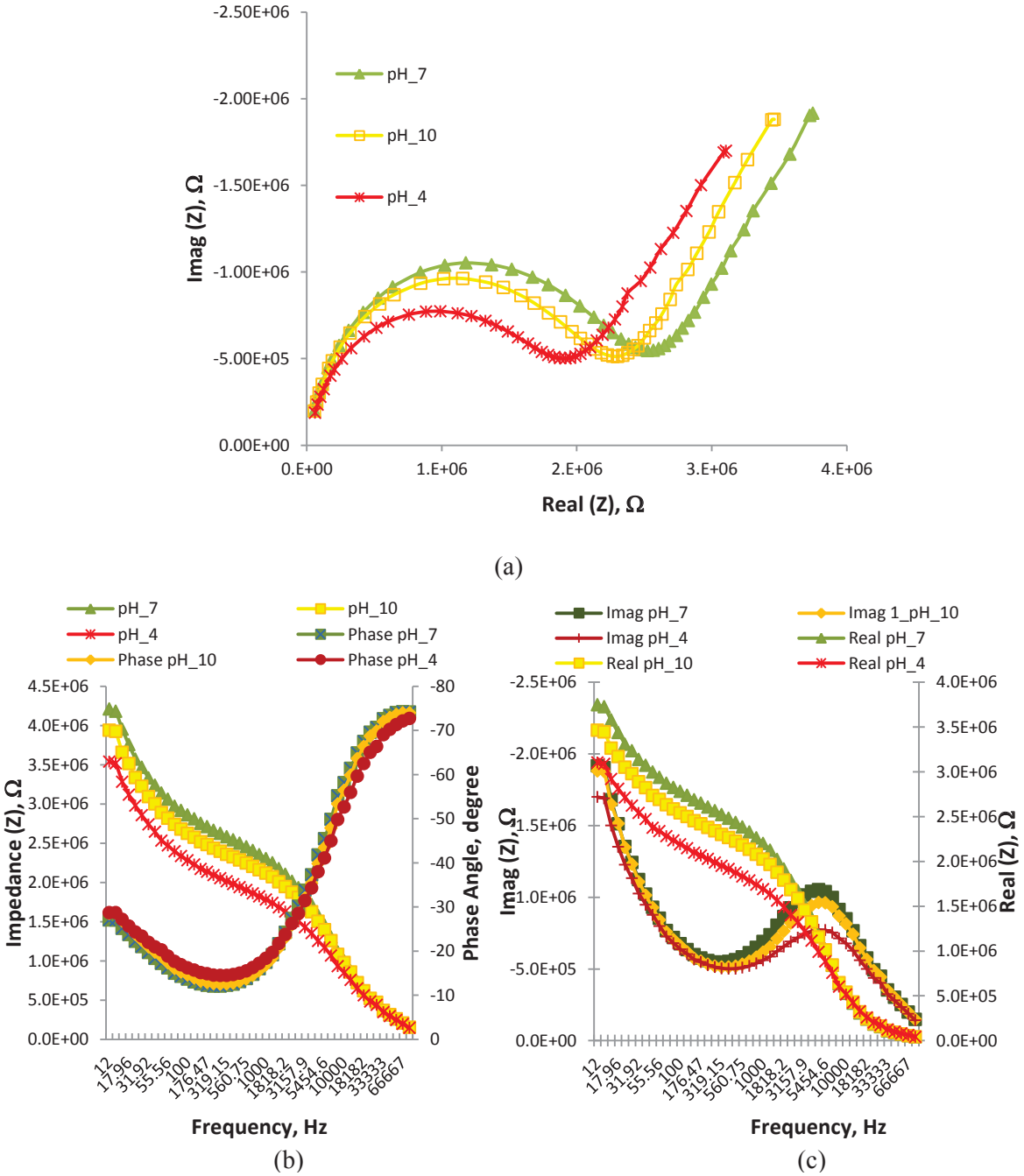

Figure 4.22: pH characterization of Glass 1_5 sensor; (a) Nyqusit plot showing complex impedance plane (b) Impedance and phase measurement plot (c) Impedance behaviour in showing the Real, Z and the Imaginary, Z

The percentage of sensitivity measurement from Equation 4.1 was calculated taking pH 7 (neutral) as a reference. Results are shown in Figure 4.23 where Alumina sensor of 1_5 configuration has shown better sensitivity measurement. Therefore, Alumina sensor of 1_5 configuration has shown better sensing performance compared to Glass sensor.

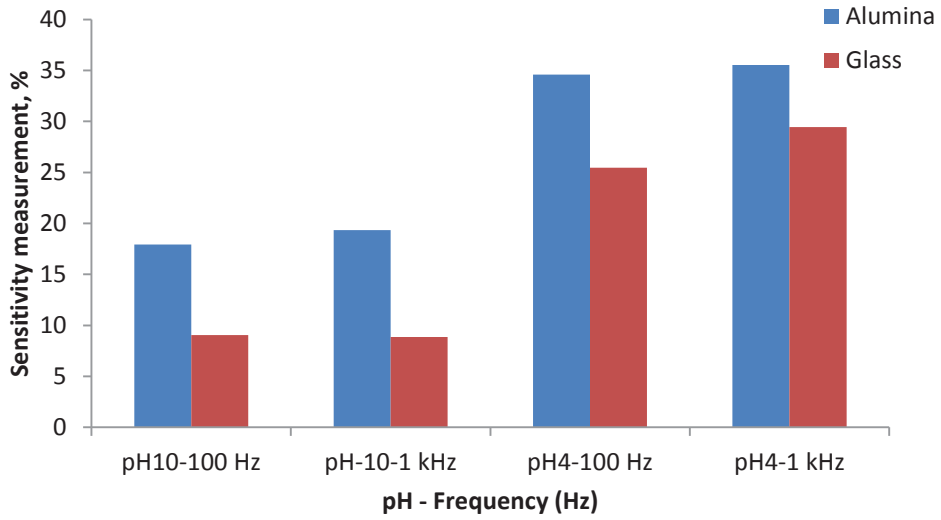

Figure 4.23: Sensitivity measurement of Alumina and Glass sensors for pH buffers at 100 Hz and 1 kHz

4.5 Experiments with peptides related to Domoic Acid

Experiments were conducted to analyse the sensor performance with pure chemicals which are related to food poisoning. The experiments were conducted in a desiccator to control the temperature and humidity. The experiments were conducted at room temperature between 23°C – 26°C with humidity between 40% - 50%. Two peptide derivatives namely sarcosine and proline were used for this experiment, which are structurally and closely related to domoic acid. N-methyl glycine or sarcosine represents the simplest structure and the proline molecule is arguably the most important amino acid in peptide conformation, containing the basic structural similarity to the domoic acid. Figure 4.24 shows the chemical structure of the target molecules. These peptides were readily available at laboratory and since the domoic acid is too expensive for reproducibility of the experiments, therefore, these two chemicals were chosen. Each chemical was diluted in MilliQ water (control) and the solutions were prepared for 1 mg/ml each. Small amount of 40 µl of each solution was taken for sensor measurement.

The exposure time of 12 minutes was established after a few experiments with the same chemicals of same molarity. These measurements were observed frequently for any changes in measurement signals. The percentage of sensitivity measurement can be calculated using Equation 4.1. It was observed from the experimental results that Alumina sensors give a good response to the target molecules. The results show there is significant high ion concentrations of peptides in solution compare to the control solution. Figures 4.25 (a), (b) and (c) show the Nyquist plots of each Alumina sensor for different peptides. Only sensor with configurations 1_5 and 1_3 response very well to the different peptides and it is possible to discriminate the different peptides from the output of the sensor. The Nyquist plots of 1_5 and 1_3 sensors have shown better results. The plots show a large semi-circle curve with a single time constant which indicates slow electron transfer from solution to electrode because the presence of inclarac coating. Sensor 1_11 has shown less response to the peptides since it has higher impedance value which limits the mobility of electron flow through the system. The Bode plots in Figures 4.26 (a) and (b) show the impedance and phase angles of both configurations (1_5 and 1_3). The change of impedance and phase angle is particularly small for different peptides.

The impedance behaviour were plotted to analyse the real part and the imaginary part as shown in Figures 4.27 (a) and (b) respectively. It is clearly observed that at a particular frequency range (0.3 kHz – 2 kHz) there is a significant change of the imaginary part of the system and the real part also changes for frequency less than 1 kHz. The real part changes due to the ionic conductivity of the solution and the imaginary changes due to permittivity or dielectric constant changes of the solution which resulting the electron flow. The change of real part and imaginary part is higher for 1_5 configuration as compared to 1_3, which indicates that 1_5 configuration has better sensing performance. Figure 4.28 shows the normalized percentage of current sensitivity measurement for different peptides with respect to control. It is observed that the percentage difference of target molecules is higher for Alumina 1_5 sensor compared to 1_3 sensor which indicates that 1_5 configurations can distinguish better between different peptides. As for 1_11 sensor, since the measurement only valid after 120 Hz and above (because of very high impedance to be captured by the LCR meter between 12 Hz – 120 Hz), that is why in the figure it shows no change until the

frequency reach 120 Hz and it is noticed that there is very small change of this percentage for 1_11 sensor.

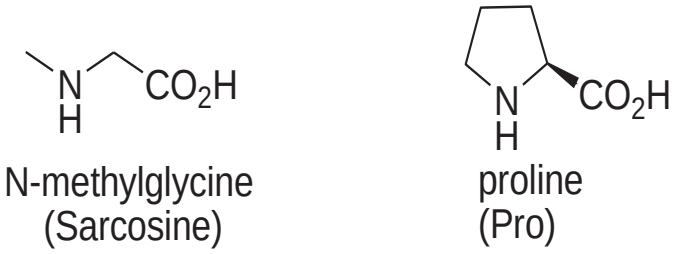

Figure 4.24: The target molecules of two different peptides

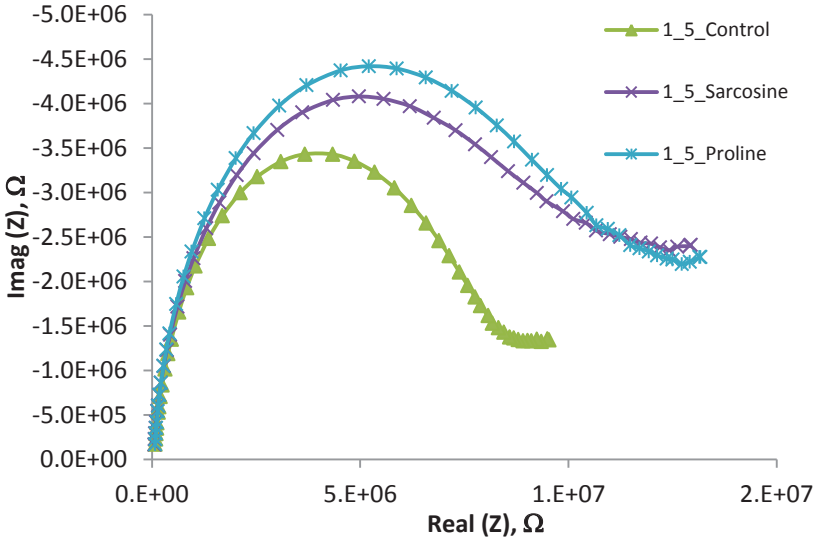

(a)

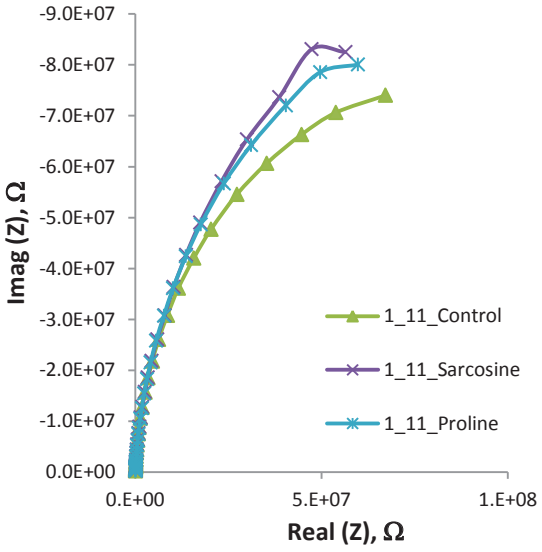

(b)

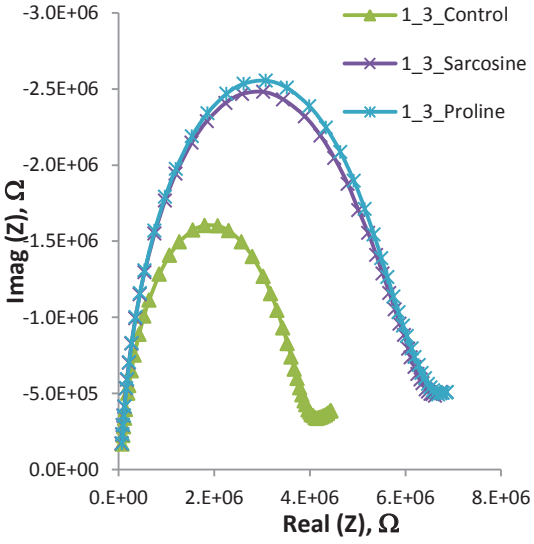

(c)

Figure 4.25: Nyqusit plot of two different peptides and control for; (a) Alumina, 1_5 configuration (b) Alumina 1_11 configuration and (c) Alumina 1_3 configuration

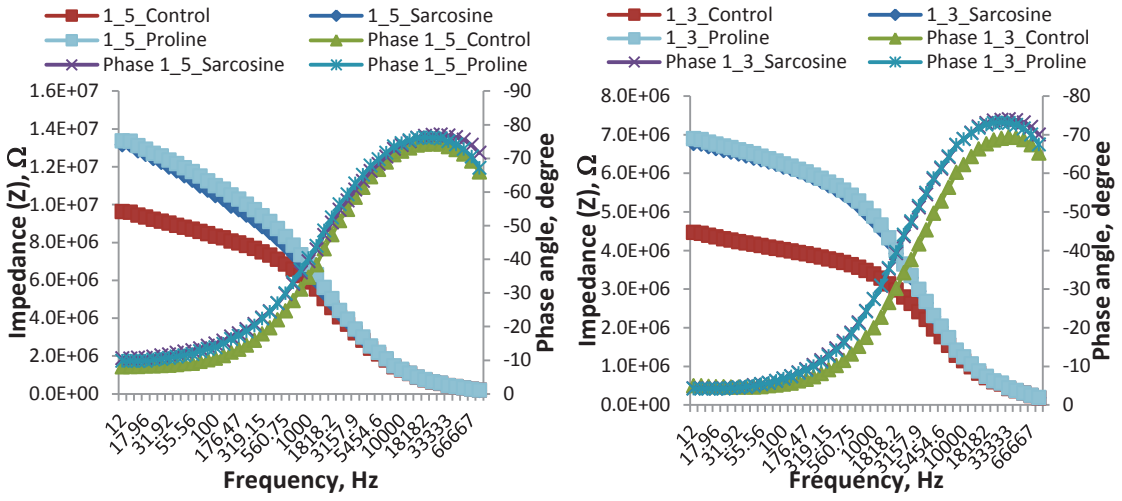

(a) (b)

Figure 4.26: Bode plot of impedance (Z) and phase angle of; (a) Alumina 1_5 configuration and (b) Alumina 1_3 configuration

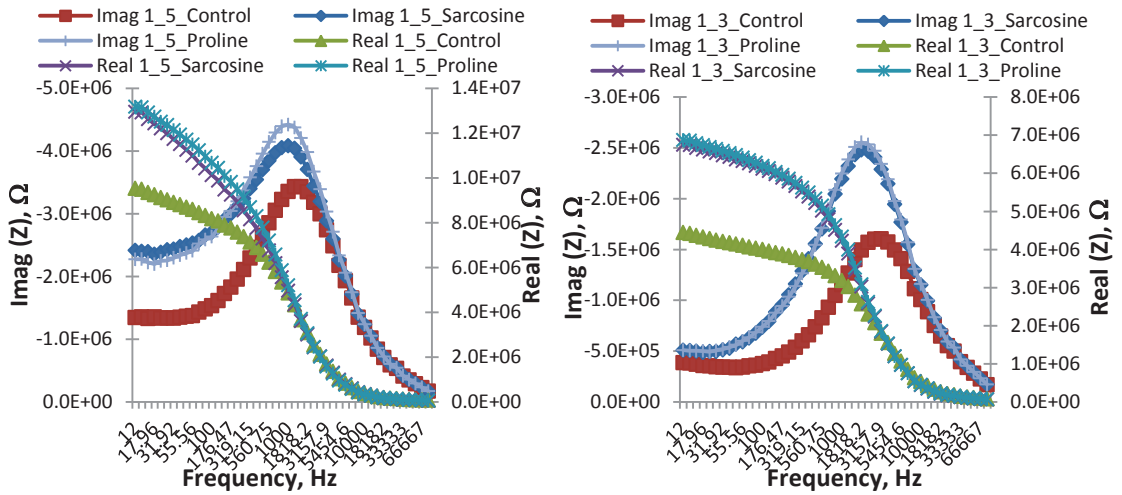

(a) (b)

Figure 4.27: Impedance behavior of Real part and Imaginary part of Sarcosine, Proline and control for; (a) Alumina 1_5 configuration and (b) Alumina 1_3 configuration

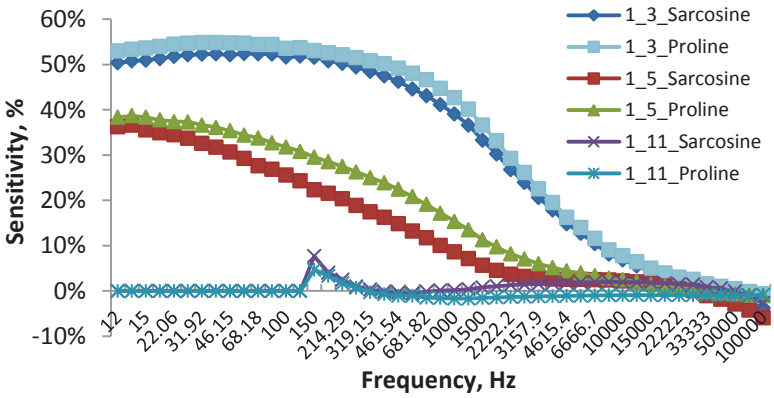

Figure 4.28: Sensitivity measurement for different configuration of peptides with respect to control

4.6 Initial experiments with LPS O111:B4

Experiments were conducted to evaluate the structure of the Lipopolysaccharides (LPS) from LPS O111:B4. The commercial product of LPS O111:B4 was purchased from Sigma-Aldrich, USA. This pure LPS product was extracted using phenol extraction which contains less than 3% of protein [226]. 100 mg of O111:B4 was diluted into 100 ml of MilliQ water (with minimal salt medium). The pH of each solution was measured using pH meter model 420A from Orion Research Inc. with the new pHoenix Tuff Tip® Combination pH electrode model 5733534-003B. It was observed that the pH reading of MilliQ water was 6.50 and pH of LPS O111:B4 solution was 6.59. The measurement was taken immediately after the sample preparations to avoid any contamination. It can be said that the signal measurements from the experiments conducted using these pure LPS will not be affected by protein or pH of each samples.

A small amount (40 µl) of each solution was pipetted using 10 µl pipettor onto the sensor. The change of impedance and the phase angle were recorded. Figure 4.29 shows the Nyquist plot of the LPS O111:B4 and control (MilliQ). The sensor shows a significant result to discriminate between the target LPS with the control. The Nyquist plot shows diffusion occurs at low frequency and then followed by the charge transfer given by a semi-circle curve. The impedance and phase angles are shown in Figure 4.30 (a). The impedance spectra of real part and imaginary part are shown in Figure 4.30 (b). It was observed the real part only changes at frequency between 12Hz – 1 kHz but the imaginary part changes between 12 Hz – 5 kHz. It is noticed that any change in absolute value of the real part of the signal is negligible at certain frequency between 1 kHz – 5 kHz. So the effect of conductivity does not have any influence on the signal. Moreover to eliminate the effect of water on the results, the amount of water used in the experiments has been kept constant. Therefore, the change of measured signal is due to the change of the effective permittivity of the solutions. Results from the experiments have shown that Alumina sensor with configuration 1_5 can be used to detect LPS or endotoxins.

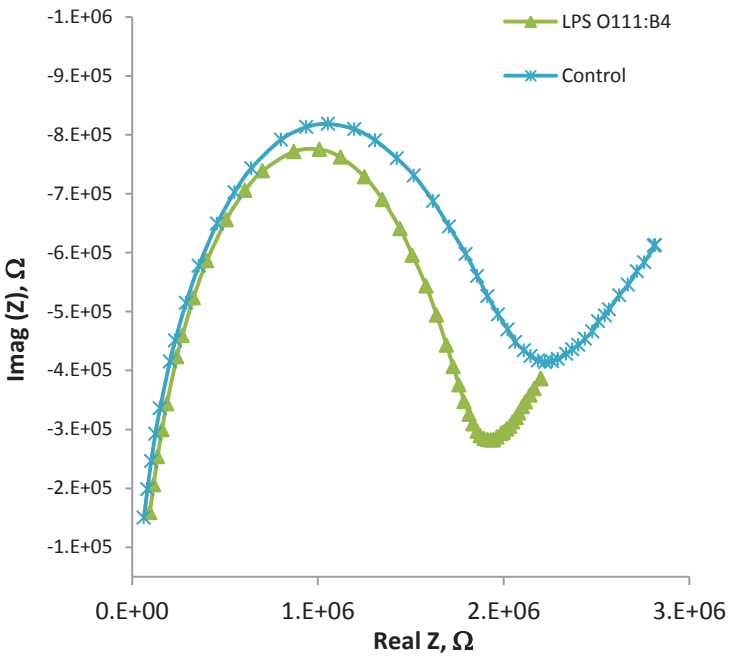

Figure 4.29: The Nyquist plot of LPS O111:B4 and Control for Alumina 1_5 configuration

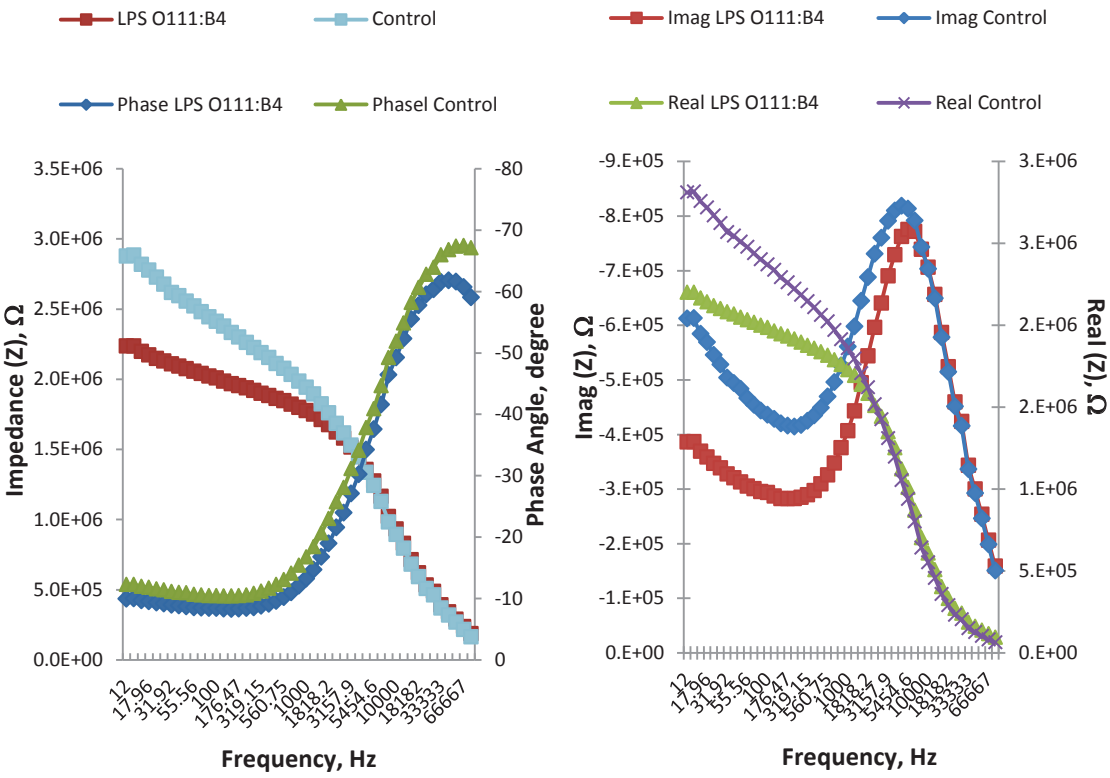

(a) (b)

Figure 4.30: (a) Bode plot of impedance (Z) and phase angle of 1_5 configuration and (b) The impedance spectra of LPS O111:B4 and Control for Alumina 1_5 configuration

4.7 Conclusion

Results and analyses of different fabricated sensors of different substrate and different configurations of electrode structure have been discussed. The sensors were analysed based on Impedance Spectroscopy (IS) method. It is important to observe from the experimental results that all sensors should behave like a capacitive sensor where the change of imaginary part (reactance) should be higher compared to the change of real part (resistive) as a function of frequency. Impedance characteristic of all sensors were first studied with respect to air. It was observed that sensors with configuration 1_11 show highest impedance which indicates lower capacitance value. Sensors of configuration 1_5 and 1_3 have shown lower impedance value. Silicon sensors have shown better performance in term of low impedance, high capacitance value and high sensing signal with low noise. Experiments were also conducted to study the sensor behaviour in ionic solution (NaCl) and in the buffers of different pH values. All sensors have different response to different chemicals which indicate the sensor performance. All sensors (FR4, Alumina and Glass) with configuration 1_5 of pitch length of 250 μm have shown better response of different chemicals. Among these configurations it was observed Alumina sensor with configuration 1_5 has shown better sensing performance. It was also observed that the high concentrations of ionic solutions can degrade or corrosive the inclarac coatings. It is also shown from the results that selective coating materials on sensor electrodes is important to achieve selectivity of target molecules for better sensing performance. The incralac coating was introduced just to retard the electron transfer from the electrolyte to electrodes and it does not show any selectivity towards the target molecule. The solution with high concentration of ions was observed to have a significant change on sensor response due to change in conductivity and dielectric permittivity. In order to achieve the selectivity, a particular cross-linker and binding molecules need to be carefully studied and analysed. Further investigations were conducted to study different coating materials on sensor electrodes. Most of the work has been done on coating sensors of different cross-linkers on silicon sensors which has shown better capacitive sensor behaviour compared to previous sensors. The results, analysis and discussion for sensitivity, selectivity and stability of the coated sensors have been discussed in Chapter 5 and Chapter 6.

CHAPTER 5

Coating and Immobilization of Sensors

5.1 Introduction

The selectivity of the sensors to certain bio-molecules has been discussed in this chapter. This includes testing of different types of coating materials, different coating methods, and immobilization of specific bio-molecules on coated sensors. A new structure, which is different than the conventional interdigital structure, has been adopted for higher sensitivity. The configuration of the electrode structure chosen was 1_5 configuration (five negative electrodes between two positive electrodes) as shown in Figure 5.1 The analysis of this configuration has been reported in [227]. FR4 sensors were chosen since they were easily fabricated at Massey University fabrication laboratory. In this research work these sensors were tested with different coating materials. A new type of silicon based interdigital sensor, which has a basic structure of 1_5 configuration, was also fabricated and coated. The details of which will be discussed further in Chapter 6.

5.2 Coating of Sensors

Coatings of sensors are very important in chemical sensing or bio sensing applications. Coatings are normally applied to improve surface properties of the substrate, such as adhesion, appearance, wetability, for corrosion resistance, wear resistance, and scratch resistance. A cross-linker facilitates the immobilization of biomolecules onto particular substrate surface [228]. Different coating materials (cross-linkers) and coating techniques have been chosen and tested. Figure 5.2 shows interdigital sensors fabricated on FR4 coated with different materials. The Carboxyl-funtional polymer [229], APTES (3-aminopropyltrietoxysilane) [228, 230] and Thionine (a blue organic dye) [231, 232] were introduced as coating materials which have been widely used in the development of chemical sensors and biosensors. The objective is to study if these coatings could improve the performance and the selectivity of the sensors.

All coating materials were selected and optimised to be stable in water, as the measurements were taken place in aqueous media. Moreover, the coatings have been designed to have available carboxylic or amine functional groups. The use of these functional groups is a widely used technique to bind specific biomolecules. Different coating techniques were applied in order to study how different techniques contribute to the sensor performance. If the simplest coating technique gives a desirable result, it can be used for subsequent experiments without the necessity of sophisticated machines and tedious procedures. The electro-spinning method and spin coating method are examples of coating procedures which need specific machines and technical procedures to operate, while the dip-coating method is a manual procedure, not requiring such machines or procedures, used widely in coating materials. The thickness of the coating materials were observed in between 800 nm – 1000 nm on the electrode surface.

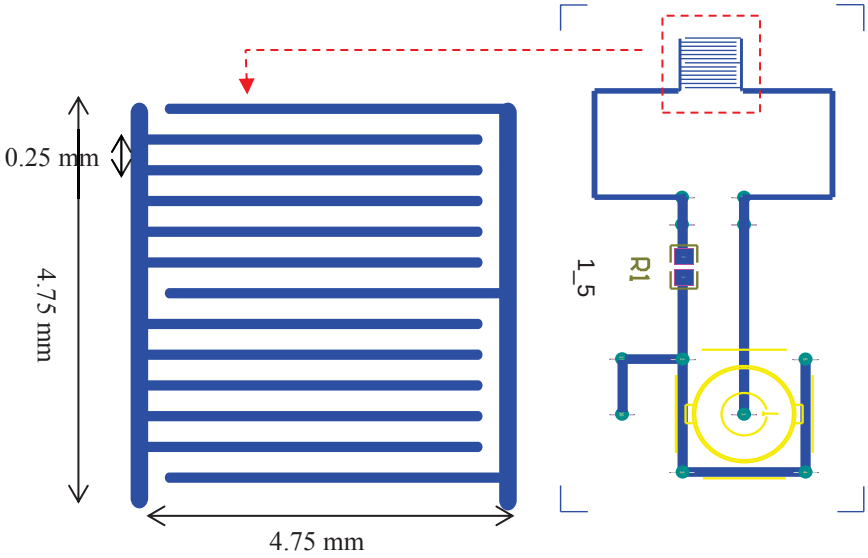

Figure 5.1: Interdigital sensor design: 1_5 configuration

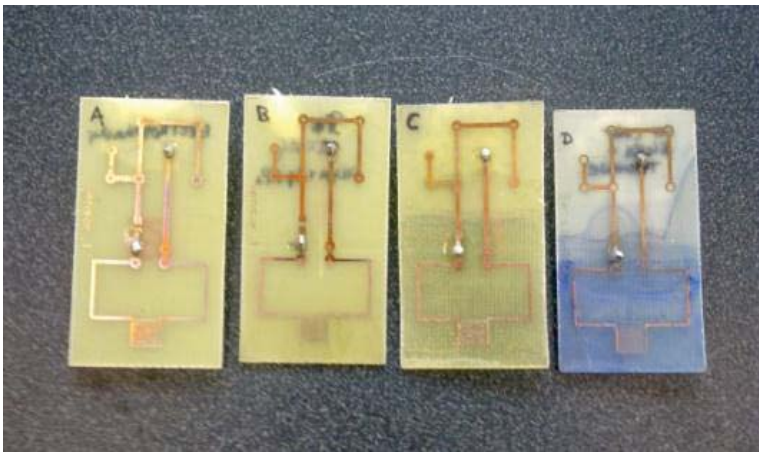

Figure 5.2: Fabricated interdigital sensors on FR4 with different coating materials

5.2.1 Electrospining Method

The schematic view of the electro-spinning process is shown in Figure 5.3. A polymeric solution was placed into a syringe and a high voltage (23kV) was applied between the needle and a cathode screen. The polymer was then accelerated towards the cathode, and the electric field pulls the materials, forming a thin polymer fiber. The substrates were placed at the cathode, where the fibers are collected, forming a mat. Various diameter fibers, as thin as 50 nm, can be obtained by controlling the conditions of the polymeric solutions and the voltage and distance from the needle and the cathode. In this particular case a carboxyl-funtional polymer labelled as Coating A was used. The carboxyl-terminated functional groups are widely used in biological applications [233] for immobilization of amine-molecules, such as proteins, etc. The experimental conditions were adjusted to form sub-micron diameter fibers. The final fibers were water insoluble, and their constituent material can be considered a hydrogel. This kind of material has a high affinity for water and ionic solvents.

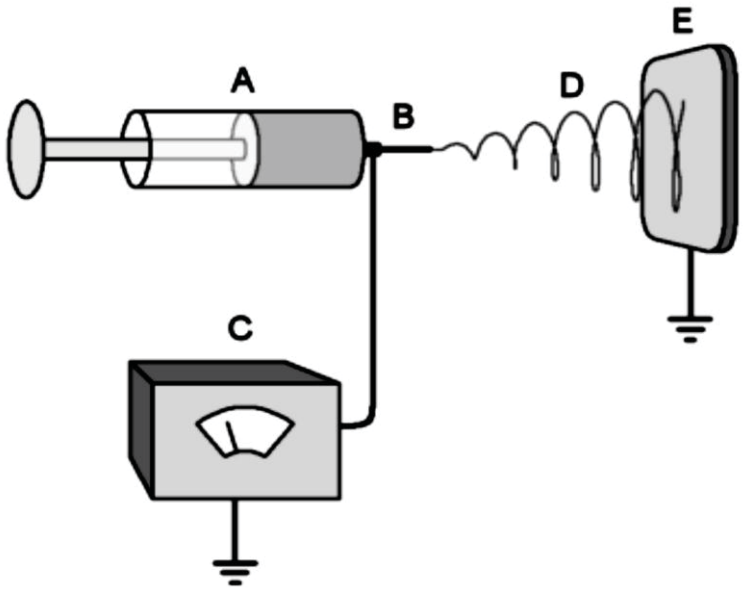

Figure 5.3: Schematic view of the electro-spinning process, where A is the syringe where the desired polymer is placed, B is the anode needle, C is a high voltage source, E is the cathode screen and D is the electrospun fiber accelerated by the electrical field.

5.2.2 Spin-Coating Method

The Spin-Coating technique as shown in Figure 5.4 is based on a rotation of the substrate at high speeds (from 1500 to 5000 rpm). If the desired solution is placed onto the substrate, and the sample is rotated, the centrifugal forces push the excess solution away. Equilibrium is reached between the centrifugal forces from the rotation, and the viscous forces inside the solution. In the final step, the solvent evaporates away, leaving a uniform thin solid film. This technique makes it easy to obtain uniform coatings as thin as 40 nm. In this particular case a carboxylic functional polymer labelled as Coating B [234], which is stable in water and has a hydrogel nature, was spin-coated over the interdigitated electrodes. Accurate measurement of the thickness of the coating is difficult due to the non-uniform profile of the substrate, however, it is within 800 nm. In this case the polymer was doped with a small amount of silver nanoparticles, with the objective of achieving more impact in the capacity variations of the coating.

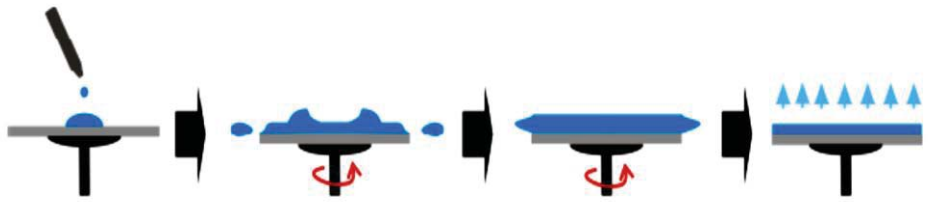

Figure 5.4: Schematic view of the spin coating process. The material is spun off the substrate by simply spinning the sample stage at a constant speed while the solvent evaporates away, leaving homogeneous thin film coating.

5.2.3 Dip-Coating Method

The Dip-Coating technique uses a similar physical phenomenon as Spin-Coating, but without spinning the sample. In this case the thinning of the fluid layer is achieved by reaching the equilibrium between the viscous forces inside the film and gravity (instead of the spinning force). Firstly, the substrate was immersed into the desired solution, and subsequently impregnation was carried out by lifting the substrate at a very controlled speed. During this step the fluid layer was thinned by the effect of gravity until the solvent was partially evaporated. Finally the substrate was hold, to allow the solvent to evaporate completely. This process can be repeated several times to ensure stabilisation of the film at the end of each step. The initial solution was prepared from a chemical

precursor of silica. The PCB substrates were immersed into the solution and lifted at a speed of 4 mm/min. A total of four layers were deposited and two different coatings fabricated using this technique. Figure 5.5 shows the schematic view of the dip-coating method. The silica coatings were immersed in an APTES solution [235], to provide a coating of amino functional groups and labelled as Coating C. Coating D was then obtained by adding Thionine [236] (an organic dye widely used in bio applications such as protein marking, cellular wall staining, etc.) to the silica precursor solution. Following that, the fabrication process was carried out normally. The resulting film was strongly bluish. In fact, due to the high staining power of Thionine, the whole PCB acquired a blue aspect.

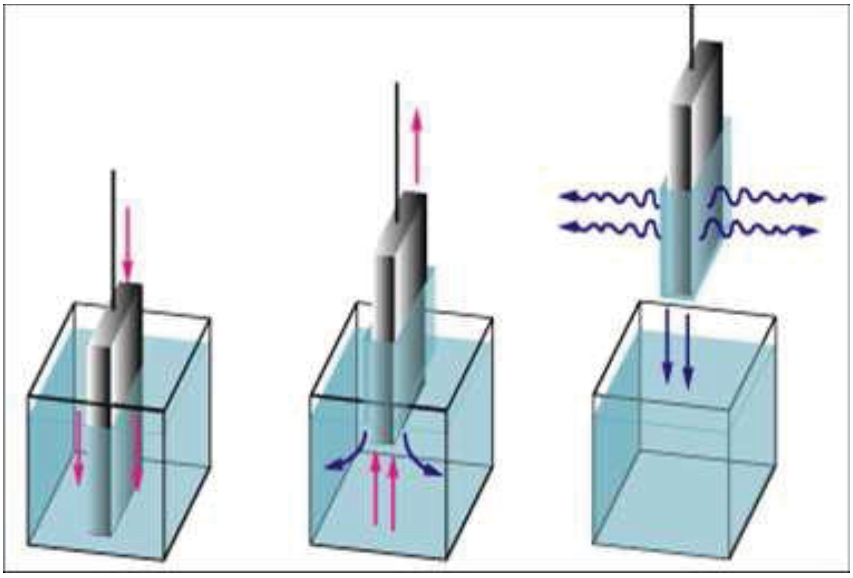

Figure 5.5: Schematic view of the dip-coating process. After the substrate is immersed into the desired solution, it is pulled-up at a very controlled speed (usually very low), and finally the sample is hold until the solvent is properly evaporated.

5.2.4 Optical Microscopy Characterization

Optical microscopy was carried out for particle characterization of the coated material on interdigital sensors. The optical micrographs images have been taken using a Leica DM 2500M as shown in Figure 5.6. The microscope is equipped with four magnification power of 10x, 20x, 40x, and 100x. It has also a CCD camera with an additional magnification of 10x. These images were taken to observe the particle distribution of the coating material introduced onto the interdigital sensors.

Figure 5.6: The Leica DM 2500M

5.2.4.1 Bare sensor

A few micrograph images of the bare electrodes were taken to have a reference of the aspect before the different coatings were coated. As it is shown in the micrograph images in Figure 5.7 the copper electrodes have slightly rough surface, and its surface is about tenth of microns above the PCB substrate. Normally the PCB fabrication will produce copper thickness of 34 µm on the substrate. The only thing that is noticeable is the irregular profile of the electrodes, probably because the widths of the electrode fingers are very near of the milling tool definition. We believe that this irregular shape does not affect to the sensor performance.

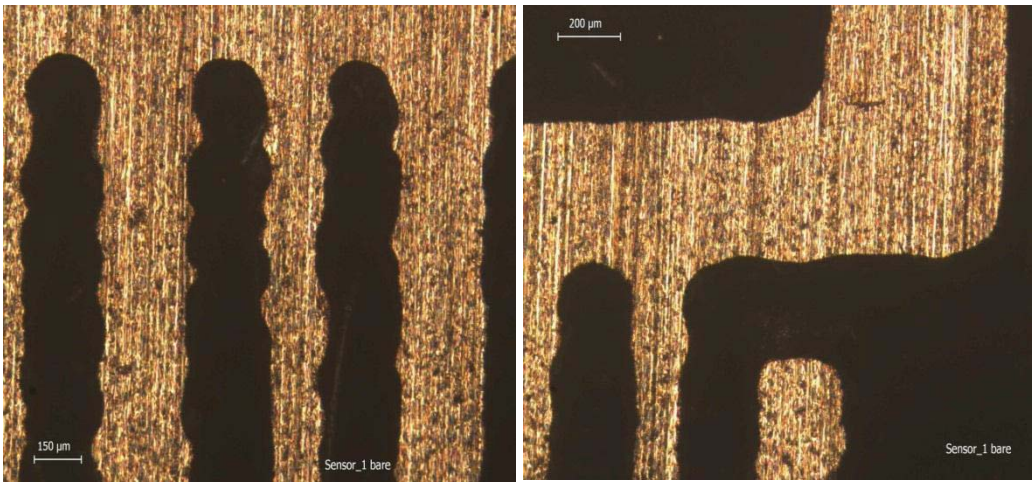

Figure 5.7: Micrograph images of the bare electrodes.

5.2.4.2 COATING A - Electrospun of Carboxylic functional polymer

Coating A was coated using electro-spinning method. Figure 5.8 shows the sample of electrospun fibre onto the test glass substrate. The picture shows the fibre diameter is around 500 nm after drying under normal room temperature. The picture in Figure 5.9 shows how the electrospun membrane on the interdigital sensors. The 1000x micrograph image in Figure 5.9 shows closed up picture of the electrospun membrane on the electrode and in between the electrode spacing. It was observed the electrospun membrane was well distributed on the sensor electrodes as shown in Figure 5.10.

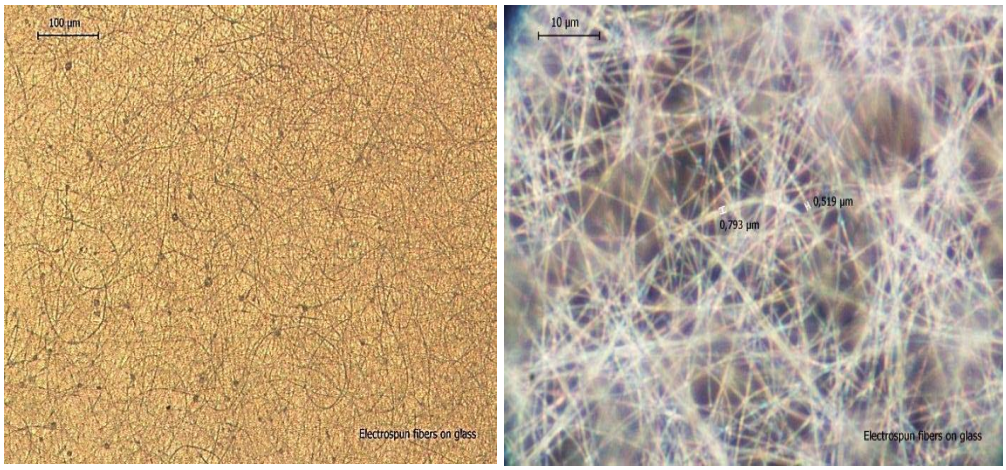

Figure 5.8: Electrospun fiber mats onto test glass substrates. In the picture at the right is shown how the average fiber diameter is around 500nm when the fibers were dry, and place under normal room conditions.

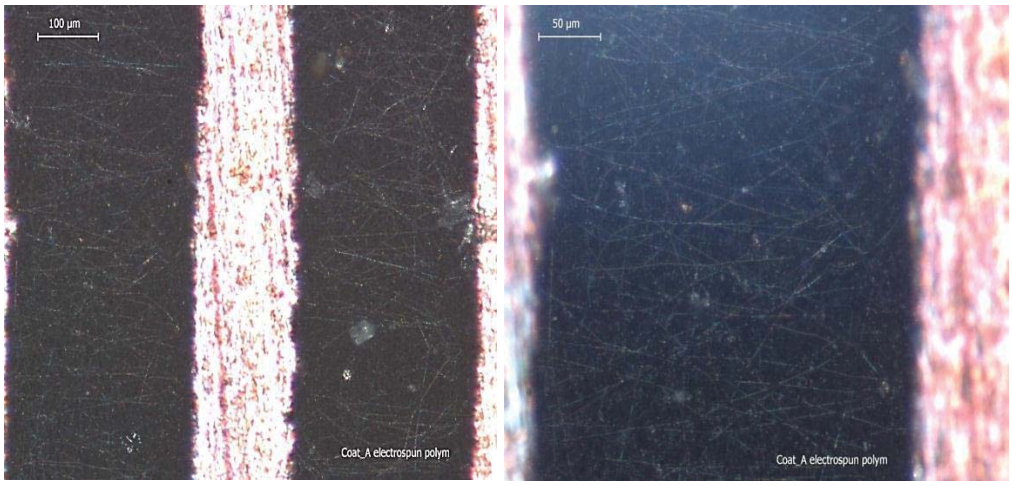

Figure 5.9: Micrograph images of the electrospun fiber mats over the sensors surface. The detail shows the polymeric fibers onto the PCB substrate between two of the electrodes.

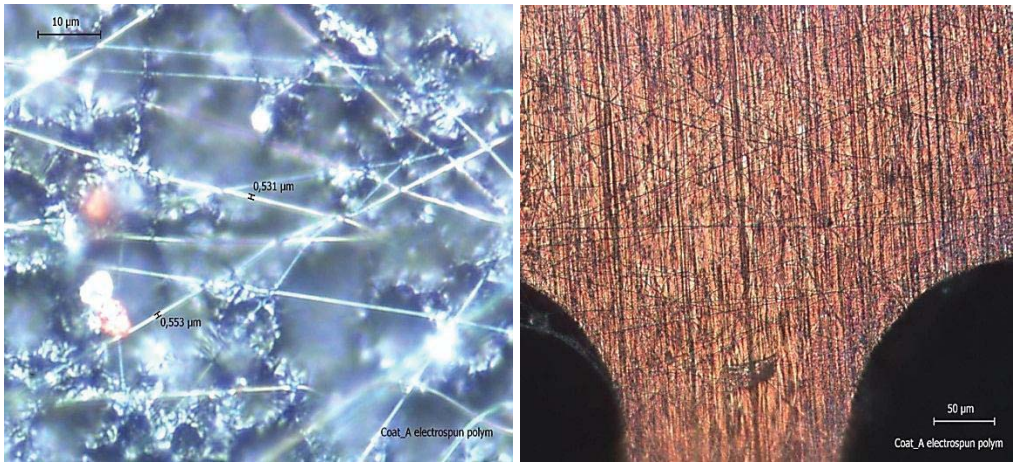

Figure 5.10: Left - 1000x micrograph of polymer nano-fibers over the PBC substrate on the electrode.

5.2.4.3 COATING B - Spin coated Carboxylic functional polymer

Coating B was coated using spin coating method. Figure 5.11 shows the 50x micrograph of the polymeric hydrogel coating (carboxyl-polymer). Figure 5.12 shows the 100x micrograph of uniform coated sensor with coating B.

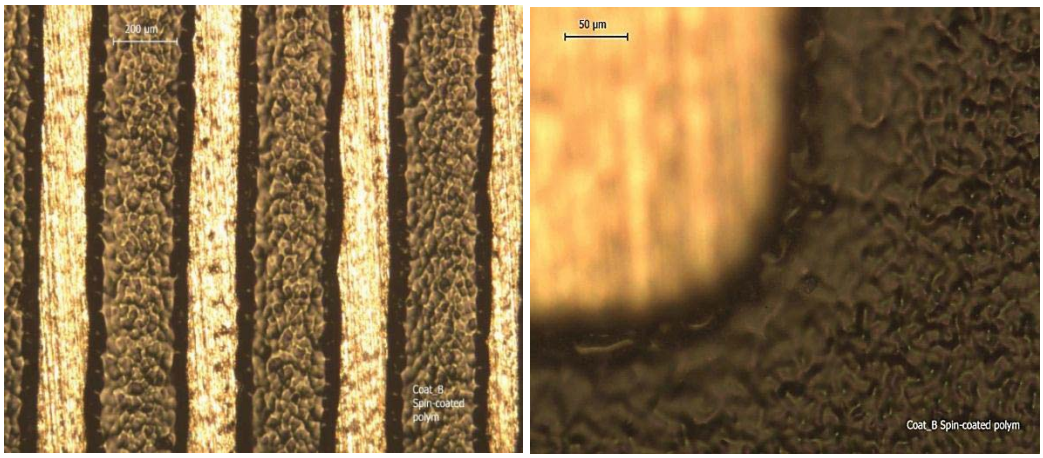

Figure 5.11: Left - 50x micrograph images of the electrodes. Between them it is visible the polymeric hydrogel coating. Right - 100x micrograph image of a detail of one electrode. The coating is uniform and covers the whole sensor.

5.2.4.4 COATING C - Dip-Coated silica coating funcitonalized with APTES

Coating C was coated using dip-coated silica funtionalized with APTES. Figure 5.12 shows the details of the micrograph imagess of coated sensor. The images between two electrodes are visible showing the silica coating with cracks surface. This effect appears

during the drying of the coatings, and it is typical of the silica coatings due to its low elasticity.

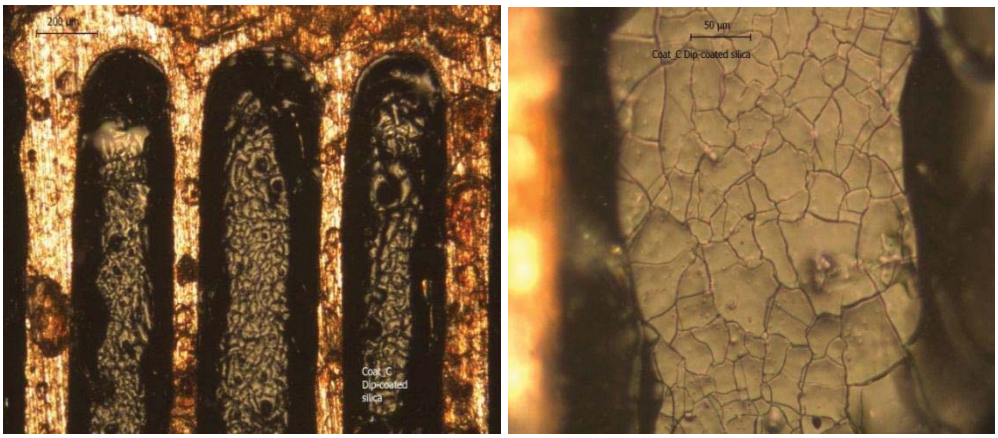

Figure 5.12: Micrograph images of the coated area with APTES.

5.2.4.5 COATING D - Dip coated silica with Thionine

Coating D was coated using dip-coated silica with Thionine. Figure 5.13 shows the micrograph images of coated sensor. Although the coating matrix is also silica a different cracking pattern is observed due to the presence of the Thionine inside the film.

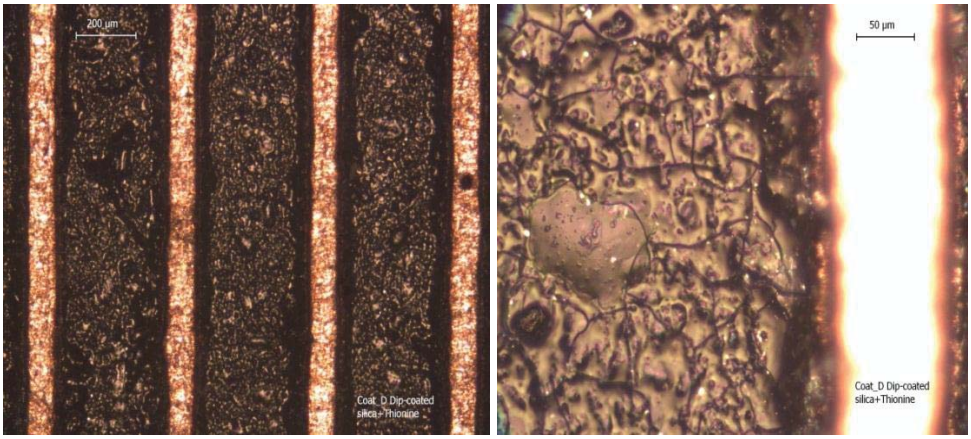

Figure 5.13: Micrographs of the pre-cursor silica with Thionine coatings.

Four different coatings (A, B, C and D) have been coated on FR4 sensors from three different coatings materials (Carboxylic functional polymer, APTES and Thionine). There were three different coating methods have been used. The next step is to immobilize these coated sensors with selected biomolecules which can bind to endotoxin structure.

5.3 Immobilization of Polymyxin B

Immobilization techniques have been used widely to immobilize DNA, cells, enzymes, metal, polysaccharides, etc [237]. The applications are commonly used in biomedicine, biotechnology, bioagriculture, bioenergy, bioenviroment and bioengineering research. In order to make the sensors selectively pick up the target biomolecules (endotoxin), Polymyxin B has been introduced. Polymyxin B (PmB), is an antimicrobial peptide produced by the Gram-positive bacterium-*Bacillus,* has been immobilized on the coated sensors because of its specific binding properties to LPS. PmB has been introduced for detection of endotoxins [148]. Figure 5.14 shows the chemical structure of PmB molecules. Immobilization of PmB involves several buffers which need to be prepared.

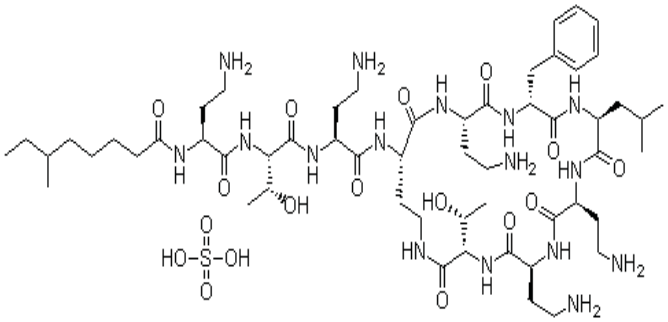

Figure 5.14: PmB chemical structure

5.3.1 Preparation of Borate Buffer

The Borate Buffer of 0.05 M with pH 8.0 was prepared. Firstly, borax (Sodium Tetraborate, $Na_2B_40_7.10H_20$) and boric acid (H_3BO_3) were prepared. Then, boric acid was added to borax solution until the desired pH is reached. The solution was diluted with MilliQ water to the desired molarity. The stock solution preparation as follows;

Borax solution

Sodium tetraborate ($Na_2B_40_7*10H_20$) MW = 381.37 g/mol (pH 9.28)

0.05M = 19.0685 gm/L (Dilute 19.0685 g of sodium tetraborate in one litre of MilliQ water)

Boric Acid solution

Boric acid ($H_3BO_{3)}$ MW= 61.83 g/mol (pH 5.20)

0.05 M = 3.0915 gm/L (Dilute 3.0915 g of boric acid in one litre of MilliQ water)

5.3.2 Preparation of Phosphate Buffer

The phosphate buffer of molarity 0.05 M with pH 5.2 in 0.1 M NaCl has been prepared. Stock solution A of potassium dihydrogen phosphate (KH_2PO_4) was first prepared followed by preparation of stock solution B of disodium hydrogen phosphate ($Na_2HPO_4.2H_2O$). Stock solution A of 975 ml was mixed with stock solution B of 25 ml to make 1000 ml of phosphate buffer. The stock solution preparation as follows;

Sodium Chloride solution

Sodium chloride (NaCl) MW = 58.44 g/mol

0.1M = 5.844 gm/L (Dissolve 5.844 g of NaCl in one litre of MilliQ water.)

Potassium Dihydrogen Phosphate stock solution (A)

Potassium Dihydrogen Phosphate (KH_2PO_4) MW = 136.1 g/mol

0.05M = 6.805 gm/L (Dilute 6.805 g of KH_2PO_4 in one litre of 0.1M NaCl)

Disodium Hydrogen Phosphate stock solution (B)

Disodium Hydrogen Phosphate ($Na_2HPO_4.2H_2O$) MW = 178 g/mol

0.05M = 8.90 gm/L (Dilute 8.90 g of $Na_2HPO_4.2H_2O$ in one litre of 0.1M NaCl)

5.3.3 Immobilization Process

All coated sensors were incubated in Polymyxin B (40 ml, 1 mg/ml in 0.05 M Borate Buffer, pH 8.0) at room temperature on a slow shaker (125 rpm) for 24 h. The sensors were then washed with Borate Buffer (0.05 M, pH 8.0), MilliQ water, Phosphate Buffer (0.05 M, pH 5.2, in 0.1 M NaCl) and finally finishing with MilliQ water. This will remove the residues of other molecules and leaving only PmB molecules attached to the coated sensors. The immobilized sensors were then dried under nitrogen flow. The immobilization process is shown in Figure 5.12 for 24 hours incubation in PmB. And Figure 5.16 shows the drying process under the nitrogen flow. The sensors were kept in clean dry container before the experiments with endotoxin solution were conducted.

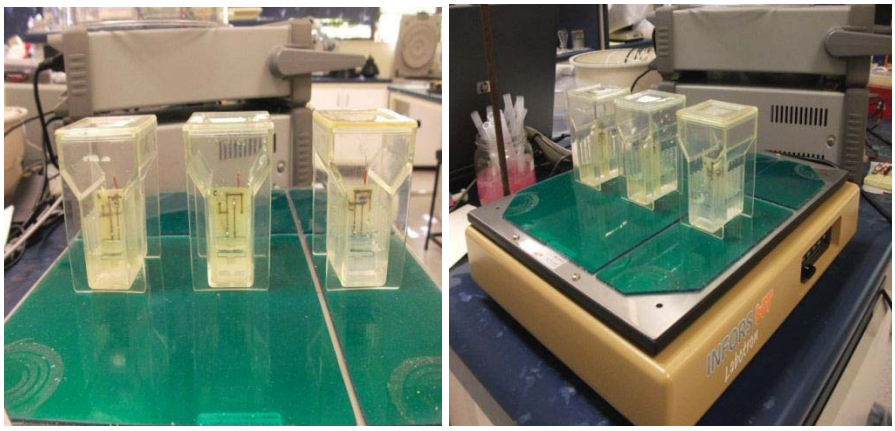

Figure 5.15: 24 hours incubation of sensor in PmB with slow shaker of 125 rpm; FR4 sensors

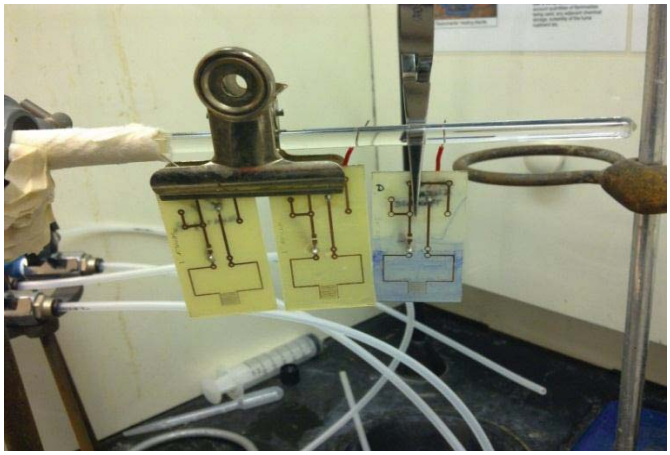

Figure 5.16: Drying sensors under nitrogen flow; FR4 sensors

5.4 Conclusion

FR4 sensors with 1_5 configuration were tested with different coating materials. FR4 sensors were chosen since they were easily fabricated at Massey University fabrication laboratory. Different coating materials with different coating methods have been discussed. The coatings were observed to be uniformly distributed on the electrodes and covered the whole sensing area of FR4 sensors. The experiment was conducted to study which coating materials bind very well to PmB which will show better response to the endotoxin (LPS) bio-molecules. Different coating techniques give different response on sensing performance. The thickness of coating materials is important to achieve better selectivity of the coated sensors. New type of silicon based interdigital sensors were successfully coated, immobilized and tested as discussed in Chapter 6. In this chapter different thickness coatings will be discussed.

CHAPTER 6

Experimental Investigation with Endotoxins

6.1 Introduction

The chapter has discussed on the selectivity, stability and sensitivity of coated sensors with APTES and immobilization of PmB and their responses to endotoxins. In this chapter, detailed analysis of the sensing results obtained from impedance spectroscopy (IS) method has been presented. Analysis using Principal Component Analysis (PCA) has been used for the analysis. The discussions mainly focused on the new silicon sensors and improved type of these sensors towards endotoxin detection.

6.2 Impedance Spectroscopy Analysis

Impedance Spectroscopy (IS) is a popular analytical tool for analysis of material electrode interface due to the involvement of a simple electrical measurement but can also be used to study many complex material variables such as mass transport, corrosion, chemical reactions, dielectric properties and others [111]. In Chapter 4, the basic IS has been introduced on how data can be presented and plotted. A flow diagram in Figure 6.1 was developed by McDonald[111], depicts a guideline of a general characterization procedure using IS. The flow diagram has been used as a guideline for this work and analysis.

Most of the analysis conducted in the research work involved mixed kinetic and diffusion process. A single time constant dispersion which can be related to constant phase element (CPE) and finite Warburg impedance and other related parameter has been analysed with the help of equivalent circuit. CPE refers to an equivalent electrical circuit component that models the behaviour of a double layer capacitance [238] and is given by;

$$Z_{CPE} = \frac{1}{Q_0(j\omega)^n} \quad \textbf{6.1}$$

where ω is the angular frequency and *j* is the imaginary unit with $Q_0 = 1/|Z|$ at ω = 1 rad/s. The constant phase is always -(90*n)°, for n is $0 \leq n \leq 1$. The case n = 1 describes an ideal capacitor while the case n = 0 describes a pure resistor.

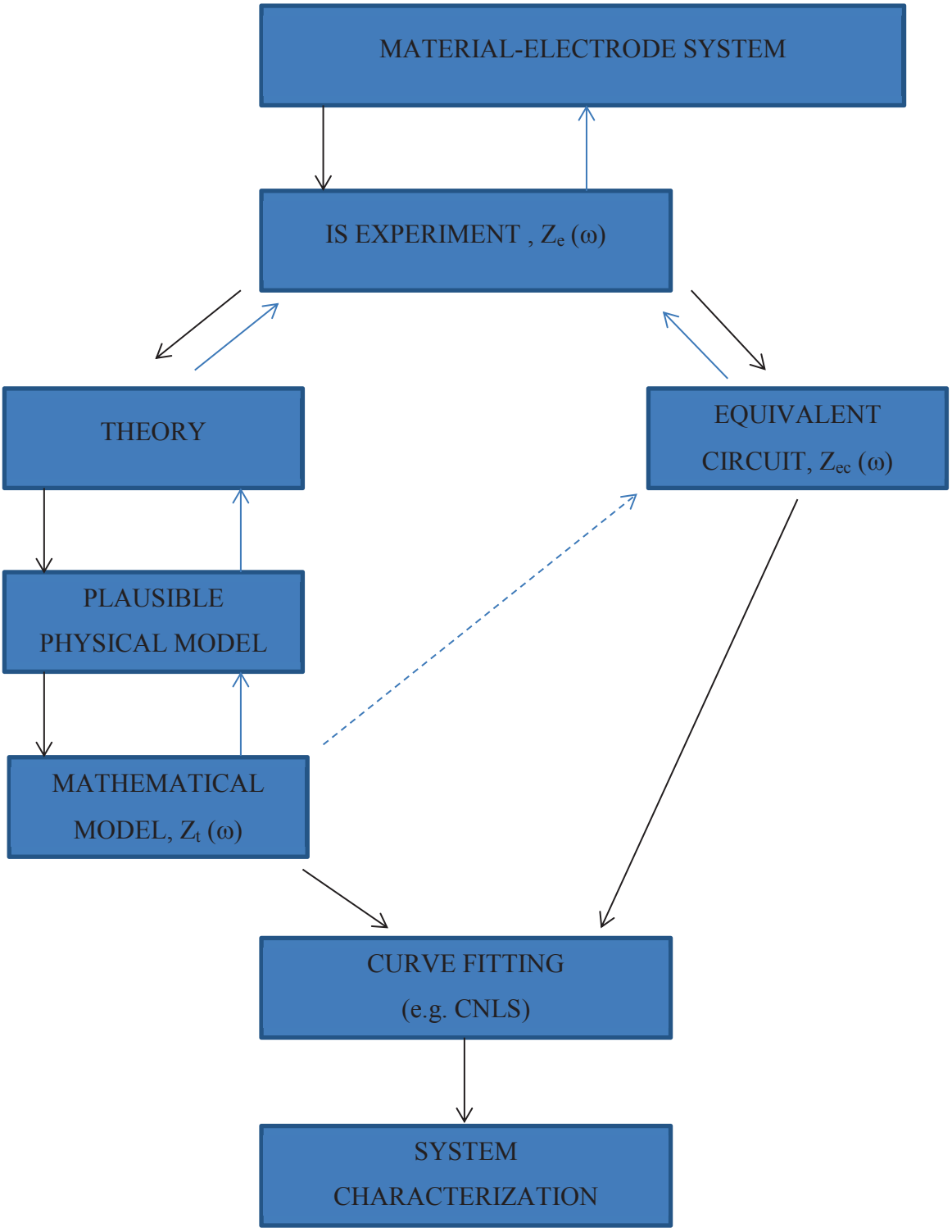

Figure 6.1: Flow diagram for the measurement and characterization of a material-electrode system for IS analysis [111]

One simple and most commonly used cell model is Randles cells model [239]. The Randles cells include double-layer capacitance, C_{dl}, solution resistance, R_s and charge/electron transfer resistance, R_{ct} as shown in Figure 6.2. Based on Randles cells the equation below has been derived [239];

$$Z(\omega) = R_s + \frac{R_{ct}}{1+\omega^2 R_{ct}^2 C_{dl}^2} - \frac{j\omega R_{ct}^2 C_{dl}}{1+\omega^2 R_{ct}^2 C_{dl}^2} \quad \textbf{6.2}$$

where the real part (Z') is given by;

$$Z'(\omega) = R_s + \frac{R_{ct}}{1+\omega^2 R_{ct}^2 C_{dl}^2} \quad \textbf{6.3}$$

and the imaginary part (Z") is given by;

$$Z''(\omega) = -\frac{\omega R_{ct}^2 C_{dl}}{1+\omega^2 R_{ct}^2 C_{dl}^2} \quad \textbf{6.4}$$

The impedance spectra from the experimental results showing electrode-solution interface were related to the mixed kinetic and diffusion process. The equivalent circuit model for the mixed kinetic and diffusion process is shown in Figure 6.2. This model was introduced by Randles in the Discussion of the Faraday Society in 1947 [239] which include Warburg impedance, Z_W as addition element. The Warburg impedance is given by;

$$Z_W = \frac{\sigma_w}{\sqrt{j\omega}} \quad \textbf{6.5}$$

where σ_w is Warburg coefficient. It appears that the characteristic of the Warburg impedance is a straight line with a slope of 45° at lower frequency. This relates to the diffusion control at lower frequency and charge transfer control at higher frequency. The Nyquist plot in Figure 6.3 shows the diagonal line of diffusion process (Warburg impedance) at low frequency and charge transfer at higher frequency as illustrated by a semi-circle curve with single time constant. Figure 6.4 shows the bode plots of absolute impedance, Z, (ohm-cm^2) and also phase angle (degree) with respect to frequency, *f*, in Hz.

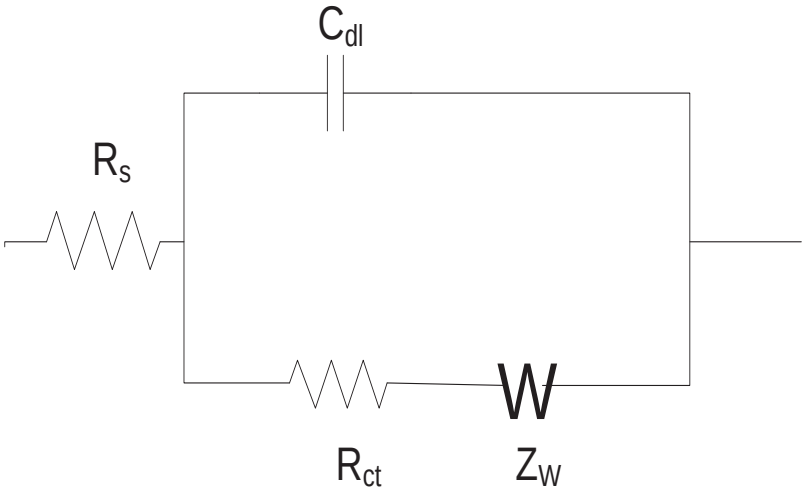

.

Figure 6.2: Equivalent circuit model for mixed kinetic and diffusion [239]

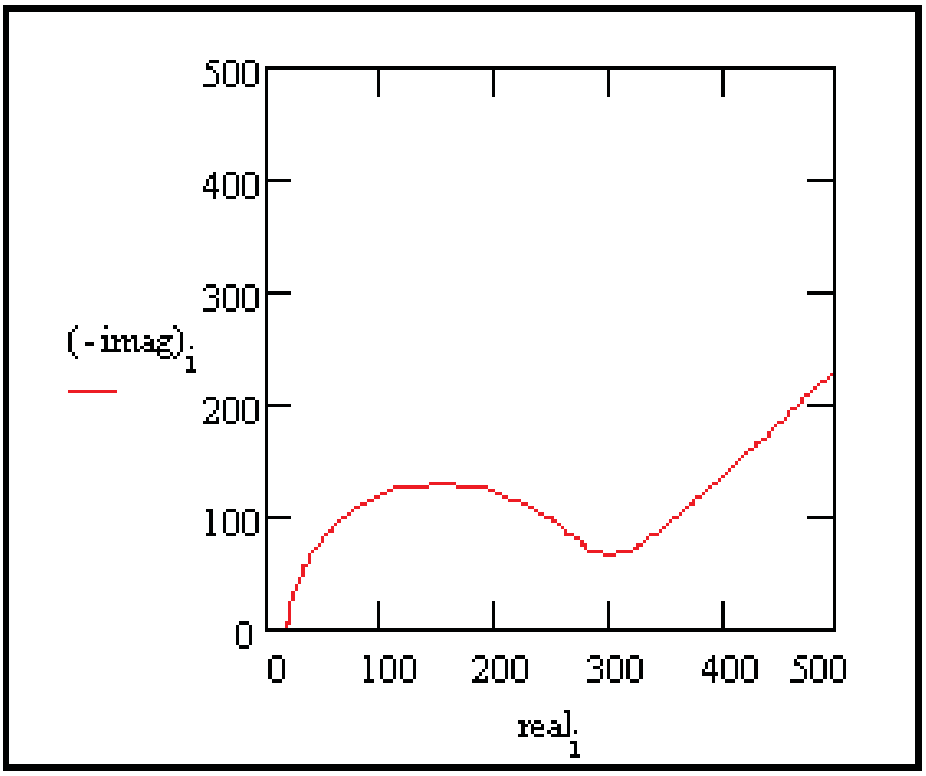

Figure 6.3: The Nyquist plot of complex impedance plane [239]

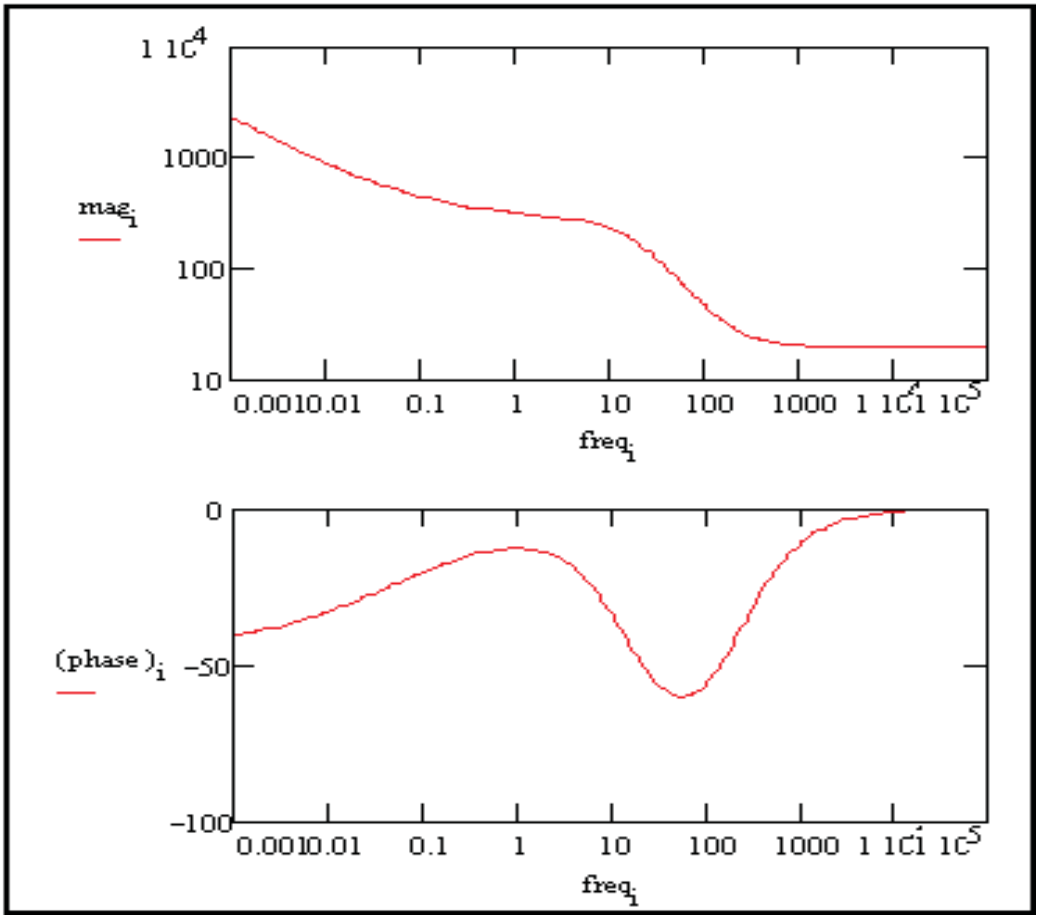

Figure 6.4: The Bode plot of absolute impedance (Z) and phase angle [239]

The complex nonlinear least squares fitting method (CNLS) method has been used widely to fit the experimental impedance spectra for various applications such in as physico-chemical process [240], for corrosion monitoring [241], study of material dielectric properties [242], fuel cell [243] and others [244]. The CNLS fitting method was introduced by Macdonald and Garber in 1977 [245] to fit the impedance spectroscopy data to either equivalent circuits or to a mathematical model. All related parameters can be defined by fitting the model that are simultaneously adjusted to yield an optimum fit to the data [222]. Example of CNLS fitting techniques is shown in Figure 6.5 for corrosion monitoring conducted by Roy Research Group, Physics Department, Clarkson University, Potsdam New York [246]. CNLS also provides estimation of standard deviation values which are important to determine how well the parameters behave with the chosen equivalent circuit or mathematical model. These standard deviations also give important information on which parameters are significant, less significant or not significant to the introduced model. The fitting procedures minimizes the weighted sum of squares of the real and imaginary residuals

as being discussed by Macdonald in [247]. A residual is defined as the difference between a data value at a given frequency and the corresponding value calculated from the model. While the weights used are the inverses of the estimated error variance for a given real data value and that for the corresponding imaginary value. In CNLS fitting, weighting is the most subjective part where it can have crucial effects on the results and thus is decided as prime importance [222]. The details of this subject can be referred to [111, 248]. The CNLS fitting for any impedance spectra is given by;

Consider merit function: $$S = \sum_{j=1}^{N} \frac{1}{W_j} * \left|Z_j - \hat{Z}_j\right|^2 \quad \textbf{6.6}$$

And for relative weighting is given by;

$$S = \sum_{j=1}^{N} \frac{1}{|Z_j|^2} * \left|Z_j - \hat{Z}_j\right|^2 \quad \textbf{6.7}$$

where W_j: Weight factors

Zj: Measured impedance

$\hat{Z}_j$: Modelled impedance

Standard CNLS software can be used for fitting experimental data which is LEVM software by Macdonald[248] and EquivCrt by Boukamp[249].

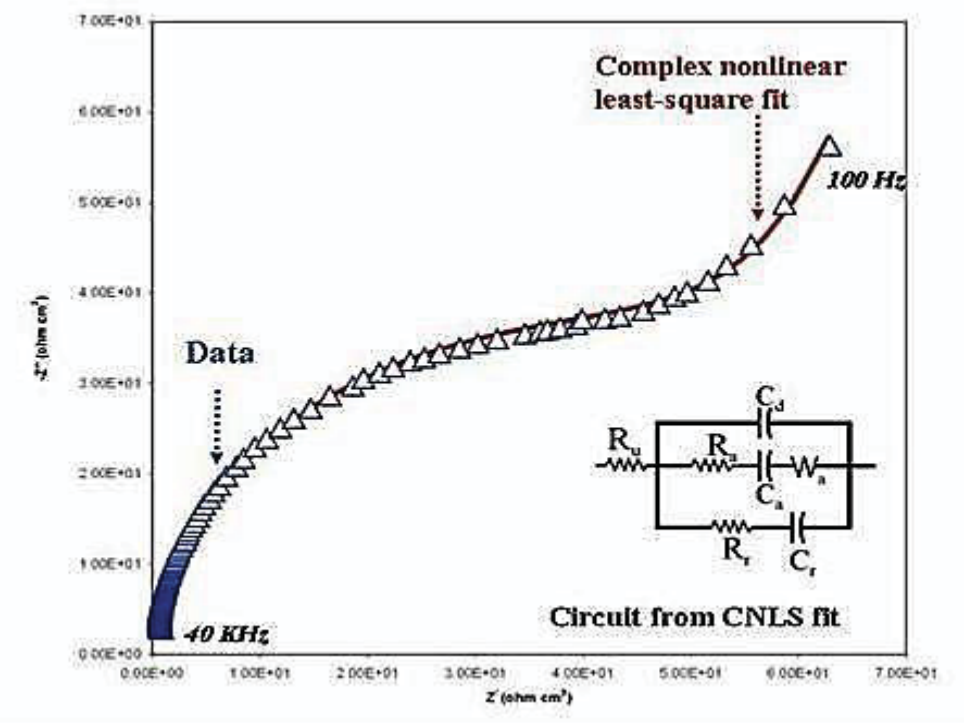

Figure 6.5: CNLS fitting of corrosion monitoring experimental impedance spectra; an example spectrum[246]

6.3 Principal Component Analysis

Principal component analysis (PCA) is a statistical method based on multivariate analysis which was first introduced in 1901 by Pearson [250]. Later on Hotelling in 1933, continued to develop PCA independently [251]. PCA is a technique to reduce the dimensionality of a data set by taking linear combinations of the original variables, to generate the new axes known as principal components [252]. Consider set of data in Figure 6.6 of two variables that have been plotted which having same variance and highly correlated to each other. A vector could be passed through along these clouds of data with a second vector perpendicular to the first vector [253], with both vectors passing through the centroid of the data as shown in Figure 6.6. The coordinates of all data of the data points relative to these perpendicular vectors can be found and replotted as shown in Figure 6.7. It was observed in the new reference plot, the variance is greater along the 1^{st} axis compared to 2^{nd} axis and the spatial relationship of those points is unchanged.

Each linear combination explains the most variance in the data set and each linear combination is uncorrelated with the others. Eigenvalue associated with each principal component explains how much variation in the data set. They are usually expressed as a percentage of the total variation in the data set. Eigenvectors are just the linear combinations of the original variables (in the simple or rotated factor space) that described how variables "contribute" to each factor axis. Therefore, the PCA can be achieved in five steps which are described as;

Step 1: Subtract the mean to produce a data set whose mean in zero

Step 2: Calculate the covariance matrix (or correlation)

Step 3: Calculate the eigenvectors and eigenvalues of the covariance matrix

Step 4: Choose components and form a feature vector

Step 5: Derive the new data

These steps can be achieved by using any statistical software that utilized the PCA tools as given in the sample program Figure 6.8. The program was run using Statistical Analysis System software (SAS 9.2) [254].

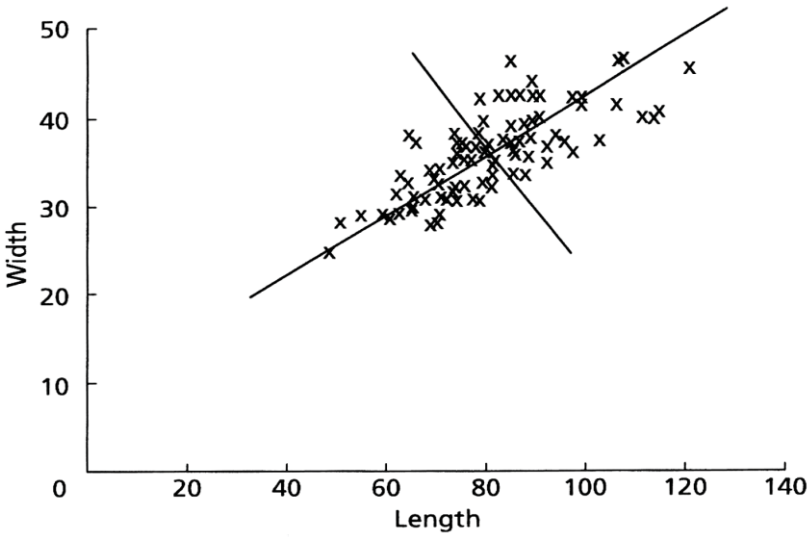

Figure 6.6: Sample data plotted of two variables (source: figure taken from Swan et.al.[255])

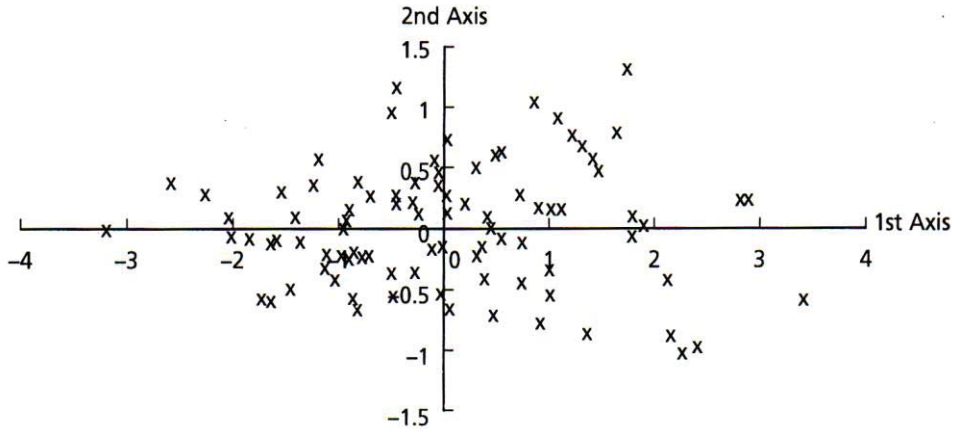

Figure 6.7: Data replotted on new axis (source: figure taken from Swan et.al.[255])

PCA has been used for sensor analysis and also in impedance spectroscopy data classification. PCA was used for sensor validation in structural health monitoring; to perform detection, isolation and reconstruction of a faulty sensor [256]. Different type of citrus juices can be differentiated using PCA and this is based on the sensing signals from electronic nose [257]. In impedance spectroscopy the PCA has been used to minimize dimensionality of data by eliminating redundancy without losing any information content and without a need for any physical knowledge about the investigated impedance [258]. PCA was applied to multiple impedance measurements to study the coating system on metals. It was found out that the PCA able to indicate poor samples and show the cause of the poor coating behaviour [259]. PCA also has

been used to distinguish samples in natural water that has been polluted with phenolic compound. PCA plots can successfully differentiate between Milli-Q water and different phenol compound of different concentrations [260]. Impedance measurement has been carried out using electronic tongue to detect endotoxin and other microbiological contaminants in water for haemodialysis and intravenous infusion. The data interpretation was done using Principal Component Analysis [261].

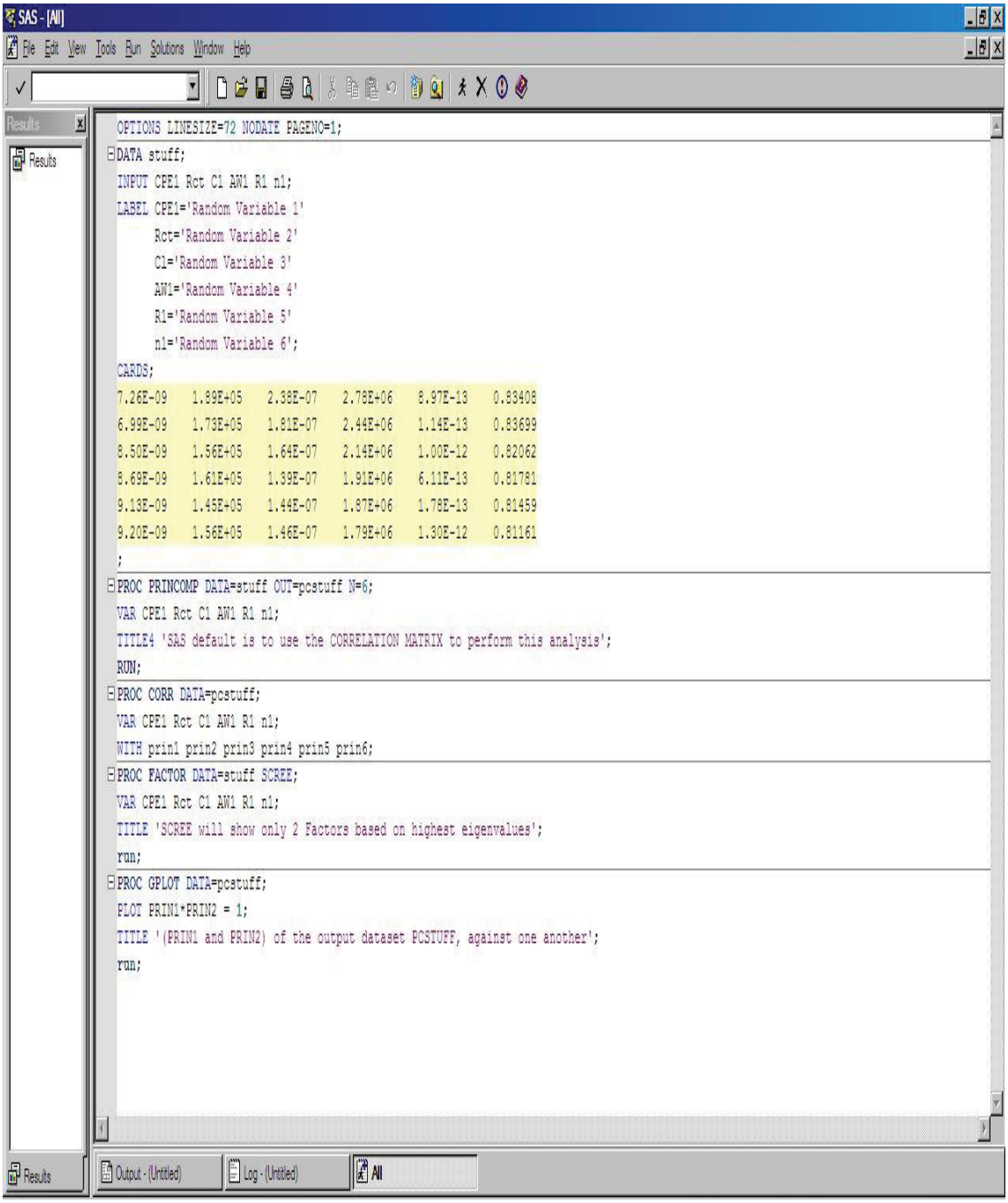

Figure 6.8: Sample program of PCA using SAS 9.2 application software

6.4 Analysis on Endotoxin

6.4.1 Coated FR4 Sensors (1_5 configuration)

Experiments were conducted to evaluate the response of endotoxin or Lipopolysaccharides (LPS) from LPS O111:B4. The LPS was purchased from Sigma-Aldrich. The LPS were extracted using phenol extraction which contains less than 3% of protein [226]. Different concentrations of LPS O111:B4 in the range of 0.1 μg/ml to 1000 μg/ml were prepared for the experiments. The pH of each solution was measured using pH meter model 420A (Orion Research Inc.) with the new pHoenix Tuff Tip® Combination pH electrode model 5733534-003B. It was observed that the pH reading of Control (MilliQ) was 6.69 and pH of LPS O111:B4 solution was around 6.80. Impedance measurements were taken immediately after sample preparations.

The configuration of the electrode structure chosen was 1_5 configuration (five negative electrodes between two positive electrodes) as already discussed in Chapter 4. 1_5 configuration was selected since it has better sensing performance and the analysis of this configuration was reported in [227]. The sensors have been coated with different coating materials as described in Chapter 5. Coating A is a carboxyl-functional polymer of electrospun membrane; Coating B is also carboxyl-functional polymer but was prepared using spin coating method. Coating C is a pre-cursor silica functionalized with APTES and Coating D is pre-cursor silica functionalized with Thionine. The impedance characteristics of the coated sensors are shown in Figure 6.9. Figure 6.9(a) shows the Nyquist plot of all coated sensors with respect to air (without test sample), where it can be seen that impedance characteristics of each sensor have changed due to the presence of PmB molecules on the sensor layer. Figure 6.9(b)-(d) show the Nyquist plot of coated sensors with material B, C and D for different concentrations of LPS. The response of the sensor with coating A was not significant for analysis therefore it will not be discussed further in the work. The impedance measurement of the sensor with coating A was inconsistent for three replications. It was found that the thickness layer of the coating A was easily degraded after immobilization process. The PmB molecules failed to bind to the coating material A, therefore it was decided that coating material A was not appropriate for this experiment. The results from the impedance spectra (Figure 6.9) can be modelled using the Randles and Ershler equivalent circuit to investigate the electrode-solution interface. There are two main processes that can be analysed from the

results: the diffusion-limited process and the charge transfer process, which can both be represented by double-layer capacitance, C_{dl}, solution resistance, R_s charge/electron transfer resistance, R_{ct} and Warburg impedance, Z_w. The equation in 6.2 has been used to represent the impedance measurements of the LPS solutions. The Nyquist plot shows a semi-circular region followed with a straight line at different frequency ranges. The semi-circular region occurs at higher frequency ranges to represent the charge transfer process, while a straight line at lower frequency ranges corresponds to a diffusion-limited process [262]. The results of the Nyquist plot in Figure 6.9 (b)-(d) showing only sensors coated with C and D follow these characteristics at low concentrations of LPS (0.1 µg/ml – 10 µg/ml). This is because, for the case of very fast charge/electron transfer process, the impedance spectra only shows the linear part, while a very slow charge/electron transfer process is indicated by a large semi-circular region.

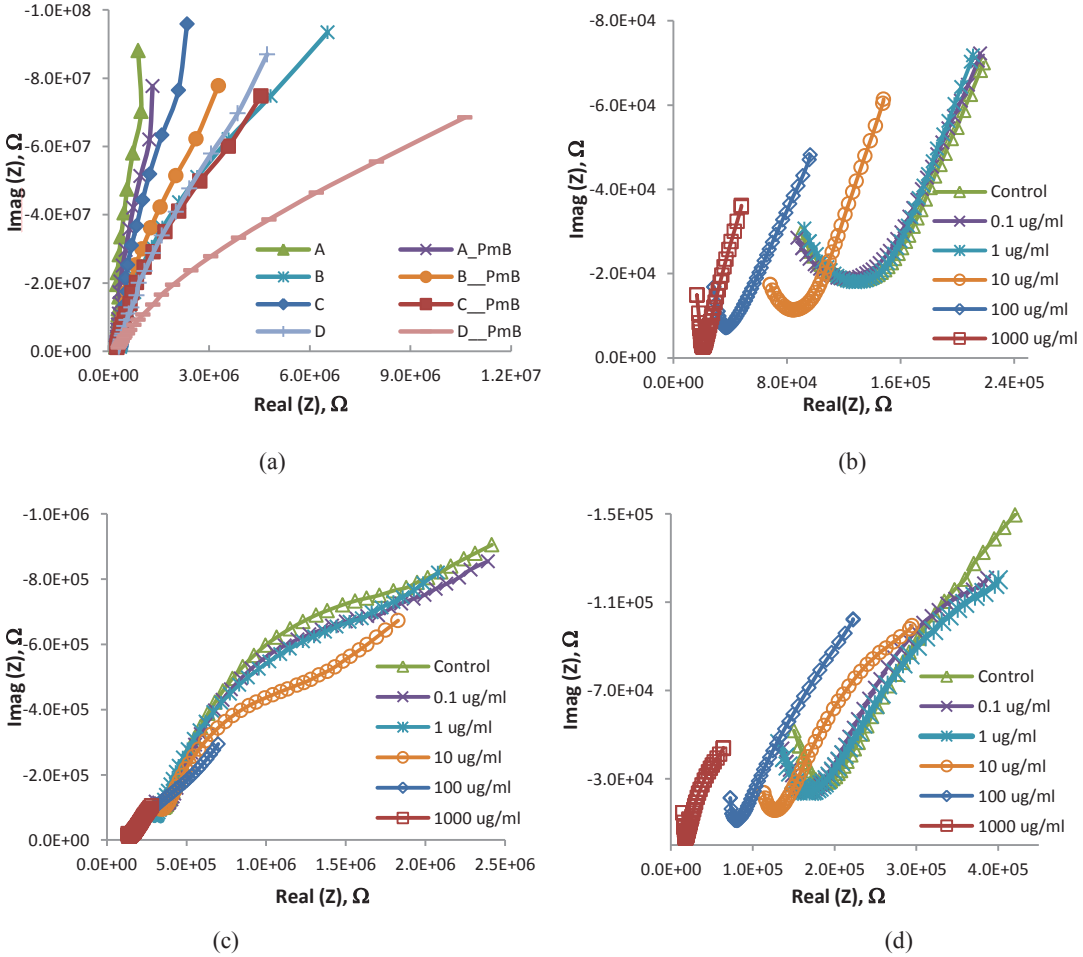

Figure 6.9: The Nyquist plot showing impedance characteristics of coated sensors for (a) Before and after PmB immobilization with respect to air (b) Coating B with LPS at different concentrations (c) Coating C with LPS at different concentrations and (d) Coating D with LPS at different concentrations.

[A: Sensor coated with Carboxyl-Polymer (Electro-Spinning) C: Sensor coated with APTES (Dip-Coating)]

[B: Sensor coated with Carboxyl-Polymer (Spin Coating) D: Sensor coated with Thionine (Dip-Coating)]

These results indicate that the immobilized PmB on coating C and D has shown better bio-affinity events that delay the electron transfer to the electrodes due to the binding of large biomolecules of LPS on the PmB surface. Sensitivity measurement at 1 kHz was chosen since at this particular frequency the change in impedance and phase angle are significantly high for different concentrations of LPS. The sensitivity with respect to different concentrations of LPS is shown in Figure 6.10, and the sensitivity (%) is given by;

$$\%\ Sensitivity = \frac{I_{LPS} - I_{Control}}{I_{Control}} * 100\% \qquad \textbf{6.8}$$

where I_{LPS} is the LPS current at 1 kHz, and $I_{Control}$ is the current of the Control solution at 1 kHz.

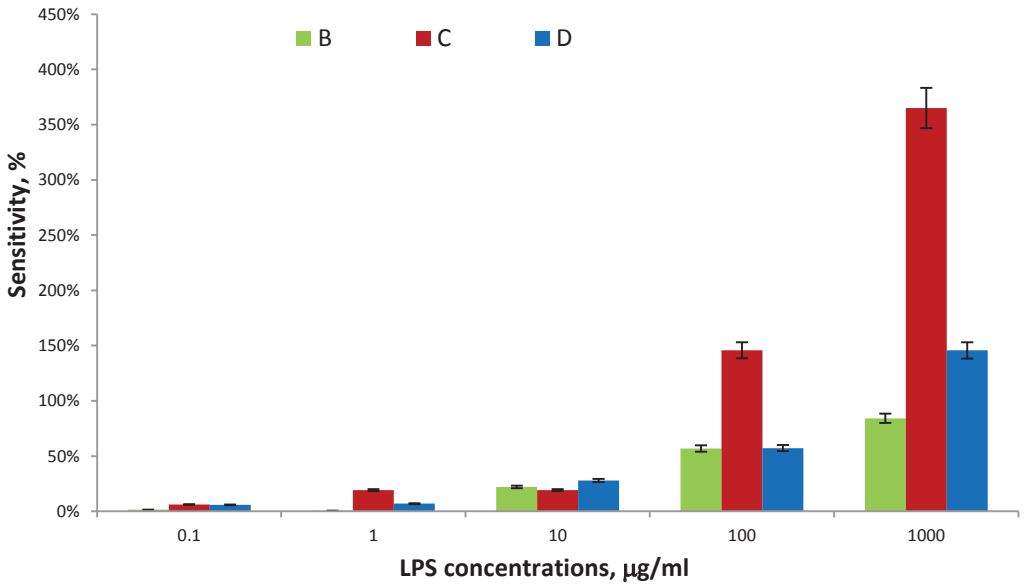

Figure 6.10: The sensitivity of sensing signal with different concentrations of LPS at 1 kHz for coatings B, C and D

Sensor coated with C has been observed to have better sensitivity measurements for different concentrations of LPS. Figure 6.11 shows the Bode plot of impedance, Z, and phase measurement for coated sensor C with different concentrations of LPS. The impedance and phase angle were observed to have a significant change due to the presence of different bio-molecules of LPS on the PmB surface.

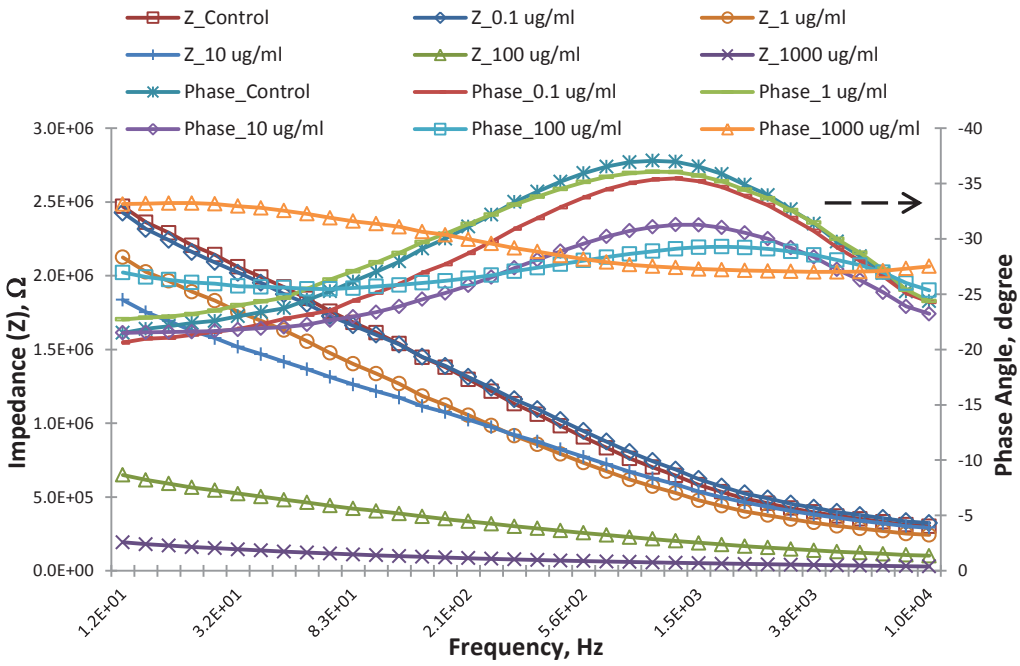

Figure 6.11: The Bode plot showing impedance (Z) and phase angle of coated sensor C (APTES) for different LPS concentrations

These results can be further analysed by using PCA for data classification. The empirical impedance data can be analysed using a simple constant phase-element (CPE) model, as shown in Figure 6.12. The CPE model illustrates the diffusion and charge transfer processes of coated sensors with LPS. The equivalent circuit model as shown in Figure 6.12 was based on CPE parameters at low and high frequencies [259]. Since the analysis is based on CPE, it is easier to describe using equation 6.1. Six variables were identified, which are classified into *Yl*, *nl* and *Rl* for low frequency measurement data, and *Yh*, *nh* and *Rh* for high frequency measurement data. The PCA was conducted using SAS software, which is widely used for statistical analysis [254]. The histograms at the lowest concentrations of 0.1 µg/ml were chosen for analysis and are shown in Figure 6.13. Clearly, the percentage of the first two principal components (PC1 and PC2 ≈ 99%) represents the total information reflected by the six parameters. Sensor coated with coating C shows better correlation between principal components. Figure 6.14 shows the PCA plots of all parameters of coated sensor with coating C. It was observed that all parameters are related to each other for control and at lower concentrations of LPS. However, at higher concentrations of LPS the results are not significant. At lower concentrations it follows the model introduced where the parameters were distributed in the same region, however, as the concentrations increased the charge transfer process

became rapid and therefore the model was rendered irrelevant. These results show that the sensors coated with coating C (APTES) and then immobilized with PmB have improved selectivity and better sensing performance with the target bio-molecule of LPS compared to other coated sensors.

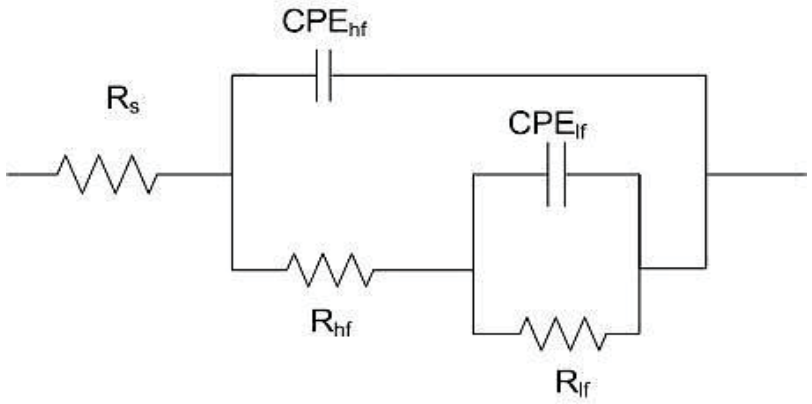

Figure 6.12: The CPE equivalent circuit model for analysis of impedance parameters where, R_s - Solution resistance, CPE_{hf} and CPE_{lf} - CPE represents double layers at high and low frequencies, R_{hf} and R_{lf} - Resistance at high and low frequencies.

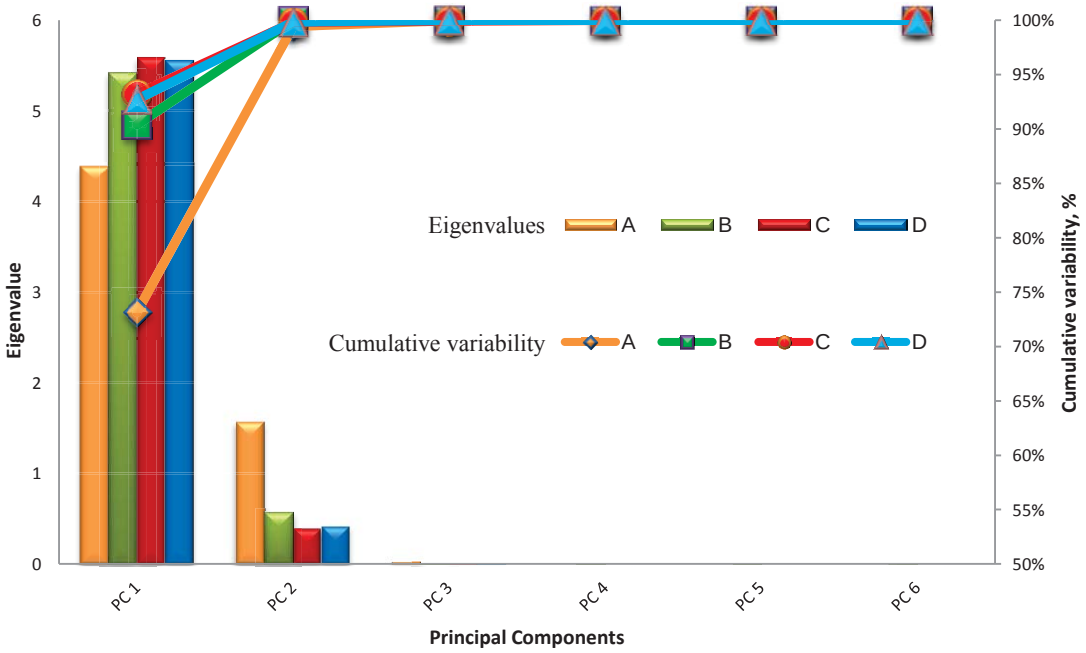

Figure 6.13: Histogram of eigenvalues and cumulative variance of four different Coatings at 0.1 µg/ml

[A: Sensor coated with Carboxyl-Polymer (Electro-Spinning) C: Sensor coated with APTES (Dip-Coating)]

[B: Sensor coated with Carboxyl-Polymer (Spin Coating) D: Sensor coated with Thionine (Dip-Coating)]

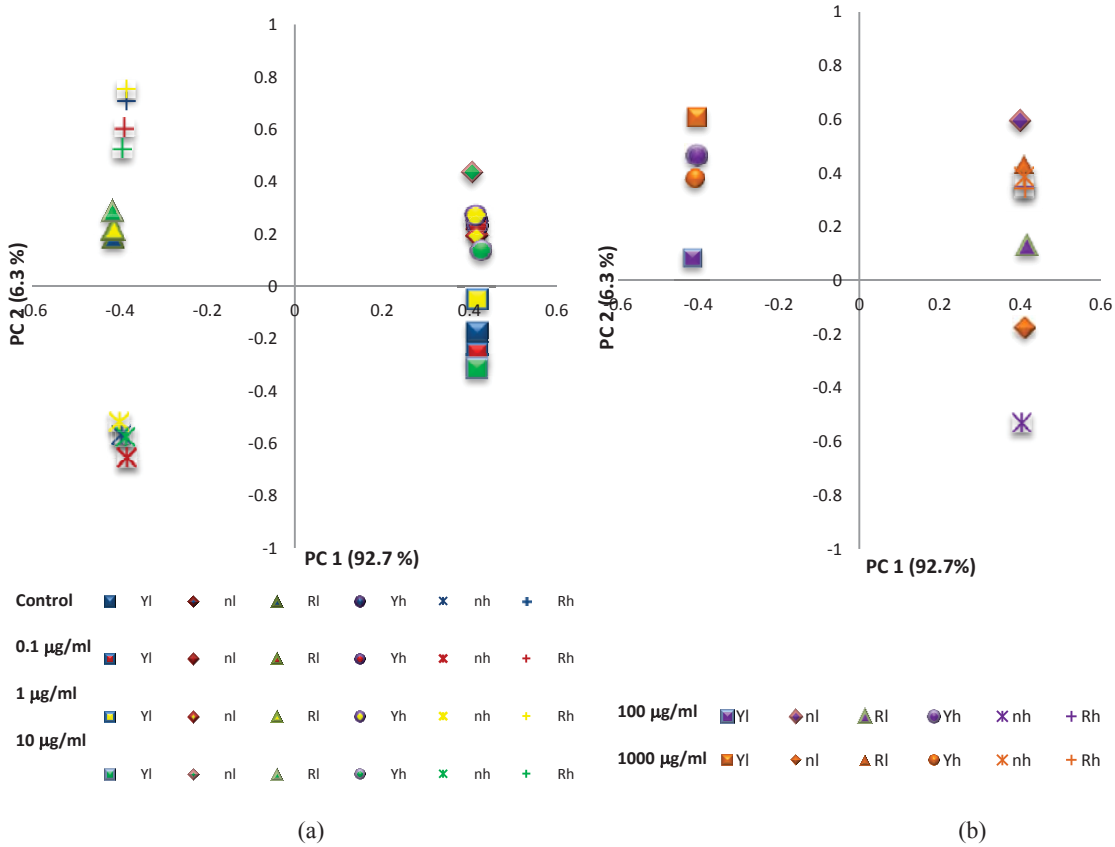

Figure 6.14: PCA plots of the 1st and 2nd principal components of coated sensor C (APTES) at; (a) lower concentration of LPS and control, and (b) higher concentrations of LPS
[Measurement data at low frequency: Yl - CPE constant nl – CPE power Rl – Solution resistance]
[Measurement data at high frequency: Yh – CPE constant nh – CPE power Rh – Solution resistance]

6.4.2 Coated Silicon Sensors (1_5 configuration)

Further experiments were conducted using the same procedures by coating APTES and immobilized PmB on new interdigital sensors fabricated using thin film technology on silicon/silicon dioxide (Si/SiO_2) substrates. The sensor electrodes were fabricated with 1_5 configuration of electrode structure which produced better output signal, low impedance and improved sensitivity. The sensor dimension is 10 mm by 10 mm with sensing area of 2.5 mm by 2.5 mm. The sensor was fabricated to have multiple 1_5 configurations with pitch length of 50 µm and electrode width of 25 µm. Details of the sensors fabrication have been discussed in Chapter 2. Pre-cursor silica was prepared by mixing 16.75 ml of TEOS (Tetraethylorthosilicate) with 20.82 ml Ethanol (EtOH) and 7.43 ml Milli-Q water to make 45 ml solution. A few droplets of hydrochloric acid, HCl (0.1 M) were added to get an acid solution of pH 3 to pH 4. Then, it was proceed

with the dip-coating process as shown in Figure 6.15 and then dried at room temperature in the dry coupling jar. The APTES functionalization is carried after silicate layer was fabricated on sensors. The APTES solution is prepared by mixing 5 % of APTES with 95 % of ethanol v/v. All sensors were dipped in APTES solution for 15 minutes and then dry under the nitrogen flow as shown in Figure 6.16. Then all sensors are baked in vacuum oven at 120°C for 2 hours (Figure 6.17). The thickness of a single layer was observed between 200 nm – 300 nm from the electrode surface. PmB immobilization is then carried out as shown in Figure 6.18.

Figure 6.15: Dip-coating process for Silicon sensors

Figure 6.16: Drying process under nitrogen flow

Figure 6.17: Vacuum oven at 120° C for 2 hours

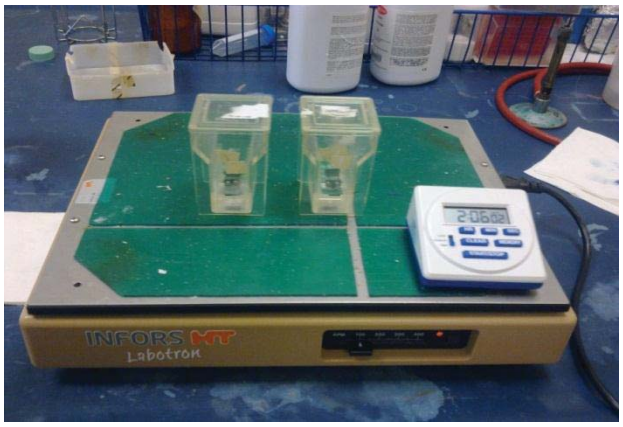

Figure 6.18: PmB immobilization process

Scanning electron microscope (SEM) has been used to take images of bare electrodes, APTES-coated electrodes and PmB molecules immobilized electrodes. A SEM image of bare electrode before coating process is shown in Figure 6.19. Figure 6.20 shows the SEM images of APTES film before and after PmB molecules immobilized on sensor electrode. The coating appears to crack at certain places which is due to improper dipping (lifting speed too fast) and improper drying process or may be because of the effect of slightly high percentage of ethanol in the dipping solution. The crack only happens for a single layer of dip-coating but as the dipping process was repeated for multiple layers the cracks disappears because the silicate filled up the cracks area. The crack does not affect the sensor measurement but precautions were taken to reduce these cracks during dip-coating process. It was observed that the PmB molecules were immobilized on the APTES film and were spread quite uniformly thoughout the electrodes as shown in Figure 6.21 (a). Figure

6.21(b) shows the thickness of a single layer of pre-cursor silica with APTES film which is about 268.3 nm on electrode surface.

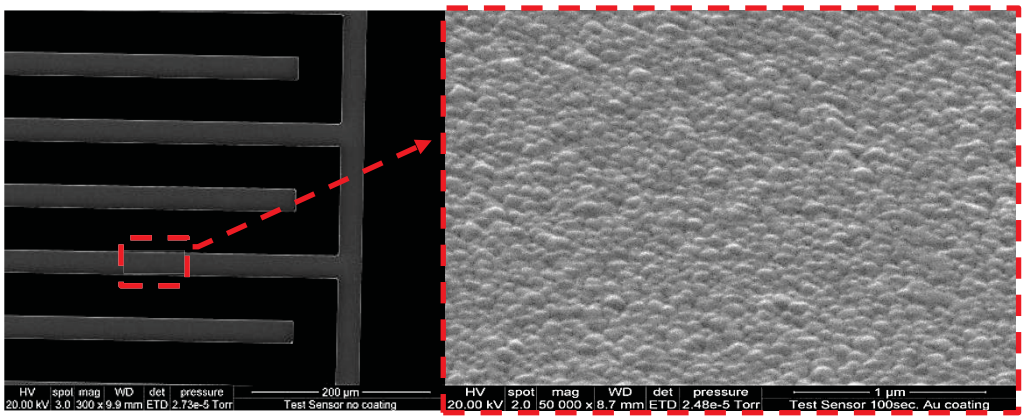

Figure 6.19: SEM image of bare electrode

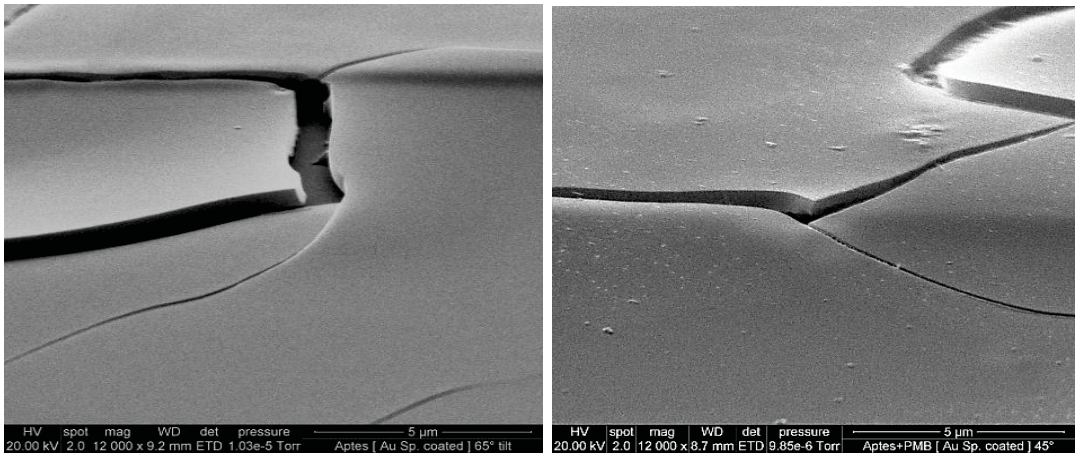

Figure 6.20: SEM images, showing APTES film before and after PmB immobilization

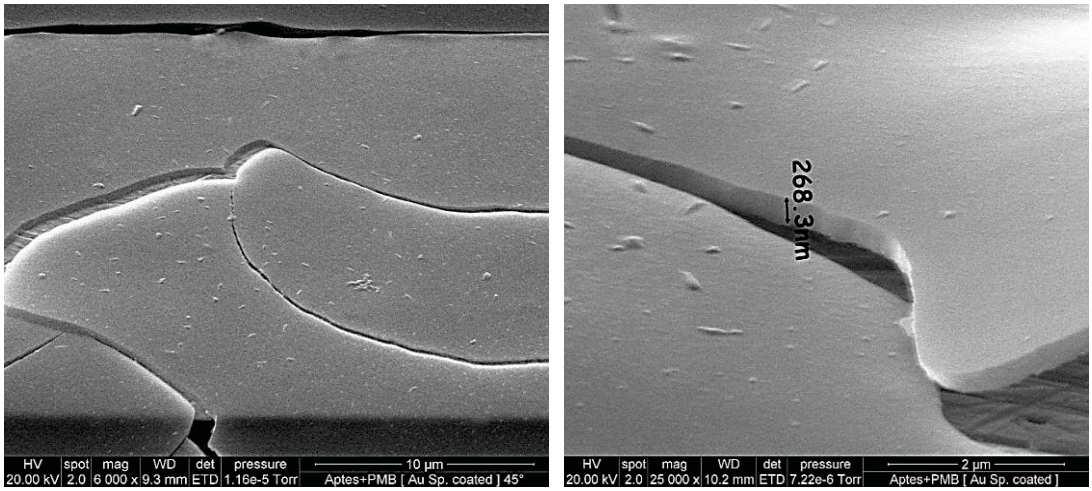

(a) (b)

Figure 6.21: (a) SEM images, showing PmB molecules on sensors and (b) SEM images, coating thickness of a single layer of dip-coating APTES

The sensors were tested with LPS O111:B4 of concentrations between 0.1 μg/ml to 1000 μg/ml. The characteristic impedance changed drastically as the concentrations of LPS increased as shown in Figure 6.22. The Nyquist plot in Figure 6.22 shows the impedance spectra at different concentrations of LPS, which describes the diffusion-limited process and the charge transfer-limited process. At low frequencies (12 Hz -100 Hz) the Nyquist plot shows a diagonal line with a phase angle close to 45 degrees relating to the diffusion process and Warburg impedance, Z_w. The charge transfer process occurs at frequencies above 150 Hz and this is related to charge transfer resistance, R_{ct}. This happens when electrons enter the electrode and electrode ions (metal ions) diffuse into the electrolyte. The double layer capacitance exists on the interface between the electrodes and the LPS solution. The separation between charges in the electrodes and ion charges of the solution is very small. The additional parameter of adsorption capacitance, C_{ad} was introduced since there is a significant effect of this parameter due to the fabricated sensor electrodes being sputtered with gold [263]. Since the LPS binds to the PmB molecules on the coated electrode surface, the adsorption of LPS molecules on PmB molecules create the adsorption capacitance. The Bode plots in Figure 6.23 show the total impedance, phase measurements, and real and imaginary parts of the impedance spectra for different concentrations. The parameters were estimated using complex non-linear least squares (CNLS) fitting method to fit the measured impedance spectra. The relevant equivalent circuit model is shown in Figure 6.24. The total impedance, $Z(\omega)$ is given by [263];

$$Z(\omega) = R_s + \frac{1}{j\omega C_{dl} + \frac{1}{R_{ct} + \frac{\sigma_W}{\sqrt{j\omega}} + \frac{1}{j\omega C_{ad}}}} \qquad \textbf{6.4}$$

Where Warburg impedance; $Z_W = \frac{\sigma_w}{\sqrt{j\omega}}$, σ_w is Warburg coefficient and j is the imaginary unit.

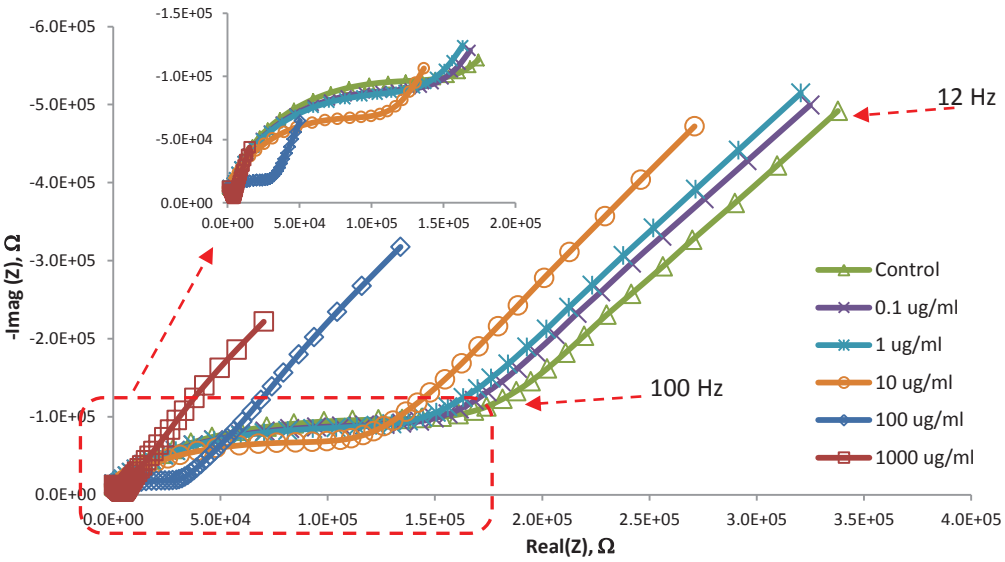

Figure 6.22: The Nyquist plot showing results of coated silicon based interdigital sensor with different LPS concentrations. The plot shows diffusion limited process at low frequency (12 Hz – 100 Hz) and charge transfer process at frequency above 150 Hz.

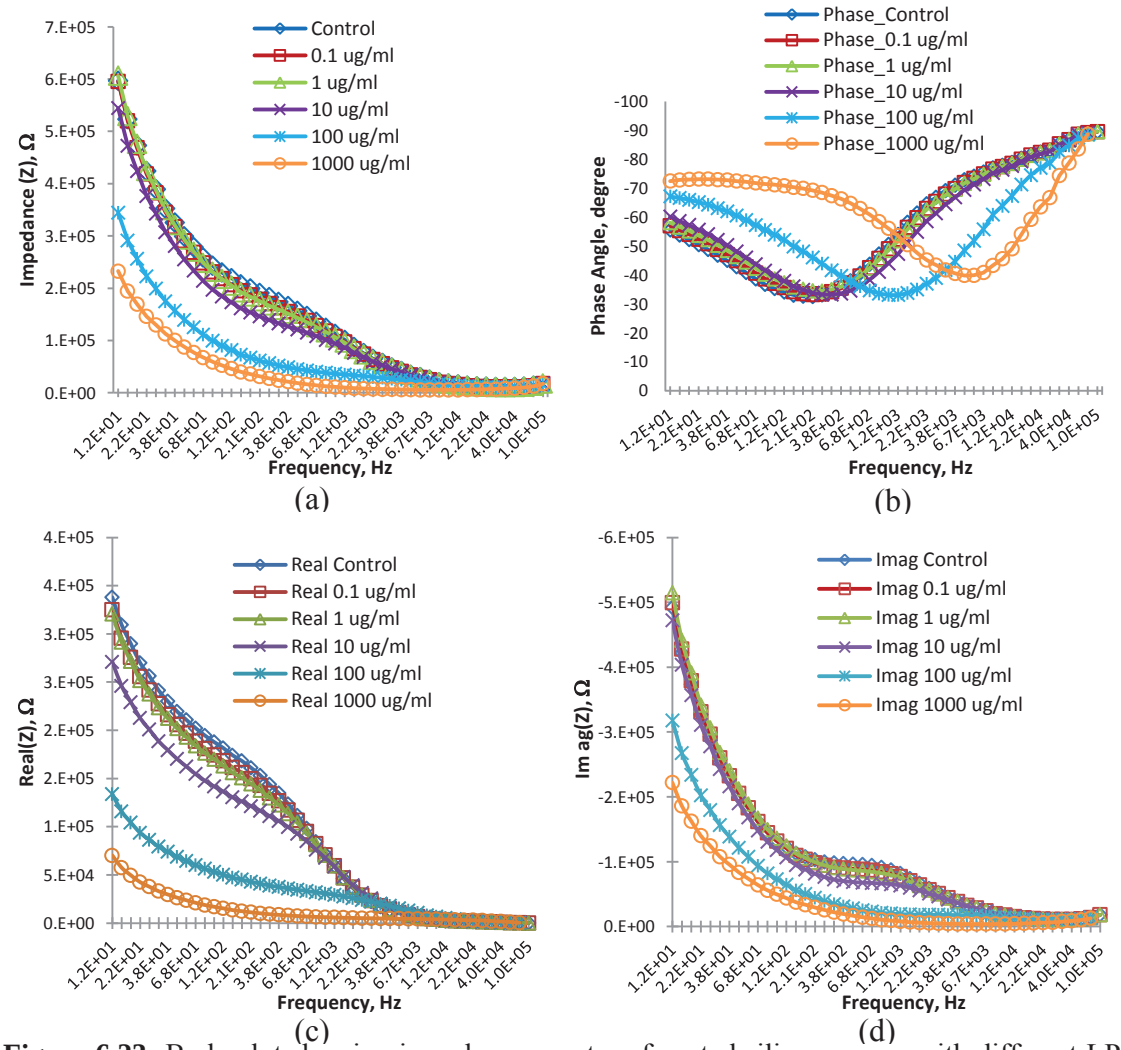

Figure 6.23: Bode plot showing impedance spectra of coated silicon sensor with different LPS concentrations; (a) Impedance (b) Phase Angle (c) Real part and (d) Imaginary part.

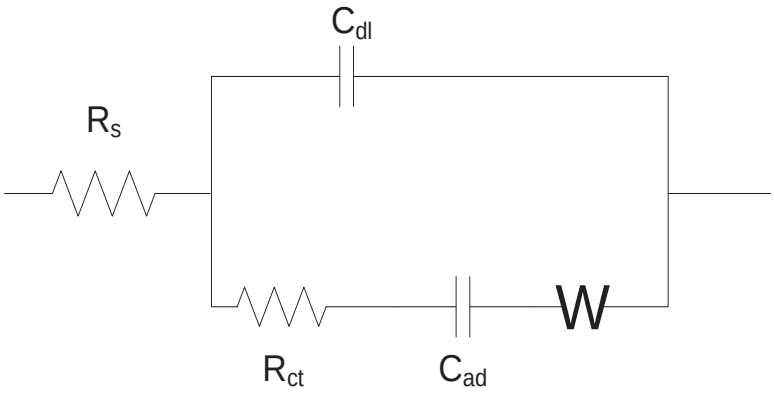

Figure 6.24: The equivalent circuit model showing mixed kinetics and diffusion process of impedance parameters of R_s – solution resistance, C_{dl} – double layer capacitance/constant phase element, R_{ct} – charge transfer resistance, C_{ad} – adsorption capacitance and W – Warburg impedance (Z_w).

Amplitude weighting of real and imaginary part has been used. Consider N number of points and M number of parameters, where ω is the angular frequency, $P_1 \ldots P_M$ are the parameters and amplitude weighting of residuals, r, given by [264];

$$r_{amplitude}(\omega, P_1 \ldots P_M) = r_i{}^2/(N-M) \quad \textbf{6.5}$$

and sum of squares of residuals given by;

$$S = \sum_{i=1}^{N} r_i{}^2 = \sum_{i=1}^{N} \frac{\left(Z'_{iexpt} - Z'_{ical}\right)^2 + \left(Z''_{iexpt} - Z''_{ical}\right)^2}{Z'_i{}^2 + Z''_i{}^2} \quad \textbf{6.6}$$

where

Z'_{iexpt}– Measured Real part

Z'_{ical}– Calculated Real part

Z''_{iexpt}– Measured Imaginary part

Z''_{ical}– Calculated Imaginary part

Z'_i – Amplitude of Real part

Z''_i - Amplitude of Imaginary part

Figure 6.25 shows the results of the calculated data with the experimental data fitted using CNLS method. All estimated parameters for LPS at 0.1 μg/ml – 100 μg/ml are shown in Table 6.1. It was observed that the parameters can be obtained from the

equivalent circuit model introduced and give significant values of estimated parameters with errors less than 5% for concentrations of 0.1 µg/ml – 10 µg/ml. However, as concentration increases (> 100 µg/ml) the fitting function was not significant and the error percentage was high, above 5 %, as shown in the Table 6.1 for parameters C_{dl}, R_{ct} and Z_w. It was observed that the fitting function was adequate for measured impedance spectra and the calculated spectra given r^2 (residual mean squares) in the range of 10^{-4}. The r^2 value should be very small, to indicate very less average deviation between measured and fitted spectra.

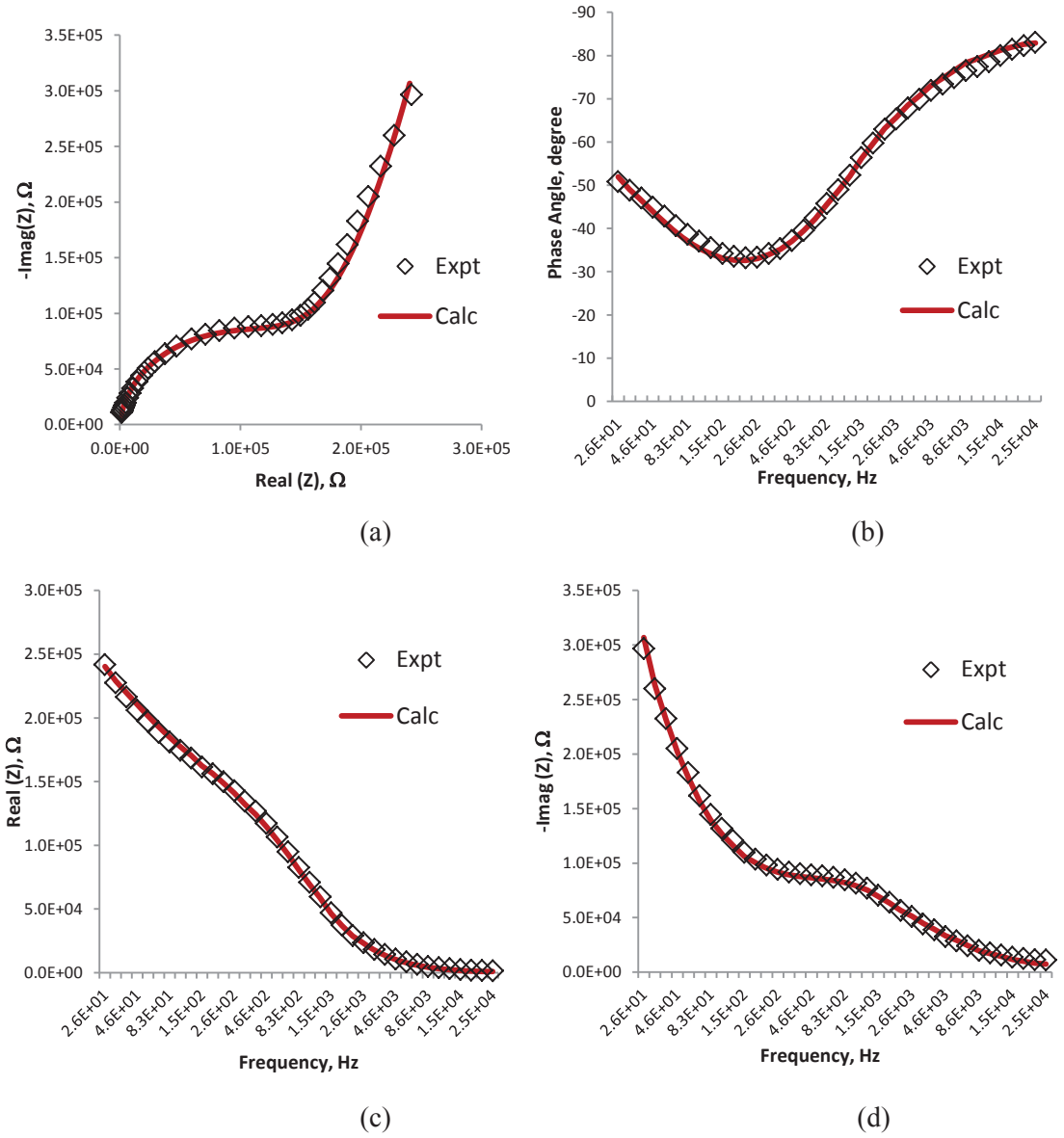

Figure 6.25: Results of curve fitting showing Nyquist plot (a) and Bode plot of LPS O111:B4 concentration of 0.1 µg/ml in the frequency range of 26 Hz – 25 kHz showing (b) the phase angle, (c) and (d) showing real and imaginary parts respectively. Experimental impedance spectra are presented by the squares and the optimization parameters using non-linear least squares method are indicated by solid lines.

Table 6.1: Results of the calculated parameters, percentage of errors and residual mean squares from non-linear least squares fitting for LPS concentrations of 0.1 μg/ml – 100 μg/ml.

Parameter (unit)	LPS Solution							
	0.1 μg/ml		1 μg/ml		10 μg/ml		100 μg/ml	
	Value	Error (%)	Value	Error (%)	Value	Error (%)	Value	Error (%)
C_{ad} (F)	3.61E-08	3.1208	3.47E-08	3.4318	3.76E-08	2.7215	5.49E-08	3.9596
R_s (Ω)	6.60E+02	2.8347	7.20E+02	3.4286	8.00E+01	2.6131	1.32E+03	2.441
R_{ct} (Ω)	1.34E+05	3.2511	1.29E+05	3.9552	9.97E+04	4.0774	2.42E+04	14.422
Z_w (Ω)	1.72E+06	3.4892	1.78E+06	3.9593	1.57E+06	3.6884	9.52E+05	5.4408
C_{dl} (F)	9.55E-10	3.1098	1.01E-09	3.6404	9.03E-10	3.7977	7.07E-10	18.971
r^2	4.851E-04		5.859E-04		4.395E-04		6.782E-04	

Principal component analysis (PCA) was used to analyse these parameters in order to study how these parameters were related. Results of three replications of each data set for different concentrations were analysed. Their parameters were clustered based on the principal components derived from PCA. It is shown in Figure 6.26 that the percentage of variance of five principal components are 88.05%, 11.75%, 0.181%, 0.0175% and 0.0015%. The cumulative percentage of principal components one and two (PC 1 and PC 2) is 99.8% which indicated that these two principal components can be used to represent those calculated impedance parameters. PC 1 and PC 2 components were plotted to observe how these parameters were related at different concentrations of LPS. Figure 6.27 shows the PCA plots of the first two principal components to indicate calculated impedance parameters at different concentrations. As shown in Figure 6.27 (a) at lower concentrations the parameters were related and have high correlation values, but as the concentration of LPS increases (Figure 6.27 (b)) the parameters behave differently, which is not significant for analysis. This is because at high concentrations the parameters showing at different region which indicates the charge transfer is too fast where the coating of PmB failed to bind to LPS and did not retard the electron flow to the electrodes. Figure 6.28 shows the PCA plot of the two principal components for concentrations of 0.1 μg/ml – 100 μg/ml for three replications. This result has shown that those related parameters can be used to show different electrochemical processes. Processes involving electrodes and charges are related to the electrical double layer (C_{dl}), diffusion (Z_w) and charge transfer (R_{ct}) is shown in the 1st region. The 2nd region of the PCA plots shows the adsorption process which involves

LPS molecules bound to PmB molecules on coated electrode surfaces that create adsorption capacitance, C_{ad}. Finally, the 3rd region shows the solution resistance, R_s of the LPS solution. These new improved interdigital sensors have shown better results compared to the initial sensors fabricated on FR4.

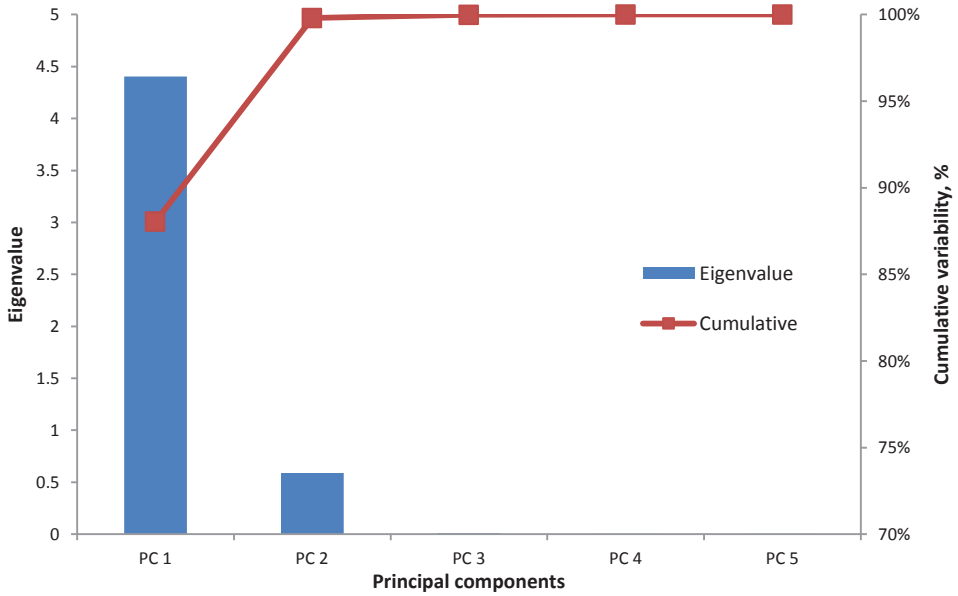

Figure 6.26: Histogram of eigenvalues and cumulative variance of the five principal components

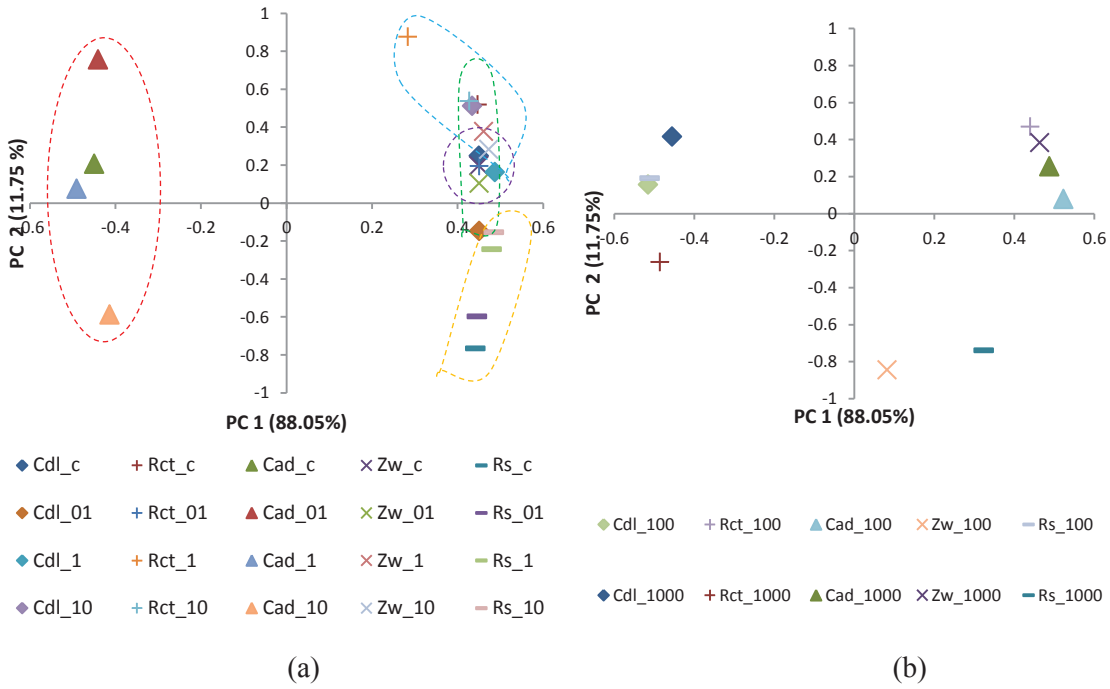

(a) (b)

Figure 6.27: PCA plot for each calculated parameters at different concentrations of LPS (a) Control and LPS concentrations between 0.1 µg/ml – 10 µg/ml (b) LPS concentrations between 100 µg/ml – 1000 µg/ml

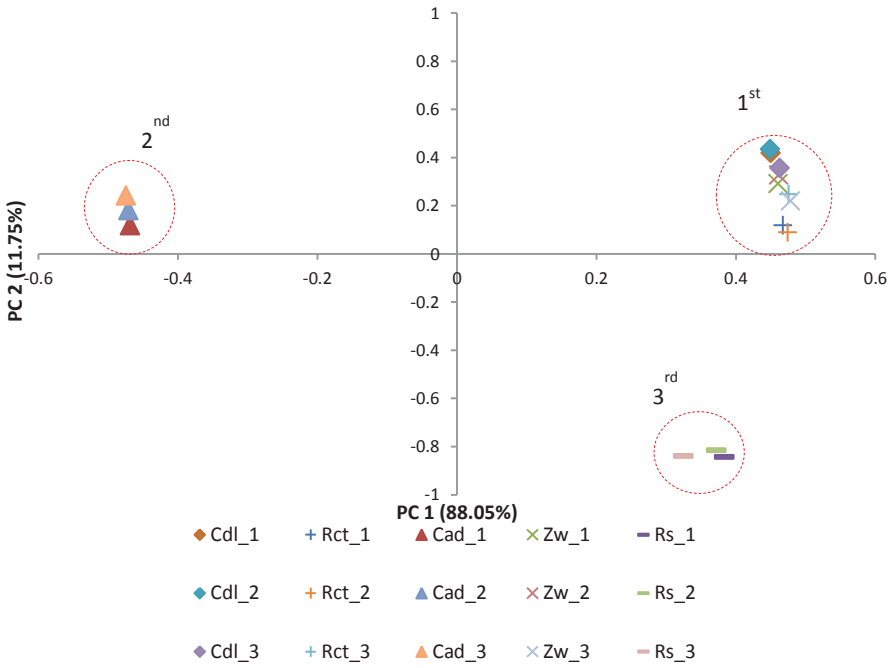

Figure 6.28: PCA plot for measurement of three replications of LPS at different concentrations (0.1 μg/ml – 100 μg/ml) for data classification of calculated parameters

6.5 Validation of Sensor Measurement using Standard Chromogenic LAL Endotoxin Test Kit

This experiment was conducted to verify the sensitivity of novel interdigital sensors using a standard chromogenic endotoxin test kit. Limulus Amebocyte Lysate (LAL) was discovered by Dr. Frederik Bang in 1950 [51]. The first trial of LAL assay for endotoxin detection was reported by Levin and Bang in 1964 [265]. They have developed a sensitive assay for endotoxin detection using material lysed from Limulus amebocytes [266]. Since then the LAL assay kit has been used widely as a standard procedure to identify endotoxins in food or non-food samples. A ToxinSensor™ Chromogenic LAL Endotoxin Assay Kit was purchased from GenScript USA Inc. The standard endotoxin purchased has lower level of endotoxin unit (EU) per milliliter (1 ng/ml = 10 EU/ml). This test kit has been widely used as a standard to quantify endotoxin in a solution. The assay kit is designed to be a quantitative in vitro end-point endotoxin test for human and animal parental drugs, biological products and medical devices. This method utilizes a modified Limulus Amebocyte Lysate (LAL) and a synthetic colour producing substrate to detect endotoxin chromogenically. The kit is

able to detect a minimum endotoxin limit of 0.005 EU/ml and a measurable concentration range of 0.005 EU/ml to 1 EU/ml. The details of the description on the assay kit, preparation methods and analysis can be found in GenScript technical manual no. 0354, update date 10112011.

6.5.1 Description of The Assay Kit

The ToxinSensor™ Chromogenic LAL Endotoxin Assay Kit (Genscript, USA Inc.) is shown in Figure 6.29 and the kit contents are shown in Table 6.2. The kit was stored in the 4 °C cold room.

Figure 6.29: ToxinSensor™ Chromogenic LAL Endotoxin Assay Kit

Table 6.2: Contents of ToxinSensor™ Chromogenic LAL Endotoxin Assay Kit

Kit Contets	**32 Assays**
Cat. No.	L00350
LAL Reagent Water	2 bottles x 50 ml
Limulus Amebocyte Lysate (LAL)	2 Vials
E.coli Endotoxin Standard	2 Vials
Chromogenic Substrate	2 Vials
Buffer S for Color-stabilizer #1	50 ml
Color-stabilizer #1	2 Vials
Color-stabilizer #2	2 Vials
Color-stabilizer #3	2 Vials
Endotoxin-free tubes	50
Endotoxin-free Tips, 200 µl	1 box (96 tips)
Incubation rack	1

6.5.2 Endotoxin Quantitative Detection Protocol

All testing has been performed in the control laboratory room temperature of 22°C – 25°C and all equipment and products used were endotoxin-free. All specimens or samples to be tested were stored in 4 °C cold room to stop any bacteriological activity and all specimens must be endotoxin-free. The work bench were clean and aseptic techniques were used at all times. The target concentrations for endotoxin test were prepared. Standard endotoxin was dissolved in LAL reagent water and the concentrations were prepared for 0.1 EU/ml, 0.05 EU/ml, 0.025 EU/ml, and 0.01EU/ml. The pH of the sample was between pH 6-8 for good linearity as mentioned by the manual. Table 6.3 shows the target concentrations of endotoxin for testing.

Table 6.3: Required sample preparation for endotoxin test

Sample no.	1	2	3	4
Concentration (EU/ml)	0.1 EU/ml	0.05 EU/ml	0.025 EU/ml	0.01 EU/ml
Concentration (ng/ml)	0.2 ng/ml	0.01 ng/ml	0.005 ng/ml	0.002 ng/ml

6.5.2.1 Reagent Preparation

Limulus Amebocyte Lysate (LAL)

Lysate was reconstituted by adding 1.7 ml of LAL reagent water and swirled gently. The reconstituted lysate can be stored at -20 °C for one week.

Chromogenic Substrate

The chromogenic susbtrate was reconstituted by adding 1.7 ml of LAL reagent water to a concentration of ~2 mM. The substrate solution can be stored in 2°C – 8°C for one month.

Stop Solution (Color stabilizer #1)

Color stabilizer #1 or stop solution was reconstituted by adding 10 ml of buffer S. The solution was stored in in 2°C – 8°C and is stable for one week.

Color Stabilizer #2 and #3

Both color stabilizer #2 and #3 were reconstituted by adding 10 ml of LAL reagent water. Both were stored in 2°C – 8°C and is stable for one week.

Standard Endotoxin Solutions

The potency of the standard endotoxin given was 6 EU. Therefore to make a standard endotoxin of 5 EU/ml, 1.2 ml of LAL reagent water was added to the lyophilized endotoxin standard. The stock solution was vortex for 15 minutes.To make 1 EU/ml standard solution, 0.2 ml of standard endotoxin stock solution was diluted with 0.8 ml of LAL reagent water. The 1 EU/ml standard solutions was used to establish standard curve. The endotoxin concentration range of samples were prepared for 0.01 – 0.1 EU/ml. The recommended concentrated endotoxin solution was 0.1, 0.05, 0.025 and 0.01 EU/ml. The standard curve will have 4 points of concentrated endotoxin solution. Figure 6.30 shows how serial dilution on endotoxin solutions were prepared for the test. Each dilution was mixed thoroughly for 30 seconds with a vortex mixer.

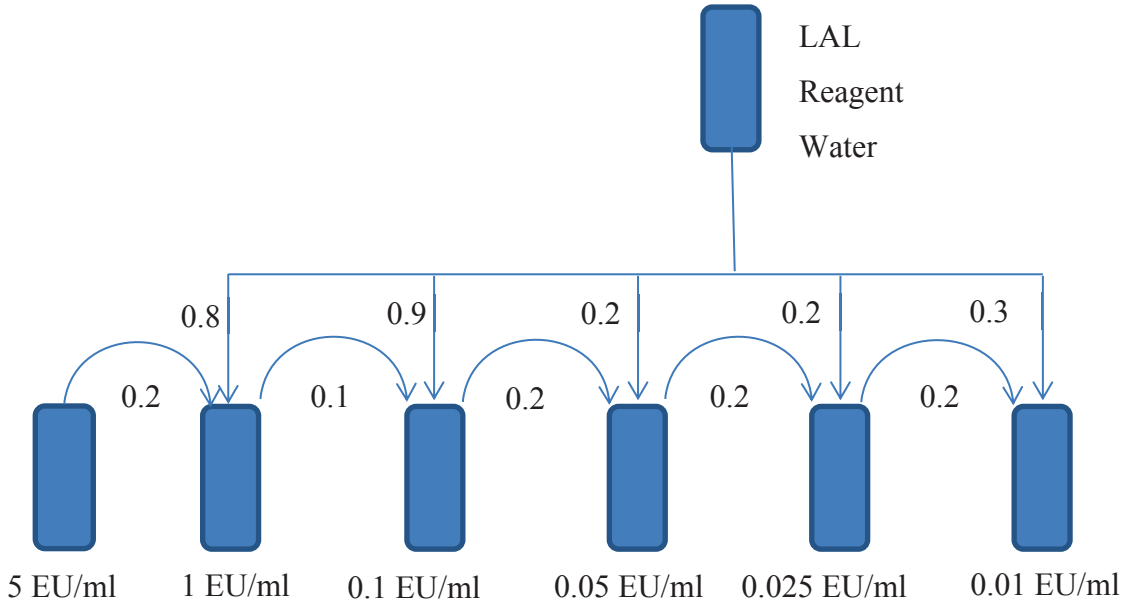

Figure 6.30: Serial dilution of standard endotoxin

6.5.2.2 Test Procedure

The test procedure was performed as follows;

1. These test procedures were conducted in lamina flow chamber to avoid contamination.
2. 100 µl of standards, samples and LAL reagent water were carefully dispensed into different vials and were labelled S1, S2, S3, and S4 for standard endotoxin solutions and LAL reagent water was labelled blank. Bubbles must be avoided when preparing each solution.
3. Each vial was added with 100 µl of reconstituted LAL and swirled gently to mix well. All vials were capped to avoid any contamination.
4. The next step was to incubate all vials at 37°C ± 1°C for 45 minutes.
5. After proper incubation, 100 µl of reconstituted chromogenic substrate was added to each vial. Each vial was swirled gently and the incubated for 6 minutes at 37°C ± 1°C.
6. 500 µl of reconstituted stop solution (colour stabilizer #1) was added to each vial and swirled gently to mix well. Then, 500 µl of colour stabilizer #2 was added to each vial and mixed well and finally 500 µl of colour stabilizer #3 was added to each vial and swirled gently to mix well. Bubbles must be avoided at any process of mixing. Each standard mixture change colour as shown in the Figure 6.31.
7. Spectrophotometer was used to read the absorbance of each reaction at 545 nm with distilled water used as calibration for zero absorbance. Each vial was put into the spectrophotometer and the absorbance value at 545 nm was recorded. The whole procedure can be summarized in Table 6.4.

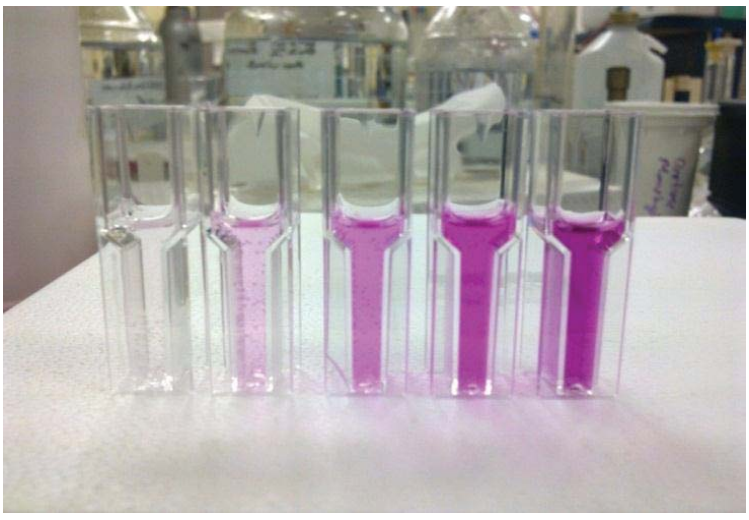

Figure 6.31: Blank solution and standard endotoxins ready for spectrophotometer measurement

Table 6.4: LPS preparation for endotoxin test

Item	Standards	Blank
Test Sample or Standards (ml)	0.1	
LAL Reagent Water (ml)		0.1
LAL (ml)	0.1	0.1
Mix well and incubate at 37°C ± 1°C (min)	45	45
Substrate solution (ml)	0.1	0.1
Mix well and incubate at 37°C ± 1°C (min)	6	6
Stop Solution (Color-stabilizer #1) (ml)	0.5	0.5
Color-stabilizer #2 (ml)	0.5	0.5
Color-stabilizer #3 (ml)	0.5	0.5
Mixed well and read the absorbance at 545 nm		

6.5.2.3 Calculation of Endotoxin Concentration

According to the standard conditions, the absorbance at 545 nm shows a linear relationship with the concentration in range of 0.01 – 0.1 EU/ml. Plots of the absorbance for four standards and a blank are shown in Figure 6.32. On the x-axis the plots corresponding to endotoxin concentration while the normalized absorbance of four standards on the y-axis. A best-fit straight line among these points was drawn and hence determined the endotoxin concentrations of samples graphically. The following data of standard endotoxin are shown in Table 6.5. According to the manual, the absolute value of the coefficient of correlation (r) for the individual mean absorbance of the standard vs. their corresponding endotoxin concentration should be ≥ 0.980. The plots in Figure 6.31 shows that the standard curve of standard endotoxin has high correlation with R^2=0.9821. The result is in line with result from the technical manual.

Table 6.5: Absorbance of Standard Endotoxin at 545 nm

Tube No.	Sample	Absorbance at 545 nm	Δ Absorbance
0	LAL Reagent Water (Blank)	0.036	0.000
1	0.01 EU/ml Standard	0.225	0.188
2	0.025 EU/ml Standard	0.619	0.582
3	0.05 EU/ml Standard	1.193	1.157
4	0.1 EU/ml Standard	1.895	1.859

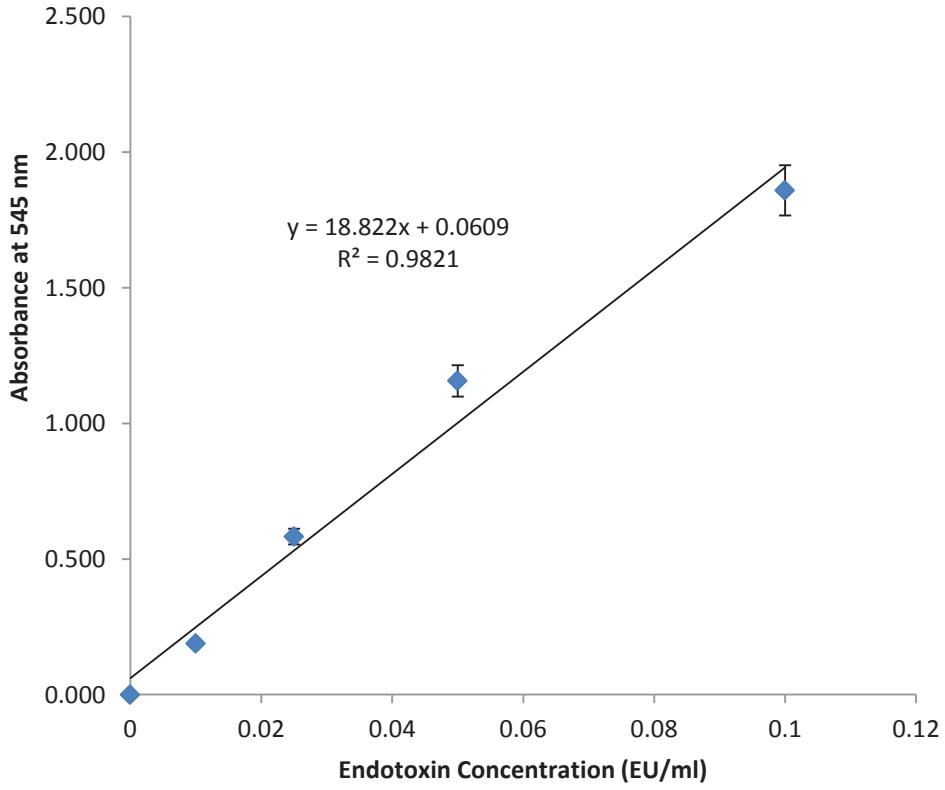

Figure 6.32: Standard curve for the quantification of standard endotoxin in chromogenic assay

6.5.3 Sensitivity Measurement of Novel Sensors

The silicon sensors were coated with 3-layers of pre-cursor silica and APTES. The sensors were immobilized with PmB (1 mg/ml) for 24 hours. Standard endotoxins of 0.01 EU/ml, 0.05 EU/ml and 0.1 EU/ml were analysed. The CNLS fitting was used to fit the impedance spectra data to the equivalent circuit model that has been discussed before. The Nyquist plot of the impedance spectra is shown in Figure 6.33 (a). The Bode plot in Figure 6.33(b) shows the impedance and phase angle of standard endotoxin of different concentrations. The Figure 6.33(c) shows the real and imaginary part of the standard endotoxin at different concentrations. It was observed the sensor is able to access the endotoxin at very low endotoxin limit of 0.01 EU/ml which is equivalent to 1 pg/ml (1 ng/ml = 10 EU/ml). The normalized current sensitivity was calculated for each standard endotoxin using the definition of sensitivity from Equation 6.8. The sensitivity of normalized current for frequency 12 Hz to 18 kHz is shown in Figure 6.33(d). Figure 6.34 shows the percentage of sensitivity at 100 Hz and 1 kHz. These sensors respond very well at frequency 100 Hz compared to their respond at 1 kHz. It can be said that at lower frequency (< 1kHz) the sensor will have better performance.

Complex non-linear least square (CNLS) fitting procedure has been implemented to estimate the parameters based on equivalent circuit model which has been discussed before. Figure 6.35, 6.36 and 6.37 shows the result of CNLS fitting for 0.01 EU/ml, 0.05 EU/ml, and 0.1 EU/ml respectively. Analyses of results have shown that the fitting values for the parameters introduced from the equivalent circuit can be estimated. Table 6.6 shows the parameter obtained from the CNLS fitting. These parameters were plotted against the endotoxin standards to observe their correlations and to study the significant pattern of impedance behaviour.

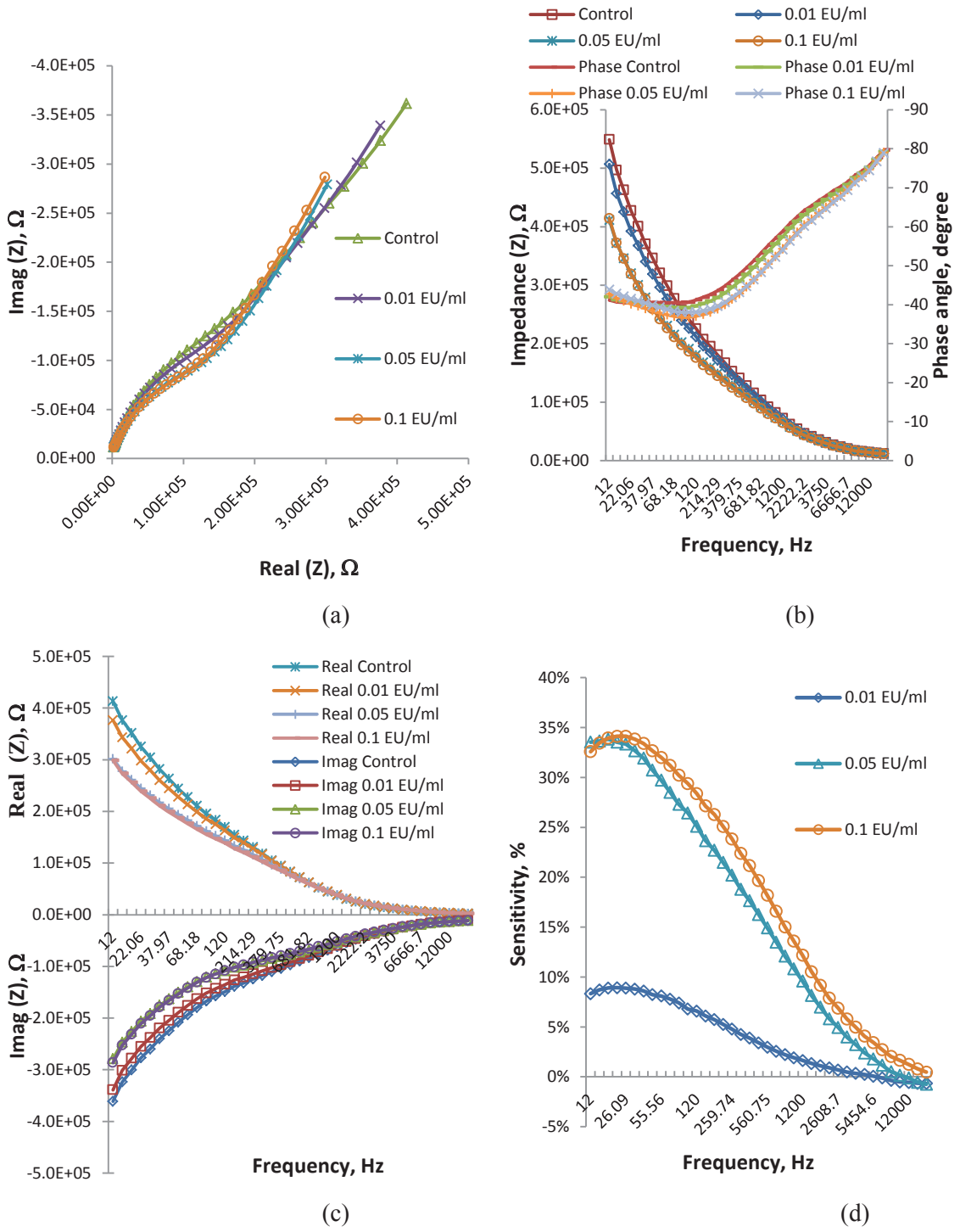

Figure 6.33: (a) Nyquist plot of standard endotoxin of concentrations 0.01 EU/ml, 0.05 EU/ml and 0.1 EU/ml (frequency 12 Hz – 18 kHz); (b) Bode plot showing Impedance (Z) and Phase Angle of standard endotoxin of concentrations 0.01 EU/ml, 0.05 EU/ml and 0.1 EU/ml (frequency 12 Hz – 18 kHz); (c) Impedance spectra real and imaginary part for standard endotoxin of concentrations 0.01 EU/ml, 0.05 EU/ml and 0.1 EU/ml (frequency 12 Hz – 18 kHz) and (d) Current sensitivity measurement of standard endotoxin of frequency 12 Hz – 18 kHz.

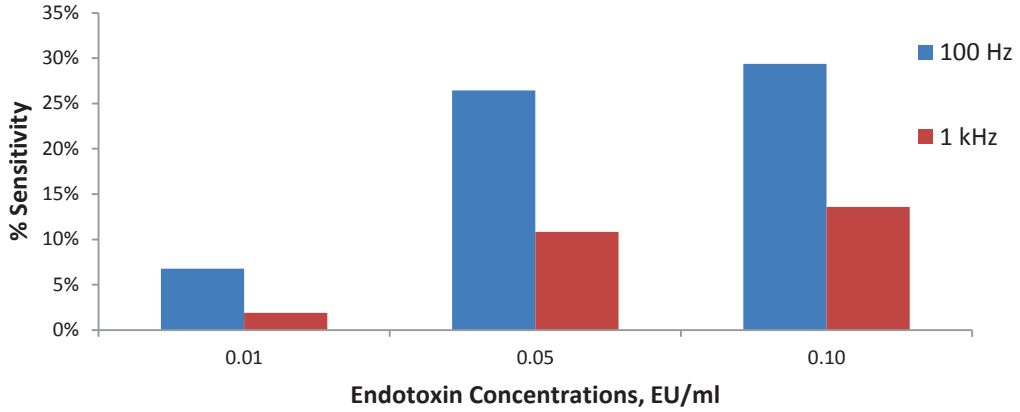

Figure 6.34: Normalized current sensitivity for different concentrations at different frequency of 100 Hz and 1 kHz

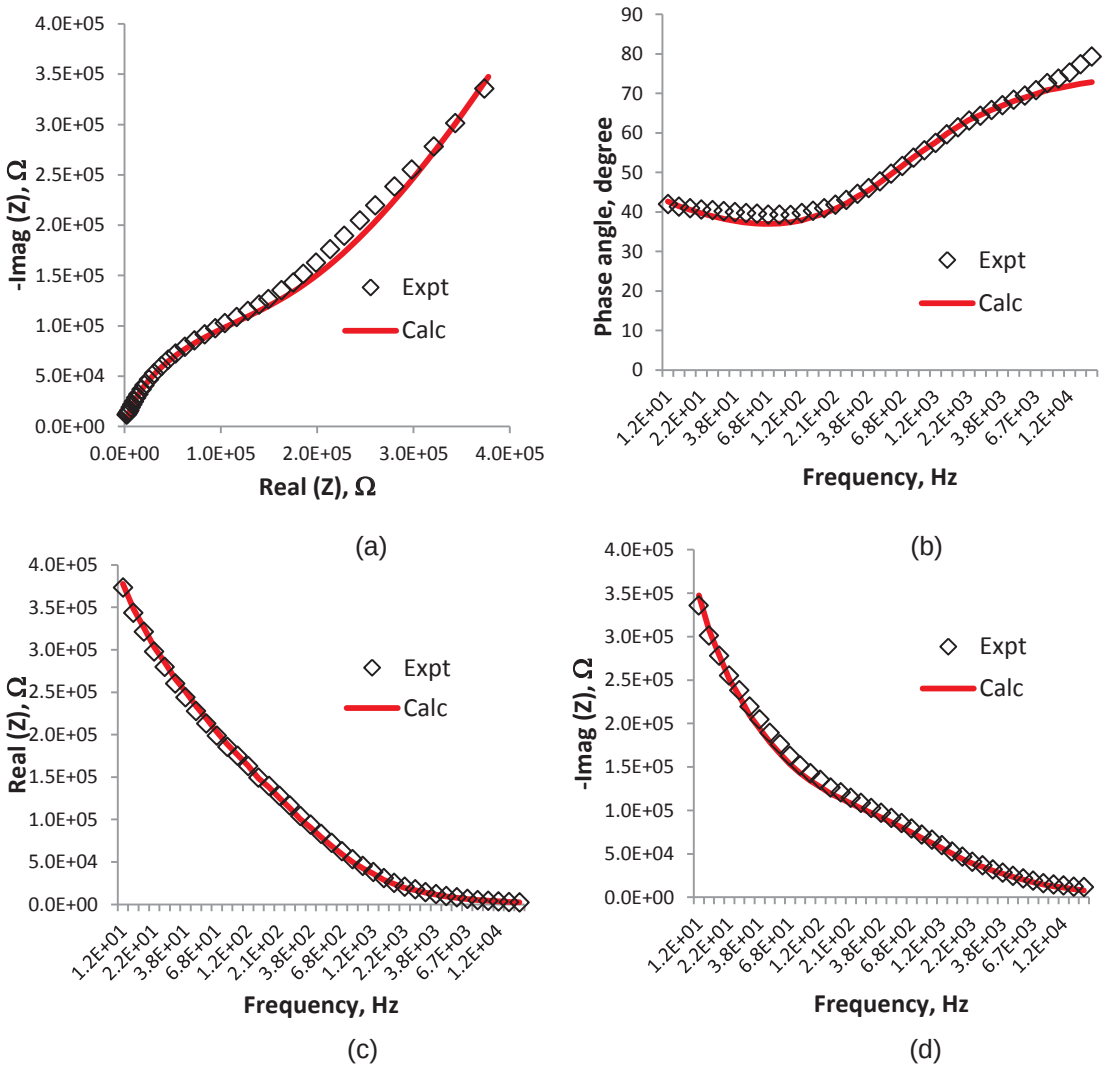

Figure 6.35: Results of curve fitting showing Nyquist plot (a) and Bode plot of standard endotoxin of 0.01 EU/ml in the frequency range of 12 Hz – 18 kHz showing (b) the phase angle, (c) and (d) showing real and imaginary parts respectively. Experimental impedance spectra are presented by the squares and the optimization parameters using non-linear least squares method are indicated by solid lines.

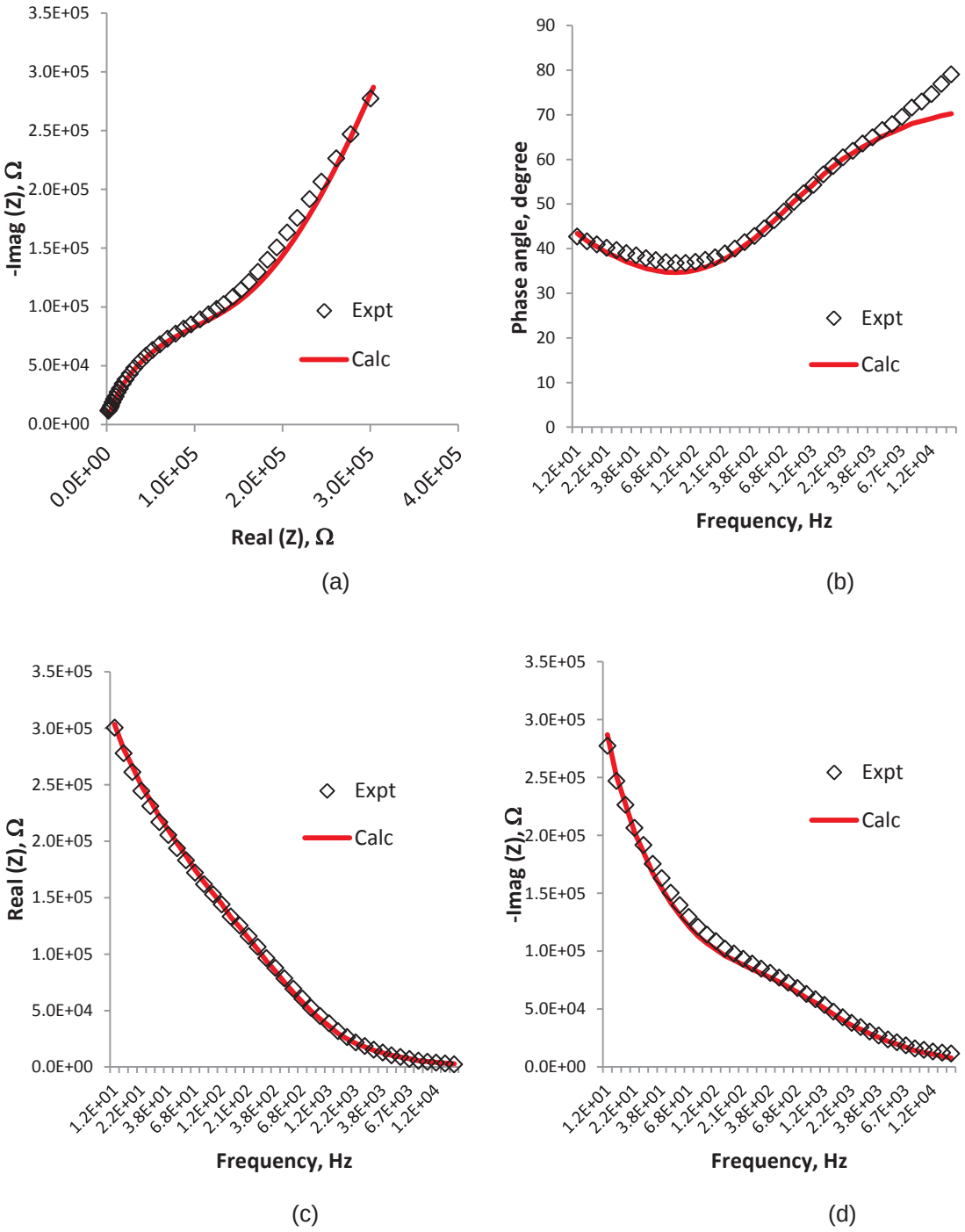

Figure 6.36: Results of curve fitting showing Nyquist plot (a) and Bode plot of standard endotoxin of 0.05 EU/ml in the frequency range of 12 Hz – 18 kHz showing (b) the phase angle, (c) and (d) showing real and imaginary parts respectively. Experimental impedance spectra are presented by the squares and the optimization parameters using non-linear least squares method are indicated by solid lines.

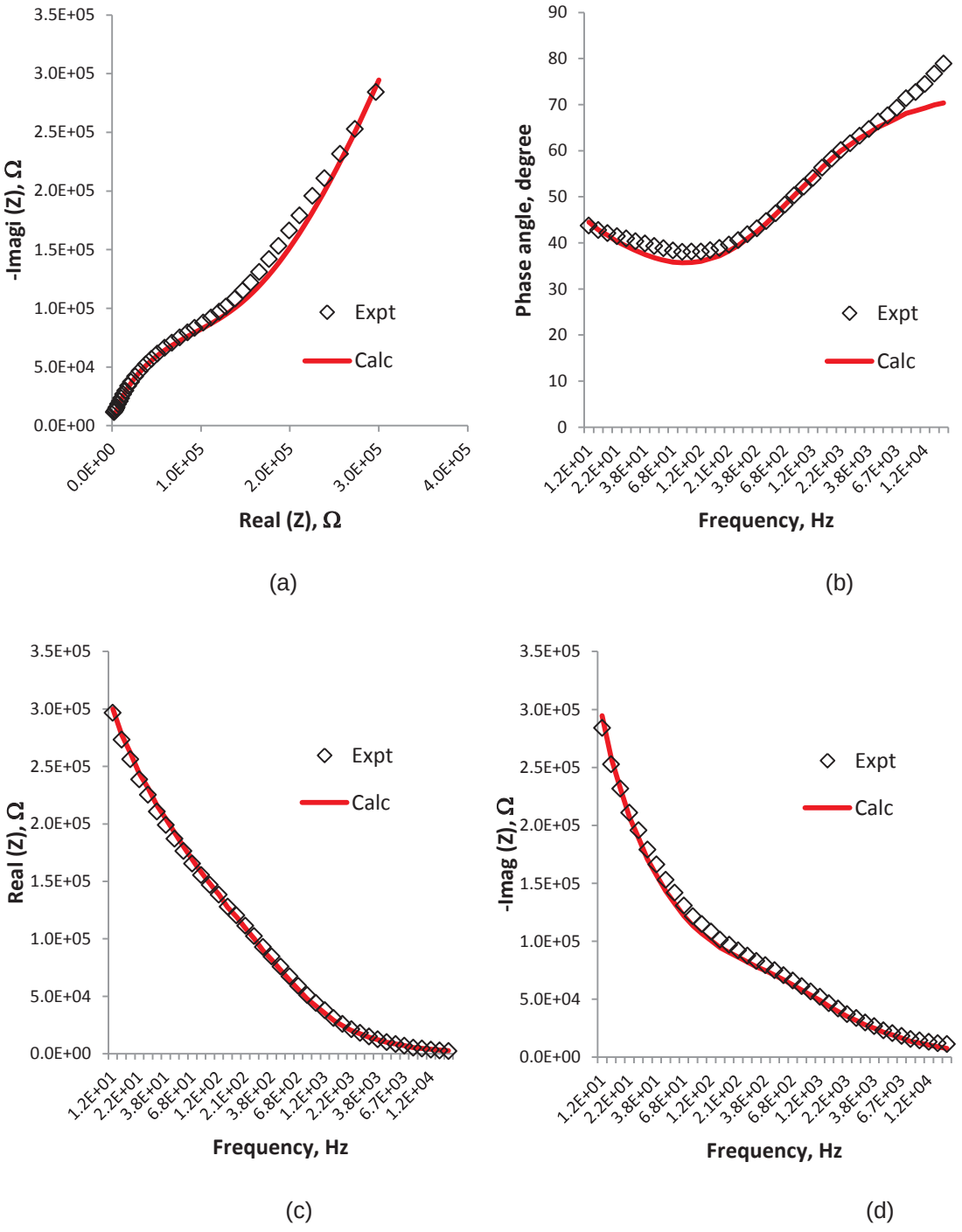

Figure 6.37: Results of curve fitting showing Nyquist plot (a) and Bode plot of standard endotoxin of 0.1 EU/ml in the frequency range of 12 Hz – 18 kHz showing (b) the phase angle, (c) and (d) showing real and imaginary parts respectively. Experimental impedance spectra are presented by the squares and the optimization parameters using non-linear least squares method are indicated by solid lines

Table 6.6: Results of the calculated parameters and percentage of errors from complex non-linear least squares fitting for standard endotoxin of concentrations between 0.01 EU/ml – 0.1 EU/ml

Parameter (unit)	Standard Endotoxin Solution		
	0.01 EU/ml	**0.05 EU/ml**	**0.1 EU/ml**
C_{ad} (F)	1.813E-07	1.39E-07	1.46E-07
R_s (Ω)	1.14E+02	1.23E+02	1.30E+02
R_{ct} (Ω)	1.7304E05	1.61E+05	1.57E+05
Z_w (Ω)	2.4431E06	1.90E+06	1.79E+06
C_{dl} (F)	6.95E-09	8.69E-09	9.20E-09

Figure 6.38(a) shows the spectrophotometer results of absorbance at 545 nm for standard endotoxin of 0.01 EU/ml, 0.05 EU/ml and 0.1 EU/ml with correlation of r^2 = 0.9833. Results of double layer capacitance, C_{dl} and adsorption capacitance, C_{ad} with different concentrations of standard endotoxin are shown in Figure 6.38(b) and Figure 6.38(c) having correlation of r^2 = 0.7534 and r^2 = 0.8477 respectively. C_{dl} increases as concentrations increase but C_{ad} reduces as the concentrations increase. But the increase of C_{dl} is very small since the double layer capacitance has very small value compared to adsorption capacitance. The Warburg impedance as shown in Figure 6.38(d) has better correlation with standard endotoxin with r^2 = 0.9331, but this correlation only occurs at lower frequency since the diffusion process involve at low frequency range. The charge transfer resistance, R_{ct} and solution resistance, R_s are shown in Figure 6.38(e) and Figure 6.38(f) respectively. R_{ct} has better correlation compared to R_s which has shown poor correlation with standard endotoxin concentrations. This is because at high frequency where the impedance is very small and close to the solution resistance, the value of the parameter, R_s cannot be exactly estimated. All parameters have shown good correlation with standard endotoxin concentrations except for R_s. It can be said that these parameters can be used to predict the amount of endotoxin in EU/ml at certain frequency range. Further experiments and analyses need to be conducted to study the relationship and would recommend for future work.

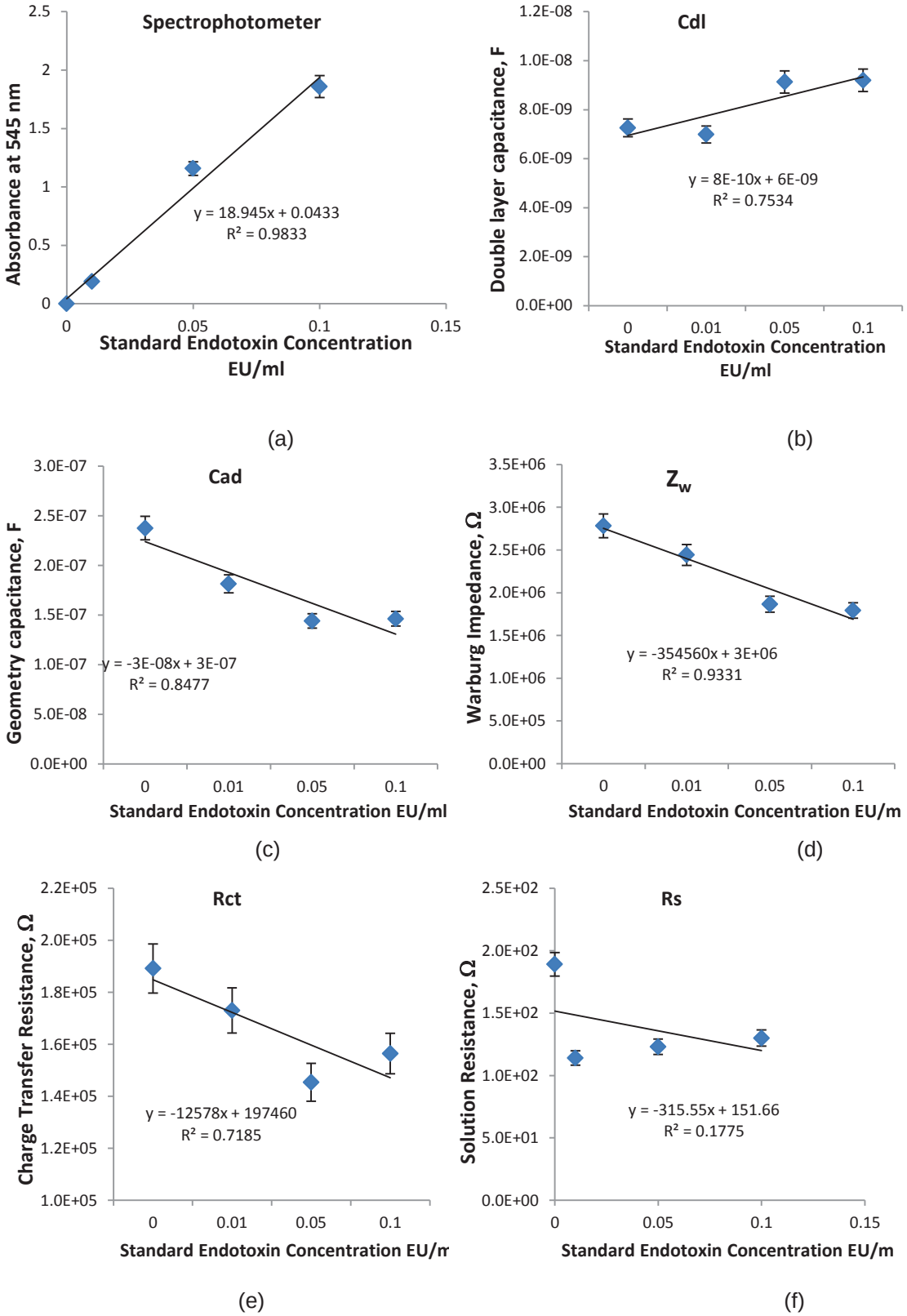

Figure 6.38: (a) Results of absorbance at 545 nm using Spectrophotometer; (b) Results of double layer capacitance, C_{dl} for different concentrations; (c) Results of adsorption capacitance, C_{ad} for different concentrations; (d) Warburg impedance, Z_W for different concentrations, (e) Charge transfer resistance, R_{ct} for different concentrations; and (f) Solution resiatance, R_S for different concentrations

6.6 Stability and Reproducibility of Sensing Performance

Experiments were conducted to study the effect of different thicknesses of coatings on the sensitivity and selectivity of the sensors. The latest modified silicon sensors in which silicon nitride (Si_3N_4) was introduced as a layer in the sensor fabrication process which improved sensor sensitivity. Six sensors were coated with multiple layers of dip-coating to investigate the effect of different coating thicknesses. The dip-coating of pre-cursor silica with APTES were coated on the sensors from one to six layers. Each layer was dried completely before adding the next layer of coatings. Finally, all sensors were immobilized with PmB. The SEM (Scanning Electron Microscope) image of a single layer of pre-cursor silica with APTES has been taken and measured about 268.3 nm on the electrode surface.

The AFM (Atomic Force Microscope) images were also taken to analyze the coated sensors and to study their surface layers. The electrode width is 25 μm and the AFM only can scan maximum of 20 μm in length. Therefore the needle position of AFM was placed almost at the middle of single electrode and scanning through 20 um from the centre of the electrode to electrode edge and continue scanning on silicon oxide (without electrode). Figure 6.39 shows the AFM image of bare (non-coated) electrode. The smooth surface of non-coated electrode was observed and the edge of the electrode is clearly seen. The image of APTES with PmB was taken and shown in Figure 6.40. It was observed the electrode surfaced was covered uniformly with pre-cursor silica with APTES film and the PmB molecules were immobilized on the APTES layer after successful immobilization process. The thickness of the coated electrode can be estimated by comparing both AFM images. It was found out that the height of bare electrode from the surface is about 700 nm (A) whereas the height of coated electrode with APTES is 1000 nm (B), as shown in Figure 6.41. The needle height in z-axis was not changed for both scanning measurements therefore the thickness of the layer can be estimated. It was found out that the thickness for a single layer measured by SEM and AFM almost the same which is between 250 nm – 300 nm. From these observations the thickness layers of dip-coating procedure can be estimated from 1-layer to 6-layer of dip-coated pre-cursor silica with APTES. Table 6.7 shows the thickness measurements of all coated sensors.

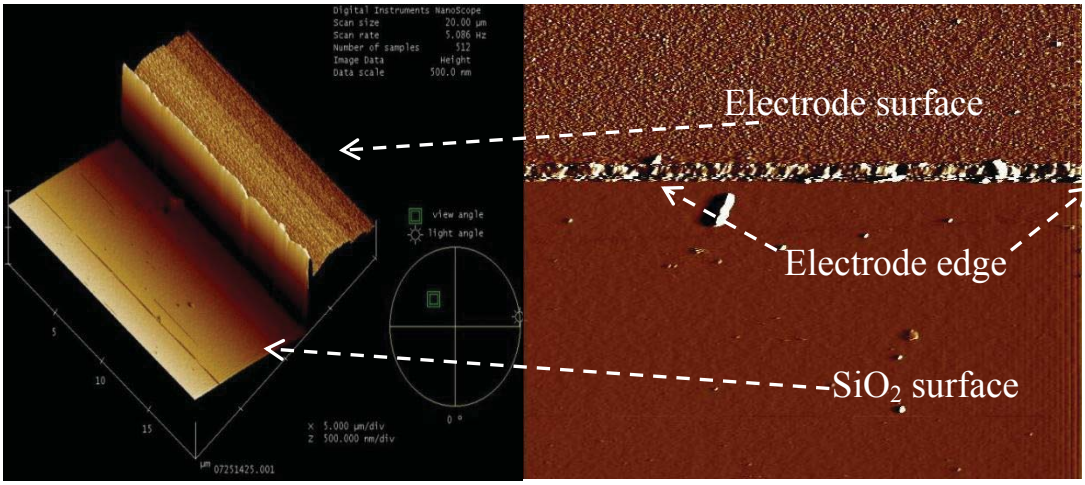

Figure 6.39: AFM images of non-coated electrode

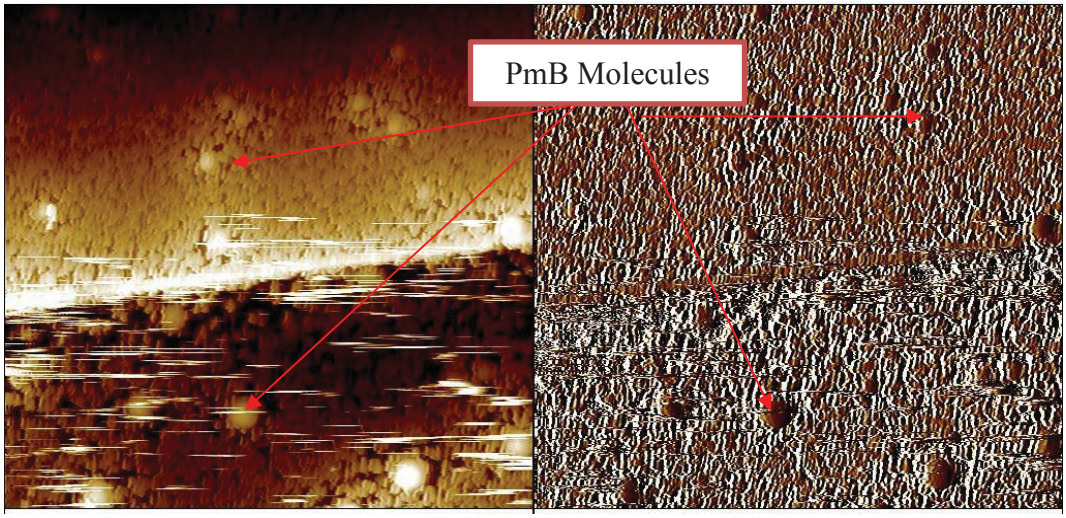

Figure 6.40: AFM images of a single layer of dip-coating precursor silica with APTES and PmB immobilization

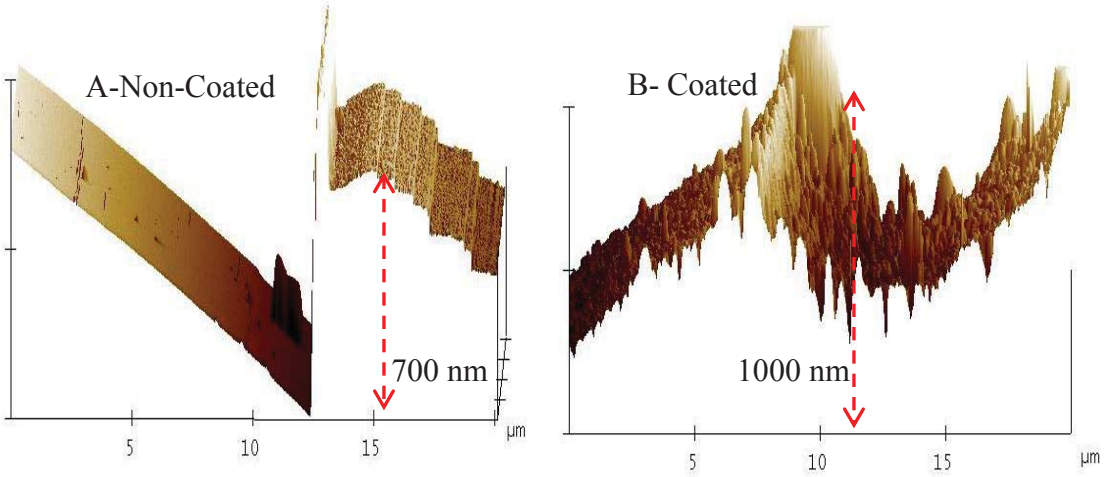

Figure 6.41: AFM images of a single layer on z-axis to measure thickness coating of; (A) Non-coated electrode (≈700 nm) (B) Coated electrode (≈1000 nm)

Table 6.7: Thickness measurement of different layers of dip-coated sensors

Sensor	1	2	3	4	5	6
Thickness Layer	1 Layer	2 Layer	3 Layer	4 Layer	5 Layer	6 Layer
Measurement (nm)	268.3	536.6	804.9	1073.2	1341.5	1609.8

An endotoxin concentration of 0.05 EU/ml (5 pg/ml) was prepared for the experiments. Eight microliter was pipetted on the sensing area and the data was measured. It was observed that the current measurement of the sensors has significantly changed for different thickness coatings applied on the sensor electrodes. Figure 6.42 shows that the current measurements were high for sensors with one coating layer to four coating layers. It was observed that the current increases as the frequency increases since charge transferred happens rapidly between the electrolyte and electrodes. It was also observed that as the thickness increases the total impedance increases and the current reduces. The optimum layers required for dip-coating of pre-cursor silica with APTES for this experiment is three layers (≈ 800 nm). The Nyquist plot for non-coated sensors and coated sensors with different thickness is shown in Figure 6.43. The Bode plot of impedance and phase angle is shown in Figure 6.44(a). Note that there is a significant difference between non-coated and coated sensors as shown in both Figures 6.44(a) and (b). The impedance of non-coated sensor is very low since the charge transfer is very fast. The phase angle also shows huge difference between coated and non-coated sensors. The real part and imaginary part of the non-coated and coated sensors is shown in Figure 6.44(b).

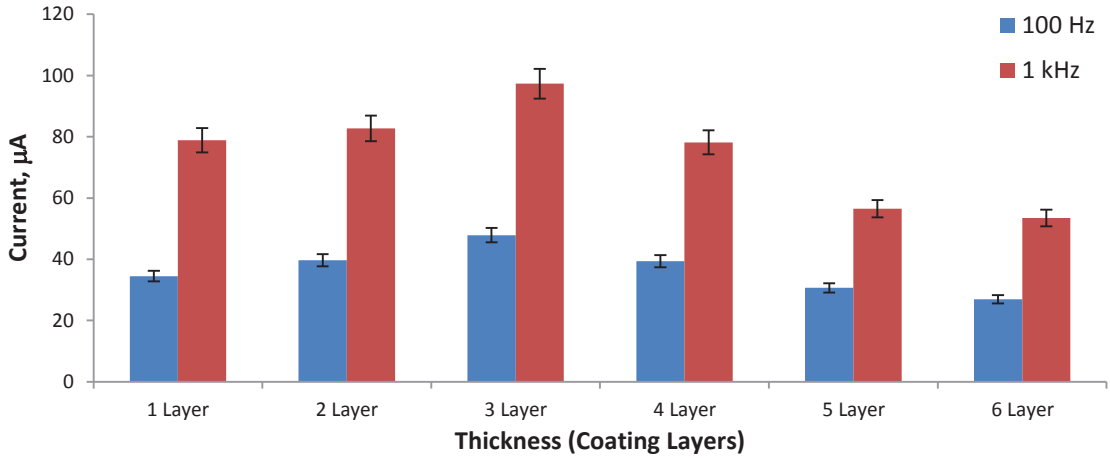

Figure 6.42: Current measurement at two different frequencies for different thickness layers of coated sensors

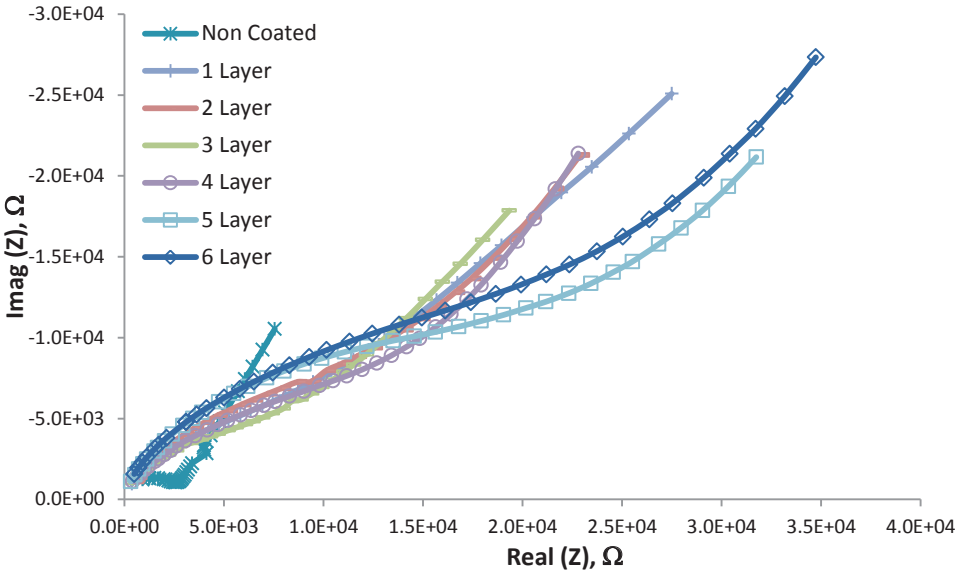

Figure 6.43: Nyquist plot of different thickness layers with 0.05 EU/ml of endotoxin (frequency 55 Hz – 100 kHz)

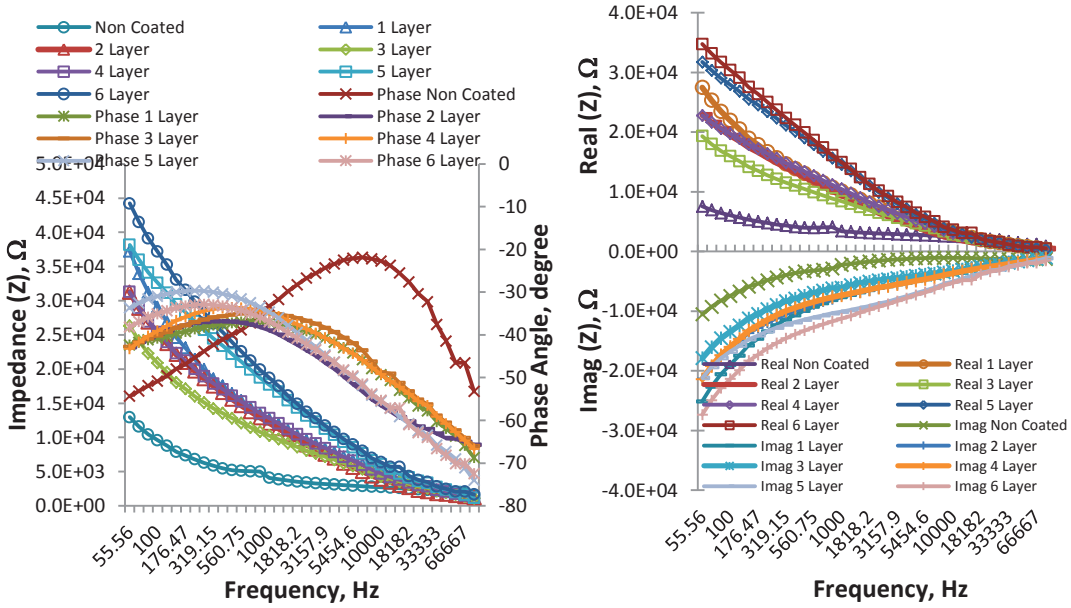

(a) (b)

Figure 6.44: (b) Bode plot showing Impedance (Z) and Phase Angle of different thickness of coated sensors and (b) Impedance spectra showing real part and imaginary part of different thickness of coated sensors with endotoxin (0.05 EU/ml)

Further experiments were carried out to study the sensor sensitivity between 3-layer coatings with 5-layer coatings. Three concentrations of endotoxin at 0.01 EU/ml, 0.1 EU/ml and 1 EU/ml were prepared. Eight microliter of each concentration was pipetted on each sensor and data was measured. Before next measurement was taken the sensors were rinsed in 96% ethanol to remove any bound molecules. Figure 6.45 shows the Nyquist plot of 3-layers coating of different concentrations of endotoxin. The

Nyqusit plot shows diffusion and charge transfer process as being discussed before in previous experiments. It was observed, the 3-layers coating can differentiate clearly endotoxin of different concentrations. The Bode plot in Figure 6.46(a) shows the impedance and phase angle of 3-layers coating. The impedance spectra in Figure 6.46(b) show the real part and the imaginary part of 3-layers coating with different endotoxin concentrations. In order to easily understand the sensitivity of sensor with 3-layers coating, the percentage sensitivity of normalized current were plotted. The normalized current sensitivity was analysed at 100 Hz and 1 kHz as shown in Figure 6.47. It is also shown in figure, as the concentrations increase the current increases which will increase the percentage of normalized current. The same analyses were conducted to sensor of 5-layers coating. Results of the Nyquist plot and the Bode plots are shown in Figure 6.48, 6.49(a) and 6.49(b) respectively. The percentage of sensitivity is shown in Figure 6.50. Results have shown that sensor with 5-layer coating has lower sensitivity measurement compared to 3-layer coatings. It was also observed that these new improved silicon sensors has better sensitivity measurement compared to previous silicon sensors because for 3-layers coating sensors the percentage sensitivity has significantly increased.

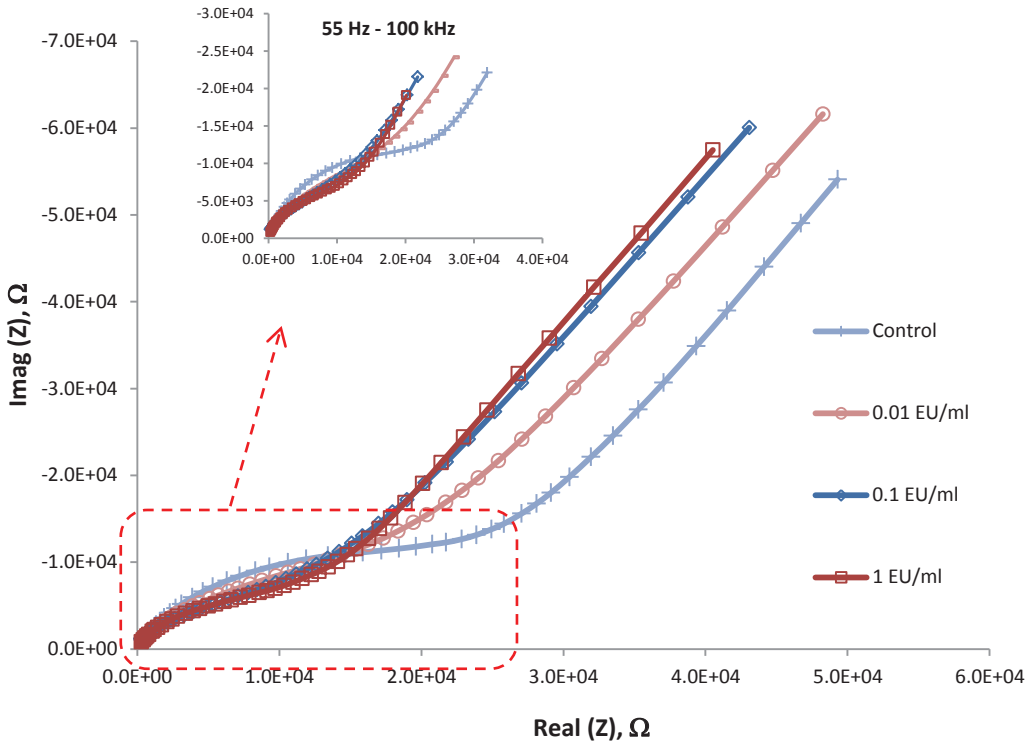

Figure 6.45: Nyquist plot of different concentration of endotoxin for 3-layer coated sensor

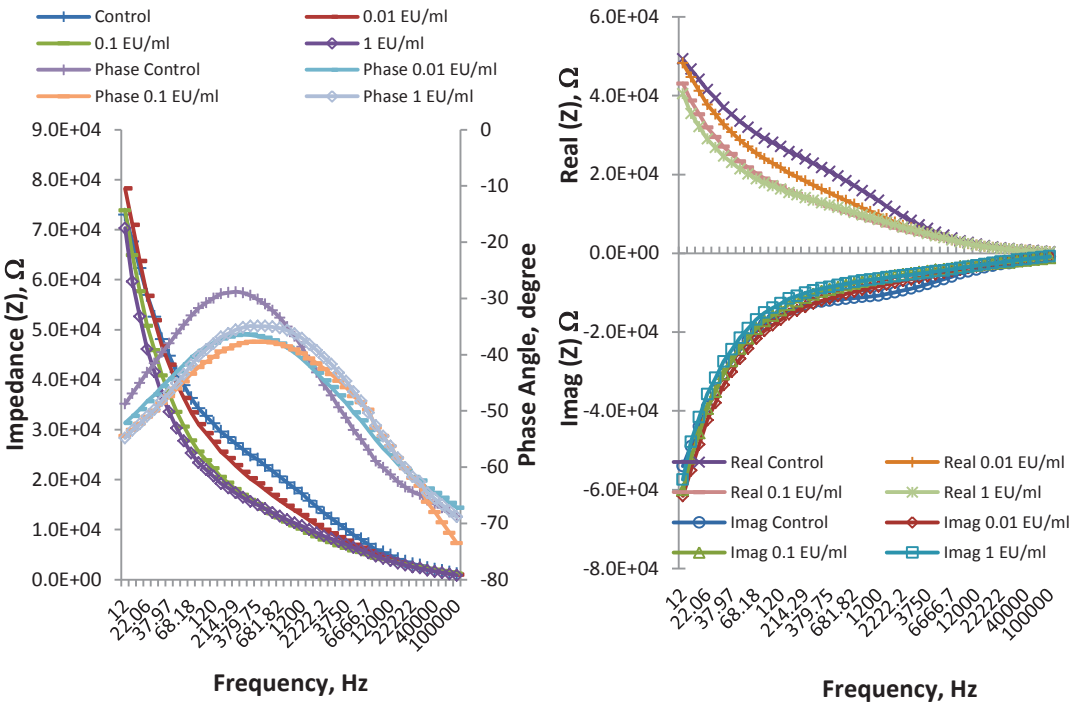

(a) (b)

Figure 6.46: (a) Bode plot showing Impedance (Z) and Phase Angle of different concentration of endotoxin for 3-layer coated sensor and (b) Impedance spectra of different concentrations of endotoxin for 3-layer coated sensor; Real part and Imaginary part

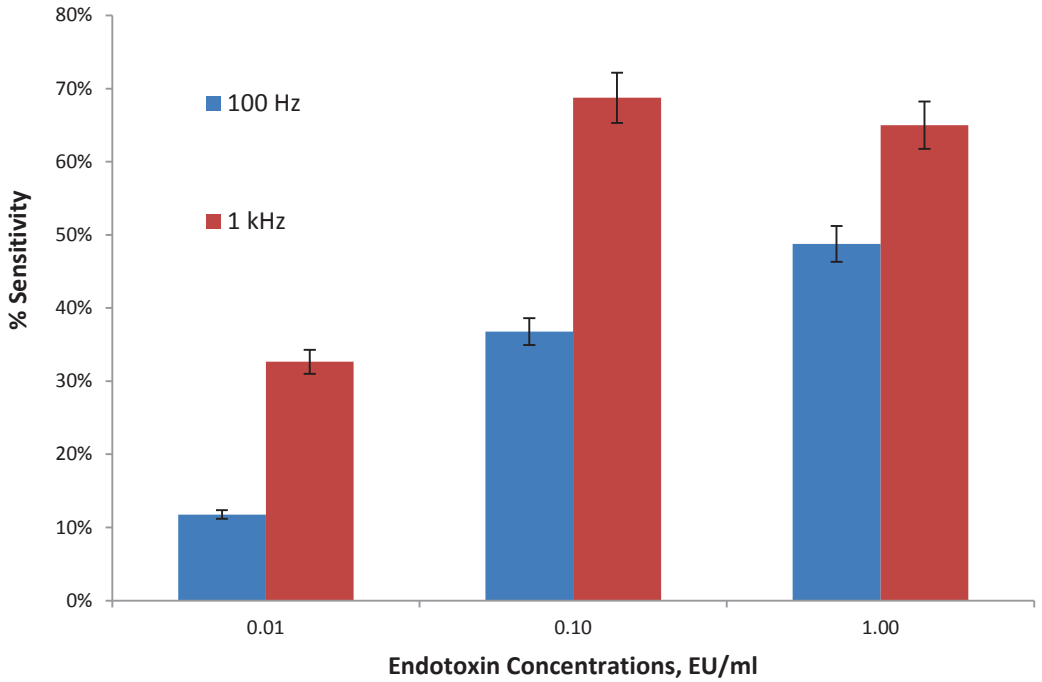

Figure 6.47: Normalized current sensitivity for different concentrations of 3-layer sensor at different frequency

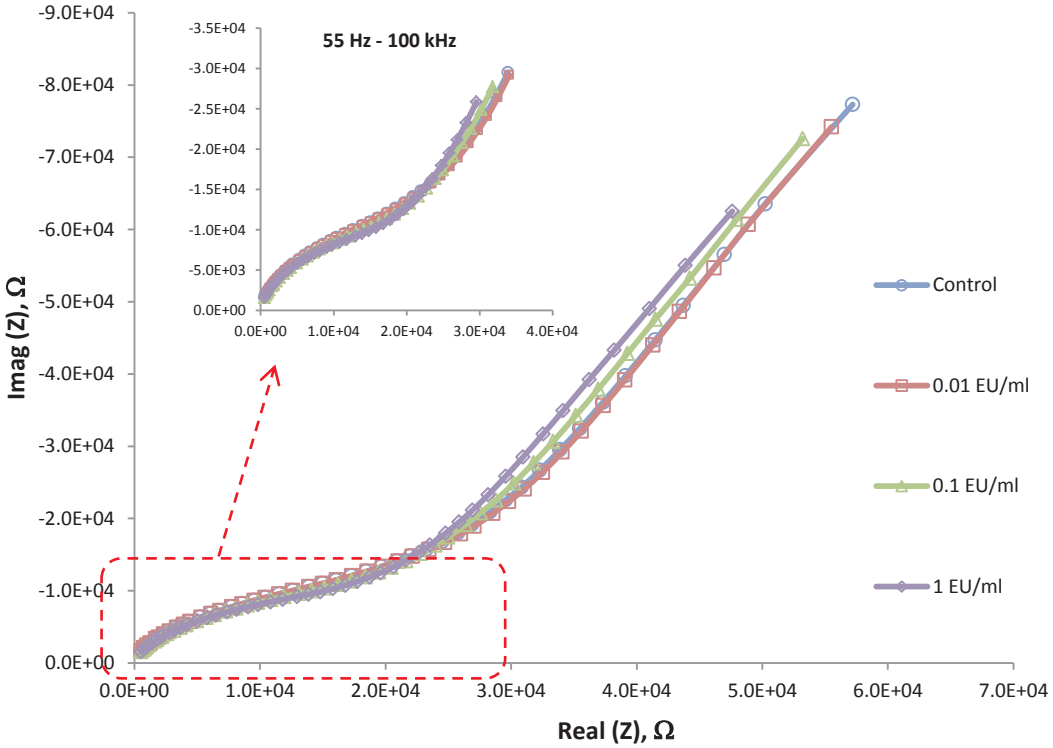

Figure 6.48: Nyquist plot of different concentration of endotoxin for 5-layer coated sensor

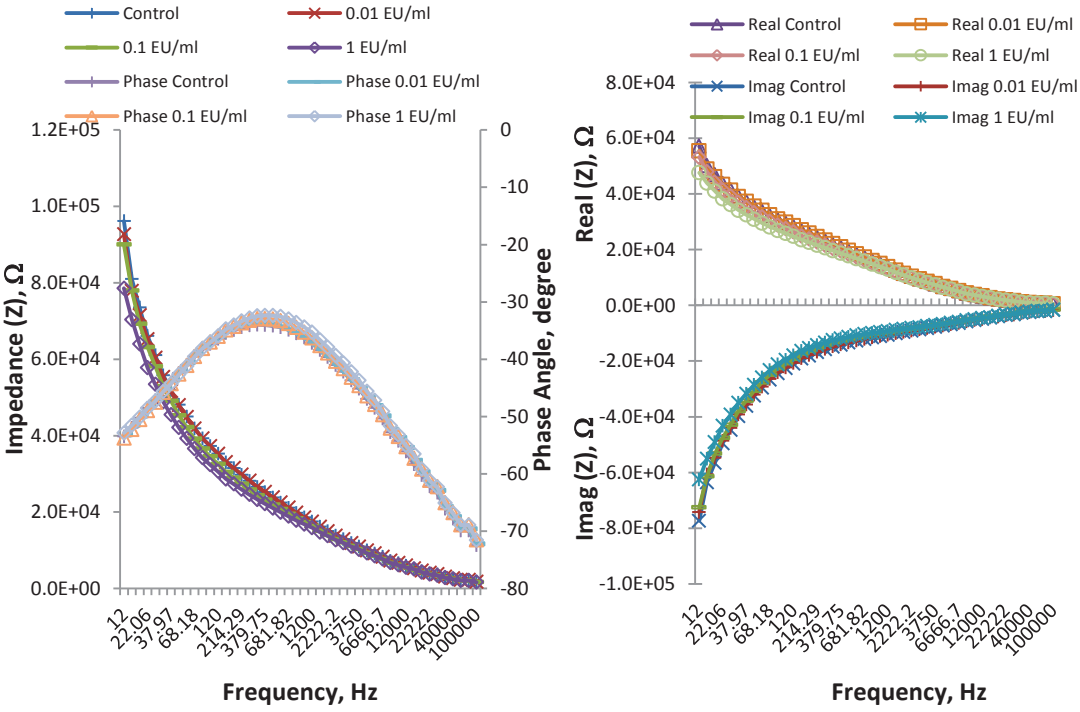

(a) (b)

Figure 6.49: Bode plot showing (a) Impedance (Z) and Phase Angle of different concentration of endotoxin for 5-layer coated sensor and (b) Impedance spectra of different concentrations of endotoxin for 5-layer coated sensor; Real part and Imaginary part

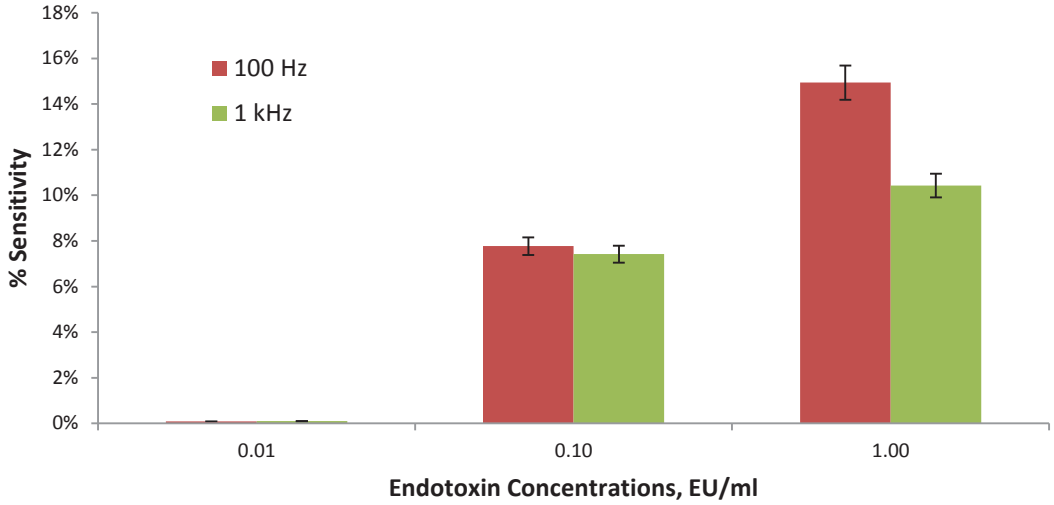

Figure 6.50: Normalized current sensitivity for different concentrations of 5-layer sensor at different frequency

The experiments were conducted to study the stability and reproducibility of the 3-layers coating sensor with multiple measurements of endotoxin (0.01 EU/ml). The experiment was repeated nine times and for each measurement, the sensor was rinsed with 96% ethanol to clean and remove any bound molecules on the sensors. Experimental results of impedance characteristics are shown in Figure 6.51(a) and results of current measurement are shown in Figure 6.51(b), where the stability of the coated sensor was observed to change after six continuous measurements. It can be said that the coating has stability for continuous measurement for up to six times before the coating materials start to degrade or loose its properties.

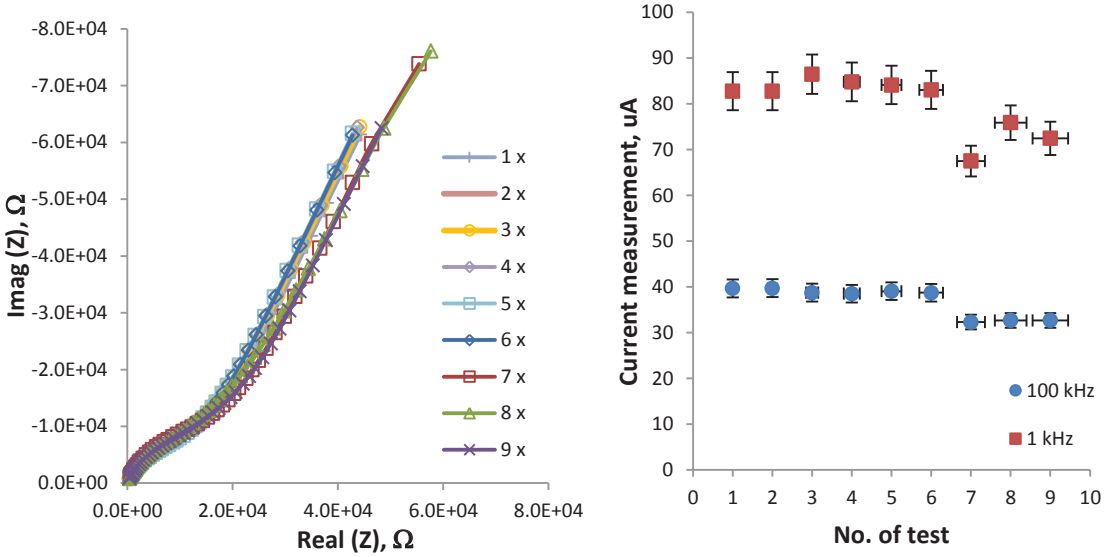

Figure 6.51: (a) Nyquist plot showing result of testing sensor for stability and reproducibility after multiple measurements (endotoxin 0.01 EU/ml) (b) Current measurement at frequency of 100 Hz and 1 kHz with respect to number of repetition tests.

6.7 Conclusion

Sensors of 1_5 configuration (FR4) have been successfully coated with different cross-linkers and then immobilized with PmB. Endotoxin from LPS O111:B4 (0.1 μg/ml to 1000 μg/ml) was used for experiments and it was found that sensor coated with APTES and immobilized with PmB has shown better selectivity to the LPS O111:B4 bio-molecules. The results show a mixed kinetic and diffusion process which are represented by double-layer capacitance, C_{dl}, solution resistance, R_s charge/electron transfer resistance, R_{ct} and Warburg impedance, Z_w. The immobilized PmB on coating C (APTES) and D (Thionine) has shown better bio-affinity events that retard the charge transfer due to the binding of large biomolecules of LPS on the PmB surface. Sensitivity measurement at 1 kHz has shown sensor with APTES has better sensing performance. Analyses were carried out using equivalent circuit model and PCA. PCA has shown sensor with APTES has better percentage of cumulative variance. It also showed that at low concentration the impedance parameters were related but not significant as the concentration increases.

New silicon sensors have been coated with pre-cursor silica and APTES before immobilization with PmB. These sensors have shown better sensitivity and selectivity to the target molecules. SEM images were taken to analyse the coating surface with APTES and immobilization of PmB molecules. Analyses of result with LPS O111:B4 have shown these silicon sensors have shown better diffusion and charge transfer process and can discriminate well between different concentrations of LPS O111:B4. The complex non-linear least squares (CNLS) fitting method was used to fit the measured impedance spectra based on chosen equivalent circuit model. Results have shown that the parameters obtained from the equivalent circuit model introduced give significant values of estimated parameters with errors less than 5% for concentrations of 0.1 μg/ml – 10 μg/ml but not significant as concentration increases (> 100 μg/ml). PCA results have shown how the parameters were related and can identify process which related to the diffusion, charge transfer and adsorption of molecules on sensors' surface.

Experiments were carried out to analyse the sensor performance with standard endotoxin. It was observed that the sensors can detect the endotoxin as low as 0.01 EU/ml which is equivalent to 1 pg/ml. The results of sensitivity measurement were compared with the absorbance results from Spectrophotometer. The estimated

parameter from CNLS fitting method can be used to estimate the endotoxin concentrations. More experiment need to be conducted in finding this relationship as recommended for future work.

Further experiments were conducted on new improved silicon sensors with standard endotoxins. Results have shown these improve silicon sensors increase the percentage of sensitivity compared to previous silicon sensors. Selectivity, stability and sensitivity of different thickness of coated sensors were analysed. It was found that the thickness of one layer of coating to four layers of coating give very good results. The optimum thickness is about 3-layers coating which equivalent to 800 nm. The comparison of sensor sensitivity was performed for 3-layers coating and 5-layers coating. Analyses have shown sensor of 3-layers coating have better results. The reproducibility and stability of the coated sensors were tested by multiple standard endotoxin measurement and it was observed that the sensors give a good reproducibility and stability up to six continuous measurements before the coating degrades.

CHAPTER 7

Food Sample Test and Analysis

7.1 Introduction

This chapter has presented several experiments and analysis of sensing responses towards food samples. The evaluations of sensors for non-contaminated food and contaminated foods with endotoxins have been carried out. Several food samples have been chosen for this experiment which includes skimmed milk, drinking water, cucumber, beef and chicken meat. The silicon sensors of 1_5 configuration with 3-layers of coating were prepared for the experiments. These sensors were then immobilized with Polymyxin B, PmB.

7.2 Food Samples Preparation

Solid food samples (cucumber, beef and chicken) were cut in small pieces and then blended with a kitchen blender to prepare them in slurry. The solid food samples were then autoclaved to kill any bacteria or germs that may produce toxins in the food samples. The liquid from each food samples was collected after autoclaved and then centrifuged to achieve total separation of liquid from the remaining solid food. All food samples prepared for the experiment is free from any contamination. 100 µl of non-contaminated sample was then added with 100 µl of endotoxin of concentration 0.05 EU/ml in clean Eppendorf tubes. Both non-contaminated and contaminated samples were measured and analysed.

7.3 Analysis on Food Samples

Each food sample was pipetted (8 µl) onto the sensors and data was measured. Result of impedance characteristics of the skimmed milk and drinking water are shown in Figure 7.1. Impedance spectra of drinking water for non-contaminated and contaminated sample was observed more significant compared to milk. The Nyquist

plot and the Bode plot in Figure 7.1 have shown better discrimination between drinking water of non-contaminated and contaminated samples. This is because in drinking water less content of other substance that may affect the sensor measurement but in milk the fat content may have appreciable effect on sensor readings. Figure 7.2 shows the result of impedance characteristic for cucumber, beef and chicken samples. Among these three samples, result of contaminated and non-contaminated of chicken samples has shown better discrimination. It was clearly shown from the Nyquist plot and Bode plot comparing results of non-contaminated with contaminated samples with endotoxin.

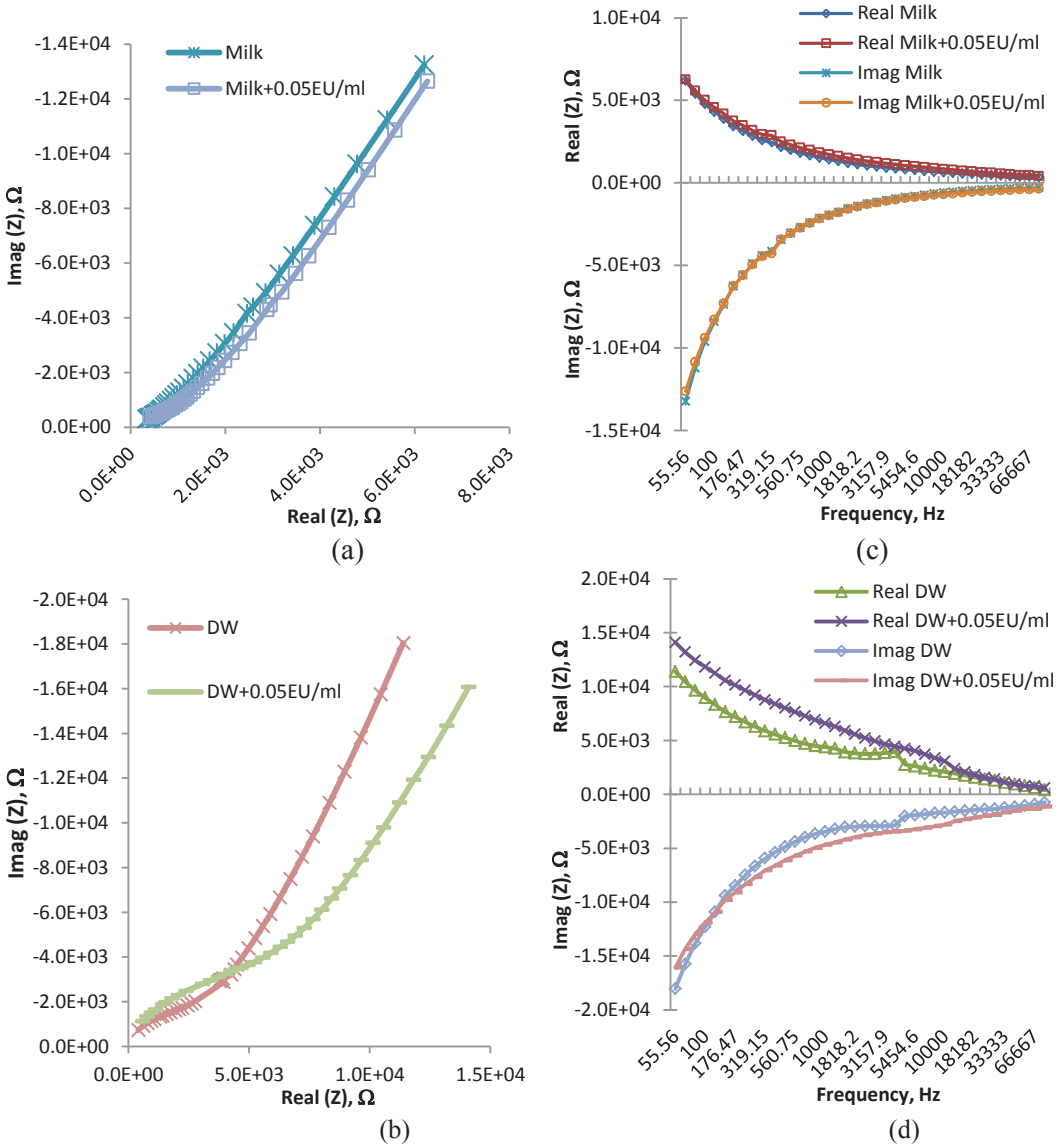

Figure 7.1: Nyquist plot showing (a) Non-contaminated and contaminated milk with endotoxin (0.05 EU/ml) and (b) Non-contaminated and contaminated drinking water (DW) with endotoxin (0.05 EU/ml) and Bode plot of impedance spectra showing (c) Real part and imaginary part of non-contaminated and contaminated milk with endotoxin (0.05 EU/ml) and (d) Real part and imaginary part of non-contaminated and contaminated drinking water (DW) with endotoxin (0.05 EU/ml)

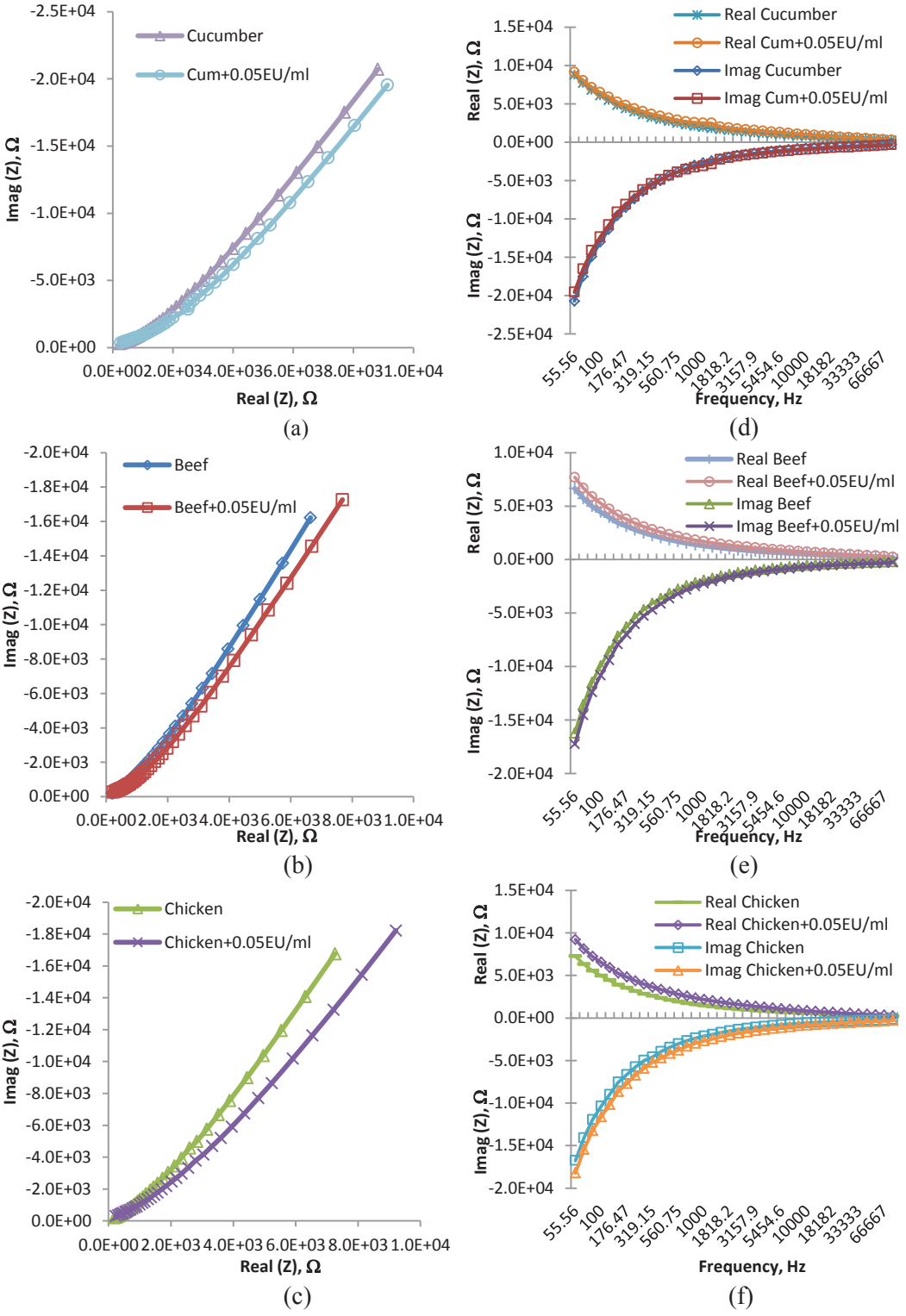

Figure 7.2: Nyquist plot showing (a) Non-contaminated and contaminated cucumber with endotoxin (0.05 EU/ml) (b) Non-contaminated and contaminated beef with endotoxin (0.05 EU/ml) and (c) Non-contaminated and contaminated chicken with endotoxin (0.05 EU/ml). Bode plot of impedance spectra showing (d) Real part and imaginary part of non-contaminated and contaminated cucumber with endotoxin (0.05 EU/ml) (e) Real part and imaginary part of non-contaminated and contaminated beef with endotoxin (0.05 EU/ml) and (f) Real part and imaginary part of non-contaminated and contaminated chicken with endotoxin (0.05 EU/ml)

To have better understanding which food samples have better response to the sensor measurement, the current measurements were analyzed. Current measurements at two frequencies of 100 Hz and 1 kHz have been chosen for analysis. Figure 7.3 shows the results of the current measurement of different food samples at frequency 100 Hz and 1 kHz. It was observed that at 100 Hz there is significant current change between non-contaminated and contaminated drinking water, beef and chicken only whereas there was less change of current measurement for the milk and cucumber. But as the frequency increases to 1 kHz all food samples shows better result in term of current change between non-contaminated sample and contaminated samples with endotoxin. The current measurements of the contaminated samples indicate that the sensors response to the contaminated endotoxin in food samples. The percentage of sensitivity measurement of normalized current between non-contaminated and contaminated food samples has been derived as in equation below;

$$\%\, Sensitivity = \frac{I_N - I_C}{I_N} * 100 \qquad \textbf{7.1}$$

where I_N – Current of non-contaminated sample

I_C – Current of contaminated sample

Result of the sensitivity measurement of different contaminated food samples is shown in Figure 7.4. It was found that the drinking water, beef and chicken have shown better sensitivity measurement at both frequencies compared to milk and cucumber. The drinking water show highest percentage of sensitivity measurement compared to other food samples. This is because the effect of other substance was less compare to other food samples which have fat, protein, acidic or others. The developed interdigital sensing approach is able to detect contaminated food samples with endotoxin at 0.05 EU/ml. It can be said that the sensors can detect the presence of endotoxin in contaminated food samples.

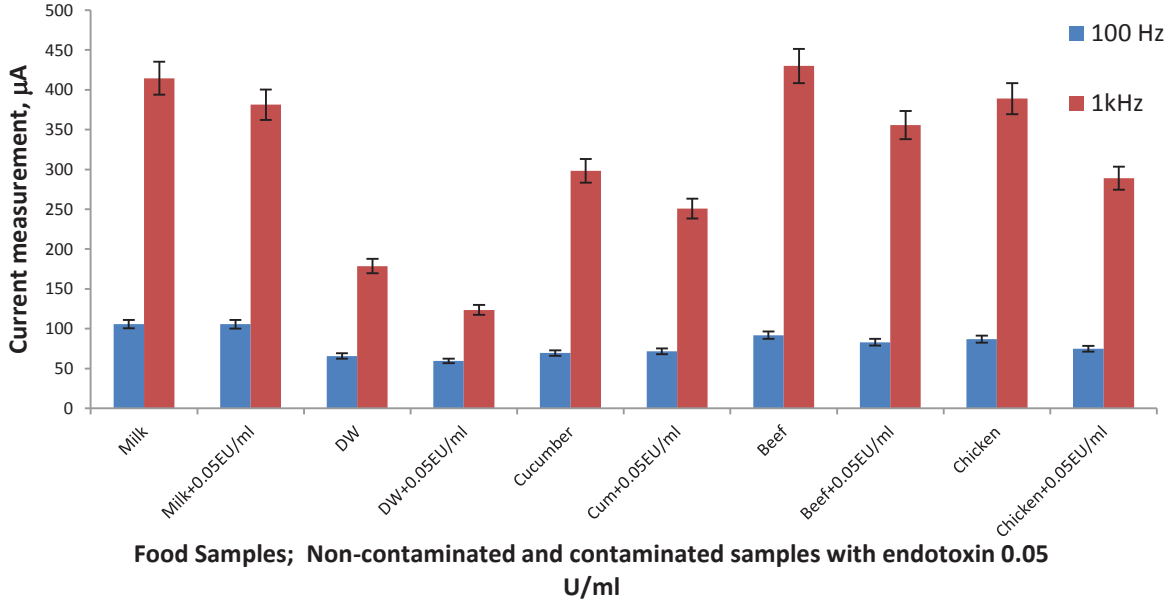

Figure 7.3: Current measurement for food samples test of non-contaminated sample and sample contaminated with 0.05 EU/ml of endotoxin at 100 Hz and 1 kHz

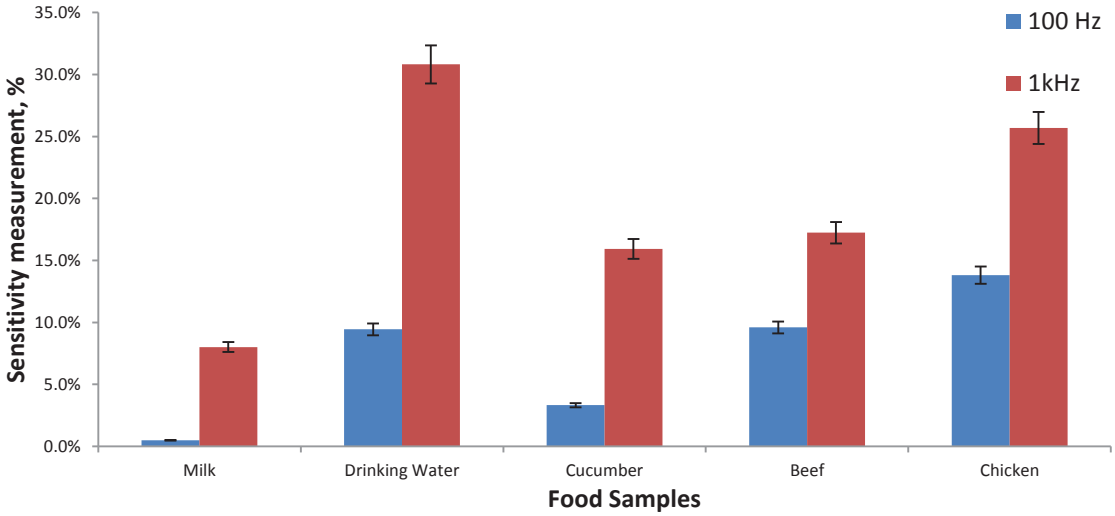

Figure 7.4: Percentage of sensitivity measurement of normalized current measurement of different contaminated food samples at 100 Hz and 1 kHz

Experiment with contaminated drinking water (DW) was conducted at different temperature setting. The experiment was conducted to study the effect of surrounding temperature to sensor readings or sensor measurements. Three different of temperature setting have been set; at 4°C, room temperature, 20°C – 25°C and at 35°C. The same experimental setup was prepared where the sensor was kept in clean desiccator and auto measurement using LabVIEW interfaced with LCR 821. The experiment was performed in the incubator of temperature setting 4°C, and 35°C while experiment at room temperature was conducted in normal laboratory condition. Figure 7.5 shows the Nyqusit plot of DW at three different temperature conditions. It was observed the temperature different has significant effect on

sensor measurements. Figure 7.6 shows the Bode plot and the impedance spectra of real and imaginary part of the DW at different temperature conditions. It was clearly shown that the impedance changed significantly but the phase angles only shown slightly changed as the temperature of surrounding changed. The impedance decrease as the temperature increases. Figure 7.7 shows the current measurement of contaminated drinking water at different temperatures. Result has shown that as the temperature increases, the current also increases.

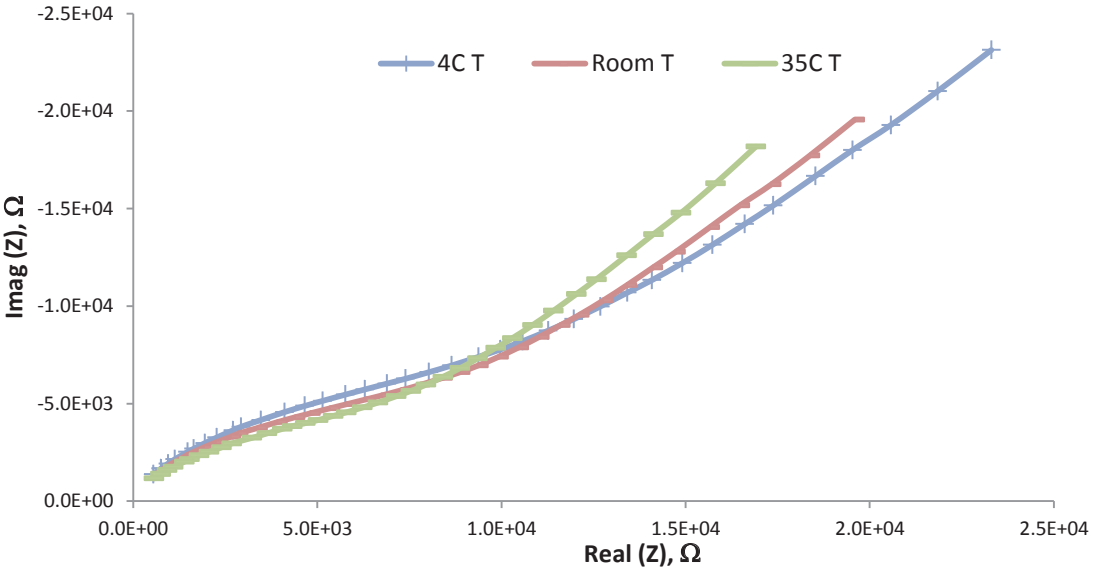

Figure 7.5: Nyquist plot showing contaminated DW with 0.05 EU/ml at different temperatures (Room Temperature 20°C - 25°C)

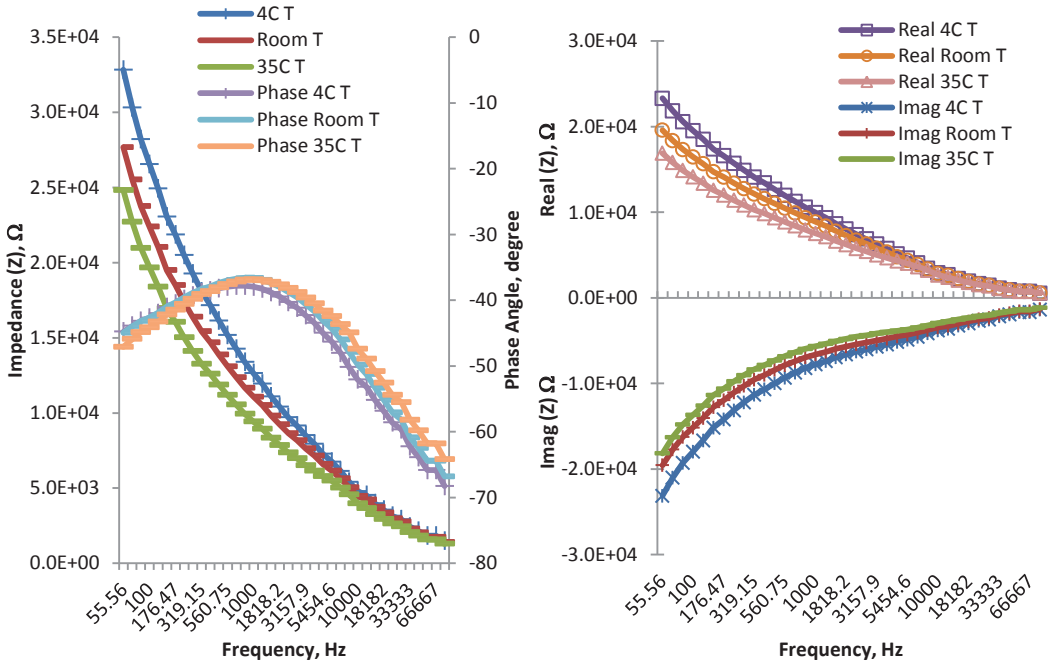

(a) (b)

Figure 7.6: (a) Bode plot showing Impedance (Z) and Phase Angle for contaminated DW with 0.05 EU/ml at different temperatures and (b) Impedance spectra of real part and imaginary part of contaminated DW with endotoxin at different temperatures (Room Temperature 20°C - 25°C)

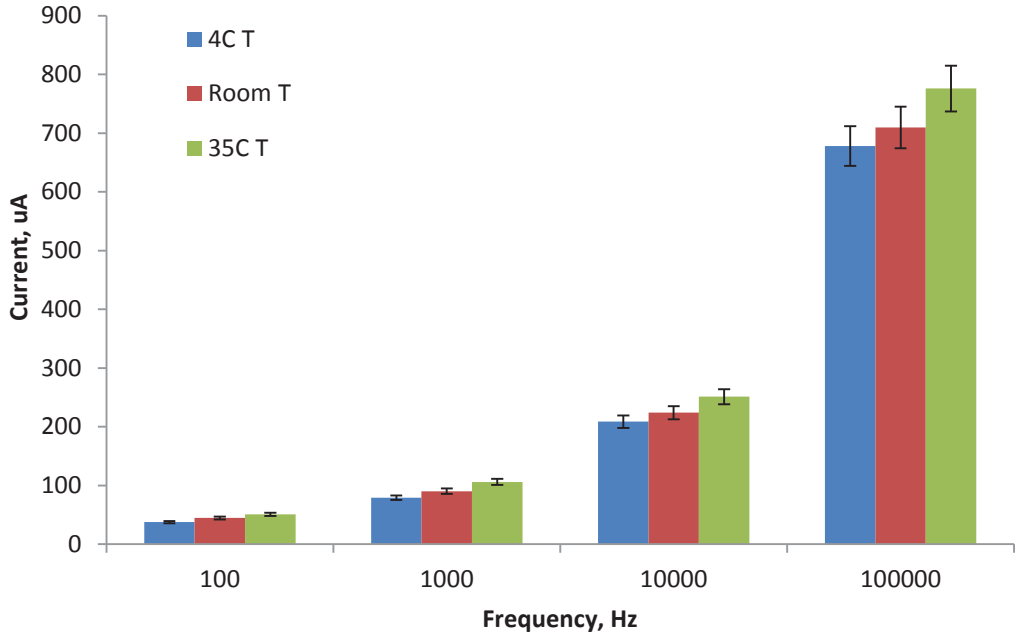

Figure 7.7: Current measurement of contaminated drinking water at different temperatures.

7.4 Conclusion

Experiments to analyse non-contaminated and contaminated food samples with endotoxin have been conducted. The contaminated food samples with 0.05 EU/ml of endotoxin can be detected using the silicon sensors of 1_5 configuration. It was observed that the drinking water, beef and chicken have shown better sensitivity measurement at frequency of 100 Hz and 1 kHz, compared to milk and cucumber. The results of percentage of sensitivity current measurement have shown the contaminated drinking water show highest percentage of sensitivity compared to other food samples. Further experiments were conducted to study the effect of temperature conditions on sensor measurement for contaminated drinking water. It was found that the different temperature conditions have significant effect on sensor measurement, so it may good to have the test done at the same temperature condition to eliminate the effect of temperature during measurements.

CHAPTER 8

Conclusion and Future Research

8.1 Conclusions

Planar interdigital sensing approach has been widely used for various applications. The thesis contained the contribution of the research works towards the development of novel interdigital sensor for bacterial endotoxin detections. The important research components from literature reviews, design, analysis and fabrications, experimental procedures, measurement, coating and immobilization, selectivity and sensitivity, detail analysis, statistical analysis and food analysis have been discussed thoroughly. The research works conducted have successfully developed a novel sensor for endotoxin detection.

In the first Chapter, the author has highlighted the problem statement which is the bacterial food poisoning caused by Gram-negative bacteria. The literature review covers wide range of related topics of the foodborne diseases worldwide and in New Zealand, the economic cost caused by foodborne diseases and the number of incidences. The conventional detection methods of pathogens and endotoxin have been discussed. The current trend of sensing methods based on biosensors and chemical sensors applications and the different transduction techniques of biosensors and chemical sensors have been described. The description of planar interdigital sensors, design and methodology and lastly the related research works at Massey University has been discussed in Chapter 1 of the thesis.

In Chapter 2, the operating principles of planar interdigital sensors have been discussed. Three novel interdigital sensors have been designed and fabricated. The optimum number of negative electrodes is important in the design consideration of interdigital sensors. New structure of planar interdigital sensors which is different from conventional electrode structure has been introduced. The sensors were designed to have different number of negative electrodes in between positive electrodes. Analyses of capacitive circuit were observed that the uniformity of electric field distribution with

highest capacitance value within the sensor's geometry contributes to the highest sensitivity. Further analyses were conducted using finite element analysis. Modelling using COMSOL Multiphysics has been conducted to evaluate the electric field strength and intensity, capacitance value, and distribution of electric field though out each sensor geometry. It was found the configurations of electrode structure having negative electrode between five to thirteen has the highest capacitance value within two positive electrodes. Therefore three new configurations, 1_11, 1_5, and 1_3 have been fabricated. All designs have same electrode width, pitch length, sensing area and total numbers of electrodes (positive and negative). The combination of electrodes were designed as follows; 1-11-1, 1-5-1-5-1 and 1-3-1-3-1-3-1. It was found the electric field for 1_11 configuration was uniformly distributed compared to other configurations but the field becomes weak as it approaches the center of the sensor geometry. 1_11 configuration has the lowest capacitance value compared to other configurations. The capacitance value highest for 1_3 configuration since it has more positive electrodes. The 1_5 configuration has the average, which means it has quite uniform electric field distribution throughout the sensing geometry and higher capacitance value compared to 1_11 configuration.

The sensors have been fabricated using different method of manufacturing. Smart fruitful collaborative partnerships have been established to manufacture these sensors. Collaborations have been developed with Northern Illinois University, USA, Southern Taiwan University, Taiwan and King Abdullah University of Science and Technology, Saudi Arabia. Each manufacturing technique of sensors fabrications used different substrates. Due to different values of permittivity of different substrate, the capacitance values and corresponding impedance values are influenced by these substrates. Initially three different substrates have been introduced; FR4, Alumina and Glass. Then, a new silicon based interdigital sensors were fabricated. These sensors were fabricated on silicon/silicon dioxide wafer which is widely used in the ICs industries. The sensors were developed in miniature size with multiple configurations of electrode structures of different configurations. These silicon based sensors provide better opportunity of low cost fabrication process where more sensors can be fabricated from a single silicon wafer. These sensors are expected to have better sensing performance, which provide high sensitivity, low impedance and better sensing signal with low noise.

The experimental setup, instrumentation and measurement method have been discussed in Chapter 3. High precision LCR meter interfaced with the auto measurement of LabVIEW program has been established. Details of the experimental setup, connection cables and instruments settings were mentioned in the chapter. The LabVIEW programs were successfully developed to measure and save automatically the absolute impedance, operating frequency, phase angles, the imaginary and the real part. The Basic theory of measurement method using Impedance Spectroscopy (IS) has also been discussed.

Experiments, results and analyses of different fabricated sensors of different substrate and different configurations of electrode structure have been discussed in Chapter 4. Impedance characteristic of all sensors were first studied with respect to air. All sensors behave as capacitive sensors showing the change of imaginary part (reactance) of the impedance is higher compared to the real part (resistive) at low frequency range (< 10 kHz). The real part does not change much as the frequency increased from 12 Hz – 100 kHz. This is because for good capacitive sensors only imaginary part changes as a function of frequency whereas the real part should not have any effect. It was observed that sensors with configuration 1_11 show highest impedance which indicates lower capacitance value and sensors with 1_3 configuration has lowest impedance value. Characteristic impedance of different substrates showing sensors fabricated on FR4 has slightly higher impedance compared to Alumina and Glass substrates. Silicon sensors have shown better output signal in term of low impedance, and high sensing signal with low noise.

Characteristic impedances of fabricated sensors in ionic solution (NaCl) and in the buffers of different pH values have been analysed. All sensors have different response to different chemicals which indicate the sensor performance. All sensors (FR4, Alumina and Glass) of configuration 1_5 show better response to different chemicals. Alumina 1_5 has shown better sensing performance compared to other sensors. It was also observed that the high concentrations of ionic solutions can degrade or corrosive the inclarac coatings. It is also shown from the results that selective coating materials on sensor electrodes is important to achieve selectivity towards target molecules for better sensing performance. The inclarac coating used in the experiments was just to delay the electron transfer from the electrolyte to electrodes and it does not show any selectivity towards the target molecule. The solution with high concentration

of ions was observed to have a significant change on sensor response due to change in conductivity and dielectric permittivity.

In order to make the sensors selective, a particular cross-linker and binding molecules need to be coated and immobilized on sensing electrodes. FR4 sensors with 1_5 configuration have been coated with different coating materials (cross linker). Different coating materials with different coating processes have been discussed. Three different coating materials which have been introduced were carboxyl-functional polymer, APTES and Thionine. The coatings were observed to be uniformly distributed on the electrodes surface and covered the whole sensing area of FR4 sensors. Optical micrograph images were taken to study and analyse surface coated electrodes. The immobilization steps and procedures of Polymyxin B (PmB) have also been discussed in Chapter 5 of the thesis.

In Chapter 6, detail descriptions of IS, equivalent circuit model and principal component analysis (PCA) have been discussed. Sensors of 1_5 configuration (FR4) have successfully been coated with different cross-linkers and then immobilized with Polymyxin B (PmB). Endotoxins from LPS O111:B4 of concentrations 0.1 μg/ml to 1000 μg/ml were used for experiments and it was found that sensor coated with APTES and immobilized with PmB has shown better selectivity to LPS O111:B4 bio-molecules. The results have shown mixed kinetic and diffusion process which are represented by double-layer capacitance, C_{dl}, solution resistance, R_s charge/electron transfer resistance, R_{ct} and Warburg impedance, Z_w. The immobilized PmB on APTES has shown better bio-affinity events that retard the charge transfer due to the binding of large biomolecules of LPS on the PmB surface. Sensitivity measurement at 1 kHz has shown sensor with APTES has better sensing performance. Analyses were carried out using equivalent circuit model and PCA. PCA has shown sensor with APTES has better percentage of cumulative variance. PCA also shown that at low concentration the impedance parameters were related but not significant as the concentration increases.

New silicon sensors have been coated with pre-cursor silica with APTES and then immobilized with PmB. These sensors have shown better sensitivity and selectivity to the target molecules. Scanning electron microscope (SEM) and atomic force microscope (AFM) images were taken to analyse the coating surface with APTES and

immobilization of PmB molecules. The images of non-coated sensors and coated sensors were studied and the thickness of a single layer coating was estimated. Analyses of result with LPS O111:B4 were observed that these silicon sensors have shown better diffusion and charge transfer process and can discriminate well between different concentrations of LPS O111:B4. The complex non-linear least squares (CNLS) fitting method was used to fit the measured impedance spectra based on chosen equivalent circuit model. Results have shown that the parameters obtained from the equivalent circuit model introduced give significant values of estimated parameters with errors less than 5% for concentrations of 0.1 μg/ml – 10 μg/ml but not significant as concentration increases (> 100 μg/ml). The residual means square, r^2 was very small indicates that less average deviation between measured and fitted points. PCA results were clustered and observed how the parameters were related and can identify process which related to the diffusion, charge transfer and adsorption of molecules on sensors' surface.

Experiments have been carried out to analyse the sensor performance with standard endotoxin. It was observed that the sensors can detect the endotoxin as low as 0.01 EU/ml which is equivalent to 1 pg/mL. The results of sensitivity measurement were compared with the absorbance results from Spectrophotometer. The estimated parameter from CNLS fitting method can be used to estimate the endotoxin concentrations. More experiment need to be conducted in finding this relationship as recommended for future work. Experiments have been conducted on new improved silicon sensors with standard endotoxins. Results have shown these improved silicon sensors increase the percentage of sensitivity compared to previous silicon sensors. Selectivity, stability and sensitivity of different thickness of coated sensors were analysed. It was observed that the thickness of one layer of coating to four layers of coating give very good results. The optimum thickness layer is 3-layers coating which is equivalent to 800 nm. The comparison of sensor sensitivity was performed for 3-layers coating and 5-layers coating. Analyses have shown sensor of 3-layers coating have shown better results. The reproducibility and stability of the coated sensors were tested by multiple measurement of standard endotoxin and it was observed the sensors give a good reproducibility and stability up to six continuous measurements before the coating degraded.

In Chapter 7, different food samples and drinks have been used to analyse non-contaminated and contaminated food samples with endotoxin. The results of contaminated food samples with 0.05 EU/ml of endotoxin can be detected using the developed sensors. It was found that the drinking water, beef and chicken have shown better sensitivity measurement at frequency of 100 Hz and 1 kHz, compared to milk and cucumber. Result of percentage of sensitivity current measurement has shown the contaminated drinking water show highest percentage of sensitivity compared to other food samples. Further experiments have been conducted to study the effect of temperature conditions on sensor measurement for contaminated drinking water. It was found that the difference in temperature conditions has significant effect on sensor measurement; therefore it is important to conduct experiments in the same temperature setting to eliminate effect of temperature.

The works presented in the thesis have shown significant contributions to research and society where the planar interdigital sensors can be coupled with biosensing or chemical sensing techniques to developed a low cost, fast and reliable sensing system for bacterial endotoxin. Further research works have to be conducted to improve the sensing performance and also to develop the prototype of bacterial endotoxin detection based on planar interdigital sensors.

8.2 Future Work

Further research work need to be conducted to enhance the sensitivity and selectivity of developed sensors. These can be achieved by improving the coating method with spin coating or electro spinning methods where selectable and specific thickness coating and uniform layers of cross linker can be established. The uniform coated layers will produce uniform distributions of immobilized binding biomolecules to capture the target molecules. Analyses of results can be further carried out especially in selecting equivalent circuit model to estimates parameters. So far the introduced equivalent circuit does not consider the coating capacitance. This analysis required extensive studies on different coated layers and their exposure time where the solutions/samples being measured. For this analysis new measuring instruments is needed which operates at very low frequency in millihertz (mHz) at low voltage. If the coating capacitance

contributes to the sensing measurements at very low frequency measurement, then the result of Nquist plot should show two semi circles with two time constants. It is important to conduct these experiments in the future so that we can have better estimations of the actual impedance parameters involve during measurement.

To develop a prototype based on the developed sensors is highly recommended for future works. The developed prototype can be microcontroller based sensing system for a stand-alone device or sensing prototype connected to a laptop for detail analysis can be developed. The development of standalone prototype should consist; microcontroller unit, interdigital sensors (coated and immobilized), signal conditioning circuit, dual power supply powered by batteries and a display unit. The system may require a set of different frequencies that can be selected and measurement can be taken at selected frequency ranging from low frequency to high frequency. Based on the experimental results the chosen frequency range is below than 1 kHz. The sensors should be easily dismantle or taken out from the prototype, so that a new sensors can be slot in or replaced.

The sensors may be fabricated with shield electrodes covering the sensing area to terminate the electric field fringes on the shield electrodes. Since the electric field distribution of the planar interdigital sensor is open and not constrained, some of the total field may not be used for the material characterization. One of the option may be tried to restrict the electric field is by adopting an electric shield. Experiment need to be conducted whether this shielding strategy will improve the sensing performance and will not affect the output sensing signals.

To develop a microfluidics device based on interdigital sensors may be an interesting challenge that can be considered. This is because the use of microfluidics device has been popular in biomedical and biosensors applications. It is also good if different biosensing techniques coupled with interdigitals sensors such as immobilization of DNA or enzymes types of bio-recognition. This is to explore the novel sensors response to new bio recognition and detection of specific pathogens.

References

[1] Phil Bereano, Brewster Kneen, Meriem Louanchi, Marta Rivera Ferre, and T. Philipott, *Food safety for whom? Corporate wealth vs people's health*. Barcelona: GRAIN, 2011.

[2] S. On, E. Lim, L. Lopez, P. Cressey, and R. Pirie, *Annual Report Concerning Foodborne Disease In New Zealand*. Christchurch: Enviromental Science and Research Limited (ESR), 2011.

[3] E. Scallan, R. M. Hoekstra, F. J. Angulo, R. V. Tauxe, M. A. Widdowson, S. L. Roy, J. L. Jones, and P. M. Griffin, "Foodborne Illness Acquired in the United States-Major Pathogens," *Emerging Infectious Diseases,* vol. 17, pp. 7-15, Jan 2011.

[4] Hall G. and K. M., *Foodborne illness in Australia. Annual incidence circa 2000*. Canberra: Australian Government Department of Health and Aging, 2005.

[5] G. K. Adak, S. M. Long, and S. J. O'Brien, "Trends in indigenous foodborne disease and deaths, England and Wales: 1992 to 2000," *Gut,* vol. 51, pp. 832-841, Dec 2002.

[6] A. H. Havelaar, A. V. Galindo, D. Kurowicka, and R. M. Cooke, "Attribution of Foodborne Pathogens Using Structured Expert Elicitation," *Foodborne Pathogens and Disease,* vol. 5, pp. 649-659, Oct 2008.

[7] D. Gadiel, *The economic cost of foodborne disease in New Zealand*. Sydney: Applied Economics Pty Ltd, 2010.

[8] E. Alocilja and S. Radke., "Market Analysis of Biosensor for Food Safety," *Biosensors & Bioelectronics,* vol. 18, pp. 841-846, 2003.

[9] A. B. Wagner, "Bacterial Food Poisoning," *Texas Agric. Ext. Publication* pp. 1-6, 1989.

[10] S. Hauschildt, W. Brabetz, A. B. Schromm, L. Hamann, P. Zabel, E. T. Rietschel, and S. Muller-Loennies, "Structure and activity of endotoxins," *Handbook of experimental pharmacology,* vol. 145, pp. 619-667, 2000.

[11] U. Seydel, A. B. Schromm, R. Blunck, and K. Brandenburg, "Chemical structure, molecular conformation, and bioactivity of endotoxins," *Cd14 in the Inflammatory Response,* vol. 74, pp. 5-24, 2000.

[12] O. Lazcka, F. J. Del Campo, and F. X. Munoz, "Pathogen detection: A perspective of traditional methods and biosensors," *Biosensors & Bioelectronics,* vol. 22, pp. 1205-1217, Feb 15 2007.

[13] FAO/WHO, "Microbiological Risk Assessment Series: Hazard Characterization for Pathogens in Food and Water," vol. 3, W. H. O. W. Food and Agriculture Organization (FAO), Ed., ed: WHO Library Cataloguing, 2003, pp. 1-76.

[14] V. Velusamy, K. Arshak, O. Korostynska, K. Oliwa, and C. Adley, "An overview of foodborne pathogen detection: In the perspective of biosensors," *Biotechnology Advances,* vol. 28, pp. 232-254, Mar-Apr 2010.

[15] P. Leonard, S. Hearty, J. Brennan, L. Dunne, J. Quinn, T. Chakraborty, and R. O'Kennedy, "Advances in biosensors for detection of pathogens in food and water," *Enzyme and Microbial Technology,* vol. 32, pp. 3-13, Jan 2 2003.

[16] S. Ratnam, S. B. March, R. Ahmed, G. S. Bezanson, and S. Kasatiya, "Characterization of Escherichia coli Serotype 0157:H7," *Journal of Clinical Microbiology,* vol. 26, pp. 2006-2012, October 1988.

[17] E. Leoni and P. P. Legnani, "Comparison of selective procedures for isolation and enumeration of Legionella species from hot water systems," *Journal of Applied Microbiology,* vol. 90, pp. 27-33, Jan 2001.

[18] S. S. Iqbal, M. W. Mayo, J. G. Bruno, B. V. Bronk, C. A. Batt, and J. P. Chambers, "A review of molecular recognition technologies for detection of biological threat agents," *Biosensors & Bioelectronics,* vol. 15, pp. 549-578, Dec 2000.

[19] K. S. Gracias and J. L. McKillip, "A review of conventional detection and enumeration methods for pathogenic bacteria in food," *Canadian Journal of Microbiology,* vol. 50, pp. 883-890, Nov 2004.

[20] C. S. Chen and R. A. Durst, "Simultaneous detection of Escherichia coli O157 : H7, Salmonella spp. and Listeria monocytogenes with an array-based immunosorbent assay

using universal protein G-liposomal nanovesicles," *Talanta,* vol. 69, pp. 232-238, Mar 15 2006.

[21] M. Magliulo, P. Simoni, M. Guardigli, E. Michelini, M. Luciani, R. Lelli, and A. Roda, "A rapid multiplexed chemiluminescent immunoassay for the detection of Escherichia coli O157 : H7, Yersinia enterocolitica, salmonella typhimurium, and Listeria monocytogenes pathogen bacteria," *Journal of Agricultural and Food Chemistry,* vol. 55, pp. 4933-4939, Jun 27 2007.

[22] A. Qadri, S. Ghosh, K. Prakash, R. Kumar, K. D. Moudgil, and G. P. Talwar, "Sandwich Enzyme Immunoassays for Detection of Salmonella-Typhi," *Journal of Immunoassay,* vol. 11, pp. 251-270, 1990.

[23] P. A. Chapman, A. T. C. Malo, C. A. Siddons, and M. Harkin, "Use of commercial enzyme immunoassays and immunomagnetic separation systems for detecting Escherichia coli O157 in bovine fecal samples," *Applied and Environmental Microbiology,* vol. 63, pp. 2549-2553, Jul 1997.

[24] F. Vazquez, E. A. Gonzalez, J. I. Garabal, S. Valderrama, J. Blanco, and S. B. Baloda, "Development and evaluation of an ELISA to detect Escherichia coli K88 (F4) fimbrial antibody levels," *Journal of Medical Microbiology,* vol. 44, pp. 453-463, Jun 1996.

[25] A. Farzan, R. M. Friendship, and C. E. Dewey, "Evaluation of enzyme-linked immunosorbent assay (ELISA) tests and culture for determining Salmonella status of a pig herd," *Epidemiology and Infection,* vol. 135, pp. 238-244, Feb 2007.

[26] E. Galikowska, D. Kunikowska, E. Tokarska-Pietrzak, H. Dziadziuszko, J. M. Los, P. Golec, G. Wegrzyn, and M. Los, "Specific detection of Salmonella enterica and Escherichia coli strains by using ELISA with bacteriophages as recognition agents," *European Journal of Clinical Microbiology & Infectious Diseases,* vol. 30, pp. 1067-1073, Sep 2011.

[27] C. Rozand and P. C. H. Feng, "Specificity Analysis of a Novel Phage-Derived Ligand in an Enzyme-Linked Fluorescent Assay for the Detection of Escherichia coli O157:H7," *Journal of Food Protection,* vol. 72, pp. 1078-1081, May 2009.

[28] Maria De Giusti, Daniela Tufi, Caterina Aurigemma, Angela Del Cimmuto, Federica Trinti, Alice Mannocci, and A. Boccia, "Detection of Escherichia coli O157 in raw and cooked meat: comparison of conventional direct culture method and Enzyme Linked Fluorescent Assay (ELFA)," *Italian Journal of Public Health,* vol. 8, p. 28, 2011.

[29] I. Abdel-Hamid, D. Ivnitski, P. Atanasov, and E. Wilkins, "Highly sensitive flow-injection immunoassay system for rapid detection of bacteria," *Analytica Chimica Acta,* vol. 399, pp. 99-108, Nov 8 1999.

[30] A. Valdivieso-Garcia, A. Desruisseau, E. Riche, S. Fukuda, and H. Tatsumi, "Evaluation of a 24-hour bioluminescent enzyme immunoassay for the rapid detection of Salmonella in chicken carcass rinses," *Journal of Food Protection,* vol. 66, pp. 1996-2004, Nov 2003.

[31] A. Rasooly and R. S. Rasooly, "Detection and analysis of staphylococcal enterotoxin A in food by Western immunoblotting," *International Journal of Food Microbiology,* vol. 41, pp. 205-212, Jun 16 1998.

[32] J. H. Meng and M. P. Doyle, "Introduction. Microbiological food safety," *Microbes and Infection,* vol. 4, pp. 395-397, Apr 2002.

[33] P. M. Fratamico, "Comparison of culture, polymerase chain reaction (PCR), TaqMan Salmonella, and Transia Card Salmonella assays for detection of Salmonella spp. in naturally-contaminated ground chicken, ground turkey, and ground beef," *Molecular and Cellular Probes,* vol. 17, pp. 215-221, Oct 2003.

[34] M. A. Jensen, J. A. Webster, and N. Straus, "Rapid Identification of Bacteria on the Basis of Polymerase Chain Reaction-Amplified Ribosomal DNA Spacer Polymorphisms," *Applied and Environmental Microbiology,* vol. 59, pp. 945-952, Apr 1993.

[35] P. Belgrader, W. Benett, D. Hadley, J. Richards, P. Stratton, R. Mariella, and F. Milanovich, "Infectious disease - PCR detection of bacteria in seven minutes," *Science,* vol. 284, pp. 449-450, Apr 16 1999.

[36] R. Naravaneni and K. Jamil, "Rapid detection of food-borne pathogens by using molecular techniques," *Journal of Medical Microbiology,* vol. 54, pp. 51-54, Jan 2005.

[37] O. Traore, C. Arnal, B. Mignotte, A. Maul, H. Laveran, S. Billaudel, and L. Schwartzbrod, "Reverse transcriptase PCR detection of astrovirus, hepatitis A virus, and poliovirus in experimentally contaminated mussels: Comparison of several extraction and concentration methods," *Applied and Environmental Microbiology,* vol. 64, pp. 3118-3122, Aug 1998.

[38] R. Morales-Rayas, P. F. G. Wolffs, and M. W. Griffiths, "Simultaneous separation and detection of hepatitis A virus and norovirus in produce," *International Journal of Food Microbiology,* vol. 139, pp. 48-55, Apr 30 2010.

[39] S. Russell, S. Frasca, I. Sunila, and R. A. French, "Application of a multiplex PCR for the detection of protozoan pathogens of the eastern oyster Crassostrea virginica in field samples," *Diseases of Aquatic Organisms,* vol. 59, pp. 85-91, Apr 21 2004.

[40] S. H. Lee, M. Joung, S. Yoon, K. Choi, W. Y. Park, and J. R. Yu, "Multiplex PCR Detection of Waterborne Intestinal Protozoa: Microsporidia, Cyclospora, and Cryptosporidium," *Korean Journal of Parasitology,* vol. 48, pp. 297-301, Dec 2010.

[41] S. T. Lambertz, C. Nilsson, S. Hallanvuo, and M. Lindblad, "Real-time PCR method for detection of pathogenic Yersinia enterocolitica in food," *Applied and Environmental Microbiology,* vol. 74, pp. 6060-6067, Oct 2008.

[42] A. Mukhopadhyay and U. K. Mukhopadhyay, "Novel multiplex PCR approaches for the simultaneous detection of human pathogens: Escherichia coli O157 : H7 and Listeria monocytogenes," *Journal of Microbiological Methods,* vol. 68, pp. 193-200, Jan 2007.

[43] S. Yaron and K. R. Matthews, "A reverse transcriptase-polymerase chain reaction assay for detection of viable Escherichia coli O157 : H7: investigation of specific target genes," *Journal of Applied Microbiology,* vol. 92, pp. 633-640, 2002.

[44] S. H. Choi and S. B. Lee, "Development of Reverse Transcriptase-polymerase Chain Reaction of fimA Gene to Detect Viable Salmonella in Milk," *Journal of Animal Science and Technology,* vol. 46, pp. 841-848, 2004.

[45] Genscript. (2012, 20th August 2012). *Direct PCR System - Direct multiplex PCR amplication of more than 1000 amplicons (http://www.genscript.com/direct_pcr.html ed.).*

[46] A. K. Abbas and A. H. Lichtman, *Cellular and Molecular Immunology*, 5th ed. Philadelphia: Elsevier Saunders, 2005.

[47] J. L. Ding and B. Ho, "A new era in pyrogen testing," *Trends in Biotechnology,* vol. 19, pp. 277-+, Aug 2001.

[48] S. Hoffmann, A. Peterbauer, S. Schindler, S. Fennrich, S. Poole, Y. Mistry, T. Montag-Lessing, I. Spreitzer, B. Loschner, M. van Aalderen, R. Bos, M. Gommer, R. Nibbeling, G. Werner-Felmayer, P. Loitzl, T. Jungi, M. Brcic, P. Brugger, E. Frey, G. Bowe, J. Casado, S. Coecke, J. de Lange, B. Mogster, L. M. Naess, I. S. Aaberge, A. Wendel, and T. Hartung, "International validation of novel pyrogen tests based on human monocytoid cells," *Journal of Immunological Methods,* vol. 298, pp. 161-173, Mar 2005.

[49] J.L. Ding and B. Ho, *Endotoxin Detection – from Limulus Amebocyte Lysate to Recombinant Factor C* vol. Volume 53. Berlin: Springer, 2010.

[50] P. S. Thorne, S. S. Perry, R. Saito, P. T. O'Shaughnessy, J. Mehaffy, N. Metwali, T. Keefe, K. J. Donham, and S. J. Reynolds, "Evaluation of the Limulus Amebocyte Lysate and Recombinant Factor C Assays for Assessment of Airborne Endotoxin," *Applied and Environmental Microbiology,* vol. 76, pp. 4988-4995, Aug 2010.

[51] F. B. Bang and J. L. Frost, "The Toxic Effect of a Marine Bacterium on Limulus and the Formation of Blood Clots," *Biological Bulletin,* vol. 105, pp. 361-362, 1953.

[52] FDA, *Bacterial Endotoxins/Pyrogens*. New Hampshire: Dept. of Health, Education and Welfare Public Health Service Food and Drug Administration 1985.

[53] Henning G. Kristensen, Agnes Artiges, and Peter Castle, "Bacterial endotoxin," *European Pharmacopoeia 5.0,* vol. 1, 2005.

[54] J. Ryan, *Endotoxins and Cell Culture*, TC-305 Rev.1 ed. Lowell: Corning Inc., 2008.

[55] D. D. Morris, N. Crowe, J. N. Moore, and L. L. Moldawer, "Endotoxin-Induced Production of Interleukin-6 by Equine Peritoneal-Macrophages Invitro," *American Journal of Veterinary Research,* vol. 53, pp. 1298-1301, Aug 1992.

[56] J. C. M. Dumoulin, P. P. C. A. Menheere, J. L. H. Evers, A. P. G. Kleukers, M. H. E. C. Pieters, M. Bras, and J. P. M. Geraedts, "The Effects of Endotoxins on Gametes and Preimplantation Embryos Cultured Invitro," *Human Reproduction,* vol. 6, pp. 730-734, May 1991.

[57] E. Snyman and J. V. Vandermerwe, "Endotoxin-Polluted Medium in a Human Invitro Fertilization Program," *Fertility and Sterility,* vol. 46, pp. 273-276, Aug 1986.

[58] T. M. Mckenna, "Prolonged Exposure of Rat Aorta to Low-Levels of Endotoxin Invitro Results in Impaired Contractility - Association with Vascular Cytokine Release," *Journal of Clinical Investigation,* vol. 86, pp. 160-168, Jul 1990.

[59] P. Colburn, E. Kobayashi, and V. Buonassisi, "Depleted Level of Heparan-Sulfate Proteoglycan in the Extracellular-Matrix of Endothelial-Cell Cultures Exposed to Endotoxin," *Journal of Cellular Physiology,* vol. 159, pp. 121-130, Apr 1994.

[60] C. H. Sibley, A. Terry, and C. R. H. Raetz, "Induction of Kappa-Light Chain Synthesis in 70z/3 B-Lymphoma Cells by Chemically Defined Lipid-a Precursors," *Journal of Biological Chemistry,* vol. 263, pp. 5098-5103, Apr 15 1988.

[61] J. Epstein, M. M. Lee, C. E. Kelly, and P. K. Donahoe, "Effect of Escherichia-Coli Endotoxin on Mammalian-Cell Growth and Recombinant Protein-Production," *In Vitro Cellular & Developmental Biology,* vol. 26, pp. 1121-1122, Dec 1990.

[62] S. Y. Tao and T. M. Mckenna, "In-Vitro Endotoxin Exposure Induces Contractile Dysfunction in Adult-Rat Cardiac Myocytes," *American Journal of Physiology-Heart and Circulatory Physiology,* vol. 267, pp. H1745-H1752, Nov 1994.

[63] T. Mattern, A. Thanhauser, N. Reiling, K. M. Toellner, M. Duchrow, S. Kusumoto, E. T. Rietschel, M. Ernst, H. Brade, H. D. Flad, and A. J. Ulmer, "Endotoxin and Lipid-a Stimulate Proliferation of Human T-Cells in the Presence of Autologous Monocytes," *Journal of Immunology,* vol. 153, pp. 2996-3004, Oct 1 1994.

[64] J. J. Wille, J. Park, and A. Elgavish, "Effects of Growth-Factors, Hormones, Bacterial Lipopolysaccharides, and Lipoteichoic Acids on the Clonal Growth of Normal Ureteral Epithelial-Cells in Serum-Free Culture," *Journal of Cellular Physiology,* vol. 150, pp. 52-58, Jan 1992.

[65] M. J. Usher, *Sensors and transducers* London: Macmillan, 1985.

[66] R. M. White, "A Sensor Classification Scheme," *Ieee Transactions on Ultrasonics Ferroelectrics and Frequency Control,* vol. 34, pp. 124-126, Mar 1987.

[67] A. Hulanicki, S. Glab, and F. Ingman, "Chemical Sensors Definitions and Classification," *Pure and Applied Chemistry,* vol. 63, pp. 1247-1250, Sep 1991.

[68] Y. X. Wang, Z. Z. Ye, and Y. B. Ying, "New Trends in Impedimetric Biosensors for the Detection of Foodborne Pathogenic Bacteria," *Sensors,* vol. 12, pp. 3449-3471, Mar 2012.

[69] T. R. J. Holford, F. Davis, and S. P. J. Higson, "Recent trends in antibody based sensors," *Biosensors & Bioelectronics,* vol. 34, pp. 12-24, Apr 15 2012.

[70] T. Vo-Dinh and B. Cullum, "Biosensors and biochips: advances in biological and medical diagnostics," *Fresenius Journal of Analytical Chemistry,* vol. 366, pp. 540-551, Mar-Apr 2000.

[71] C. N. Kotanen, F. G. Moussy, S. Carrara, and A. Guiseppi-Elie, "Implantable enzyme amperometric biosensors," *Biosensors & Bioelectronics,* vol. 35, pp. 14-26, May 15 2012.

[72] S. Chemburu, E. Wilkins, and I. Abdel-Hamid, "Detection of pathogenic bacteria in food samples using highly-dispersed carbon particles," *Biosensors & Bioelectronics,* vol. 21, pp. 491-499, Sep 15 2005.

[73] S. H. Chen, V. C. H. Wu, Y. C. Chuang, and C. S. Lin, "Using oligonucleotide-functionalized Au nanoparticles to rapidly detect foodborne pathogens on a piezoelectric biosensor," *Journal of Microbiological Methods,* vol. 73, pp. 7-17, Apr 2008.

[74] D. Zhang and E. C. Alocilja, "Characterization of nanoporous silicon-based DNA biosensor for the detection of Salmonella Enteritidis," *IEEE Sensors Journal,* vol. 8, pp. 775-780, May-Jun 2008.

[75] P. Banerjee and A. K. Bhunia, "Cell-based biosensor for rapid screening of pathogens and toxins," *Biosensors & Bioelectronics,* vol. 26, pp. 99-106, Sep 15 2010.

[76] L. Silbert, I. Ben Shlush, E. Israel, A. Porgador, S. Kolusheva, and R. Jelinek, "Rapid chromatic detection of bacteria by use of a new biomimetic polymer sensor," *Applied and Environmental Microbiology,* vol. 72, pp. 7339-7344, Nov 2006.

[77] A. Singh, D. Arutyunov, C. M. Szymanski, and S. Evoy, "Bacteriophage based probes for pathogen detection," *Analyst,* vol. 137, pp. 3405-3421, 2012.

[78] A. G. Rand, J. M. Ye, C. W. Brown, and S. V. Letcher, "Optical biosensors for food pathogen detection," *Food Technology,* vol. 56, pp. 32-+, Mar 2002.

[79] K. Narsaiah, S. N. Jha, R. Bhardwaj, R. Sharma, and R. Kumar, "Optical biosensors for food quality and safety assurance-a review," *Journal of Food Science and Technology-Mysore,* vol. 49, pp. 383-406, Aug 2012.

[80] S. M. Tripathi, W. J. Bock, P. Mikulic, R. Chinnappan, A. Ng, M. Tolba, and M. Zourob, "Long period grating based biosensor for the detection of Escherichia coli bacteria," *Biosensors & Bioelectronics,* vol. 35, pp. 308-312, May 15 2012.

[81] R. Bharadwaj, V. V. R. Sai, K. Thakare, A. Dhawangale, T. Kundu, S. Titus, P. K. Verma, and S. Mukherji, "Evanescent wave absorbance based fiber optic biosensor for label-free detection of E. coli at 280 nm wavelength," *Biosensors & Bioelectronics,* vol. 26, pp. 3367-3370, Mar 15 2011.

[82] A. M. Valadez, C. A. Lana, S. I. Tu, M. T. Morgan, and A. K. Bhunia, "Evanescent Wave Fiber Optic Biosensor for Salmonella Detection in Food," *Sensors,* vol. 9, pp. 5810-5824, Jul 2009.

[83] S. H. Ko and S. A. Grant, "A novel FRET-based optical fiber biosensor for rapid detection of Salmonella typhimurium," *Biosensors & Bioelectronics,* vol. 21, pp. 1283-1290, Jan 15 2006.

[84] T. Geng, M. T. Morgan, and A. K. Bhunia, "Detection of low levels of Listeria monocytogenes cells by using a fiber-optic immunosensor," *Applied and Environmental Microbiology,* vol. 70, pp. 6138-6146, Oct 2004.

[85] S. H. Ohk, O. K. Koo, T. Sen, C. M. Yamamoto, and A. K. Bhunia, "Antibody-aptamer functionalized fibre-optic biosensor for specific detection of Listeria monocytogenes from food," *Journal of Applied Microbiology,* vol. 109, pp. 808-817, Sep 2010.

[86] P. Villalobos, M. I. Chavez, Y. Olguin, E. Sanchez, E. Valdes, R. Galindo, and M. E. Young, "The application of polymerized lipid vesicles as colorimetric biosensors for real-time detection of pathogens in drinking water," *Electronic Journal of Biotechnology,* vol. 15, Jan 15 2012.

[87] T. J. Gnanaprakasa, O. A. Oyarzabal, E. V. Olsen, V. A. Pedrosa, and A. L. Simonian, "Tethered DNA scaffolds on optical sensor platforms for detection of hipO gene from Campylobacter jejuni," *Sensors and Actuators B-Chemical,* vol. 156, pp. 304-311, Aug 10 2011.

[88] W. Su, M. Lin, H. Lee, M. Cho, W. S. Choe, and Y. Lee, "Determination of endotoxin through an aptamer-based impedance biosensor," *Biosensors & Bioelectronics,* vol. 32, pp. 32-36, Feb 15 2012.

[89] M. D. Marazuela and M. C. Moreno-Bondi, "Fiber-optic biosensors - an overview," *Analytical and Bioanalytical Chemistry,* vol. 372, pp. 664-682, Mar 2002.

[90] Kerstin Länge, Bastian E. Rapp, and Michael Rapp, *Surface acoustic wave biosensors: a review* vol. 391. Berlin: Springer-Verlag, 2008.

[91] Y. X. Wang, Z. Z. Ye, C. Y. Si, and Y. B. Ying, "Subtractive Inhibition Assay for the Detection of E. coli O157:H7 Using Surface Plasmon Resonance," *Sensors,* vol. 11, pp. 2728-2739, Mar 2011.

[92] O. Torun, I. H. Boyaci, E. Temur, and U. Tamer, "Comparison of sensing strategies in SPR biosensor for rapid and sensitive enumeration of bacteria," *Biosensors & Bioelectronics,* vol. 37, pp. 53-60, Aug-Sep 2012.

[93] D. C. Zhang, Y. R. Yan, Q. Li, T. X. Yu, W. Cheng, L. Wang, H. X. Ju, and S. J. Ding, "Label-free and high-sensitive detection of Salmonella using a surface plasmon resonance DNA-based biosensor," *Journal of Biotechnology,* vol. 160, pp. 123-128, Aug 31 2012.

[94] Bi, *Application of SPR to Bacteriology: Endotoxin/Protein Interaction Studies* vol. 109. Tempe: Biosensing Instrument, Inc, 2012.

[95] Y. Li, W. A. Dick, and O. H. Tuovinen, "Fluorescence microscopy for visualization of soil microorganisms - a review," *Biology and Fertility of Soils,* vol. 39, pp. 301-311, Apr 2004.

[96] L. J. Goeller and M. R. Riley, "Discrimination of bacteria and bacteriophages by Raman spectroscopy and surface-enhanced Raman spectroscopy," *Applied Spectroscopy,* vol. 61, pp. 679-685, Jul 2007.

[97] S. Mura, G. Greppi, M. L. Marongiu, P. P. Roggero, S. P. Ravindranath, L. J. Mauer, N. Schibeci, F. Perria, M. Piccinini, P. Innocenzi, and J. Irudayaraj, "FTIR nanobiosensors for Escherichia coli detection," *Beilstein Journal of Nanotechnology,* vol. 3, pp. 485-492, Jul 3 2012.

[98] A. Ramachandran, S. Wang, J. Clarke, S. J. Ja, D. Goad, L. Wald, E. M. Flood, E. Knobbe, J. V. Hryniewicz, S. T. Chu, D. Gill, W. Chen, O. King, and B. E. Little, "A universal biosensing platform based on optical micro-ring resonators," *Biosensors & Bioelectronics,* vol. 23, pp. 939-944, Feb 28 2008.

[99] P. Arora, A. Sindhu, N. Dilbaghi, and A. Chaudhury, "Biosensors as innovative tools for the detection of food borne pathogens," *Biosensors & Bioelectronics,* vol. 28, pp. 1-12, Oct 15 2011.

[100] M. Aizawa, "Principles and Applications of Electrochemical and Optical Biosensors," *Analytica Chimica Acta,* vol. 250, pp. 249-256, Oct 1 1991.

[101] A. L. Ghindilis, P. Atanasov, M. Wilkins, and E. Wilkins, "Immunosensors: Electrochemical sensing and other engineering approaches," *Biosensors & Bioelectronics,* vol. 13, pp. 113-131, Jan 1 1998.

[102] J. J. Gau, E. H. Lan, B. Dunn, C. M. Ho, and J. C. S. Woo, "A MEMS based amperometric detector for E-Coli bacteria using self-assembled monolayers," *Biosensors & Bioelectronics,* vol. 16, pp. 745-755, Dec 2001.

[103] Y. Li, P. Cheng, J. H. Gong, L. C. Fang, J. Deng, W. B. Liang, and J. S. Zheng, "Amperometric immunosensor for the detection of Escherichia coli O157:H7 in food specimens," *Analytical Biochemistry,* vol. 421, pp. 227-233, Feb 1 2012.

[104] S. Jizhou, B. Chao, Q. Lan, and X. Shanhong, "A Micro Amperometric Immunosensor immobilized with Electropolymerized Staphylococcal Protein A for the Detection of Salmonella Typhimurium," *2009 4th Ieee International Conference on Nano/Micro Engineered and Molecular Systems, Vols 1 and 2,* pp. 295-298, 2009.

[105] M. Pohanka and P. Skladai, "Electrochemical biosensors - principles and applications," *Journal of Applied Biomedicine,* vol. 6, pp. 57-64, 2008.

[106] Kauffmann J.M and Guilbault G.G, "Potentiometric enzyme electrodes.," *Bioprocess Technology,* vol. 15, pp. 63-82, 1991.

[107] C. Ercole, M. Del Gallo, L. Mosiello, S. Baccella, and A. Lepidi, "Escherichia coli detection in vegetable food by a potentiometric biosensor," *Sensors and Actuators B-Chemical,* vol. 91, pp. 163-168, Jun 1 2003.

[108] J. R. Sandifer and J. J. Voycheck, "A review of biosensor and industrial applications of pH-ISFETs and an evaluation of Honeywell's "DuraFET"," *Mikrochimica Acta,* vol. 131, pp. 91-98, 1999.

[109] A. G. Gehring, D. L. Patterson, and S. I. Tu, "Use of a light-addressable potentiometric sensor for the detection of Escherichia coli O157 : H7," *Analytical Biochemistry,* vol. 258, pp. 293-298, May 1 1998.

[110] L. Yang and R. Bashir, "Electrical/electrochemical impedance for rapid detection of foodborne pathogenic bacteria," *Biotechnology Advances,* vol. 26, pp. 135-150, Mar-Apr 2008.

[111] E. Barsoukov and J. R. Macdonald, *Impedance Spectroscopy Theory, Experiment and Applications*, 2nd ed. Hoboken, New Jersey: John Wiley & Sons Ltd., 2005.
[112] S. Radke and E. Alocilja., "Design and Fabrication of a Microimpedance Biosensor for Bacterial Detection," *IEEE Sensors Journal,* vol. 4, pp. 434-440, August 2004.
[113] L. J. Yang, Y. B. Li, C. L. Griffis, and M. G. Johnson, "Interdigitated microelectrode (IME) impedance sensor for the detection of viable Salmonella typhimurium," *Biosensors & Bioelectronics,* vol. 19, pp. 1139-1147, May 15 2004.
[114] L. J. Yang, Y. B. Li, and G. F. Erf, "Interdigitated array microelectrode-based electrochemical impedance immunosensor for detection of Escherichia coli O157 : H7," *Analytical Chemistry,* vol. 76, pp. 1107-1113, Feb 15 2004.
[115] M. S. Mannoor, S. Y. Zhang, A. J. Link, and M. C. McAlpine, "Electrical detection of pathogenic bacteria via immobilized antimicrobial peptides," *Proceedings of the National Academy of Sciences of the United States of America,* vol. 107, pp. 19207-19212, Nov 9 2010.
[116] Z. Mubammad-Tahir and E. C. Alocilja, "A conductometric biosensor for biosecurity," *Biosensors & Bioelectronics,* vol. 18, pp. 813-819, May 2003.
[117] S. Pal, W. Ying, E. C. Alocija, and F. P. Downes, "Sensitivity and specificity performance of a direct-charge transfer biosensor for detecting Bacillus cereus in selected food matrices," *Biosystems Engineering,* vol. 99, pp. 461-468, Apr 2008.
[118] Selma Mutlu, *Mass Sensitive Biosensors: Principles and Applications in Food*. Boca Raton, Florida: CRC Press, 2010.
[119] K. A. Marx, "Quartz crystal microbalance: A useful tool for studying thin polymer films and complex biomolecular systems at the solution-surface interface," *Biomacromolecules,* vol. 4, pp. 1099-1120, Sep-Oct 2003.
[120] K. S. Carmon, R. E. Baltus, and L. A. Luck, "A piezoelectric quartz crystal biosensor: The use of two single cysteine mutants of the periplasmic Escherichia coli glucose/galactose receptor as target proteins for the detection of glucose," *Biochemistry,* vol. 43, pp. 14249-14256, Nov 9 2004.
[121] Z. H. Shen, M. C. Huang, C. D. Xiao, Y. Zhang, X. Q. Zeng, and P. G. Wang, "Nonlabeled quartz crystal microbalance biosensor for bacterial detection using carbohydrate and lectin recognitions," *Analytical Chemistry,* vol. 79, pp. 2312-2319, Mar 15 2007.
[122] R. M. White and F. W. Voltmer, "Direct Piezoelectric Coupling to Surface Elastic Waves," *Applied Physics Letters,* vol. 7, pp. 314-316, 1965.
[123] M. I. Rocha-Gaso, C. March-Iborra, A. Montoya-Baides, and A. Arnau-Vives, "Surface Generated Acoustic Wave Biosensors for the Detection of Pathogens: A Review," *Sensors,* vol. 9, pp. 5740-5769, Jul 2009.
[124] K. Lange, B. E. Rapp, and M. Rapp, "Surface acoustic wave biosensors: a review," *Analytical and Bioanalytical Chemistry,* vol. 391, pp. 1509-1519, Jul 2008.
[125] M. U. Hammer, A. Brauser, C. Olak, G. Brezesinski, T. Goldmann, T. Gutsmann, and J. Andra, "Lipopolysaccharide interaction is decisive for the activity of the antimicrobial peptide NK-2 against Escherichia coil and Proteus mirabilis," *Biochemical Journal,* vol. 427, pp. 477-488, May 1 2010.
[126] T. M. Silk and C. W. Donnelly, "Increased detection of acid-injured Escherichia coli O157 : H7 in autoclaved apple cider by using nonselective repair on trypticase soy agar," *Journal of Food Protection,* vol. 60, pp. 1483-1486, Dec 1997.
[127] M.R. Adams and M.O Moss, *Food Microbiology*. Cambridge: The Royal Society of Chemistry, 1995.
[128] L. Goodridge, J. R. Chen, and M. Griffiths, "Development and characterization of a fluorescent-bacteriophage assay for detection of Escherichia coli O157 : H7," *Applied and Environmental Microbiology,* vol. 65, pp. 1397-1404, Apr 1999.
[129] J. Czajka and C. A. Batt, "A solid phase fluorescent capillary immunoassay for the detection of Escherichia coli O157:H7 in ground beef and apple cider," *Journal of Applied Bacteriology,* vol. 81, pp. 601-607, Dec 1996.

[130] L. S. L. Yu, S. A. Reed, and M. H. Golden, "Time-resolved fluorescence immunoassay (TRFIA) for the detection of Escherichia coli O157 : H7 in apple cider," *Journal of Microbiological Methods,* vol. 49, pp. 63-68, Mar 2002.
[131] B. W. Blais, J. Leggate, J. Bosley, and A. Martinez-Perez, "Comparison of fluorogenic and chromogenic assay systems in the detection of Escherichia coli O157 by a novel polymyxin-based ELISA," *Letters in Applied Microbiology,* vol. 39, pp. 516-522, 2004.
[132] P. Daly, T. Collier, and S. Doyle, "PCR-ELISA detection of Escherichia coli in milk," *Letters in Applied Microbiology,* vol. 34, pp. 222-226, 2002.
[133] Z. Fu, S. Rogelj, and T. L. Kieft, "Rapid detection of Escherichia coli O157 : H7 by immunomagnetic separation and real-time PCR," *International Journal of Food Microbiology,* vol. 99, pp. 47-57, Mar 1 2005.
[134] T. B. Tims and D. V. Lim, "Confirmation of viable E. coli O157 : H7 by enrichment and PCR after rapid biosensor detection," *Journal of Microbiological Methods,* vol. 55, pp. 141-147, Oct 2003.
[135] B. K. Oh, W. Lee, B. S. Chun, Y. M. Bae, W. H. Lee, and J. W. Choi, "Surface plasmon resonance immunosensor for the detection of Yersinia enterocolitica," *Colloids and Surfaces a-Physicochemical and Engineering Aspects,* vol. 257-58, pp. 369-374, May 5 2005.
[136] B. W. Brooks, J. Devenish, C. L. Lutze-Wallace, D. Milnes, R. H. Robertson, and G. Berlie-Surujballi, "Evaluation of a monoclonal antibody-based enzyme-linked immunosorbent assay for detection of Campylobacter fetus in bovine preputial washing and vaginal mucus samples," *Veterinary Microbiology,* vol. 103, pp. 77-84, Oct 5 2004.
[137] D. Ivnitski, I. Abdel-Hamid, P. Atanasov, and E. Wilkins, "Biosensors for detection of pathogenic bacteria," *Biosensors & Bioelectronics,* vol. 14, pp. 599-624, Oct 1999.
[138] S. A. Radke and E. C. Alocilja, "A high density microelectrode array biosensor for detection of E-coli O157 : H7," *Biosensors & Bioelectronics,* vol. 20, pp. 1662-1667, Feb 15 2005.
[139] L. P. Mansfield and S. J. Forsythe, "The detection of Salmonella serovars from animal feed and raw chicken using a combined immunomagnetic separation and ELISA method," *Food Microbiology,* vol. 18, pp. 361-366, Aug 2001.
[140] L. Croci, E. Delibato, G. Volpe, and G. Palleschi, "A rapid electrochemical ELISA for the detection of salmonella in meat samples," *Analytical Letters,* vol. 34, pp. 2597-2607, 2001.
[141] S. Perelle, F. Dilasser, B. Malorny, J. Grout, J. Hoorfar, and P. Fach, "Comparison of PCR-ELISA and LightCycler real-time PCR assays for detecting Salmonella spp. in milk and meat samples," *Molecular and Cellular Probes,* vol. 18, pp. 409-420, Dec 2004.
[142] Y. Y. Wong, S. P. Ng, M. H. Ng, S. H. Si, S. Z. Yao, and Y. S. Fung, "Immunosensor for the differentiation and detection of Salmonella species based on a quartz crystal microbalance," *Biosensors & Bioelectronics,* vol. 17, pp. 676-684, Aug 2002.
[143] J. D. Brewster, A. G. Gehring, R. S. Mazenko, L. J. VanHouten, and C. J. Crawford, "Immunoelectrochemical assays for bacteria: Use of epifluorescence microscopy and rapid-scan electrochemical techniques in development of an assay for Salmonella," *Analytical Chemistry,* vol. 68, pp. 4153-4159, Dec 1 1996.
[144] O. S. Wolfbeis, "Fiber-optic chemical sensors and biosensors," *Analytical Chemistry,* vol. 74, pp. 2663-2677, Jun 15 2002.
[145] Huimin Ouyang and P. M. Fauchet, "Biosensing using Porous Silicon Photonic Bandgap Structures," in *Photonic Crystals and Photonic Crystal Fibers for Sensing Applications*, Boston, MA, 2005, pp. 31-45.
[146] C. K. Joung, H. N. Kim, H. C. Im, H. Y. Kim, M. H. Oh, and Y. R. Kim, "Ultra-sensitive detection of pathogenic microorganism using surface-engineered impedimetric immunosensor," *Sensors and Actuators B-Chemical,* vol. 161, pp. 824-831, Jan 3 2012.
[147] W. J. Buttner, J. R. Stetter, and M. W. Findlay, "Chemical sensor research at the Illinois Institute of Technology International Center for Sensor Science and Engineering

(ICSSE)," *Abstracts of Papers of the American Chemical Society,* vol. 233, pp. 835-835, Mar 25 2007.

[148] S. J. Ding, B. W. Chang, C. C. Wu, C. J. Chen, and H. C. Chang, "A new method for detection of endotoxin on polymyxin B-immobilized gold electrodes," *Electrochemistry Communications,* vol. 9, pp. 1206-1211, May 2007.

[149] T. Y. Yeo, J. S. Choi, B. K. Lee, B. S. Kim, H. I. Yoon, H. Y. Lee, and Y. W. Cho, "Electrochemical endotoxin sensors based on TLR4/MD-2 complexes immobilized on gold electrodes," *Biosensors & Bioelectronics,* vol. 28, pp. 139-145, Oct 15 2011.

[150] K. G. Ong, J. M. Leland, K. F. Zeng, G. Barrett, M. Zourob, and C. A. Grimes, "A rapid highly-sensitive endotoxin detection system," *Biosensors & Bioelectronics,* vol. 21, pp. 2270-2274, Jun 15 2006.

[151] W. Limbut, M. Hedstrom, P. Thavarungkul, P. Kanatharana, and B. Mattiasson, "Capacitive biosensor for detection of endotoxin," *Analytical and Bioanalytical Chemistry,* vol. 389, pp. 517-525, Sep 2007.

[152] S. Yoshida, T. Gyoji, and K. Toda, "Position-Sensitive Photodetector Using Interdigital Electrodes on Pb2cro5 Thin-Films," *International Journal of Electronics,* vol. 68, pp. 525-531, Apr 1990.

[153] S. Averin, R. Sachot, J. Hugi, M. deFays, and M. Ilegems, "Two-dimensional device modeling and analysis of GaInAs metal-semiconductor-metal photodiode structures," *Journal of Applied Physics,* vol. 80, pp. 1553-1558, Aug 1 1996.

[154] S. H. Lee, S. L. Lee, H. Y. Kim, and T. Y. Eom, "Analysis of light efficiency in homogeneously aligned nematic liquid crystal display with interdigital electrodes," *Journal of the Korean Physical Society,* vol. 35, pp. S1111-S1114, Dec 1999.

[155] Y. J. Chen, C. L. Zhu, M. S. Cao, and T. H. Wang, "Photoresponse of SnO2 nanobelts grown in situ on interdigital electrodes," *Nanotechnology,* vol. 18, pp. -, Jul 18 2007.

[156] T. M. A. Gronewold, "Surface acoustic wave sensors in the bioanalytical field: Recent trends and challenges," *Analytica Chimica Acta,* vol. 603, pp. 119-128, Nov 12 2007.

[157] R. Weigel and R. Hauser, "Introduction to the special issue on acoustic wave sensors and applications," *Ieee Transactions on Ultrasonics Ferroelectrics and Frequency Control,* vol. 51, pp. 1365-1366, Nov 2004.

[158] S. Shiokawa and J. Kondoh, "Surface acoustic wave sensors," *Japanese Journal of Applied Physics Part 1-Regular Papers Brief Communications & Review Papers,* vol. 43, pp. 2799-2802, May 2004.

[159] B. Drafts, "Acoustic wave technology sensors," *Ieee Transactions on Microwave Theory and Techniques,* vol. 49, pp. 795-802, Apr 2001.

[160] M. Hoummady, A. Campitelli, and W. Wlodarski, "Acoustic wave sensors: design, sensing mechanisms and applications," *Smart Materials & Structures,* vol. 6, pp. 647-657, Dec 1997.

[161] J. J. Steele, M. T. Taschuk, and M. J. Brett, "Nanostructured metal oxide thin films for humidity sensors," *Ieee Sensors Journal,* vol. 8, pp. 1422-1429, Jul-Aug 2008.

[162] J. J. Steele, G. A. Fitzpatrick, and M. J. Brett, "Capacitive humidity sensors with high sensitivity and subsecond response times," *Ieee Sensors Journal,* vol. 7, pp. 955-956, May-Jun 2007.

[163] C. Y. Lee and G. B. Lee, "Humidity sensors: A review," *Sensor Letters,* vol. 3, pp. 1-15, Mar 2005.

[164] P. Furjes, A. Kovacs, C. Ducso, M. Adam, B. Muller, and U. Mescheder, "Porous silicon-based humidity sensor with interdigital electrodes and internal heaters," *Sensors and Actuators B-Chemical,* vol. 95, pp. 140-144, Oct 15 2003.

[165] M. Kitsara, D. Goustouridis, S. Chatzandroulis, M. Chatzichristidi, I. Raptis, T. Ganetsos, R. Igreja, and C. J. Dias, "Single chip interdigitated electrode capacitive chemical sensor arrays," *Sensors and Actuators B-Chemical,* vol. 127, pp. 186-192, Oct 20 2007.

[166] R. Igreja and C. J. Dias, "Dielectric response of interdigital chemocapacitors: The role of the sensitive layer thickness," *Sensors and Actuators B-Chemical,* vol. 115, pp. 69-78, May 23 2006.

[167] R. Igreja and C. J. Dias, "Organic vapour discrimination using sorption sensitive chemocapacitor arrays," *Advanced Materials Forum Iii, Pts 1 and 2,* vol. 514-516, pp. 1064-1067, 2006.
[168] R. Igreja and C. J. Dias, "Capacitance response of polysiloxane films with interdigital electrodes to volatile organic compounds," *Advanced Materials Forum Ii,* vol. 455-456, pp. 420-424, 2004.
[169] C. Ziegler, J. Maier, and H. D. Wiemhofer, "Chemical sensors and sensor technology," *Physical Chemistry Chemical Physics,* vol. 5, pp. Vii-Vii, Dec 1 2003.
[170] C. Hagleitner, A. Hierlemann, D. Lange, A. Kummer, N. Kerness, O. Brand, and H. Baltes, "Smart single-chip gas sensor microsystem," *Nature,* vol. 414, pp. 293-296, Nov 15 2001.
[171] W. Olthuis, A. J. Sprenkels, J. G. Bomer, and P. Bergveld, "Planar interdigitated electrolyte-conductivity sensors on an insulating substrate covered with Ta2O5," *Sensors and Actuators B- Chemical,* vol. 43, pp. 211-216, 1997.
[172] K. Toda, Y. Komatsu, S. Oguni, S. Hashiguchi, and I. Sanemasa, "A planar gas sensor combined with interdigitated array electrodes," *Analytical Sciences,* vol. 15, pp. 87-89, Jan 1999.
[173] K. Sundara-Rajan, L. Byrd, and A. V. Mamishev, "Moisture content estimation in paper pulp using fringing field impedance Spectroscopy," *Ieee Sensors Journal,* vol. 4, pp. 378-383, Jun 2004.
[174] K. Sundara-Rajan, L. Byrd, and A. V. Mamishev, "Measuring moisture, fiber, and titanium dioxide in pulp with impedance spectroscopy," *Tappi Journal,* vol. 4, pp. 23-27, Feb 2005.
[175] E. Fratticcioli, M. Dionigi, and R. Sorrentino, "A simple and low-cost measurement system for the complex permittivity characterization of materials," *Ieee Transactions on Instrumentation and Measurement,* vol. 53, pp. 1071-1077, Aug 2004.
[176] U. Latif and F. L. Dickert, "Conductometric Sensors for Monitoring Degradation of Automotive Engine Oil," *Sensors,* vol. 11, pp. 8611-8625, Sep 2011.
[177] X. Li, "Impedance Spectroscopy for Manufacturing Control of Material Physical Properties," Master of Science in Electrical Engineering, Department of Electrical Engineering, University of Washington, Washington, 2003.
[178] S. Baglio, S. Castorina, and N. Savalli, "Integrated inductive sensors for the detection of magnetic microparticles," *Ieee Sensors Journal,* vol. 5, pp. 372-384, Jun 2005.
[179] A. V. Mamishev, K. Sundara-Rajan, F. Yang, Y. Q. Du, and M. Zahn, "Interdigital sensors and transducers," *Proceedings of the Ieee,* vol. 92, pp. 808-845, May 2004.
[180] V. Kasturi and S. C. Mukhopadhyay, "Estimation of Property of Sheep Skin to Modify the Tanning Process Using Interdigital Sensors " in *Sensors: Advancements in Modeling, Design Issues, Fabrication and Practical Applications* vol. 21, S. C. M. a. R. Y. M. Huang, Ed., ed: Springer Berlin Heidelberg, 2008, pp. 91-110.
[181] S. C. Mukhopadhyay, S. D. Choudhury, T. Allsop, V. Kasturi, and G. E. Norris, "Assessment of pelt quality in leather making using a novel non-invasive sensing approach," *Journal of Biochemical and Biophysical Methods,* vol. 70, pp. 809-815, Apr 24 2008.
[182] S. C. Mukhopadhyay, G. Sen Gupta, and S. N. Demidenko, "Special issue on intelligent sensors - Guest Editorial," *Ieee Sensors Journal,* vol. 7, pp. 608-610, May-Jun 2007.
[183] S. C. Mukhopadhyay, "Planar electromagnetic sensors: Characterization, applications and experimental results," *Tm-Technisches Messen,* vol. 74, pp. 290-297, 2007.
[184] S. C. Mukhopadhyay, "Novel planar electromagnetic sensors: Modeling and performance evaluation," *Sensors,* vol. 5, pp. 546-579, Dec 2005.
[185] S. C. Mukhopadhyay, J. D. M. Woolley, G. S. Gupta, and S. Deidenko, "Saxophone Reed Inspection Employing Planar Electromagnetic Sensors," *IEEE Transactions on Instrumentation and Measurements,* vol. 56, pp. 2492-2503, Dec 2007.
[186] S. C. Mukhopadhyay, C. Goonerate, G. S. Gupta, and S. Demidenko, "A Low Cost Sensing System for Quality of Dairy Products," *IEEE Transactions on Instrumentation and Measurements,* vol. 55, pp. 1331-1338, August 2006.

[187] S. C. Mukhopadhyay and C. P. Gooneratne, "A Novel Planar-Type Biosensor for Noninvasive Meat Inspection," *IEEE Sensors Journal,* vol. 7, pp. 1340-1346, September 2007.

[188] A. V. Mamishev, Y. Du, J. H. Bau, B. C. Lesieutre, and M. Zahn, "Evaluation of diffusion-driven material property profiles using three-wavelength interdigital sensor," *Ieee Transactions on Dielectrics and Electrical Insulation,* vol. 8, pp. 785-798, Oct 2001.

[189] A. S. Abu-Abed and R. G. Lindquist, "Capacitive interdigital sensor with inhomogeneous nematic liquid crystal film," *Progress In Electromagnetics Research B,* vol. 7, pp. 75-87, 2008.

[190] I. Shitanda, A. Okumura, M. Itagaki, K. Watanabe, and Y. Asano, "Screen-printed atmospheric corrosion monitoring sensor based on electrochemical impedance spectroscopy," *Sensors and Actuators B-Chemical,* vol. 139, pp. 292-297, Jun 4 2009.

[191] G. Rinaldi and T. Huber, "Multi-Node Sensor for Corrosion Monitoring: Characteristics and Configuration," DR DC Atlantic TM 2010-113 ed. Dartmouth, Nova Scotia: Defence R &D C anada – Atlantic, 2010, p. 48.

[192] H. Gu and M. L. Wang, "A Monolithic Interdigitated PVDF Transducer for Lamb Wave Inspection," *Structural Health Monitoring-an International Journal,* vol. 8, pp. 137-148, Mar 2009.

[193] A. A. Nassr and W. W. El-Dakhakhni, "Improved interdigital sensors for structural health monitoring of composite retrofit systems," *Journal of Reinforced Plastics and Composites,* vol. 30, pp. 621-629, Apr 2011.

[194] I. D. Nickson, C. Boxall, and S. N. Port, "Interdigitated electrode array based sensors for environmental monitoring of caesium " in *Actinides 2009: Materials Science and Engineering*, San Francisco, California, USA, 2010, pp. 1-9.

[195] M. A. M. Yunus and S. C. Mukhopadhyay, "Novel Planar Electromagnetic Sensors for Detection of Nitrates and Contamination in Natural Water Sources," *IEEE Sensors Journal,* vol. 11, pp. 1440-1447, Jun 2011.

[196] E. Dinckaya, O. Kinik, M. K. Sezginturk, C. Altug, and A. Akkoca, "Development of an impedimetric aflatoxin M1 biosensor based on a DNA probe and gold nanoparticles," *Biosensors & Bioelectronics,* vol. 26, pp. 3806-3811, May 15 2011.

[197] O. A. Loaiza, P. J. Lamas-Ardisana, E. Jubete, E. Ochoteco, I. Loinaz, G. Cabanero, I. Garcia, and S. Penades, "Nanostructured Disposable Impedimetric Sensors as Tools for Specific Biomolecular Interactions: Sensitive Recognition of Concanavalin A," *Analytical Chemistry,* vol. 83, pp. 2987-2995, Apr 15 2011.

[198] F. Segura-Quijano, J. Sacristan-Riquelme, J. Garcia-Canton, M. T. Oses, and A. Baldi, "Towards Fully Integrated Wireless Impedimetric Sensors," *Sensors,* vol. 10, pp. 4071-4082, Apr 2010.

[199] J. Suehiro, M. Shutou, T. Hatano, and M. Hara, "High sensitive detection of biological cells using dielectrophoretic impedance measurement method combined with electropermeabilization," *Sensors and Actuators B-Chemical,* vol. 96, pp. 144-151, Nov 15 2003.

[200] P. Ertl and R. Heer, *Interdigitated impedance sensors for analysis of biological cells in microfluidic biochips* vol. 126. Berlin: Springer-Verlag, 2009.

[201] S. Rana, R. H. Page, and C. J. McNeil, "Impedance spectra analysis to characterize interdigitated electrodes as electrochemical sensors," *Electrochimica Acta,* vol. 56, pp. 8559-8563, Oct 1 2011.

[202] M. Varshney, Y. B. Li, B. Srinivasan, and S. Tung, "A label-free, microfluidics and interdigitated array microelectrode-based impedance biosensor in combination with nanoparticles immunoseparation for detection of Escherichia coli O157 : H7 in food samples," *Sensors and Actuators B-Chemical,* vol. 128, pp. 99-107, Dec 12 2007.

[203] V. Kasturi, "Quality improvement of leather tanning process using a novel sensor," Master of Engineering, School of Engineering and Advanced Technology, Massey, Palmerston North, 2008.

[204] A. R. M. Syaifudin, K. P. Jayasundera, and S. C. Mukhopadhyay, "A low cost novel sensing system for detection of dangerous marine biotoxins in seafood," *Sensors and Actuators B-Chemical,* vol. 137, pp. 67-75, Mar 28 2009.
[205] A. R. Mohd Syaifudin, K. P. Jayasundera, and S. C. Mukhopadhyay, "Initial Investigation of Using Planar Interdigital Sensors for Assessment of Quality in Seafood," *Hindawi: Journal of Sensors,* vol. 2008, p. 9, 2008.
[206] M. A. M. Yunus and S. C. Mukhopadhyay, "Development of planar electromagnetic sensors for measurement and monitoring of environmental parameters," *Measurement Science & Technology,* vol. 22, Feb 2011.
[207] C. R. Bowen, A. Bowles, S. Drake, N. Johnson, and S. Mahon, "Fabrication and finite element modelling of interdigitated electrodes," *Ferroelectrics,* vol. 228, pp. 257-269, 1999.
[208] L. A. Ramajo, D. E. Ramajo, M. M. Reboredo, D. H. Santiago, and M. S. Castro, "Evaluation and Modelling of Integral Capacitors Produced by Interdigitated Comb Electrodes," *Materials Research-Ibero-American Journal of Materials,* vol. 11, pp. 471-476, Oct-Dec 2008.
[209] A. K. Sen and J. Darabi, "Modeling and optimization of a microscale capacitive humidity sensor for HVAC applications," *IEEE Sensors Journal,* vol. 8, pp. 333-340, Mar-Apr 2008.
[210] M. S. Webster, I. V. Timoshkin, S. J. MacGregor, and M. Mattey, "Computer Aided Modelling of an Interdigitated Microelectrode Array Impedance Biosensor for the Detection of Bacteria," *Ieee Transactions on Dielectrics and Electrical Insulation,* vol. 16, pp. 1356-1363, Oct 2009.
[211] COMSOL, *COMSOL Multiphysics: Modelling Guide*, COMSOL 3.5a ed.: COMSOL AB, 2008.
[212] S. C. Mukhopadhyay, C. P. Gooneratne, G. Sen Gupta, and S. Yamada, "Characterization and comparative evaluation of novel planar electromagnetic sensors," *IEEE Transactions on Magnetics,* vol. 41, pp. 3658-3660, Oct 2005.
[213] A. R. Mohd Syaifudin, S. C. Mukhopadhyay, and P. L. Yu, "Modelling and fabrication of optimum structure of novel interdigital sensors for food inspection," *International Journal of Numerical Modelling: Electronic Networks, Devices and Fields,* pp. 456-466, 2011.
[214] G. INSTEK, *Precision LCR Meter - User Manual*, Part No. 82CR-81900MJ1 ed. Taipei, Taiwan: Good Will Instrument Co., Ltd., 2010.
[215] E. J. Olson and P. Buhlmann, "Minimizing Hazardous Waste in the Undergraduate Analytical Laboratory: A Microcell for Electrochemistry," *Journal of Chemical Education,* vol. 87, pp. 1260-1261, Nov 2010.
[216] M. Khafaji, S. Shahrokhian, and M. Ghalkhani, "Electrochemistry of Levo-Thyroxin on Edge-Plane Pyrolytic Graphite Electrode: Application to Sensitive Analytical Determinations," *Electroanalysis,* vol. 23, pp. 1875-1880, Aug 2011.
[217] J. Fischer, H. Dejmkova, and J. Barek, "Electrochemistry of Pesticides and its Analytical Applications," *Current Organic Chemistry,* vol. 15, pp. 2923-2935, Sep 2011.
[218] C. V. Vidal and A. I. Munoz, "Effect of physico-chemical properties of simulated body fluids on the electrochemical behaviour of CoCrMo alloy," *Electrochimica Acta,* vol. 56, pp. 8239-8248, Oct 1 2011.
[219] C. Wolner, G. E. Nauer, J. Trummer, V. Putz, and S. Tschegg, "Possible reasons for the unexpected bad biocompatibility of metal-on-metal hip implants," *Materials Science & Engineering C-Biomimetic and Supramolecular Systems,* vol. 26, pp. 34-40, Jan 2006.
[220] C. Xhoffer, K. Van den Bergh, and H. Dillen, "Electrochemistry: a powerful analytical tool in steel research," *Electrochimica Acta,* vol. 49, pp. 2825-2831, Jul 30 2004.
[221] D. Landolt, Ed., *Corrosion and surface chemistry of metals*. Lausanne, Switzerland.: EPFL Press, 2007, p.^pp. Pages.
[222] J. R. Macdonald, "Impedance Spectroscopy," *Annals of Biomedical Engineering,* vol. 20, pp. 289-305, 1992.

[223] M. E. Orazem and B. Tribollet, *Electrochemical Impedance Spectroscopy*, 1st ed. Hoboken, New Jersey: John Wiley & Sons, 2008.
[224] Gamry, *Application Note: Basic Of Electrochemical Impedance Spectroscopy* vol. Rev. 1.0 9/3/2010. Warminster, PA: GAMRY Instruments, 2010.
[225] E. Cano, D. Lafuente, and D. M. Bastidas, "Use of EIS for the evaluation of the protective properties of coatings for metallic cultural heritage: a review," *Journal of Solid State Electrochemistry,* vol. 14, pp. 381-391, Mar 2010.
[226] Sigma-Aldrich, *Biochemicals, Reagents and 117 Kits for Life Science Research*: Sigma-Aldrich Catalogue., 2010.
[227] A. R. M. Syaifudin, S. C. Mukhopadhyay, P. L. Yu, M. J. Haji-Sheikh, C. H. Chuang, J. D. Vanderford, and Y. Huang, "Measurements and Performance Evaluation of Novel Interdigital Sensors for Different Chemicals Related to Food Poisoning," *IEEE Sensors Journal,* vol. 11, pp. 2957 - 2965, November 2011.
[228] V. K. S. Hsiao, J. R. Waldeisen, Y. B. Zheng, P. F. Lloyd, T. J. Bunning, and T. J. Huang, "Aminopropyltriethoxysilane (APTES)-functionalized nanoporous polymeric gratings: fabrication and application in biosensing," *Journal of Materials Chemistry,* vol. 17, pp. 4896-4901, 2007.
[229] Rapiphun Janmanee, Sopis Chuekachang, Saengrawee Sriwichai, Akira Baba, and Sukon Phanichphant, "Functional Conducting Polymers in the Application of SPR Biosensors," *Journal of Nanotechnology,* p. 7, 2012.
[230] C. Chai, J. Lee, and P. Takhistov, "Direct Detection of the Biological Toxin in Acidic Environment by Electrochemical Impedimetric Immunosensor," *Sensors,* vol. 10, pp. 11414-11427, Dec 2010.
[231] J. H. O. Owino, O. A. Arotiba, N. Hendricks, E. A. Songa, N. Jahed, T. T. Waryo, R. F. Ngece, P. G. L. Baker, and E. I. Iwuoha, "Electrochemical Immunosensor Based on Polythionine/Gold Nanoparticles for the Determination of Aflatoxin B-1," *Sensors,* vol. 8, pp. 8262-8274, Dec 2008.
[232] Yu Zhang, Ruo Yuan, Yaqin Chai, Xia Zhong, and H. Zhong, "Amperometric sensor for nitrite using a glassy carbon electrode modified with thionine functionalized MWCNTs/Au nanorods/SDS nanohybrids," *Surface and Interface Analysis,* vol. 44, pp. 1233-1237, September 2012.
[233] H. J. Schneider, K. Kato, and R. M. Strongin, "Chemomechanical polymers as sensors and actuators for biological and medicinal applications," *Sensors,* vol. 7, pp. 1578-1611, Aug 2007.
[234] T. Hoare and R. Pelton, "Functional group distributions in carboxylic acid containing poly(N-isopropylacrylamide) microgels," *Langmuir,* vol. 20, pp. 2123-2133, Mar 16 2004.
[235] H. Li, J. Zhang, X. Z. Zhou, G. Lu, Z. Y. Yin, G. P. Li, T. Wu, F. Boey, S. S. Venkatraman, and H. Zhang, "Aminosilane Micropatterns on Hydroxyl-Terminated Substrates: Fabrication and Applications," *Langmuir,* vol. 26, pp. 5603-5609, Apr 20 2010.
[236] X. Y. Xu, Y. Feng, J. J. Li, F. Li, and H. J. Yu, "A novel protocol for covalent immobilization of thionine on glassy carbon electrode and its application in hydrogen peroxide biosensor," *Biosensors & Bioelectronics,* vol. 25, pp. 2324-2328, Jun 15 2010.
[237] M. M. M. Elnashar, "Review Article: Immobilized Molecules Using Biomaterials and Nanobiotechnology," *Journal of Biomaterials and Nanobiotechnology,* vol. 1, pp. 61-77, 2010.
[238] A. Lasia, "Electrochemical Impedance Spectroscopy and its Applications," in *Modern Aspects of Electrochemistry*. vol. 32, J. B. B. E. Conway, and R.E. White, Ed., ed New York: Kluwer Academic/Plenum Publishers, 1999, pp. 143-248.
[239] J. E. B. Randles, "Kinetics of Rapid Electrode Reactions," *Discussions of the Faraday Society,* vol. 1, pp. 11-19, 1947.
[240] J. R. Macdonald, *Impedance spectroscopy--Emphasizing solid materials and systems.* New York: Wiley-Interscience, 1987.

[241] C. M. Pettit and D. Roy, "Role of iodate ions in chemical mechanical and electrochemical mechanical planarization of Ta investigated using time-resolved impedance spectroscopy," *Materials Letters,* vol. 59, pp. 3885-3889, Dec 2005.
[242] J. Dzik, H. Bernard, K. Osinska, A. Lisinska-Czekaj, and D. Czekaj, "Synthesis, Structure and Dielectric Properties of Bi1-Xndxfeo3," *Archives of Metallurgy and Materials,* vol. 56, pp. 1119-1125, 2011.
[243] H. Sumi, T. Yamaguchi, K. Hamamoto, T. Suzuki, Y. Fujishiro, T. Matsui, and K. Eguchi, "AC impedance characteristics for anode-supported microtubular solid oxide fuel cells," *Electrochimica Acta,* vol. 67, pp. 159-165, Apr 15 2012.
[244] Y. Cao, T. Repo, R. Silvennoinen, T. Lehto, and P. Pelkonen, "Analysis of the willow root system by electrical impedance spectroscopy," *Journal of Experimental Botany,* vol. 62, pp. 351-358, Jan 2011.
[245] J. R. Macdonald and J. A. Garber, "Analysis of Impedance and Admittance Data for Solids and Liquids," *Journal of the Electrochemical Society,* vol. 124, pp. 1022-1030, 1977.
[246] D. ROY, *Roy Research Group: Corrosion monitoring using FT-EIS*. Clarkson University Potsdam, New York: http://people.clarkson.edu/~droy/Corrosion_EIS.htm, 2007.
[247] J. R. Macdonald and L. D. Potter, "A Flexible Procedure for Analyzing Impedance Spectroscopy Results - Description and Illustrations," *Solid State Ionics,* vol. 24, pp. 61-79, Jun 1987.
[248] J. R. Macdonald, *CNLS: LEVM / LEVMW Manual*, Version 8.11 ed. vol. 8.0. Chapel Hill: http://www.jrossmacdonald.com/LEVM/LEVMMANUAL.pdf, 2011.
[249] B. A. Boukamp, *Equivalent Circuit (EQUIVCRT.PAS): Users Manual ; the Computer Assisted Electrochemical Ac-immittance Data Analysis System for IBM-PC Computers and Compatibles, Written in Turbo Pascal Version 3.0*. AE Enschede, The Netherlands: University of Twente. Department of Chemical Technology, 1989.
[250] K. Pearson, "On lines and planes of closest fit to systems of points in space.," *Philosophical Magazine,* vol. 2, pp. 559-572, Jul-Dec 1901.
[251] H. Hotelling, "Analysis of a complex of statistical variables into principal components," *Journal of Educational Psychology,* vol. 24, pp. 417-441, 1933.
[252] I. T. Jolliffe, *Principal Component Analysis*, 2nd ed. New York: Springer, 2002.
[253] S. M. Holland, "Principal Component Analysis (PCA)," *Department of Geology, University of Georgia, Athens, GA 30602-2501,* p. 10, 2008.
[254] SAS, *SAS/STAT® 9.2 User's Guide The CLUSTER Procedure (Book Excerpt)*. Cary, NC USA: SAS Institute Inc., 2008.
[255] A R H Swan and M. Sandilands, *Introduction to geological data analysis*. Oxford ; Cambridge, Mass., USA: Blackwell Science, 1995.
[256] G. Kerschen, P. De Boe, J. C. Golinval, and K. Worden, "Sensor validation using principal component analysis," *Smart Materials & Structures,* vol. 14, pp. 36-42, Feb 2005.
[257] E. A. Baldwin, J. H. Bai, A. Plotto, and S. Dea, "Electronic Noses and Tongues: Applications for the Food and Pharmaceutical Industries," *Sensors,* vol. 11, pp. 4744-4766, May 2011.
[258] Hans-Rolf Tränkler, Olfa Kanoun, Mart Min, and Marek Rist, "Smart sensor systems using impedance spectroscopy," *Proceedings of the Estonian Academy of Sciences Engineering,* vol. 4, pp. 455–478, November 2007 2007.
[259] A. Miszczyk and K. Darowicki, "Multispectral impedance quality testing of coil-coating system using principal component analysis," *Progress in Organic Coatings,* vol. 69, pp. 330-334, Dec 2010.
[260] C. A. Olivati, A. Riul, D. T. Balogh, O. N. Oliveira, and M. Ferreira, "Detection of phenolic compounds using impedance spectroscopy measurements," *Bioprocess and Biosystems Engineering,* vol. 32, pp. 41-46, Jan 2009.

[261] J. Y. Heras, D. Pallarola, and F. Battaglini, "Electronic tongue for simultaneous detection of endotoxins and other contaminants of microbiological origin," *Biosensors & Bioelectronics,* vol. 25, pp. 2470-2476, Jul 15 2010.
[262] J. Wang, *Analytical Electrochemistry*, 3rd ed. Hoboken, New Jersey: John Wiley & Sons, 2006.
[263] Z. Kerner and T. Pajkossy, "Measurement of adsorption rates of anions on Au(111) electrodes by impedance spectroscopy," *Electrochimica Acta,* vol. 47, pp. 2055-2063, May 25 2002.
[264] A. S. Bondarenko and G. A. Ragoisha, *EIS Spectrum Analyser*: http://www.abc.chemistry.bsu.by/vi/analyser/, 2008.
[265] J. Levin and F. B. Bang, "Role of Endotoxin in Extracellular Coagulation of Limulus Blood," *Bulletin of the Johns Hopkins Hospital,* vol. 115, pp. 265-&, 1964.
[266] J. Levin, P. A. Tomasulo, and R. S. Oser, "Detection of Endotoxin in Human Blood and Demonstration of an Inhibitor," *Journal of Laboratory and Clinical Medicine,* vol. 75, pp. 903-&, 1970.

APENDICES

Lab VIEW Program Constructions for Auto-measurement

Appendix 1:

Main Panel (Main.vi)

The main panel shows the selections, controls and the display of the auto measurement data of material under test. A specific file must be named and selected before running the program. Other important parameters are number of measurements per sample test, speed, communication port, and measurement type. The voltage and average of measurements per decade (frequency) are set as default values. Figure A1.1 shows the main panel of the developed LabVIEW program.

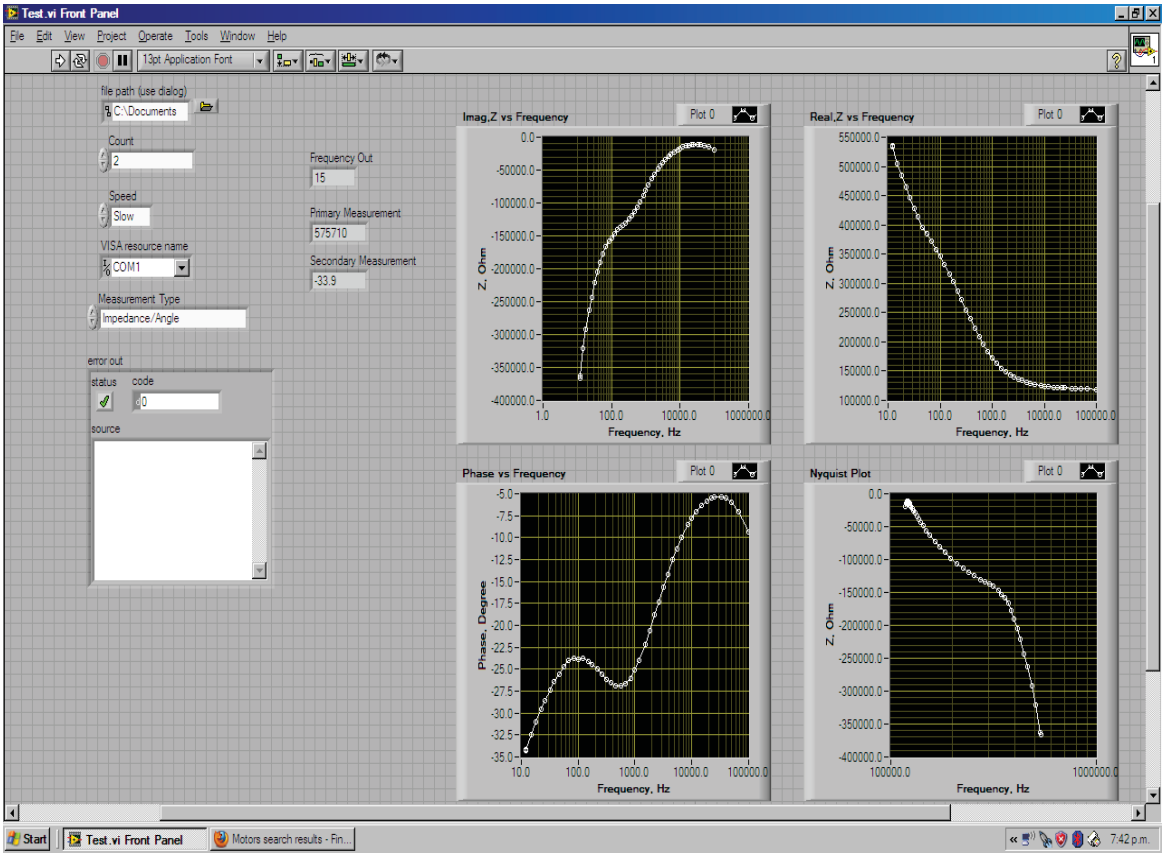

Figure A1.1: The front panel of the LabVIEW program.

The impedance data (Z) and the phase angle (θ) are two important parameters being measured from the LCR. In the system the primary measurement is for impedance, Z and the secondary measurement is for phase angle, θ. The impedance, Z measures the total amount of opposition between two terminals in an AC circuit. And the angle, θ measures the phase on which impedance is measured. The impedance measurement

plane can be seen as the polar coordinates as shown in Figure A1.2, where the Real (R_s), and Imaginary components (X_s) can be calculated (Equation A.1 – A.3). The block diagram in Figure A1.3 shows how the measurements are constructed in the LabVIEW.

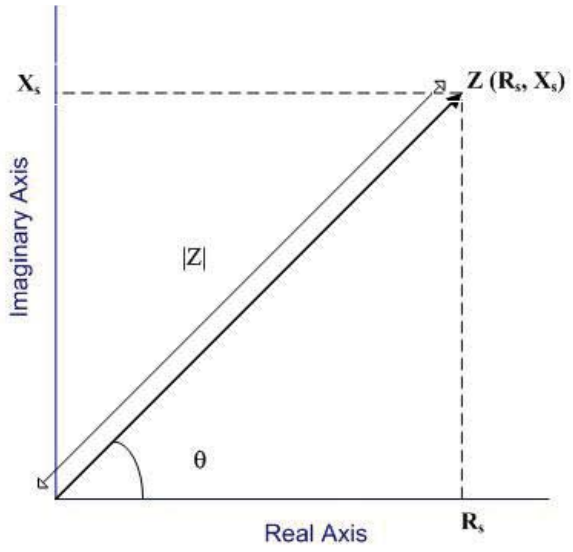

Figure A1.2: The impedance measurement plane

$$Z = |Z|\angle\theta = R_s - jX_s = R_s + 1/j(\omega C_s) \quad \textbf{A.1}$$

$$R_s = |Z|\cos\theta \quad \textbf{A.2}$$

$$X_s = 1/\omega C_s = |Z|\sin\theta \quad \textbf{A.3}$$

In the Main.vi the frequency is set to increase logarithmically from 12 Hz at step frequencies per decade which is determine by the default frequencies steps from the LCR-821. Figure A1.4 shows how the frequencies steps are constructed before it goes to Set Frequency.vi. The main block diagram is shown in Figure A1.5. The measurement data are displayed in term of Phase vs Frequency, Real (Z) vs Frequency, Imag, Z vs Frequency and Nyquist plot (complex impedance plane). All data is saved in csv format for further analysis.

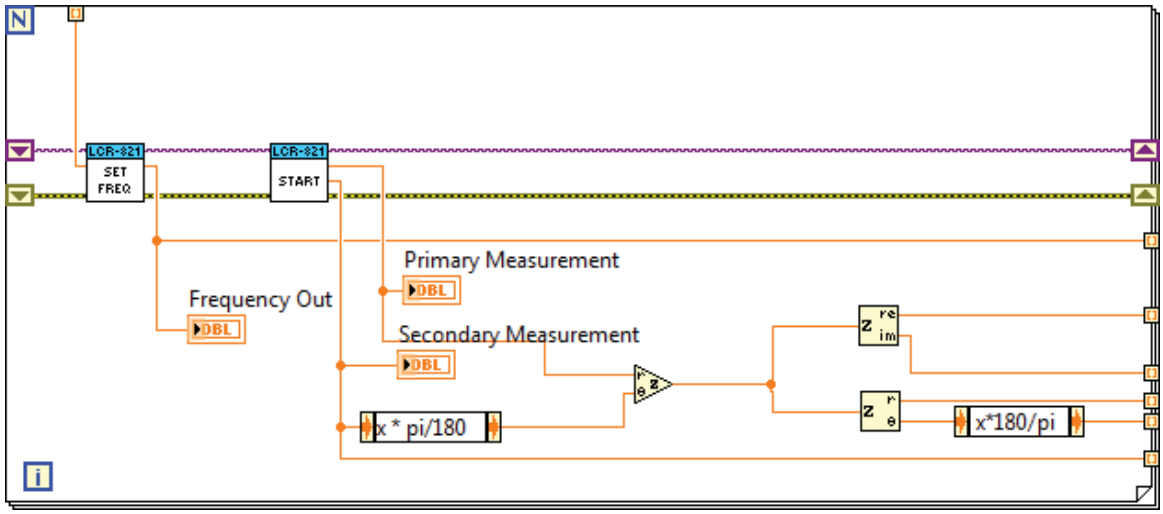

Figure A1.3: Block function to measure Impedance, Z and phase angle, θ and to calculate the Real and Imaginary components.

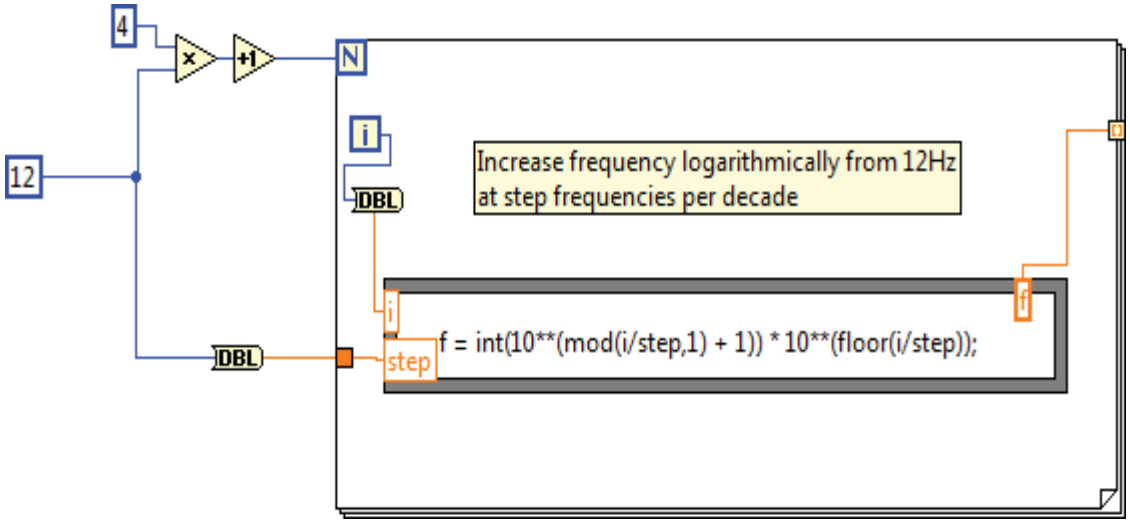

Figure A1.4: Block function to set frequency steps

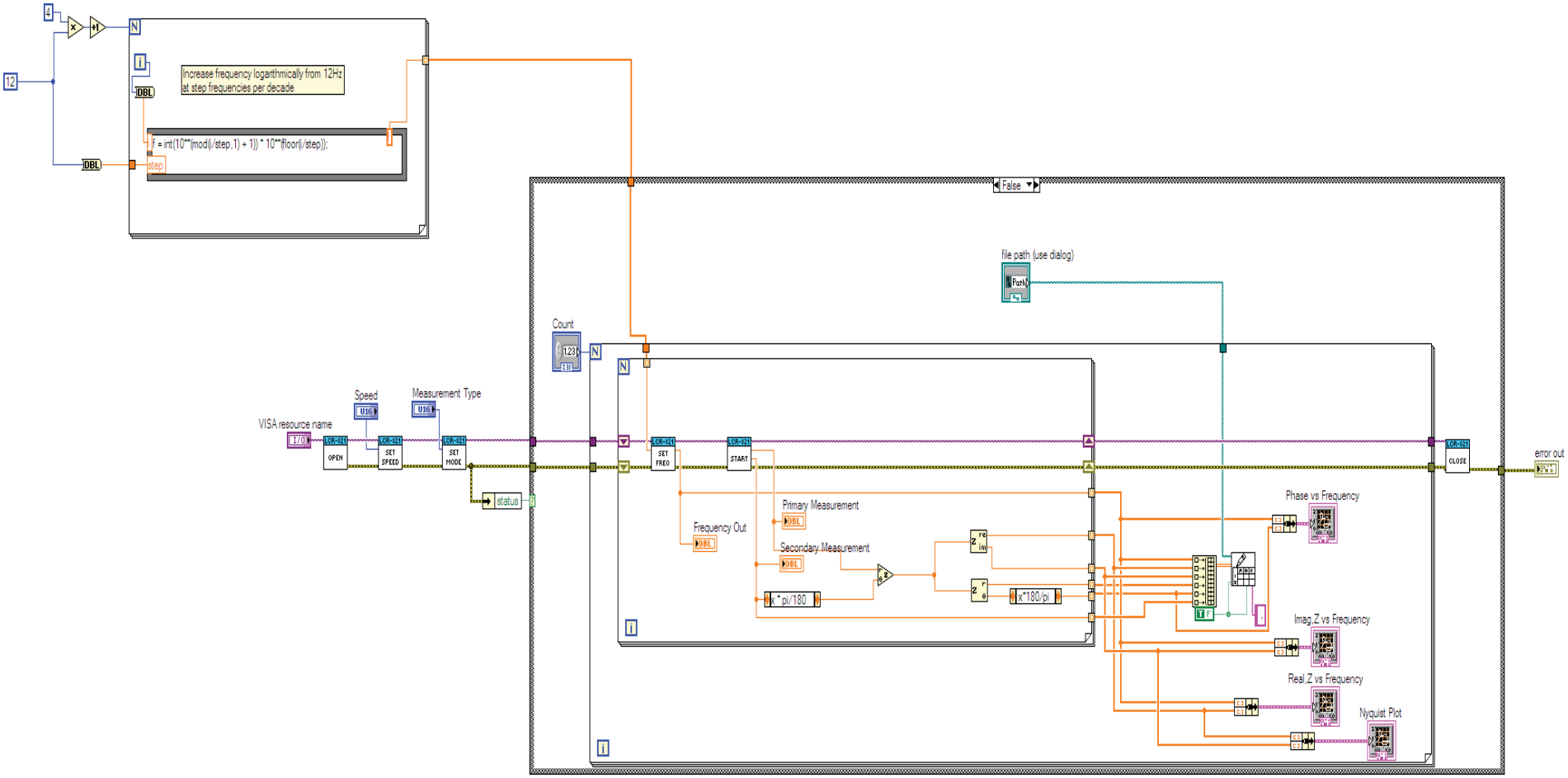

Figure A1.5: Block diagram of the main.vi

Appendix 2:

Open Panel (Open.vi)

The Open panel is to establish serial communication between LabVIEW program to LCR 821. The Open.vi will initialise the RS232 connection. Terminal program configuration setting for LCR-821 has the baud rate set to 38400, data bits-8, stop bit-1, parity-none and flow control-none. The command syntax for Open.vi is shown in Table A2.1 and Table A2.2 shows command syntax for the serial communication, RS 232. Figure A2.1 shows how the block diagram is constructed from the given syntax command.

Table A2.1: Command syntax to initiate RS232 connection

INITIATION HAS FINISHED (Initiate)	**Command**
Initiates the RS232 connection. A string is returned when the initiation has been completed.	
Syntax	COMU:OVER<^END^M>or<^J^M>
Return String	
<string>	Menu level
COMU:OVER<^END>	Connection initiation finished
Example	COMU:OVER<^END^M> COMU:OVER<^END> Communication initiation has completed "RS232 ONLINE" will be displayed on the LCR-821 display panel

Table A2.2: Command syntax for online function queries of RS232 connection status

ON-LINE		**Query**
The On-line function queries the RS232 connection status		
Query Syntax	COMU?<^END^M>or<^J^M>	
Return String		
<string>		RS232 Connection
COMU:ON..<^END^M>		Connection on
COMU:OFF.<^END^M>		Connection off
Example	COMU?<^END^M>	
	COMU:ON..<^END^M>	
	The RS232 connection is on	

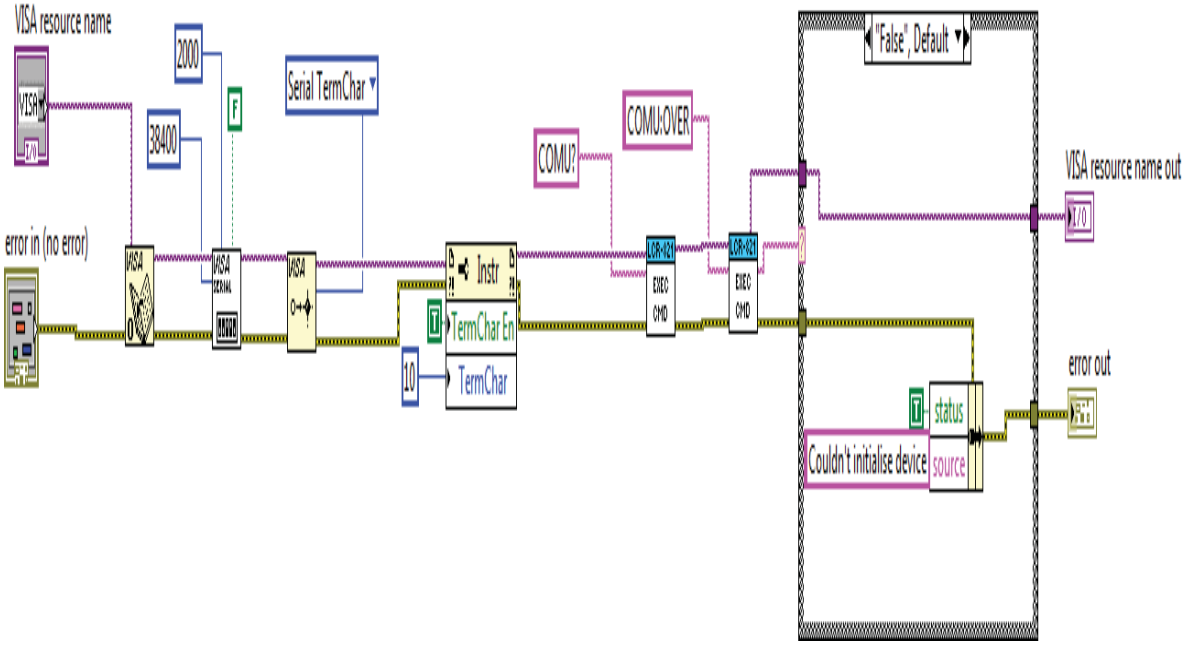

Figure A2.1: Block function of Open.vi to initiate RS232 connection

Appendix 3:

Close panel (Close.vi)

The Close panel is to terminate serial communication or RS232 between LabVIEW program to LCR 821.The command syntax for Close.vi is shown in Table A3.1 and Figure A3.1 shows how the block diagram is constructed from the given syntax command.

Table A3.1: Command syntax to terminate RS232 connection

OFF LINE	**Command**
Terminates the RS232 connection. A string is returned when the initiation has completed.	
Syntax	COMU:OFF.<^END^M>or<^J^M>
Return String	
<string> **COMU:OFF.<^END>**	RS232 connection Terminated
Example	COMU:OFF.<^END^M> COMU:OFF.<^END> The RS232 connection has been terminated

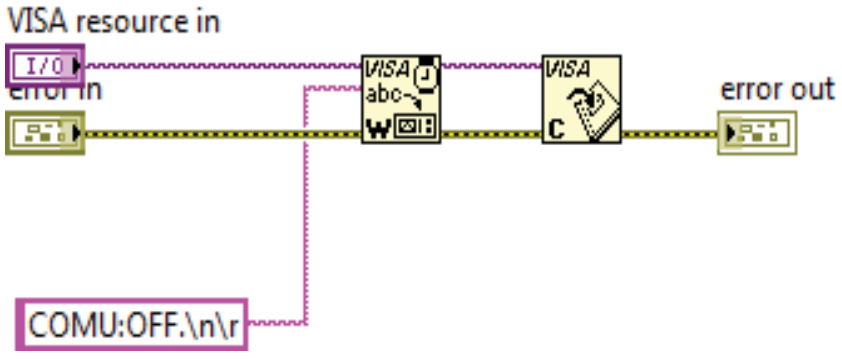

Figure A3.1: Block function of Close.vi to terminate RS232 connection

Appendix 4:

Set Speed Panel (Set Speed.vi)

The Speed panel sets the measurement speed of LCR-821. The measurement speed can be selected for FAST, SLOW and MEDIUM. The faster the measurement speed will result the lower in accuracy of the instrument. SLOW speed will has 0.05% basic measurement accuracy, FAST and MEDIUM speed has 0.1% of accuracy. The command syntax of the set speed measurement is shown in Table A4.1. Figure A4.1 shows the block diagram of the sets of speed measurements.

Table A4.1: Command syntax to set measurement speed

SPEED	**Command/Query**
The speed command set the measurement speed of the instrument. The faster the measurement speed the lower the accuracy. This command also queries the current measurement speed.	
Syntax	MAIN:SPEE:<STRING><^END^M>or<^J^M>
Parameter	
<string>	Speed
SLOW	Slow
MEDI	Medium
FAST	Fast
Example	MAIN:SPEE:SLOW<^END^M> Set the measurement speed to slow.
Query Syntax	MAIN:SPEE?<^END^M>or<^J^M>
Return String	
<string>	Speed
MAIN:SPEE:SLOW<^END>	Slow
MAIN:SPEE:MEDI<^END>	Medium
MAIN:SPEE:FAST<^END>	Fast
Query Example	MAIN:SPEE?<^END> MAIN:SPEE:MEDI<^END> Medium measuring speed is returned.

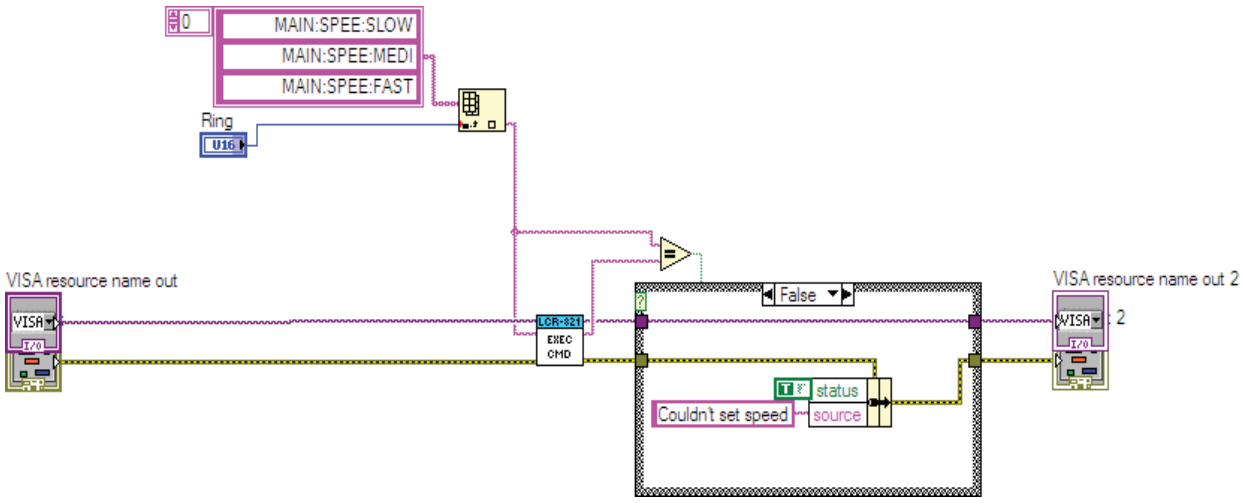

Figure A4.1: Block function of Set Speed.vi for speed measurement selection

Appendix 5:

Set Frequency Panel (Set Frequency.vi)

The Frequency panel sets the test frequency of LCR-821. The LCR-821 provides wide test frequency of 12 Hz – 100 kHz with 504 steps/decades. The command syntax of the test frequency is shown in Table A5.1. Figure A5.1 shows the block diagram for the test frequency. The frequencies steps (variables) are constructed in the Main.vi (Figure 9.5) before entering the Set Frequency.vi.

Table A5.1: Command syntax to set test frequency

FREQUENCY	**Command/Query**
Set or queries the test frequency	
Syntax	MAIN:FREQ<variable><^END^M>or<^J^M>
Parameter	
<variable> **0.01200-100.000**	Frequency (kHz) (7 characters, including a decimal) 12 Hz – 100 kHz
Example	MAIN:FREQ 0.01200<^END^M> Set the frequency t0 12 Hz (0.012 kHz)
Query Syntax	MAIN:FREQ?<^END^M>or<^J^M>
Return String	
<string> **MAIN:FREQ<variable><^END>** **(variable >=0.01200~100.00)**	Frequency Returns the test frequency in kHz
Query Example	MAIN:FREQ?<^END^M> MAIN:FREQ 0.01200<^END> Returns the current test frequency in kHz (12 Hz)

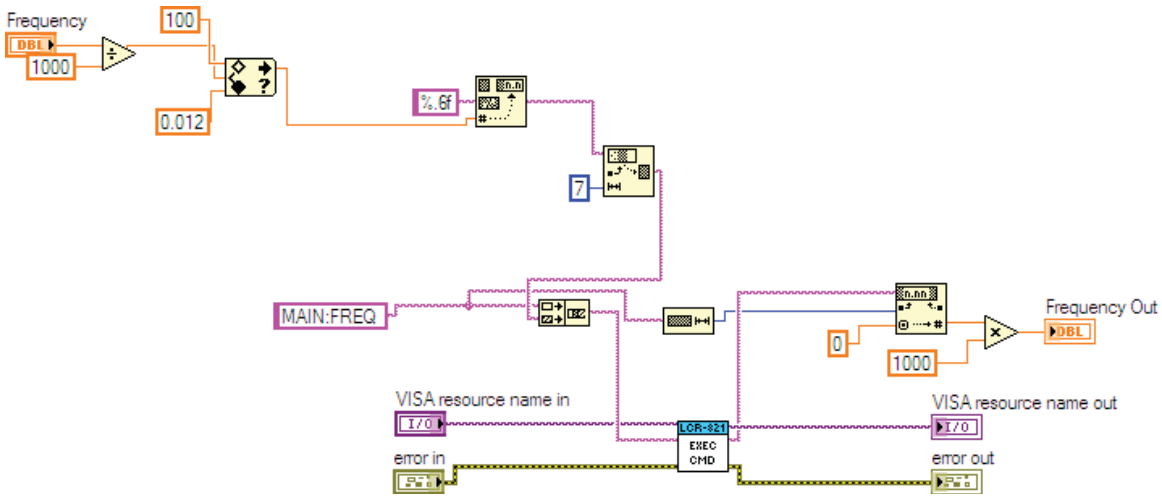

Figure A5.1: Block function of Set Frequency.vi for test frequency

Appendix 6:

Set Mode Panel (Set Mode.vi)

The Mode panel sets the measurement mode of LCR-821. The LCR-821 provides primary and secondary measurements. The command syntax of the measurement mode is shown in Table A6.1. Figure A6.1 shows the block diagram for the test frequency.

Table A6.1: Command syntax to set mode

MODE		**Command/Query**
The mode command sets the measurement mode of the instrument.		
Syntax	MAIN:MODE<string><^END^M>or<^J^M>	
Parameter		
<string>	Primary Measurement	Secondary Measurement
RQ	Resistance	Quality Factor
CD	Capacitance	Dissipation Factor
CR	Capacitance	Resistance
LQ	Inductance	Quality Factor
LR	Inductance	Resistance
ZQ	Impedance	Angle
Example	MAIN:MODE:RQ<^END^M> Set the mode to R/Q (resistance/Quality Factor)	
Query Syntax	MAIN:MODE?<^END^M>or<^J^M>	
Return String		
<string>		Current measurement mode
MAIN:MODE:RQ<^END^M>		R/Q
MAIN:MODE:CD<^END^M>		C/D
MAIN:MODE:LQ<^END^M>		L/Q
MAIN:MODE:LR<^END^M>		L/R
MAIN:MODE:ZQ<^END^M>		Z/Q
Query Example	MAIN:MODE?<^END^M> MAIN:MODE:RQ<^END^M> Returns the current measurement mode as R/Q	

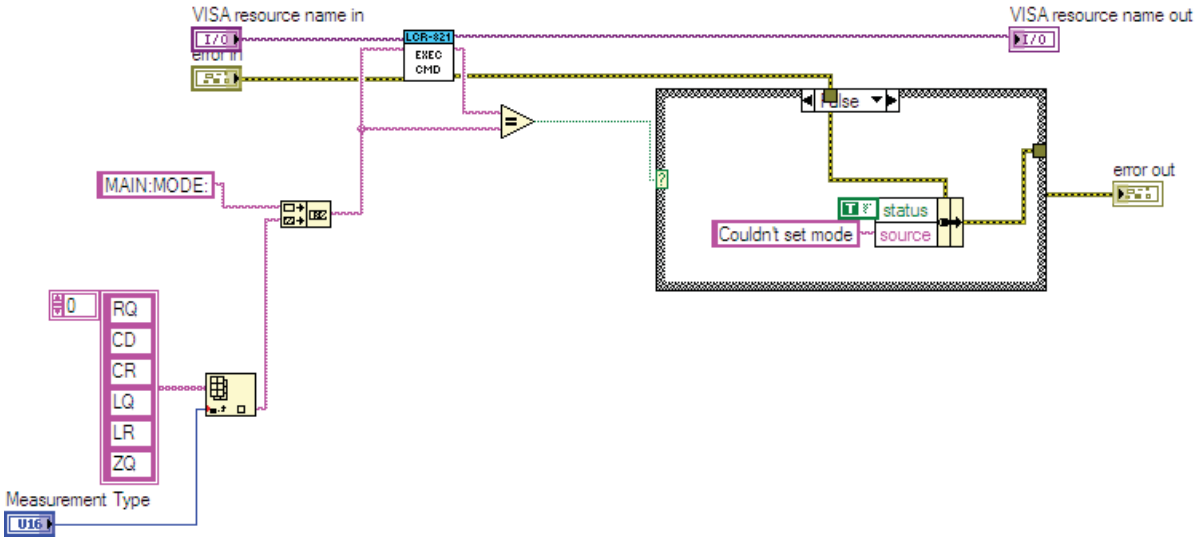

Figure A6.1: Block function of Set Mode.vi for measurement mode

Appendix 7:

Set Measurement Panel (Set Mesurement.vi)

The Start Measurement.vi provides the start measurement procedure. This is done in manual mode of the LCR-821. The manual mode allows the user to establish auto measurement programs. As the RS232 terminal connection successful, the instrument is operated in manual (MANU) mode for auto data measurement. The command syntax of the start measurement is shown in Table A7.1– Table A7.6 shows how primary measurement, secondary measurement and their limits of measurement range are programmed. Figure A7.1 shows the block diagram for the Start Measurement.vi to start primary and secondary measurement as well as indicate the limits.

Table A7.1: Command syntax for start measurement

START	**Command**
Starts a measurement in manual mode	
Syntax	MAIN:STAR<^END^M>or<^J^M>
Example	MAIN:STAR<^END^M> Starts the measurement

Table A7.2: Command syntax for primary measurement

PRIMARY FACTOR	**Measurement**
Primary factor returns the primary measurement results, and the measurement unit. This measurement is the first measurement displayed after measurements have been started.	
Return Syntax	MAIN:PRIM<value><^END>
<value> **Any 7 digit ASCII including sp(+) or (-) characters and a decimal point**	Test result Primary measurement value
Example	MAIN:PRIM 32.705><^END> The primary measurement is 32.705 (primary measurement unit)

Table A7.3: Command syntax for primary measurement exceeds measurement range

PRIMARY OV01	**Measurement**
Primary OV01 indicates that the primary measurement exceeds the measurement range of the LCR-821. For example: If the impedance of the DUT is less than the measurement range.	
Return Syntax	PRIM:OV01<^END>
Example	PRIM:OV01<^END> Note, no unit is returned

Table A7.4: Command syntax for both primary and secondary measurements exceeds measurement range

PRIMARY OVER SECONDARY OVER	**Measurement**
When both the primary and secondary factors exceed the range (OVER), OVER will be returned.	
Return Syntax	PRIM:OVER<^END>
Example	PRIM:OVER<^END> Note, no unit is returned

Table A7.5: Command syntax for secondary measurement

SECONDARY FACTOR & PRIMARY UNIT	**Measurement**
Returns the secondary measurement results and the primary unit. This measurement is the second measurement displayed after measurements have been started.	
Return Syntax	MAIN:SECO<value><unit1<^END>
<value>	Test result
Any 6 digit ASCII including sp(+) or (-) characters and a decimal point	Secoandary measurement value
<unit1>	Primary unit
nF,pF,uF	Nanofarads, picofarads, microfarads
ksp, spsp (sp=space character)	kΩ, Ω
mH, Hsp	millihenry, henry
Example	MAIN:SECO .0045nF<^END> The secondary measurement is .0045 (D) and nF is the primary measurement unit.

Table A7.6: Command syntax for Secondary measurement exceeds the measurement range

SECONDARY OVER & PRIMARY UNIT		Measurement
Secondary Over indicates that the secondary measurement exceeds the measurement range of the LCR-821. The unit returned refers to the primary measurement. Applicable for (R/Q C/D L/Q Z/θ) equivalent circuits		
Return Syntax	SECO:OVER<unit1<^END>	
<unit1>		Primary unit
nF,pF,uF		Nanofarads, picofarads, microfarads
ksp, spsp (sp=space character)		kΩ, Ω
mH, Hsp		millihenry, henry
Example	SECO:OVER nF<^END> The secondary measurement is OVER (exceed range) and nF is the primary measurement unit.	

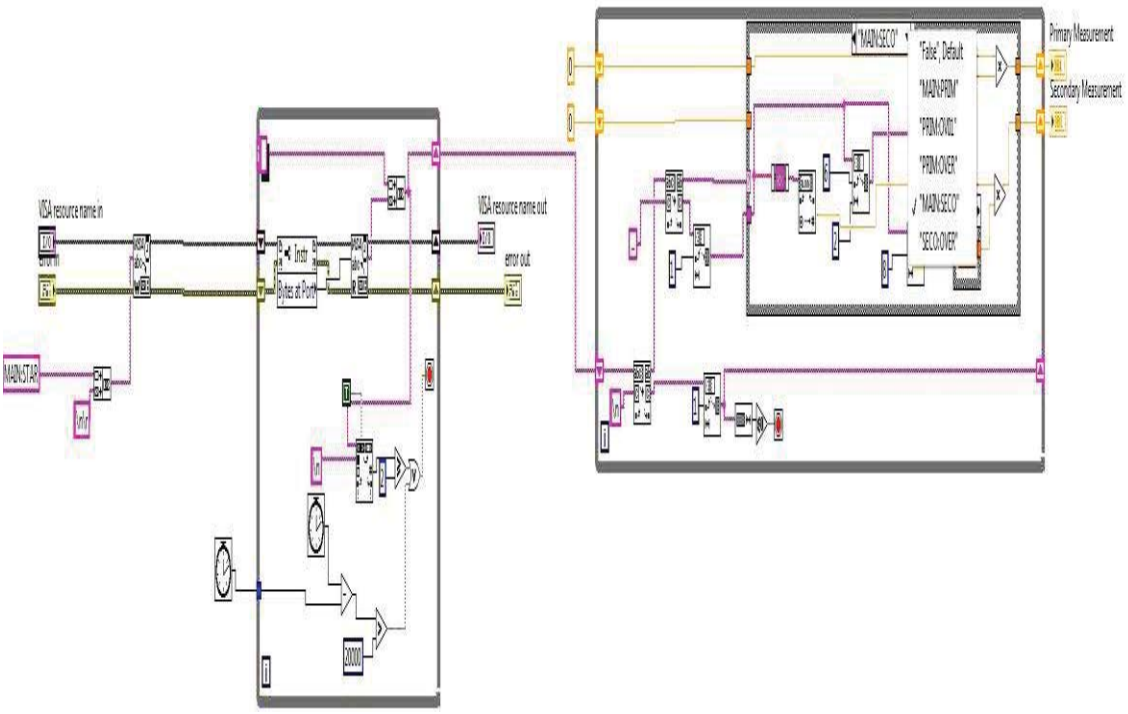

Figure A7.1: Block function of Start Measurement.vi to start measurement

Appendix 8:

Set Execute Panel (Set Execute.vi)

The Execute panel is constructed to execute each command developed in the LabVIEW. Figure A8.1 shows the block diagram of the execute command function.

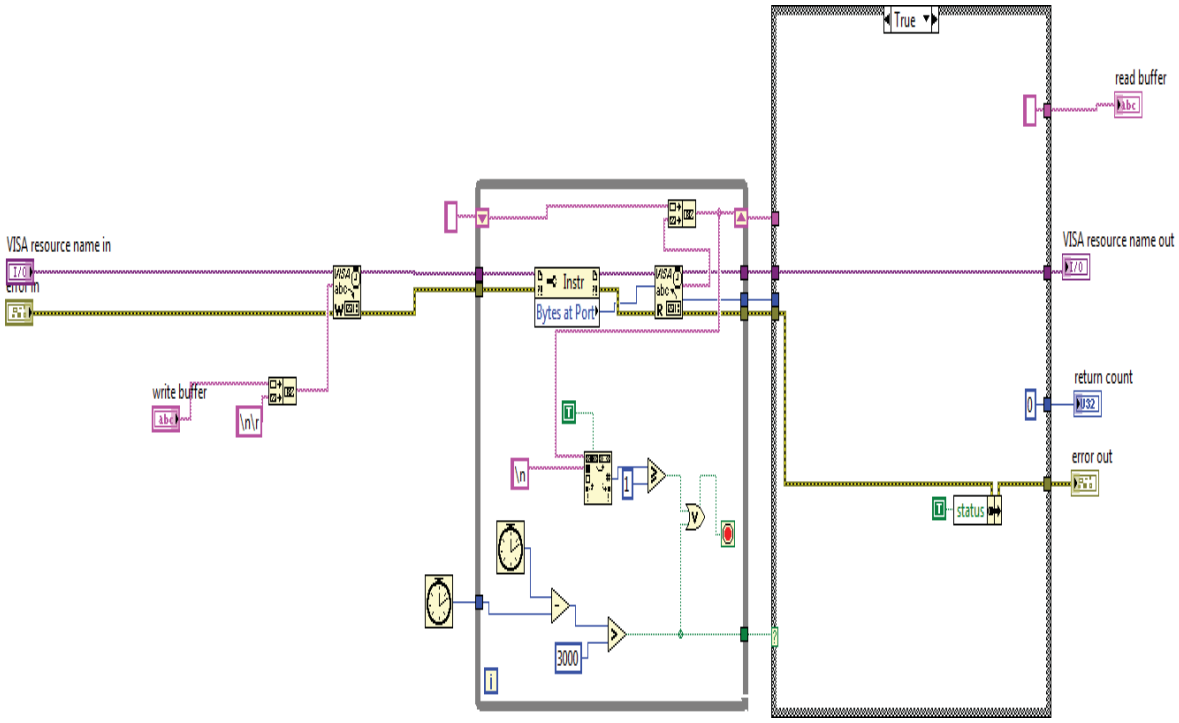

Figure A8.1: Block function of Execute command.vi to execute each command in the program